Studies on Thermodynamic Considerations and Effects of Alloying Elements upon Carburization, Coking, and Metal Dusting for Fe-Ni-Cr Alloys

(Fe-Ni-Cr 合金の浸炭、コーキングおよびメタルダスティング腐食の
熱力学的解釈および合金元素の影響に関する研究)

Yoshitaka NISHIYAMA

2005

ACKNOWLEDGEMENTS

The author would like to express his sincere gratitude to Professor S. Fujimoto for his encouragement and valuable discussions on the thesis. He would like to express his thanks to Professor T. Usui, Professor T. Tanaka, and Associate Professor S. Taniguchi for critically reviewing the manuscript.

He would like to express his thanks to Dr. T. Nishizawa, Professor emeritus at Tohoku University, for valuably suggesting the kinetics of carburization in Chapter 2.

The present study was carried out at Corporate Research and Development Laboratories, Sumitomo Metal Industries, Ltd. He wishes to express his sincere gratitude to Dr. K. Toyama, General Manager of Corporate Research and Development Laboratories for permitting the publication of this thesis. He also would like to thank to Professor Y. Komizo of Osaka University, former Assistant general manager of Corporate Research and Development Laboratories, for giving the opportunity to commence this thesis. He would like to deeply thank to Dr. T. Kudo, Senior Research Manager of Corporate Research and Development Laboratories, for his continuous encouragement and empathic comments. Dr. N. Otsuka, General Manager of Pipe & Tube Research and Development Department, is thanked for his support of the study and critically suggestions. The author expresses his special thanks to Dr. K. Moriguchi for computing the electron structure and for discussing the surface interaction (Chapter 7). He also thanks Mr. Y. Nagayama, Mr. N. Yasuda and Mr. S. Ishibashi for experimental support with the sophisticated techniques.

Finally, the author gratefully acknowledges his wife Emiko, his parents, and his wife's parents whose patient love and support enabled him to complete this work, and dedicates it to his late brother Hidetaka.

2005 Y. N.

CONTENTS

Chapter 1

INTRODUCTION

1.1 General Introduction

In carbonaceous gas environments containing hydrocarbon (H_mC_n), CO, and CO_2 at high temperatures, carbon decomposed from the gaseous phase penetrates into an alloy and combines with alloying elements such as Fe, Cr, Ti, Nb, Zr, etc. This phenomenon "carburization" enables the surface layer of materials to be hardened by controlled quenching, resulting in remarkable amelioration of abrasion resistance. Therefore, carburized materials are commonly applied to machinery such as gears, shafts, and bearings for automobiles and ships [1]. On the other hand, carburization causes undesirable issues for materials used at high temperatures in industrial furnaces, reformers, and reactors. It deteriorates mechanical properties of the materials and causes metal loss, which may result in a failure of components during use. Inspection on carburization was conducted late 1950s [2 - 4], and since then many studies have been reported [5 - 10] and reviewed [11,12]. Thermodynamic criterion for carburization of metals and alloys can be expressed as follows:

$$a_c^{gas} > a_c^{metal} \quad (1)$$

where a_c^{gas} is carbon activity in gas mixtures and a_c^{metal} carbon activity of metals and alloys. The a_c^{metal} depends on chemical composition of an alloy as well as temperature, and has been obtained for ferritic steels [13] and for austenitic alloys [14] by thermodynamic experiments. For austenitic stainless steels, it is within the orders of 10^{-2} and 10^{-3} at temperatures between 700-1,000°C. The a_c^{metal} increases with increasing alloying elements that lower the carbon solubility of the alloy and decreases with rising

temperature. According to thermodynamics, a_c^{gas} must be considered as an index to represent the carburization propensity of the gas atmosphere. Possible reactions by which carbon is transferred into the metal are as follows:

$$CO + H_2 = H_2O + \underline{C} \quad (2)$$

$$2CO = CO_2 + \underline{C} \quad (3)$$

$$C_nH_m = C_{n-1}H_{m-2} + H_2 + \underline{C} \quad (4)$$

$$CH_4 = 2H_2 + \underline{C} \quad (4')$$

where $\underline{C}$ represents dissolved carbon in the alloy, and the carbon activity at the surface of alloy in equilibrium with the ambient gas is equal to a_c^{gas}. Equilibrium constants K of these reactions are shown in Fig. 1-1 as a function of temperature. The equilibrium constants K of Eqs. (2) and (3) decrease and that of Eq. (4') increases with increasing temperature. Therefore, for lower temperatures, reactions involving CO can strongly affect carburization. At higher temperatures, reaction such as Eq. (4') that involves hydrocarbon would become important for carburization.

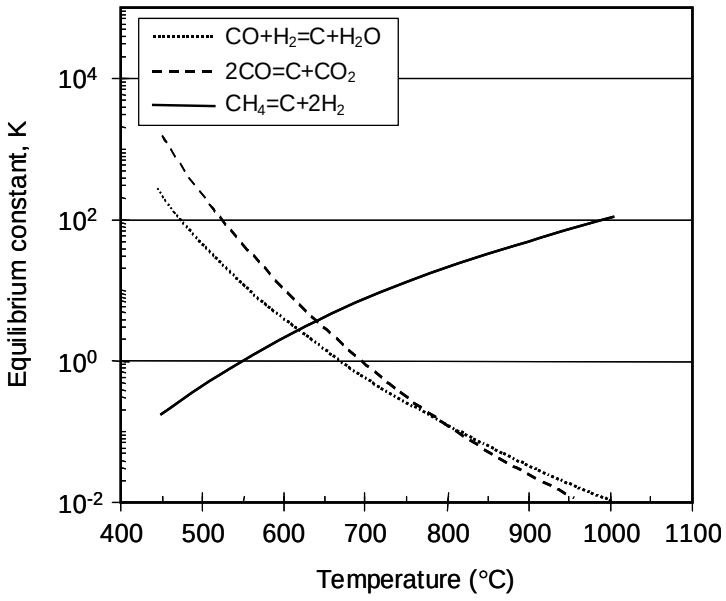

Figure 1-1 Equilibrium constants of reactions relating to carbon activity at temperatures between 450°C and 1,000°C. Data were taken from ref. [15].

When a_c^{gas}, which is derived from the above reaction under a certain gas composition, exceeds unity, carbon dissociated from carbonaceous gases deposits on the metal surface. This is called "coking" or "coke formation". These coke deposits are complex mixtures, which contain various sort of carbon with different morphology, structure, and origin. Two types of coke are generally reported to

form in the hydrocarbon processing [16,17]. One is pyrolytic carbon such as surface carbon and soot generated upon thermal decomposition of hydrocarbon, which is obtained by homogeneous reaction in the gas phase of high carbon activity at high temperatures. Morphology of this carbon is characterized by amorphous and powder-like [18]. The other is catalytic carbon formed by decomposition of hydrocarbon gas species on the metal surface catalyzed by reactive metals. This is defined by porous but hard coke that aggregated filamentous (and flake-like in some cases) carbon with fine graphite crystallites [18,19]. In addition, it is most characteristic that catalytic carbon includes small metal particles such as Fe, Ni, and Co. Pyrolytic carbon deposits on a metal inevitably during service, since its formation is affected by thermodynamic factor, i.e. gas species, gas composition, temperature, and residence time. On the other hand, if the catalytic one that is caused by alloying elements is concerned to a plant operation, the materials should be alloy-designed for components at high temperature.

In actual plants, carburization does not occur exclusively because gas atmosphere contains a low oxygen partial pressure. These gas mixtures make thermodynamic consideration complicated, although possibility of oxidation enables metals to be protected against severe carburization at high temperature. In the complex gas atmosphere, oxide sales are formed, followed by internal carburization in the metal. Oxide scales of Cr_2O_3 and spinel-type M_3O_4 (M =Cr, Fe, Ni, Mn) mainly form on the surface of Fe-Cr, Fe-Ni-Cr, and Ni-Cr alloys. Additionally, alloys containing proper content of Si and Al promote the formation of SiO_2 and Al_2O_3 scales, respectively. Generally, the Cr_2O_3 scale, which is compact and uniform, is used to protect against carburization for the alloy of components in various industrial furnaces, reformers, and reactors. Representative industrial plants relevant to carbonaceous gas atmosphere are such as ethylene pyrolysis, reformers, coal gasification plant, and CO_2-cooled reactors. Each gas condition is superimposed in C-O-H ternary system in Fig.1-2 [20]. In ethylene pyrolysis, mole fraction of hydrogen N_H is very high, while that of carbon N_C and that of

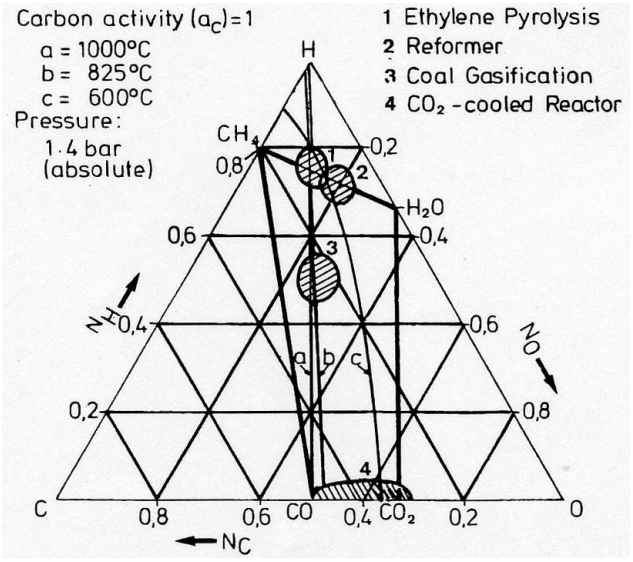

Figure 1-2 Ternary diagram for C-O-H system indicating approximate environmental regions relevant to commercial processes [20].

oxygen N_O are low, and carbon activity of the gas atmosphere takes unity within wide ranges of temperature. For the reformer to product syngas, a_c takes unity at lower temperatures, although the ratio of atomic component is almost the same as that in ethylene pyrolysis. Higher N_C and N_O, a_c takes unity only at higher temperatures in an atmosphere of coal gasification. For CO_2-cooled reactors, the N_H is almost zero; gaseous CO and CO_2 constitute ambient atmosphere. According to these thermodynamic considerations, mode of carburization may differ in each industrial plant. For the ethylene pyrolysis furnaces and syngas reformers, detailed operational provision against carburization is described below.

Ethylene pyrolysis is considered the most important process in the petrochemical industry [21]. Pyrolysis furnaces produce olefins, i.e. ethylene, propylene, and butadiene that are the building blocks in manufacturing of polymers and elastomers or converted into derivatives such as aldehydes, alcohols, glycols, etc. Olefins are primarily produced by steam cracking of large hydrocarbon (H_mC_n) molecules. A typical operating pattern for ethylene pyrolysis furnace is shown in Fig. 1-3 [22]. Feedstock of hydrocarbon such as naphtha and gases of ethane and butane is mixed with steam at a certain ratio desired, and the mixtures are passed through furnace tubes heated radiantly over 930°C. Since coke that deposits on the inner wall of radiant tubes during the cracking process reduces heat transfer efficiency and reduces the tube bore, it lowers product yields and throughput required for ethylene pyrolysis. To secure the

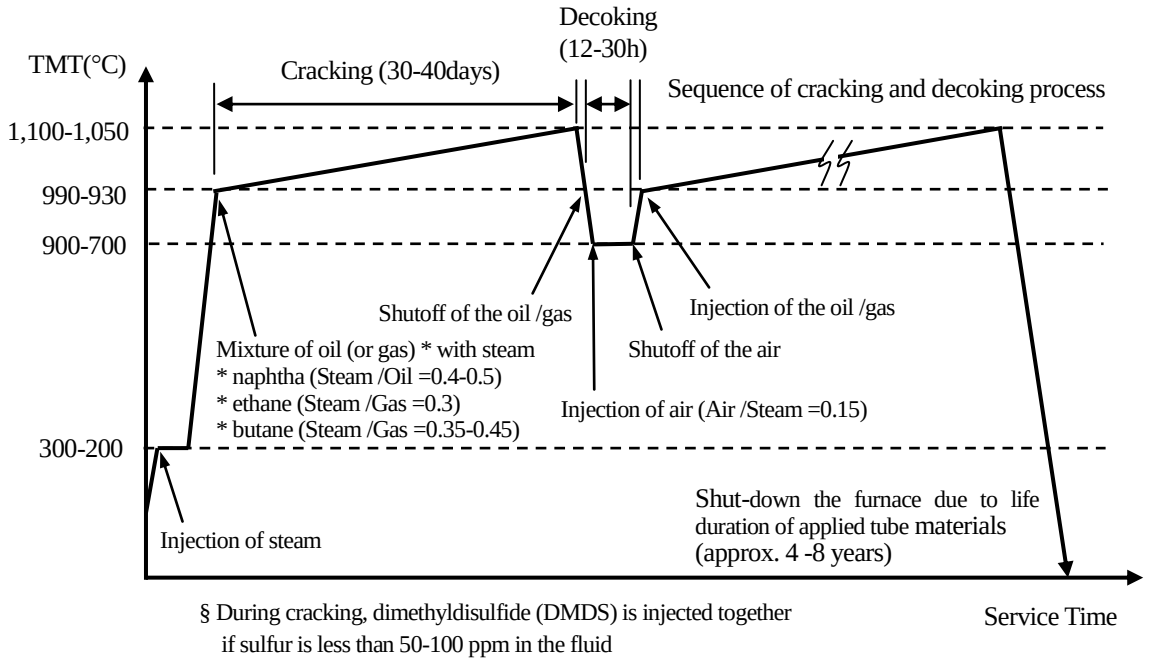

Figure 1-3 An example of plant operating pattern for an ethylene pyrolysis furnace in petrochemical industries.

constant product yield, temperature of inside fluid at outlet tubes (COT: Coil Operating Temperature) should be kept constant during the cracking process. Therefore, temperature of the outer tube surface (TMT: Tube metal Temperature) by applying heat is increased gradually, leading to severe carburization for tubing alloys because the chemical reaction of hydrocarbon-steam gas mixtures becomes severer carburizing atmosphere with increasing temperature (see Fig. 1-2). Meanwhile, in conjunction with carburization, oxidation also occurs on alloy tubes due to the existence of oxygen partial pressure originated from steam. In gas mixtures of C_2H_6-H_2O-bal.H_2 concerning ethane pyrolysis furnaces, oxygen partial pressure Po_2 increases with increasing H_2O content and with decreasing C_2H_6 content [23]. This analysis instructs us that what compound is stable depends on the gas composition; ratio of ethane to steam in this case. Therefore, potency of the oxidation struggles against the abhorrent carburization in actual plants.

Once the TMT reaches to approx. 1,100°C owing to coke formation, a decoking process during which air and dilute steam instead of naphtha or gases are enforced at temperatures between 700-900°C is carried out. Possible reactions in this procedure are:

$$C + H_2O = CO + H_2 \quad (5)$$

$$CO + 1/2O_2 = CO_2 \quad (6)$$

During this process, inside of alloy tubes is exposed to "completely" oxidizing environment. Thus, on the surface, not only the deposited coke but also alloying elements could be oxidized thermodynamically. Such a decoking process is carried out at certain intervals (normally of 30-40 days) in ethylene pyrolysis furnaces, which implies that tubing alloys are repeatedly subject to carburization and oxidation. Since the decoking process decreases product yields and throughput, olefin producers have sought effective ways over the last 20 years to lengthen the interval between decoking. Therefore, development of alloys to bear coke formation as well as carburization is still urged.

Reforming process, where syngas including CO, H_2, CO_2, and H_2O is produced from natural gas (or coal in some cases), significantly affects the end-products quality in ammonia, methanol, and hydrogen plants. New fuels, GTL (Gas to Liquids) and DME (Dimethyl Ether), are also made through "reforming " process [24 - 26]. They are in the limelight as future fuels, which will be substitution of

diesel oil for automobile and be resources for hydrogen-powered fuel cell vehicles. A typical reforming technique includes steam reforming, partial oxidation reforming (POX), auto-thermal reforming (ATR), and combined reforming [27,28], and their flows are represented in Fig. 1-4. In these processes, the following reactions proceed:

Steam Reforming: $CH_4 + H_2O = 3H_2 + CO$ (7)

POX: $CH_4 + 1/2O_2 = 2H_2 + CO$ (8)

Along with the above reactions, water-gas-shift reaction of Eq. (9) occurs in the gas atmosphere.

$$CO + H_2O = CO_2 + H_2 \quad (9)$$

In this gas atmosphere, a severe corrosion phenomenon "metal dusting", which is one of carburization mode, can occur to alloys [12,29]. This corrosion has been identified on inlet tubes and ferrules in a waste heat boiler, shown in Fig.1-4 (left). In addition, this is susceptibly occurred on tubes of a heat exchanger-type steam reformer, which is designed to improve the plant efficiency for the future (Fig. 1-4 (right)). Metal dusting forms pits and grooves on a metal surface by disintegration of metals into dust of metal particles and graphite. Coke catalyzed by the metal particles germinates at the inside of pits and grooves. This corrosion occurs under conditions of high carbon activities of $a_c > 1$, and relatively low oxygen partial pressures at intermediate temperatures between 400 to 800°C. Once metal dusting occurs, localized-catastrophic metal wastage proceeds rapidly, leading to failure of metal components of reforming plants [30,31]. This situation significantly shortens the lifetime of tube alloys. It may decrease the syngas productivity, and increase the operating cost. Therefore, corrosion resistant alloys are desired to be used for components of reforming plants.

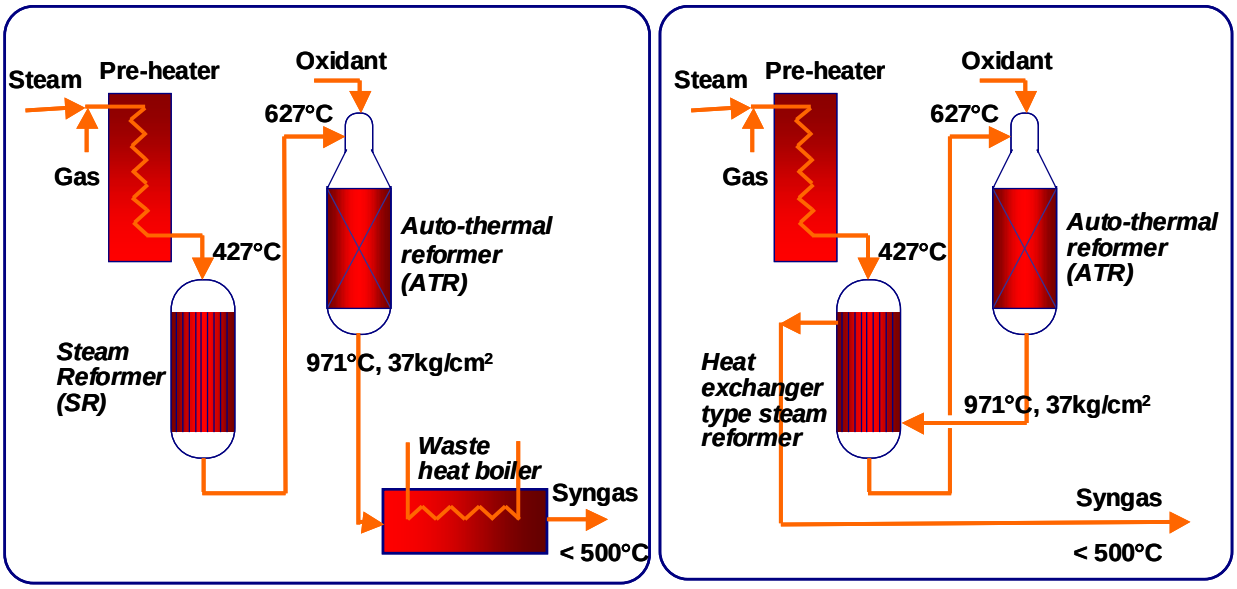

Figure 1-4 Typical examples of syngas production flow. Left figure shows combined (2-step) reforming process, followed by waste heat boiler. Right one, the same reforming process, but a steam reformer is simultaneously worked as a heat exchanger.

1.2 Background

Upon ethylene pyrolysis furnaces, simultaneous coke formation (coking) and carburization of tube alloys can deteriorate the mechanical properties of the tube materials and may result in a failure of furnace tubes. To understand carburization behavior in this environment, thermodynamic considerations are significant and have been reported [23,32 - 36]. Kane [23] has conducted thermodynamic analyses of complex gas atmosphere for ethane-feedstock pyrolysis furnaces by computational technique. For example, a gas mixture of 14%C_2H_6-30%H_2O -bal.H_2 (vol.%) provides the oxygen partial pressure, Po_2 of about 10^{-17} atm at 1,093°C, where Cr_2O_3 can be formed stably on the alloy surface as shown in Fig. 1-5.

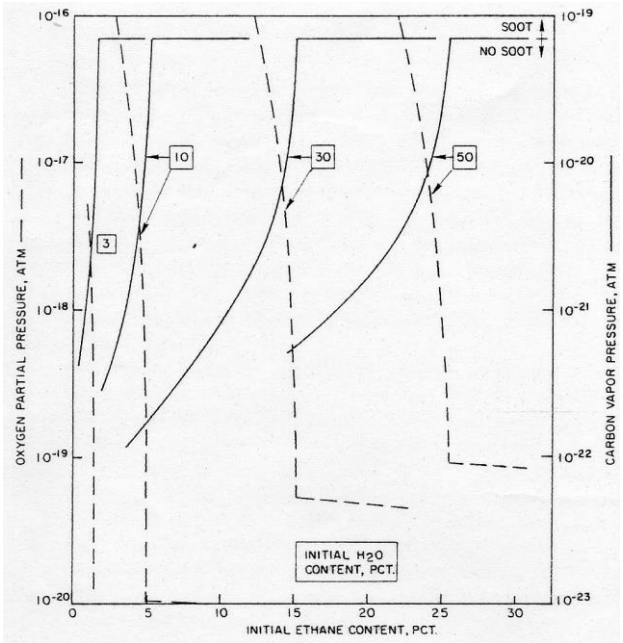

Figure 1-5 Resulting oxygen and carbon vapor pressures from equilibration of hydrogen-water vapor-ethane mixtures at 1093°C [23].

Grabke and co-workers [33] have studied a stability of Cr-oxide that is formed in CO-CO_2 gas atmospheres. At constant P_{CO}, reactions of Eqs. (10) and (11) yield temperature dependence of the ratio P_{CO_2}/P_{CO} in proportion to partial pressure of oxygen P_{O_2}.

$$7Cr_2O_3 + 33CO = 2Cr_7C_3 + 27CO_2 \quad (10)$$

$$3Cr_2O_3 + 17CO = 2Cr_3C_2 + 13CO_2 \quad (11)$$

The ratio P_{CO_2}/P_{CO} for Eq. (3) decreases with increasing temperature, and for P_{CO} = 0.345 atm in CO-CO_2 gas atmosphere, Eqs. (10) and (11) are equilibrated at about 1,040°C and 1,050°C, respectively (Fig. 1-6). Thus, in CO-CO_2 atmospheres and in contact with carbon (a_c =1), the Cr_2O_3 scale could be converted to Cr-carbides at temperatures above 1,040-1,050°C. Chu et al. [35] have also reported the conversion of Cr-oxide to Cr-carbide in a CO-CO_2 gas mixture, clearly showing its critical temperature which depends on the CO pressure, carbon activity, and the activities of Cr oxide and carbide in Fig. 1-7.

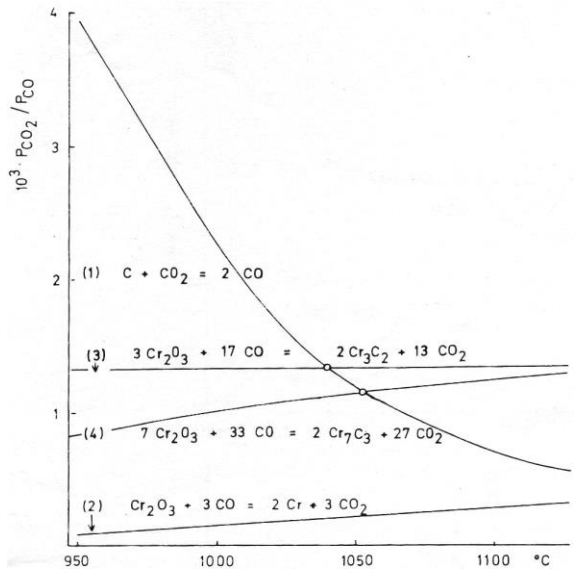

Figure 1-6 Ratio of partial pressures P_{CO_2}/P_{CO} for the given equilibria as a function of temperature, calculated for constant P_{CO} =0.345 atm. The diagram describes the conditions in the pack carburization test [33].

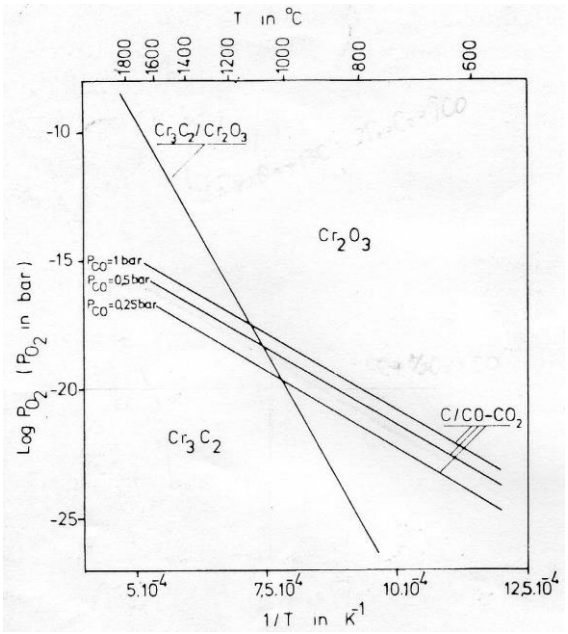

Figure 1-7 Temperature dependence of the oxygen pressures of the Cr_2O_3-Cr_3C_2 equilibrium and the C-CO-CO_2 equilibrium at three different CO pressures [35].

Colwell et al. [36] have investigated phase stability (and also metastability) of Fe-Cr and Ni-Cr alloys with various Cr content, i.e. changing Cr activity, that were reacted at 850°C and 950°C in CO-CO_2 gas mixtures and the results are expressed as Fig. 1-8. In this figure, both region of stable Cr_7C_3 and Cr_2O_3 extend with increasing Cr content (increasing of a_{Cr}), implying that higher Cr content alloys can form a protective oxide scale on the surface, but simultaneously susceptibility to carburization becomes higher so that metastable Cr-carbides may precipitate beneath the Cr_2O_3 scale. As described, the thermodynamic analyses have been conducted for Cr-O-C, Fe-Cr-O-C, and Ni-Cr-O-C system reacted with CO-CO_2 gas mixtures. These considerations give somewhat useful information relevant to the stability of Cr; however, more complicated gas atmospheres are produced in the actual pyrolysis furnaces since the gas components are not the C-O system but the C-H-O system including hydrocarbon and steam.

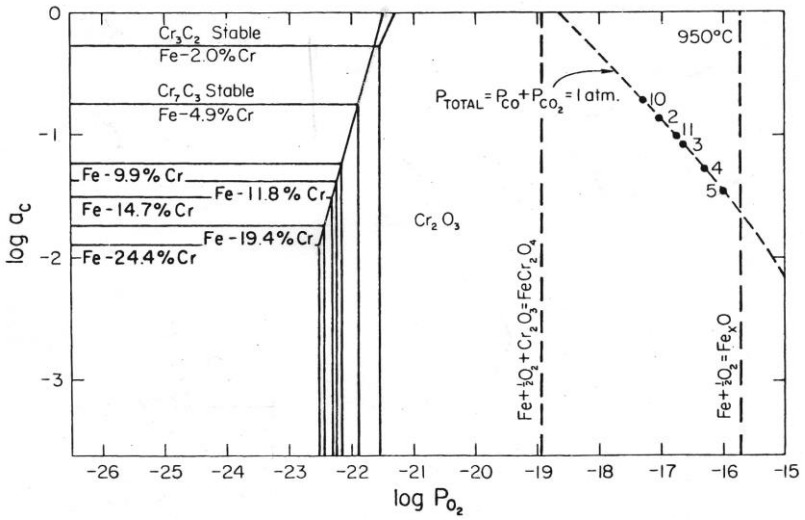

Figure 1-8 Fe-Cr-C-O phase stability plot at 950°C [36].

There are several studies where carburization tests were conducted in H_mC_n-H_2 gas mixtures [37 - 39]. These tests are considered useful for studying diffusion of carbon in steels, alloys etc., but their environments are "purely" carburizing and do not allow the oxide formation. Thus these tests could not provide a reasonable evaluation for the carburization resistance of steels and alloys in practical furnaces. In actual cracking gases, oxygen is present as H_2O, CO, and CO_2, so that there must be some Po_2 which may form oxide scales on tube surfaces. Some tests which have been conducted in carburizing atmosphere involving "oxidizing" are reported in the literature. Hemptenmacher and Grabke [40] have conducted carburization test under creep conditions for alloy 800H (UNS N8810, 21%Cr-32%Ni) in

CO-H_2O-H_2 atmospheres, showing beneficial effect of Nb and Ce against carburization. Mitchell et al. [41] have showed that Cr_2O_3 scale can protect for alloys up to 1000°C in a C_3H_6-H_2-H_2O gas atmosphere. Ganesan et al. [42] have reported that the Cr oxide scale maintained its growth on the alloy surface and acted as a diffusion barrier for carbon to enter into the underlying matrix in a CH_4-CO_2-H_2 gas atmosphere at 1,100°C. Otomo et al. [43] conducted carburization tests in a C_3H_8-CO-CO_2-H_2-N_2 gas mixture and found a similar effect of the Cr_2O_3 scale. They demonstrated the importance of Cr_2O_3 scales on the carburization resistance of steels and alloys in this environment. Young and co-workers [44,45] have performed cyclic carburization and oxidation tests: carburization was conducted at 1,000°C for 16h , followed by oxidation at 700°C for 4h. They found that the oxidation cycle caused rapid combustion of coke but did not remove surface carbides that had formed during the initial carburization cycle. Therefore, it followed that once the initial oxide was reduced to carbide, carbide was not oxidized during the subsequent oxidation cycles.

Studies on carburization [33,46] showed that Ni, Cr, Si, and Al are the effective alloying elements to increase the carburization resistance of high temperature alloys. Since the "cracking" environment in practical ethylene-pyrolysis processes involves an oxygen activity, one can rely on the protection by the uniform Cr_2O_3 scale to prevent carburization of furnace tubes. Furthermore, Si as SiO_2 scale is an effective alloying to act as a supplementary of Cr_2O_3 scale below about 1,050C, and as a substitution of Cr where oxide converts to Cr-carbides above 1,050C. Addition of carbide-forming alloying elements such as Mo, Ti, and Nb to alloys is also reported to be beneficial. On this basis, carburization-resistant alloys such as alloy HK40 (UNS J94204, 25%Cr-20%Ni, mass%) and alloy HP-mod (25%Cr-35%Ni-1.8%Si) are replacing the conventional alloy 800H for pyrolysis furnace tubes [47,48], and alloys containing higher Cr and Ni have been developed [49,50].

Classical approaches have been conducted to estimate kinetics of the internal carbide formation [37,51,52]. The expressions describing the kinetics of internal precipitation in the absence /presence of an external oxide scale have been derived [53,54]. If diffusion control is maintained, the depth ξ of the internal carburization zone is a parabolic function of the time t so that

$$\xi = (2k_p \times t)^{1/2} \tag{12}$$

Several authors [55 - 57] have experimented with another approach to present the internal carburization process using a numerical finite difference technique. This computational method, which

gives a numerical solution to Fick's 2nd law, considers an interaction between C diffusion and carbide precipitation. The calculated results have presented the carbon-profile in the alloy to some extent.

For ethylene pyrolysis furnaces, coke formation (coking) occurs and this can reduce heat transfer rate, lowering the olefin yield. At extreme cases, plugging of furnace tubes due to coking leads to localized overheating and hence to tube failure [58]. As mentioned above, two types of coke, pyrolytic and catalytic carbon, are formed at the inner wall of radiant tubes [59]. Alloying elements such as Fe, Ni, and Co that form relatively unstable carbides catalyze carbon deposition by heterogeneous reaction of gaseous hydrocarbon [60 - 62]. Tamai et al. [61] have examined carbon deposition on Fe and Ni in a CH_4 gas atmosphere, and reported that carbon deposition on Fe is faster than on Ni since Fe can diffuse in the carbon layer faster than Ni. Ohla and Grabke [62] compared coke formation on pure Fe, Ni, and Fe-Ni alloys in gas mixtures of CH_4-H_2. They showed that the rate of carbon deposition on Fe was faster than on Ni because Fe surface was not well-ordered as Ni. Ando et al. [63] investigated coke formation on Fe and Ni in CO-H_2 gas mixtures and supported the Ohla's results. Trimm et al. [65,66] showed that on Ni surface, carbon formation dominated at low temperatures, but at high temperatures, the coking rate on Ni decreased with increasing temperature due to thermal adsorption. Tokura et al. [67] investigated the coke formation on bare and preoxidized Fe and Ni in a CH_4-H_2 atmosphere at 1,000°C by a microbalance. Iron particles generated by reduction of Fe-oxides had much greater reactivity than Ni particles to catalyze deposition of coke on metal surface. Young [68] investigated the formation of carbon on pure Ni, Cu, and some heat resistant alloys in C_3H_6-H_2 and C_3H_6-H_2-H_2O gas mixtures at 700-1,000°C. Below 900°C, coking is catalyzed by Ni, but deposition of pyrolytic coke become predominant at higher temperatures. For heat resistant alloys, the amount of catalytic coke is greatly suppressed by the formation of Cr_2O_3 scale (with some Cr-carbides included), suggesting that the oxide scale does not have a high catalytic activity to coke deposition. In terms of carbon deposition on metal surfaces, these studies have demonstrated that catalytic activity of Fe is grater than Ni, especially when reduced from their oxides. Uniform formation of a Cr_2O_3 scale on heat-resistant alloys can reduce the deposition rate of carbon, since the Cr_2O_3 scale seems to be non-catalytic for the carbon deposition. Hence, alloys protected by the uniform Cr_2O_3 scale on their surface, preferably with less Fe (as Fe oxides) in the scale, are considered resistant not only to carburization but also to carbon deposition on tube surface in actual furnaces.

Many authors have investigated and proposed mechanisms for metal dusting. Hochman [69,70] has reported a fundamental mechanism for carbon steels and low-alloys, and Grabke [71 - 74] has generalized it and shown the guideline for engineering applications of the low-alloys, which can be widely accepted. The proposed mechanism is shown in Fig. 1-9, where the following steps are taking place:

a) carbon decomposed from carbonaceous gases with a_c>1 adsorbs on the metal surface, and diffuses into the metal matrix.

b) oversaturated carbon combines with the metal as cementite (M_3C; M includes Fe, Mn, and Cr) at the gas /metal interface, resulting in a reduction of carbon ingress into the metal.

c) if the decomposed carbon covers the cementite as coke, a_c at the coke / cementite interface drops to unity. This causes decomposition of the metastable cementite according to the following reaction (13).

M_3C (M includes Fe, Mn, and Cr) = 3M + C (13)

d) dissociated metal in a form of very small particles diffuses into the precipitated graphite perpendicularly aligned to the cementite, and catalyzes deposition of carbon.

In this manner, carbon steels and low-alloy steels are susceptible to metal dusting. Aspect of metal dusting for these alloys has ordinarily proven general attack.

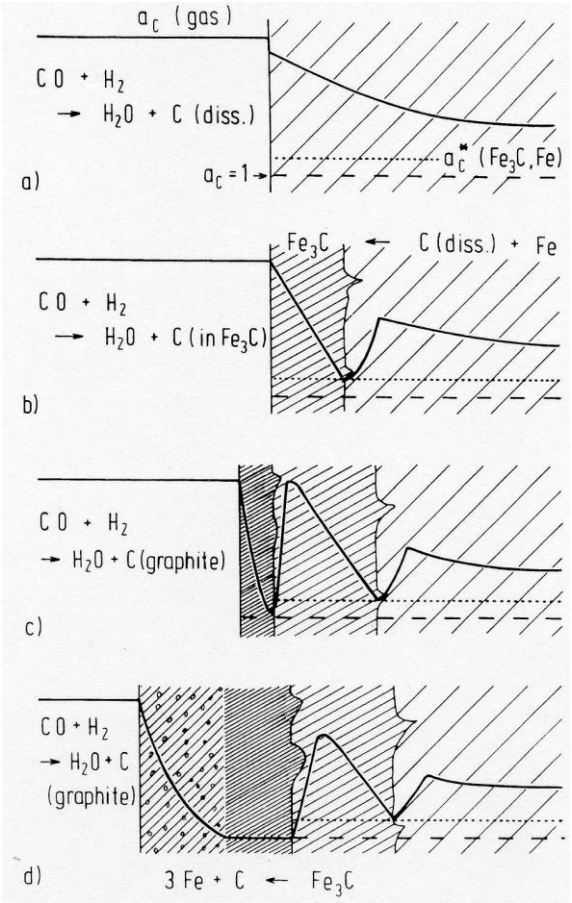

Figure 1-9 Schematics of the mechanism of metal dusting on iron and low-alloy steels [72].

Initiation and growth of metal dusting may differ between high-alloys (e.g. austenitic stainless steels and Ni-base alloys) and low-alloys. Pitting attack, which occurs on a metal surface, is common mode of metal dusting on high-alloys. The significant aspects are as follows:

e) at the initial stage, Cr_2O_3 can form on the metal surface, because Po_2 in the carbonaceous gas is sufficiently high for the formation of oxides such as Fe and Cr containing spinel-type oxide, Cr_2O_3, SiO_2, and Al_2O_3 [75,76]. None of the decomposed carbon can adsorb on and diffuse into the metal matrix while the oxide scale provides complete protection.
f) once cracks and /or flaws are generated in the oxide scale, carbon diffuses into the metal matrix through them, and then the oversaturated carbon forms mainly Cr carbides as $M_{23}C_6$ and M_7C_3.
g) continuous carbon charging into the metal matrix comes to the supersaturation at the metal surface, resulting in the precipitation of graphite directly [77 - 80].
h) growth of graphite attenuates the γ matrix in accordance with the lever low of three phases such as Cr-carbide, γ matrix, and graphite, and then the thinning γ matrix detaches from the substrate owing to the growth stress. Coke deposition is catalyzed by the detached γ matrix as metal particles.

Another mechanism for metal dusting of Cr oxide forming stainless steels with relatively low Ni is proposed from perspective of a carbon and oxygen gradient derived from thermodynamic considerations [81]. The nub of this mechanism is as follows:

i) initial behavior on the metal surface is the same as the above steps e) and f).
j) carbide dissolution followed by selective oxidation and metal particles according to the following reaction (14).

[Cr-depleted γ matrix] + carbide + CO = [γ matrix as metal particles] + oxide + carbon (14)

In the above step, it is important that the carbide acts as intermediate. Therefore, if we consider the existence of oxide at the graphite /carbide boundary, the rate-controlling factor of pit growth may differ from the previous understandings.

Thermodynamic considerations for the carbonaceous gas environment in reforming plants are

quite important to evaluate intensity of the metal dusting and to make a proper alloy selection. Parks and Schillmoller [82] have presented a corrosion map of 304 stainless steel and alloy 800 on metal dusting. As shown in Fig. 1-10, CO/CO_2 and H_2O/H_2 ratios were proposed as a corrosion index of the gas mixture. Occurrence /absence of metal dusting attack for alloys used in waste heat boilers of ammonia plants were explained by these indices. These ratios would be based on reactions (3) and (15), respectively.

$$H_2O = H_2 + 1/2O_2 \quad (15)$$

The results of a survey on the metal dusting behavior of several commercial alloys have revealed the effective alloying elements [75,76,83]. Alloys with Cr of more than 25mass% have remarkable resistance against metal dusting due to the formation of a protective C_2O_3 scale. Some ferritic stainless steels prove to be more resistant to metal dusting than austenitic stainless steels. For austenitic stainless steels, however, addition of Ni is efficient for suppression of metal dusting due to the retardation of internal carburization. A proper concentration of Ni to resist the metal dusting is more than 50% [83], and also the Fe /Ni ratio prefers to be 1 /4 in terms of the carbon diffusivity and solubility [33]. Criteria for the protection against metal dusting have been also proposed [84,85]. Each has been expressed by an experimental equivalent formula what alloying elements bear to enhance the formation of a protective oxide. Recently, Baker [86] has shown the extended summation by a regression calculation on the basis of the laboratory exposure test results.

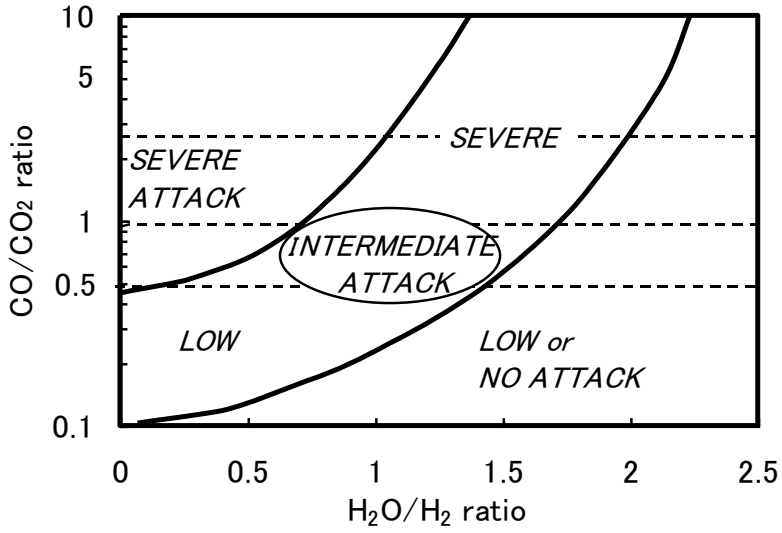

Figure 1-10 Effect of CO/CO_2 ratio on metal dusting in critical temperature range vs. steam /hydrogen ratio (as applicable to SUS 304 and alloy 800) [82].

1.3 Purposes of the Present Research

The main objectives of the research presented in this thesis are (1) to consider the thermodynamics for carbonaceous gas atmospheres in the representative industry plants, i.e. ethylene pyrolysis furnaces and syngas production reformers, and (2) to clarify the effects of alloying elements for Fe-Ni-Cr alloys upon carburization, coking, and metal dusting.

Thermodynamics:

Chemical potential such as a_c and Po_2 characterizes corrosive gas and considerations on it give a better understanding the carburization, coking, and metal dusting corrosion occurring at alloys. For ethylene pyrolysis furnaces, the chemical potential of the gas atmosphere, decomposed from hydrocarbon-steam mixtures at elevated temperatures, has been unknown because the gas reactions are complicated to predict the equilibrated gas compositions. For syngas production reformers, CO/CO_2 and H_2O/H_2 ratios were proposed as a corrosion index of the gas mixture as described in the previous section [82]. However, verification of these indices, based on either thermodynamics or kinetics of the relating reactions, is needed to generalize their idea. To deal with these complicated gas equilibria, computational analysis is one of the useful and appropriate techniques. Therefore, the author has shed light upon labyrinth of the thermodynamics for both of the ethylene pyrolysis furnace and syngas production reformer using a computational analysis in conjunction with an experimental validation of these calculated results.

Effects of alloying elements on carburization, coking, and metal dusting:

Severity of these corrosion systems is affected by alloying elements as well as ambient temperature. An oxide scale formed on the alloy surface can be a barrier against the inward carbon diffusion. Chemical potentials of the gas atmosphere, Po_2 and a_c, affect the formation of the protective oxide. Especially, conversion of Cr_2O_3 to Cr-carbides should be considered at the alloy surface above certain temperatures in an ethylene pyrolysis. Kinetics of the intended corrosion system gives suggestive information to predict degradation of alloy tubing, and is strongly affected by alloying elements. As described in the background, Ni is found to be effective against carburization and metal dusting, but others are still unclear. Thus, the quantitative ability of alloying elements should be

clarified to estimate their kinetics.

The present thesis is composed of the following 8 chapters. The main focuses in each chapter are outlined below:

Chapter 1 is the introduction of the present thesis, and describes the relevant background and the purposes of this research.

Chapter 2 describes the thermodynamic calculations to understand the carburizing environment of ethylene pyrolysis furnaces. Carburization behavior of a Cr_2O_3-forming Fe-Ni-Cr(-Si) alloys exposed in a CH_4-CO_2-H_2 gas mixture simulating the actual pyrolysis environment at 1000-1150°C is estimated and its kinetics is discussed based on internal oxidation model.

Chapter 3 describes the investigation of carburization and coking behavior of a Cr_2O_3-forming Fe-Ni-Cr-Si alloy under cyclic carburizing and oxidizing environments simulating cracking-decoking process for ethylene pyrolysis plants. Also the characteristics of the oxide scales formed in oxidizing environments are closely examined by XRD and EDS. These results are interpreted by the lowered Cr content of the γ matrix at the external surface of the alloy due to carburization.

Chapter 4 describes the evaluation of carburization and coking behavior of an Al_2O_3-forming Ni-Cr-Al alloy that has been developed in recent years. The obtained results for the alloy are compared with those for the conventional Cr_2O_3-forming alloys. The prominent effects on carburization and coking are demonstrated for the Al_2O_3-forming Ni-Cr-Al alloy.

Chapter 5 describes the thermodynamic aspects to understand the metal dusting environment of syngas production reformers. Based on the analyses, the equilibrium equations for chemical potentials, a_c and Po_2, are determined in CO-H_2-CO_2-H_2O gas mixtures at intermediate temperatures. Under the simulated gas condition, Cr_2O_3-forming Ni-base alloys are tested to evaluate the metal dusting behavior. Mechanism for pit initiation and growth (i.e. metal dusting) of Ni-base alloys is proposed from a metallurgical approach in a nonequilibrium state.

Chapter 6 describes the investigation of metal dusting behavior for various Cr and Ni content Fe-Ni-Cr steels and alloys exposed in a simulated gas mixture of CO-H_2-CO_2-H_2O. Effects of alloying elements on both initiation and growth of pits are clarified, and the kinetics of pit growth is discussed.

Chapter 7 describes the improvement of metal dusting resistance by an addition of Cu. Copper has proven to suppress the dissociation of CO molecule adsorbed on the surface of transition-metals and

Ni-Cu binary alloys exposed to a simulated gas mixture of CO-H_2-CO_2-H_2O. This mechanism, a novel approach to improve the metal dusting resistance for Ni-base alloys, is discussed in terms of an electronic theory based on d-band structure of the transition-metals.

The results obtained by the present investigation are summarized in ***Chapter 8***.

References

[1] For example, ASM handbook vol.4 "Heat Treating" (Materials Park, OH: ASM International, 1991)

[2] F.A. Prange, Corrosion 15 (1959), p.619t.

[3] W.B. Hoyt and R.H. Caughey, Corrosion 15 (1959), p.627t.

[4] F. Eberle and R.D. Wylie, Corrosion 15 (1959), p.622t.

[5] R.E. Gackenbach and J.F. Shay, Proc. 26th NACE Conf. (1970), p.363.

[6] M.W. Clark, Process Industries Corrosion (1975), p.329.

[7] D. Foley, ASME Publication no. 76 (1976), p.5.

[8] R. Schueler, Hydrocarbon Processing (1972), p.73.

[9] S. Ibarra, Metal Progress 2 (1980), p.62.

[10] H.J. Grabke, Mat. at High Temperatures 17, 4 (2000), p.1.

[11] For example, H.J. Grabke, "Carburization, A High-Temperature Corrosion Phenomenon", no. 52 (St. Louis, MO: Materials Technology Institute of the Chemical Process Industries, Inc., 1998).

[12] R.T. Jones and K.L. Baumert, "Metal Dusting - An Overview of Current Literature," CORROSION /2001, paper no.1372, (Houston, TX: NACE, 2001).

[13] T. Ellis, I.M. Davidson, and C. Bodsworth, J. Iron Steel Inst. 201 (1963), p.582.

[14] K. Natesan and T.F. Kassner, Metall. Trans. 4 (1973), p.2557.

[15] The NBS tables of chemical thermodynamic properties, selected values for inorganic and C1 and C2 organic substances in SI units, J. Phys. Chem. Ref. Data vol.2, Supplement no.2 (1982).

[16] G.L. Swales, Proc. Conf. "The Behaviour of High Temperature Alloys in Aggressive Environments" Petters, The Netherlands, Oct (1979), p.45.

[17] D.L. Trimm, Progress in Catalyst Deactivation (Ed.:J. L. Figueiredo), Martinus Nijhoff Publishers, The Hague, (1982), p.31.

[18] Y. Tong, M.K. Poindexter, and C.T. Rowe, "Inhibition of Coke Formation in Pyrolysis Furnaces" Proc 210th National Meetings, (Chicago, IL: American Chem. Soc. 1995).

[19] M.J. Bennett and J.B. Price, J. Mater. Sci. 16(1981), p.170.

[20] J.M. Harrison, J.F. Norton, R.T. Derricott, and J.B. Marriott, Werkst. Korros. 30 (1979), p.785.

[21] A.G. Wysiekierski, G. Fisher, and C.M. Schillmoller, Hydrocarbon Processing 1 (1999), p.97.

[22] For example, website on http://www.abb.com/lummus/

[23] R.H. Kane, Corrosion 36, 3 (1980), p.112.

[24] J. Thijssen, "Comparison of Exxon, Shell and Sasol Technologies and GTL Viability," Proc.

Monetizing Stranded Gas Reserves (1998)
[25] Y. Ogawa, Journal of the Japan Society of Energy and Resources (*Enerugii-Shigen*) 23, 5 (2002), p.317.
[26] Y. Ono et al., "Slury Phase Synthesis of Dimethyl Ether and Its Utilization," *NKK-giho*, 174 (2001), p.1.
[27] J.R. Rostrup-Nielsen, Catal. Today 18 (1993), p.305.
[28] J. Brightling, Nitrogen and Methanol no. 256 (2002), p.29.
[29] H.J. Grabke, Materiali in Technologije 36, 6 (2002), p.297.
[30] T. Shibasaki et al., Ammonia Technical manual 36 (1996), p.165.
[31] H. Stahl and S.G. Thomsen, Ammonia Technical manual 36 (1996), p.180.
[32] D.K. Chopra and K. Natesan, High Temp. Sci. 9 (1977), p.243.
[33] H.J. Grabke and U. Gravenhorst, and W. Steinkusch, Werkst. Korros. 27 (1976), p.291.
[34] K. Ledjeff, A. Rahmel, and M. Schorr, Werkst. Korros. 31 (1980), p.83.
[35] W.F. Chu and A. Rahmel, Oxid. Met. 15 (1981), p.331.
[36] J.A. Colwell and R.A. Rapp, Metallurg. Trans. 17A (1986), p.1065.
[37] A. Schnaas, H.J. Grabke, Oxid. Met. 12 (1978), p.387.
[38] T.A. Ramanarayanan, Mater. Sci. Eng. 87 (1987), p.113.
[39] P.J. Smith, O.Van Der Biest, J. Corish, Oxid. Met. 24 (1985), p.47.
[40] J. Hemptenmacher and H.J. Grabke, Werkst. Korros. 34 (1983), p.333.
[41] D.R.G. Mitchell, D.J. Young, W. Kleemann, Mater. Corros. 49 (1998), p.231.
[42] P. Ganesan, G.D. Smith, C.S. Tassen, "Corrosion resistance of Alloy 803 in environments applicable to fossil energy systems," CORROSION /95, paper no.470, (Houston, TX: NACE, 1995).
[43] A. Otomo, Y. Shinozaki, Y. Zaiga, S. Oishibashi, Japan Society for the Promotion of Science 123 committee report, 15 (Tokyo, Japan: 1974), p. 177-186 (in Japanese).
[44] S.P. Kinnniard, D.J. Young, D.L. Trimm, Oxid. Met. 26 (1986), p.417.
[45] M.A. Harper, M. Ducasse, D.J. Young, Corrosion 51 8 (1995), p.191.
[46] S.B. Parks, C.M. Schillmoller, Hydrocarbon Process. 3 (1996), p.53.
[47] R.H. Kane, Corrosion 37, 4 (1981), p.187.
[48] Y. Sawaragi, M. Nishi, Petrotech 18, 8 (1995), p.648.
[49] S.B. Parks, C.M. Schillmoller, Chem. Eng. World 34, 3 (1999), p.177.
[50] R. Milner, M. Phaneuf, "Comparative carburization of heat resistant alloys," CORROSION /98, paper no.431, (Houston, TX: NACE, 1998).

[51] A. Shnaas and H.J. Grabke, Wekst. Korros. 29 (1978), p.635.

[52] S. Ling, T.A. Ramanarayanan, and R. Petkovic-Luton, Oxid. Met. 40 (1993), p.179.

[53] C. Wagner, Z. Electrochem. 63 (1950), p.772.

[54] R.A. Rapp, Corrosion 21 (1965), p.730.

[55] H.G. Sockel, H.J. Christ, Mater. Sci. Eng. 87 (1987), p.119.

[56] H.J. Christ, H. Biermann, F.C. Rizzo, H.G. Sockel, Oxid. Met. 32 (1989), p.111.

[57] S. Forseth, P. Kofstad, Mater. Corros. 49 (1998), p.266.

[58] L.F. Albright, R.T.K. Baker, "Coke Formation on Metal Surface", American Chemical Society (ACS) Symposium Series 202, (Washington. D. C.: ACS, 1982).

[59] L.F. Albright and J.C. Marek, Ind. Eng. Chem. Res. 27 (1988), p.755.

[60] W.E. Slater, J. Chem. Soc. 109 (1916), p.160.

[61] Y. Tamai, Y. Nishiyama, G. Tkahashi, Kogyo Kagaku Zasshi 70, 6 (1967), p.91 (in Japanese).

[62] L.S. Lobo, D.L. Trimm, J.L. Figueiredo, "Kinetics of the Mechanism of Carbon Formation from Hydrocarbon on Metals", Proc. 5th Int. Congress on Catalysis, paper no.79 (Amsterdam, Netherlands: 1972).

[63] K. Ohla, H.J. Grabke, Wekst. Korros. 33 (1982), p.341.

[64] S. Ando, T. Nagashima, T. Shimoo, H. Kimura, J. Japan Inst. Metal. 52 6 (1988), p.553.

[65] D.L. Trimm, Applied. Catal. 5 (1983), p.263.

[66] P.R.S. Jackson, D.L. Trimm, D.J. Young, J. Mater. Sci. 21 (1986), p.3125.

[67] S. Tokura, N. Otsuka, T. Kudo, Corros. 49 7 (1993), p.561.

[68] D.J. Young, Mater. Corros. 50 (1999), p.675.

[69] R.F. Hochman and J.H. Burson. "The fundamentals of metal dusting," API Division of Refining Proc., 46 (1966), p.331.

[70] R.F. Hochman, "Basic studies of metal dusting deterioration ("metal dusting") in carbonaceous environments at elevated temperatures," Proc. of the 4th International Congress on Metallic Corrosion, NACE (1972), p.258.

[71] H.J. Grabke, R. Krajak, and Müller-Lorenz, Werkst. Korros. 44 (1993), p.89.

[72] J.C. Nava Paz and H.J. Grabke, Oxid. Met. 39, nos.5/6 (1993), p.437.

[73] H.J. Grabke, R. Krajak, and J.C. Nava Paz, Corros. Sci. 35, nos.5-8 (1993), p.1141.

[74] H.J. Grabke, C.B. Brancho-Troconis,and E.M. Müller-Lorenz, Mater. Corros. 45 (1994), p.215.

[75] H.J. Grabke, R. Krajak, E.M. Müller-Lorenz, and S. Strauß, Mater. Corros. 47 (1996), p.495.

[76] J. Klöwer, H.J. Grabke, E.M. Müller-Lorenz, and D.C. Agarwal, "Metal dusting and carburization

resistance of Ni-base alloys,'' CORROSION /97, paper no.139, (Houston, TX: NACE, 1997).

[77] R. Shneider, E. Pippel, J. Woltersdorf, S. Strauß, and H.J. Grabke, Steel Res. 68 (1997), p.326.

[78] E. Pippel, J.Woltersdorf, and R. Schneider, Mater. Corros. 49 (1998), p.309.

[79] C.M. Chun, T.A. Ramanarayanan, and J.D. Mumford, Mater. Corros. 50 (1999), p.634.

[80] C.M. Chun, J.D. Mumford, and T.A. Ramanarayanan, J. Electrochem. Soc. 147, no.10 (2000), p.3680.

[81] P. Szakalos, R. Pettersson, and S. Hertzman, Corros. Sci. 44 (2002), p.2253.

[82] S.B. Parks and C.M. Schillmoller, Stainless Steel World 9 (1997), p.44.

[83] H.J. de Bruyn, E.H. Edwin, and S. Brendryen, ''Apparent influence of steam on metal dusting,'' CORROSION /2001, paper no.1383, (Houston, TX: NACE, 2001).

[84] R.C. Schueler, Hydrocarbon Process. (1972), p.73.

[85] S.B. Parks and C.M. Schillmoller, Stainless Steel World 9, no.3 (1997), p.44.

[86] B.A. Baker, G.D. Smith, V.W. Hartmann, and L.E. Shoemaker, ''Nickel-base material solutions to metal dusting,'' CORROSION /2002, paper no.2394, (Houston, TX: NACE, 2002).

Chapter 2

THERMODYNAMIC ASPECTS UPON ETHYLENE PYROLYSIS FURNACES AND CARBURIZATION RESISTANCE OF AUSTENITIC ALLOYS IN A SIMULATED GAS MIXTURE AT ELEVATED TEMPERATURES

2.1 Introduction

Ethylene pyrolysis is considered the most important process in the petrochemical industry. Some furnace tubes used for ethylene pyrolysis often suffer severe high temperature corrosion, since the tube surfaces are heated up to about 1,100°C in contact with steam-hydrocarbon gas mixtures [1 - 6]. Simultaneous carbon deposition on tube surfaces (coking) and carburization of tube alloys can deteriorate their mechanical properties and may result in their failure. Studies on carburization [7, 8] showed that Ni, Cr, Si, and Al are the effective alloying elements to increase the carburization resistance of high temperature alloys. Addition of carbide-forming alloying elements such as Mo, Ti, and Nb to alloys is also reported to be beneficial. On this basis, carburization-resistant alloys such as alloy HK40 (UNS J94204, 25%Cr-20%Ni, mass%) and alloy HP-mod (25%Cr-35%Ni-1.8%Si) are replacing the conventional alloy 800H (UNS N8810, 21%Cr-32%Ni) for pyrolysis furnace tubes [9, 10], and accordingly alloys containing higher Cr and Ni have been developed [11, 12]. Recently, alloys containing Al to form a protective Al_2O_3 scale have been reported [13 - 15]. Coating technique also has been demonstrated in the ethylene pyrolysis furnaces [16 - 18]. Conventional Fe-Ni-Cr tubes are coated with layers of Cr-Si and /or Cr-Al on the inner surface to improve the protection against carburization as well as coking.

To evaluate the carburization resistance of steels and alloys by laboratory corrosion test, the pack

carburization test of heating specimens embedded in charcoal and $BaCO_3$ mixture is often used [19]. Although this test is simple to handle, the carburizing gas atmosphere, represented by the carbon activity (a_c) and the oxygen potential (Po_2), is left uncontrolled and the gas atmosphere in the pack can vary with time. Since evidence is lacking that the carburization environment in the pack simulates the practical pyrolysis furnaces, the results obtained by the pack carburization test cannot represent the carburization resistance of alloys in actual furnaces. There are several studies where carburization tests were conducted in C_mH_n-H_2 gas mixtures [20 - 22]. These tests are considered useful for studying diffusion of carbon in steels, alloys, etc.. However, since their environments are "purely" carburizing and not oxidizing, these tests could not provide a reasonable evaluation for the carburization resistance. In actual cracking gases, oxygen is present as H_2O, CO, and CO_2, so that there must be some Po_2, which may form oxide scales on tube surfaces. Indeed, oxide scales are usually found on metal tube surfaces between the coke layer and the substrate [23].

Some gas carburization tests in "oxidation" environments have been reported in the literature. Mitchell, Young, and Kleemann [24] have showed that the Cr_2O_3 scale can provide protection for alloys up to 1000°C in a C_3H_6-H_2-H_2O gas atmosphere. Ganesan, Smith, and Tassen [25] have reported that the Cr_2O_3 scale maintained its growth on the alloy surface and acted as a diffusion barrier for carbon to enter into the substrate alloy in a CH_4-CO_2-H_2 gas atmosphere at 1,100°C. Otomo et al. [26] conducted carburization tests in a C_3H_8-CO-CO_2-H_2-N_2 gas mixture and found a similar effect of the Cr_2O_3 scale. These laboratory gas-carburization tests have demonstrated the importance of Cr_2O_3 scales on the carburizing resistance of steels and alloys in this environment. Since the "cracking" environment in practical ethylene-pyrolysis processes involves an oxygen potential, one can rely on the protection by the uniform Cr_2O_3 scale to prevent carburization of furnace tubes. Although the formation and thermal stability of Cr_2O_3 scales are considered to be greatly affected by the oxygen potential of the cracking gas atmospheres, information is limited on Po_2 of the actual ethylene pyrolysis environments. The thermodynamic analyses have been conducted for Cr-O-C system reacted with CO-CO_2 gas mixtures [27 - 29]. These considerations give useful information relevant to the stability of Cr compounds. In the actual pyrolysis furnace, however, more complicated gas atmospheres are produced, since the gas components are not the C-O system but the C-H-O system including hydrocarbon and steam.

This chapter deals with thermodynamic aspects of carburizing environments of the cracking furnace tubes used for the actual ethylene pyrolysis. Equilibrium calculations of Po_2 and a_c were based

on a survey of the naphtha feed stocks chemistry. Based on this information, the gas composition for laboratory carburization tests was decided, and tests were conducted to evaluate the carburization resistance of four commercial Fe-Ni-Cr alloys.

2.2 Thermodynamic Analysis of Ethylene Pyrolysis Gas Atmosphere

In the ethylene pyrolysis process, thermal cracking of hydrocarbon, e.g. naphtha, ethane, and propane, is conducted by heating a gas mixture of hydrocarbon and steam in furnace tubes to obtain olefin products such as ethylene and propylene. The flow velocity of the reactant gas mixtures is so high that pyrolysis reactions are considered to occur under non-equilibrium states. However, thermodynamic equilibrium calculations are expected to be still beneficial, since they can provide an index for estimating the severity of the actual corrosion environment and for predicting the degradation of tube alloys caused by carburization. The chemical composition of some naphtha feed stocks used for ethylene production is presented in Table 2-1. Naphtha I-III in Table 2-1 are commonly used for ethylene pyrolysis. Naphtha IV and V correspond to light and heavy naphtha, respectively. Light naphtha consists mainly of hydrocarbons of C5 and C6 components, and heavy naphtha of C7 and C8 components. Upon pyrolysis, steam is added to naphtha. The steam-to-naphtha mass ratio (S/O) is usually controlled to be between 0.35 and 0.5.

Table 2-1 Examples of the chemical composition of naphtha

No.	Chemical composition (mass%)						
	C4*	C5*	C6*	C7*	C8*	C9*	C10*
I	5	25	25	20	10	15**	
II	1	44.5	34.7	13.8	4.2	1.5	0.5
III	2	11.9	16.4	17.8	27.5	24.4**	
IV	6.5	59.7	33.6	0.2	0	0	0
V	0	0.1	9.8	35.3	45.4	9.4	0

* C4 to C10 showing the number of carbon as hydrocarbon

** Sum total of C9 and C10 components

Based on these data, equilibrium Po_2 and a_c values upon pyrolysis of naphtha I-III were derived as a function of temperature by a computational calculation [30]. The calculated results are shown in Fig. 2-1, where numbers in the parentheses denote the steam /naphtha mass ratio. The equilibrium Po_2 increased with increasing the reaction temperature. For the operating temperatures of the ethylene pyrolysis furnace tubes, i.e. 900-1,100°C, Po_2 ranged between 10^{-21} and 10^{-19} atm. But the equilibrium Po_2 did not depend directly on the type of naphtha. As explained later, the effect of the steam /naphtha ratio on Po_2 is greater than that of the type of naphtha. The phase boundaries for the coexistence of Cr_3C_2 /Cr_2O_3, Cr_7C_3 /Cr_2O_3, and Cr /Cr_2O_3 at unit activity of each phase are also shown in Fig. 2-1. Upon comparing the equilibrium Po_2 of the pyrolysis gas atmosphere with these phase boundaries, Cr_2O_3 scale (and metastable Cr-carbides) is predicted to be stable for up to 1,030-1,040°C, but the scale would convert to Cr-carbides such as Cr_7C_3 and Cr_3C_2 (both are in contact with graphite) at a higher temperature. Since the metal temperature of cracking furnace tubes is designed to be about 900-1,100°C, the Cr_2O_3 scale formed on them will lose its protectiveness above 1,030-1,040°C. According to the previous literature [28], a Cr_2O_3 scale (the activity of Cr is taken as unity) remains to be stable for up to around 1,050°C in CO-CO_2 gas mixtures. Hence, the temperature where the Cr_2O_3 converts to Cr-carbides in the gas mixture of naphtha and steam (naphtha cracking) is slightly lower than that for the CO-CO_2 gas mixtures.

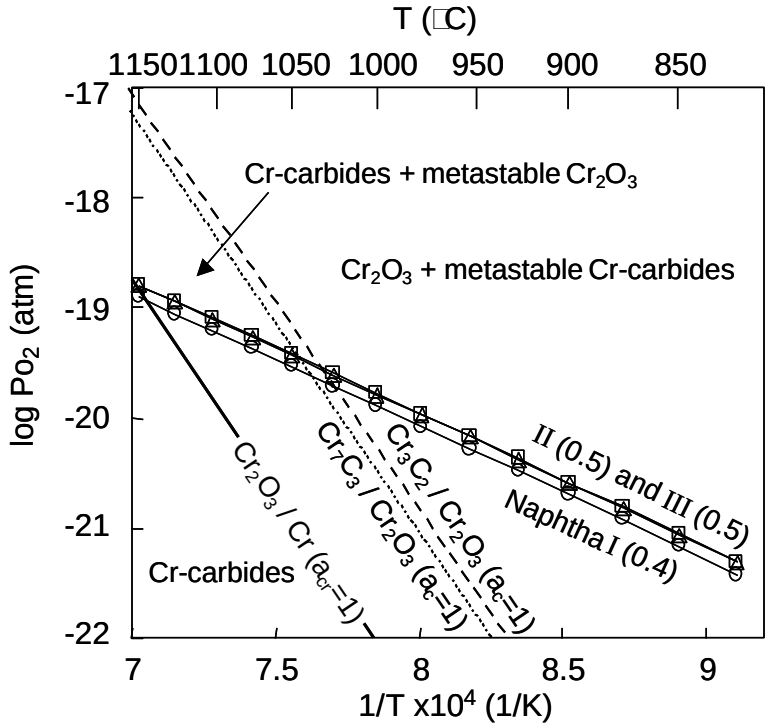

Figure 2-1 Calculated equilibrium Po_2 of gas atmosphere upon ethylene pyrolysis and equilibrium Po_2 of Cr oxide /carbide at unit activity as a function of temperature. Figure in parentheses denotes the steam /naphtha mass ratio.

The calculated equilibrium Po_2 and amount of deposited carbon (ΔC) upon pyrolysis of various naphtha at 1,100°C are shown in Fig. 2-2. The ΔC was defined as carbon deposited from one mole of raw gas mixture. Graphite was taken as the standard state of carbon. For heavy naphtha V, where the concentration of heavy C_n elements is high, ΔC was calculated to be high, but the steam /naphtha ratio may affect ΔC more than the type of naphtha. Therefore, the effect of steam /naphtha ratio on ΔC and Po_2 was examined for naphtha I and the results are plotted in Fig. 2-3. For conditions where the steam /naphtha ratio was between 0.1 and 1.0, a_c was calculated to be unity, and ΔC decreases with increasing the steam /naphtha ratio. Similarly, Po_2 increases with increasing the steam /naphtha ratio, but Po_2 changes are relatively small.

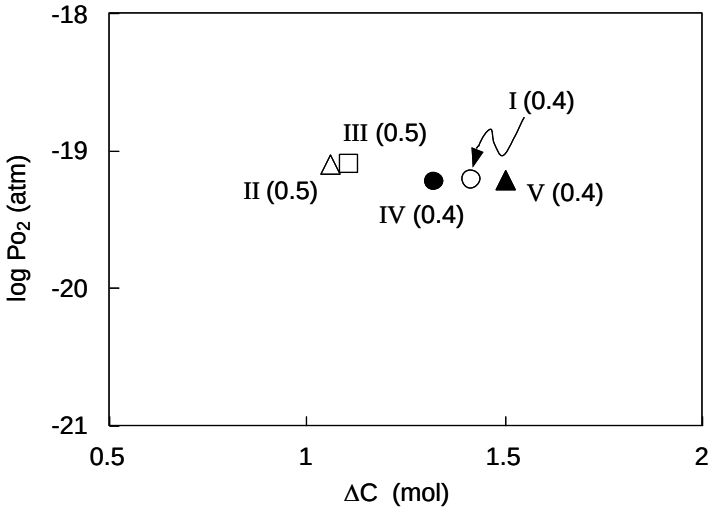

Figure 2-2 Calculated equilibrium Po_2 and ΔC for several gas atmospheres upon ethylene pyrolysis at 1,100°C. ΔC is defined as mole of carbon deposited from one mole of raw materials. The standard state of carbon was taken for graphite. Figure in parentheses denotes the steam /naphtha mass ratio.

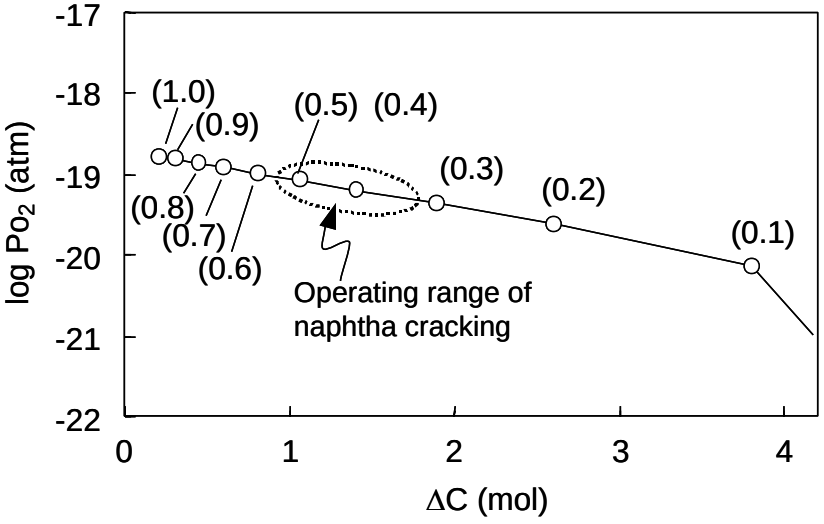

Figure 2-3 Effect of steam /naphtha mass ratio on Po_2 and ΔC at 1,100°C. Figure in parentheses denotes the steam /naphtha mass ratio for naphtha I shown in Table 2-1.

Figure 2-4 represents the effect of steam /naphtha ratio on Cr_2O_3 stability. For certain cracking conditions where the steam /naphtha ratio is less than 0.35, the temperature range where the Cr_2O_3 scale is stable becomes narrow. For example, the critical temperature above which the Cr_2O_3 scale may transform to carbides was calculated to be 970°C for a steam /naphtha ratio of 0.1, 60-70°C lower than that for the conventional steam /naphtha ratio of 0.35-0.5. Since the metal temperatures of the furnace tubes are 900-1,100°C for the usual operating conditions, this result suggests that the temperature range where protection by the Cr_2O_3 scale is thermodynamically effective would become narrow for conditions when the steam /naphtha ratio is low. From the viewpoint of Cr_2O_3 stability, a higher steam /naphtha ratio is favored (Cr is stable up to 1,070°C with steam /naphtha ratio of 1.0 for example), but this would result in the reduction of ethylene and propylene yield. Hence, carburization-resistant alloys protected not only by the Cr_2O_3 scale but also by other types of oxide scales are needed to combat the oxidation /carburization in this environment.

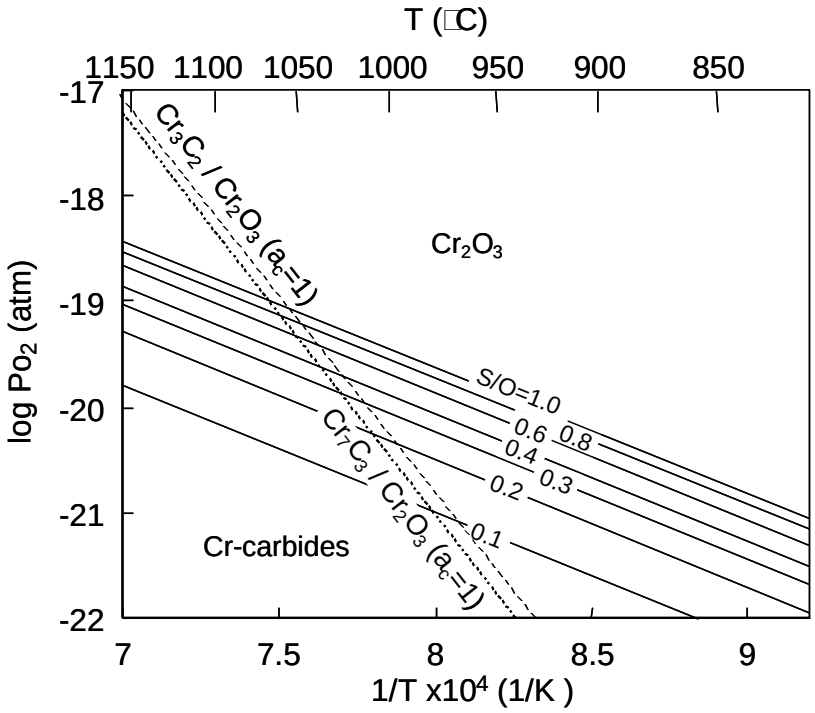

Figure 2-4 Calculated equilibrium Po_2 of gas atmosphere for different steam /naphtha mass ratio (S /O) and equilibrium Po_2 of Cr oxide /carbide at unit carbon activity as a function of temperature. Naphtha I listed in Table 2-1 is used for this calculation.

2.3 Experimental

Four commercial alloys, which have been used for furnace tubes in ethylene pyrolysis plants, were tested. The chemical composition of these alloys is presented in Table 2-2. Alloys A (HP-mod.), B (HP-mod.), and D (UNS No. N08810) are wrought alloys, while alloy C (High Cr-High Ni) is a cast alloy. The Cr content of alloys A, B, and C is larger than 25 mass%, whereas alloy D has 21%. Alloys A and C contain Si levels of 1.8% and 1.7%, respectively. Coupon specimens of 4 × 20 × 30 in mm were cut from virgin production tubes (alloys A and D), a laboratory-melted plate (alloys B), and a laboratory-melted cast ingot (alloy C). The specimen surfaces were mechanically ground to 600-grit emery paper, followed by ultrasonic cleaning in acetone.

Table 2-2 Chemical composition of the tested alloys

Alloy	Chemical composition (mass%)										Product form
	C	Si	Mn	Ni	Cr	Al	Ti	Nb	Mo	Fe	
A (25Cr-HSi)	0.14	1.8	0.4	37.6	25.3	-	0.4	-	1.3	Bal.	Wrought
B (26Cr-LSi)	0.07	0.5	0.3	35.8	25.8	0.5	0.5	0.1	0.2	Bal.	Wrought
C (32Cr-HSi)	0.45	1.7	1.1	43.1	31.8	0.1	0.1	1.2	-	Bal.	Cast
D (21Cr-LSi)	0.08	0.3	1.2	31.2	20.6	0.5	0.5	-	0.3	Bal.	Wrought

Gas carburization tests were conducted in a horizontal reaction chamber. The specimens were exposed to a gas mixture of 15%CH_4-3%CO_2-82%H_2 (vol.%) flowing at a rate of 250 sccm (standard cubic centimeters per minute) at temperatures of 1,000, 1,100 and 1,150°C. The gas composition was chosen so that the equilibrium Po_2 corresponded to the actual pyrolysis environment (the equilibrium Po_2 of the test gas mixture was calculated to be 1.02×10^{-21} atm at 1,000°C, 4.94×10^{-21} at 1,100°C, and 1.00×10^{-20} at 1,150°C). As illustrated in Fig. 2-5, eight coupon specimens were placed on a slotted alumina brick upright and set into the reaction chamber, allowing gas flow parallel to the specimen surfaces. The reaction chamber was heated in a horizontal electric furnace. The reaction chamber, with 75 mm inside diameter and a uniform-temperature zone of 200 mm length, was purged with a N_2-5vol.%H_2 gas mixture for an hour at room temperature. After complete replacement of the purge gas with the following test gas mixture, the test specimens were heated at the desired temperatures. To evaluate their carburization resistance, the "carbon increase" in the specimen was measured. This value was obtained by the

following procedures. The specimen surface was peeled at intervals of 0.5 mm thickness down to 2.0 mm depth, and then the carbon content of these chips was analyzed by the inductively coupled plasma (ICP) spectrometry. Then, values of the carbon content of the base alloys (shown in Table 2-2) were subtracted from the obtained data and the resultant values were used as the "carbon increase" in this study. Cross-sections of the specimen surfaces were investigated by optical microscopy and electron probe X-ray microanalysis (EPMA). The specimen surfaces after carburization were investigated by X-ray diffraction to identify the type of oxide scales and carbides.

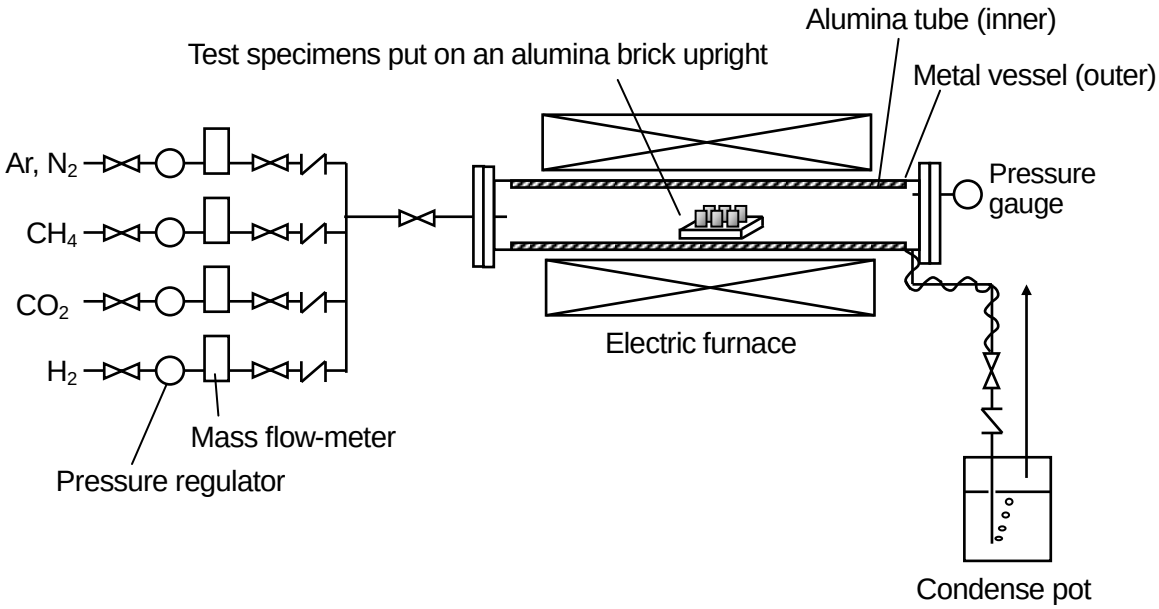

Figure 2-5 Schematic carburization test furnace design.

2.4 Results

2.4.1 Depth Profiles of the Increased Carbon

Depth profiles of the increased carbon of each alloy after exposure to 15%CH_4-3%CO_2-82%H_2 gas mixture at 1,000, 1,100, and 1,150°C are shown in Figs. 2-6 (a), (b), and (c), respectively. These carburization tests were conducted for 96h, but most coupon specimens of the 1,150°C test carburized to the specimen center. Therefore, the reaction time of the 1,150°C test was shortened to 48h. At 1,000°C, alloy D showed the worst resistance to carburization whereas alloys A and C were the best. Alloy B was slightly worse than alloys A and C. For specimens of the high-Cr alloys A, B, and C,

carburization did not proceed to a depth greater than 1.5 mm. At 1,100°C, carburization was heavier for each alloy and the carbon increase in each specimen was higher than that for the 1,000°C specimens. The carburization resistance of high-Si alloys of A (1.8%Si) and C (1.7%Si) was appreciably better than that for the low-Si alloys of B (0.5%Si) and D (0.3%Si). The low-Cr, low-Si alloy D carburized the most among the tested alloys. The high-Si alloys exhibited good resistance to the carburizing environment at 1,100°C and 1,150°C. The carburization resistance of the high-Si alloys A and C was again much better than that of the low-Si alloys B and D.

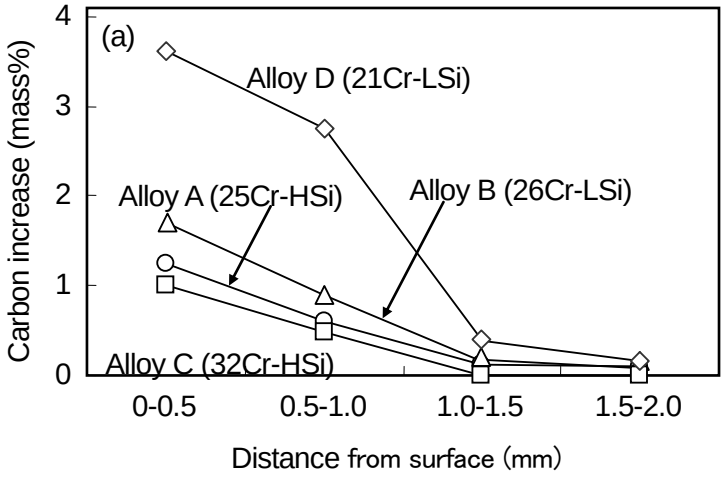

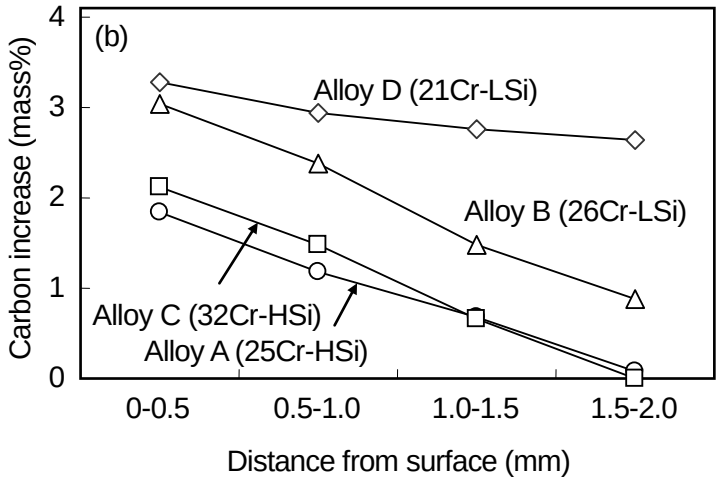

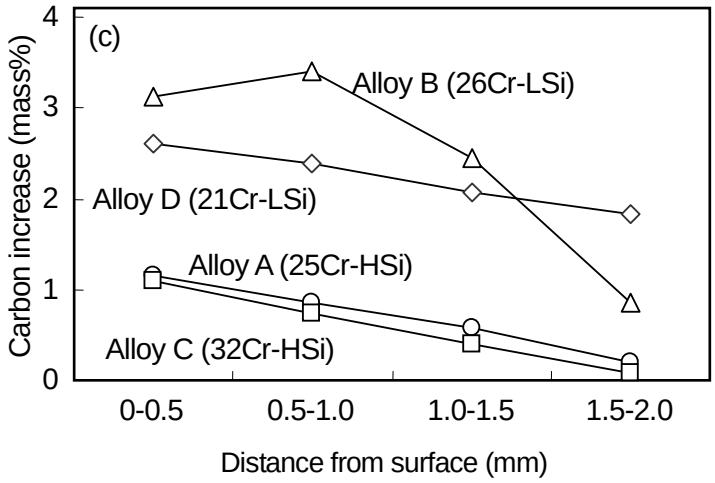

Figure 2-6 Depth profiles of carbon increase after exposure to 15%CH_4-3%CO_2-82%H_2 gas mixtures (a) at 1,000°C for 96h, (b) at 1,100°C for 96h, and (c) at 1,150°C for 48h.

2.4.2 Characterizations of Internal Carburization with Oxidation

The metallographic cross-sections of alloy A and alloy D after exposure at 1,000°C for 96h are shown in Fig. 2-7. For alloy A, a precipitation-free zone of approximately 20 μm thickness was found underneath the uniform oxide scale of about 10 μm thickness, suggesting that Cr diffused outward and that the formation of a protective Cr_2O_3 scale was completed. Intergranular precipitates with very fine intragranular precipitates, which were identified as Cr_7C_3 and $Cr_{23}C_6$, were observed in the substrate. In contrast, alloy D had no apparent precipitation-free zone underneath the external scale, indicating that the external scale consisted predominantly of less-protective spinel-type M_3O_4 oxide (M for Cr, Fe, and Mn) instead of Cr_2O_3.

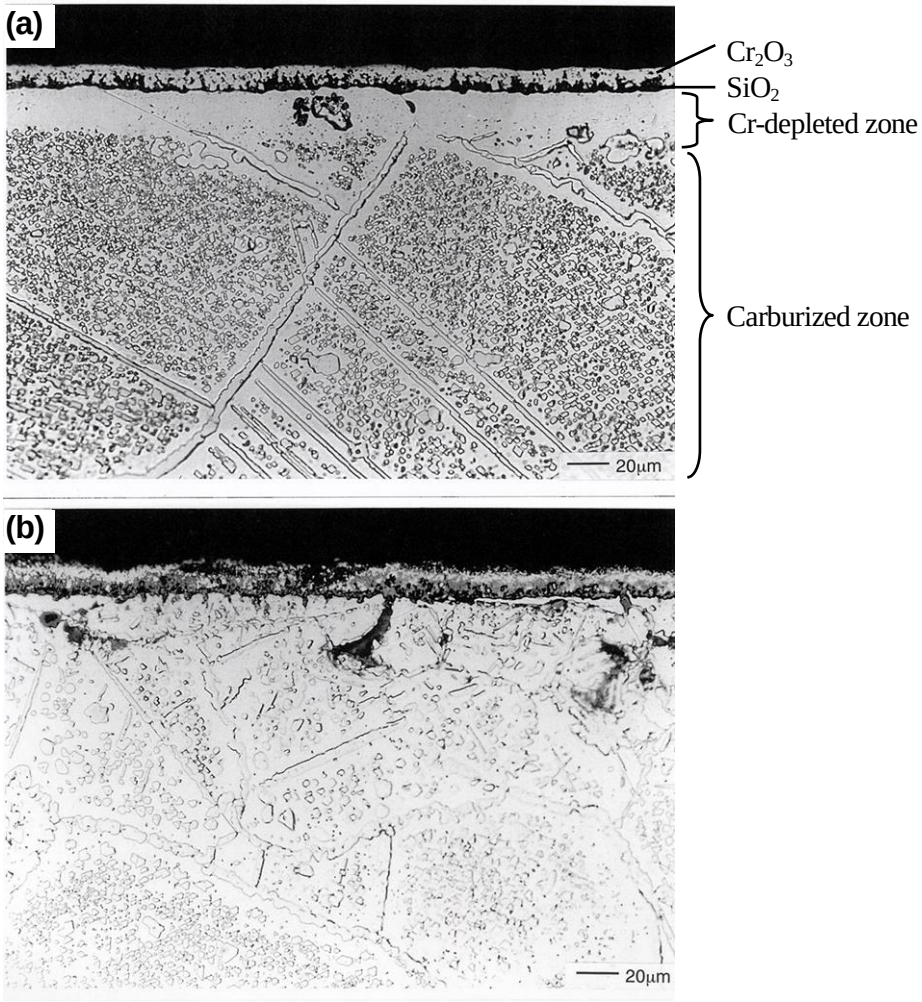

Figure 2-7 Metallographic cross-sections of alloys (a) A (25Cr-HSi) and (b) D (21Cr-LSi), reacted with 15vol.%CH_4-3%CO_2-82%H_2 at 1,000°C for 96h.

The results of X-ray diffraction presented in Table 2-3 supported this point. Diffraction peak intensity of M_2O_3 (corundum-type oxide of Cr_2O_3) was greater for alloy A than for alloy D at 1,000°C. At this temperature, the peak intensity of M_2O_3 (protective oxide scale) formed on alloys A, B, and C of more than 25%Cr was clearly much higher than that for the low-Cr alloy D. Since clearly the high-Cr alloys A, B, and C have superior carburization resistance to the low-Cr alloy D, Cr was confirmed as an effective alloying element to combat the corrosion at 1,000°C when added to alloys at more than 25%. This beneficial effect of Cr was realized by the formation of a uniform protective Cr_2O_3 scale. Above 1,100°C, Cr-carbide as Cr_7C_3 was only identified at the surface areas of all test alloys.

Table 2-3 Results of X-ray diffraction

Alloy	Test conditions		
	At 1,000°C for 96h	At 1,100°C for 96h	At 1,150°C for 48h
A (25Cr-HSi)	M_2O_3(m), M_3O_4(ww)	M_2O_3(ww), M_3O_4(ww) Cr_7C_3(w), C-graphite(w)	M_2O_3(ww), Cr_7C_3(mw), C-graphite(mw)
B (26Cr-LSi)	M_2O_3(mw), M_3O_4(ww)	M_2O_3(w) Cr_7C_3(mw), C-graphite(m)	M_2O_3(ww), Cr_7C_3(mw), C-graphite(ms)
C (32Cr-HSi)	M_2O_3(mw), M_3O_4(mw)	M_2O_3(ww), M_3O_4(w) Cr_7C_3(mw), C-graphite(w)	M_2O_3(ww), M_3O_4(ww) Cr_7C_3(mw), C-graphite(mw)
D (21Cr-LSi)	M_2O_3(ww), M_3O_4(m)	M_2O_3(ww) Cr_7C_3(m), C-graphite(m)	Cr_7C_3(mw), C-graphite(ms)

Symbols in ( ) denote relative X-ray intensity according to the following order
[strong] ss > s > ms > m > mw > w > ww [weak]

Figure 2-8 shows the metallographic cross-sections of alloys A, B, and C exposed to the 15%CH_4-3%CO_2-82%H_2 gas mixture at 1,100°C for 96h. At 1,100°C, the high-Si alloys A and C were much more resistant than the low-Si alloy B (see Fig. 2-6 (b)). For the high-Si alloy A, again, a precipitation-free zone of about 20 μm thickness was observed, indicating the enrichment of Cr in the external scale. For the high-Si alloys A and C, an external scale was definite, but for alloy B, it was not visible, suggesting that any protective scale was not formed on it at 1,100°C. Alloys A and B had chain precipitates along grain boundaries, and bulky precipitates were found in the matrix. Alloy C (initial carbon content of 0.45%) had a number of gross precipitates within the dendritic microstructure. These precipitates in alloys A, B, C, and D were identified mainly as Cr_7C_3.

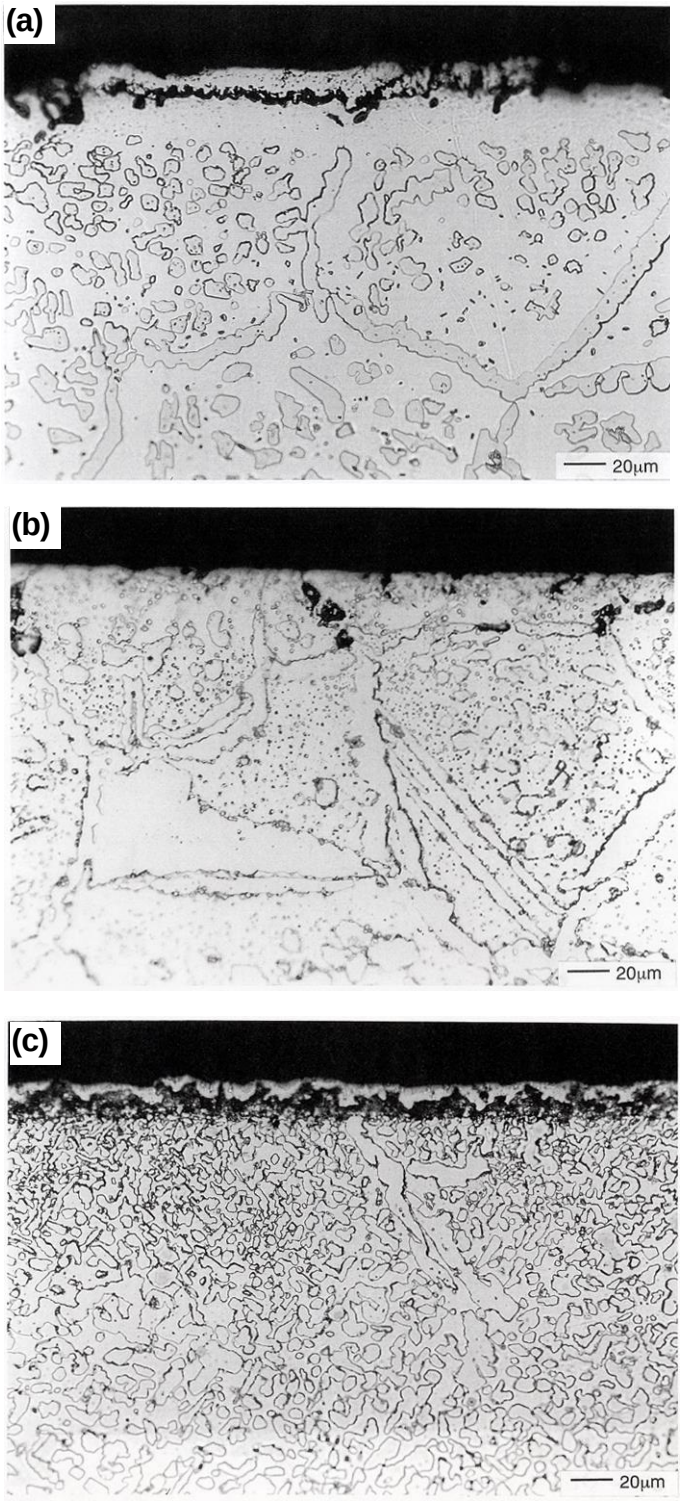

Figure 2-8 Metallographic cross-sections of alloys (a) A (25Cr-HSi), (b) B (26Cr-LSi), and (c) C (32Cr-HSi), reacted with 15vol.%CH_4-3%CO_2-82%H_2 at 1,100°C for 96h.

The results of X-ray diffraction shown in Table 2-3 indicate that the X-ray intensity of M_2O_3 for the 1,100 and 1,150°C exposure became weak compared with the 1,000°C scales, and those of carbide and graphite became evident. Since any SiO_2 scale was expected to be amorphous at 1,100°C and could not be identified by X-ray diffraction, electron probe microanalysis was performed for 1,100°C scales on the high-Si alloy A and the low-Si alloy B. Secondary electron micrographs and EPMA dot maps of the oxide scale of the high-Si alloy A and the low-Si alloy B reacted with the 15%CH_4-3%CO_2-82%H_2 gas mixture at 1,100°C are presented in Figs. 2-9 and 2-10, respectively. Chromium was found to be continuous as a Cr_2O_3 scale on alloy A, whereas it was detected in the matrix as Cr_7C_3. Silicon was enriched beneath the Cr_2O_3 scale as SiO_2, and the part of this scale was convoluted in the Cr_2O_3. For the low-Si alloy B, concentration of Cr and Si at the specimen surface was not clear. Instead, Al as Al_2O_3 concentrated sparsely at the surface since this alloy contained Al of 0.5%.

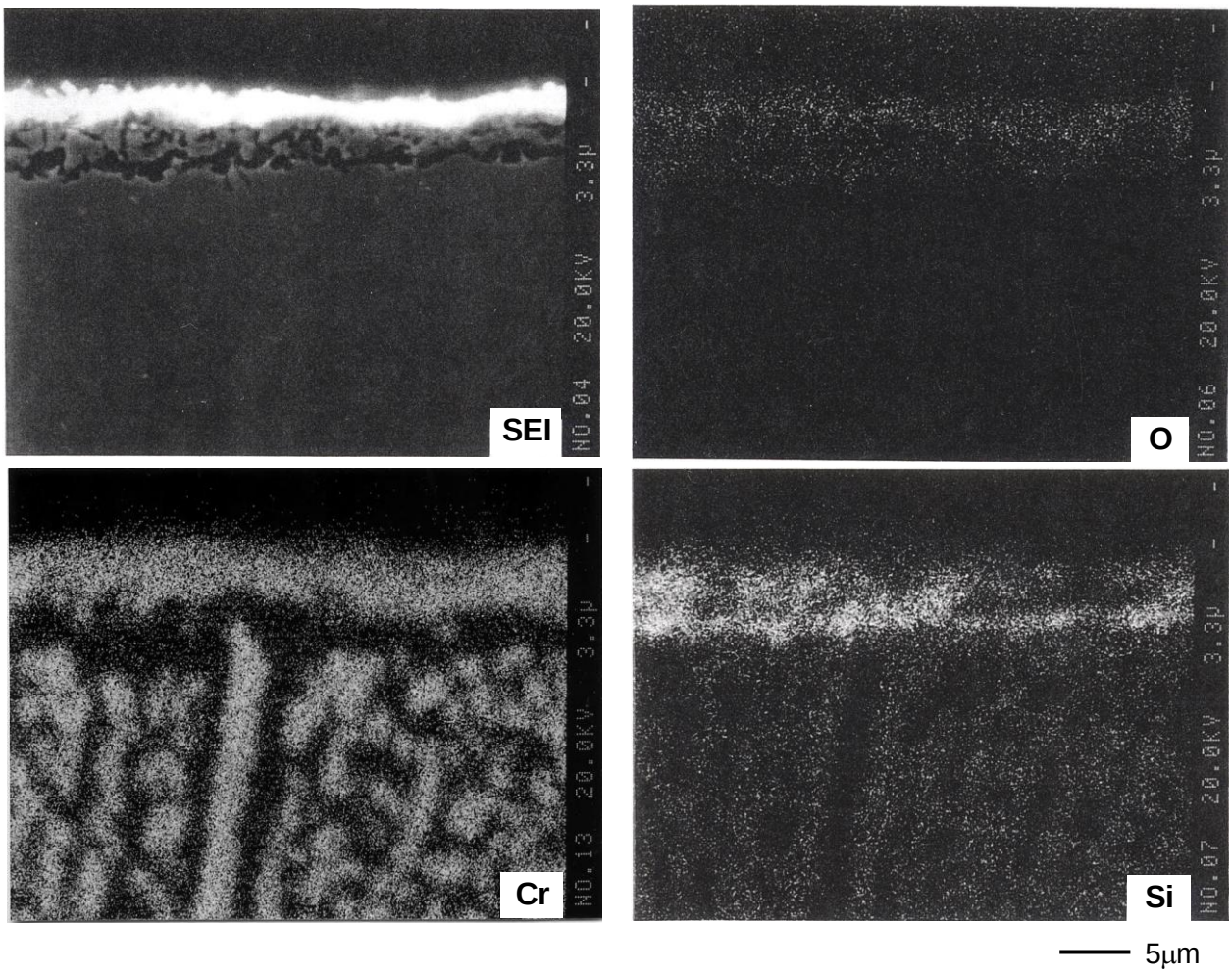

Figure 2-9 EPMA images of alloy A (25Cr-HSi) reacted with 15vol.%CH_4-3%CO_2-82%H_2 at 1,100°C for 96h.

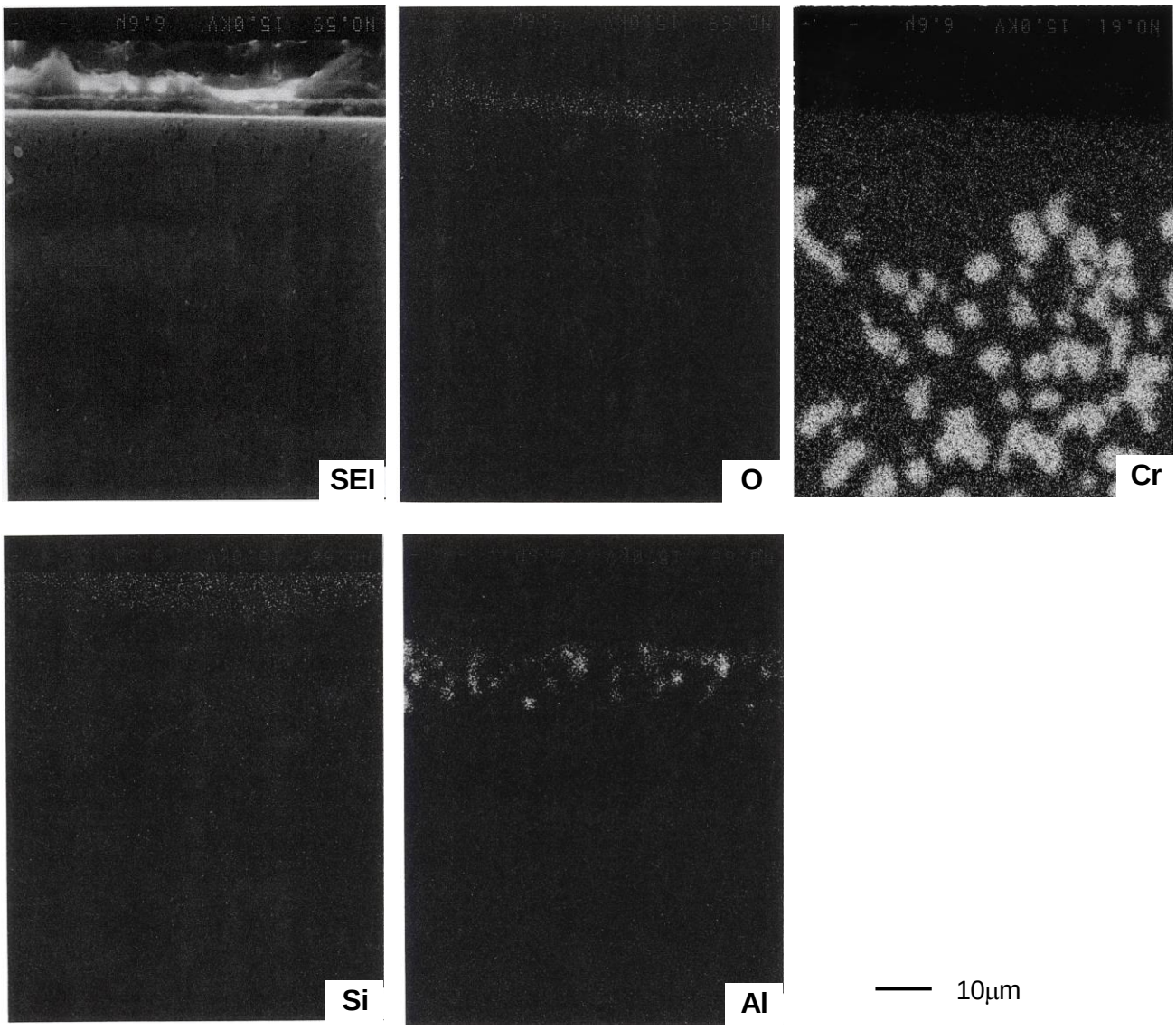

Figure 2-10 EPMA images of alloy B (26Cr-LSi) reacted with 15vol.%CH_4 -3%CO_2-82%H_2 at 1,100°C for 96h.

2.5 Discussion

The test results obtained have shown that the oxide scale formed on the alloys can influence their carburization resistance. At 1,000°C, alloys A, B, and C of more than 25%Cr had significantly better resistance than alloy D of 21%Cr (Fig. 2-6 (a)), because the formation of Cr_2O_3 scale was considered incomplete for alloy D. At 1,100 and 1,150°C, the high-Si alloy A had better resistance than the low-Si alloy B, although their Cr content was similar to each other. These results, along with the X-ray diffraction and the microscopic observations, demonstrate that the SiO_2 scale, instead of the Cr_2O_3 scale, would have protected the alloys from the harsh carburization environment at 1,100°C and 1,150°C. Therefore, the formation of a SiO_2 layer reduced carburization, since Cr_2O_3 is considered thermodynamically unstable above 1,030-1,040°C. Although 1,100 and 1,150°C scales of high-Cr alloys A, B, and C contained a small amount of M_2O_3, thermodynamic estimation suggests that the protective Cr_2O_3 scale had lost its stability and had changed to Cr-carbides such as Cr_7C_3 above 1,030-1,040°C. These results mean that at temperatures above 1,030-1,040°C, carburization-resistant alloys must contain not only Cr (to resist at low temperatures) but also Si to form a protective SiO_2 scale in the environment.

In the present tests, the carbon increase beneath the external surface of alloys (i.e. location of 0-0.5 mm depth in Fig. 2-6) and the depth of the internal carburization zone (see Fig. 2-7) of each alloy did not always correlate well with each other. For example, the carbon increase at the external surface of alloys B and D for the 1,100°C experiment was similar, but the depth of the internal carburization zone of these alloys was significantly different. Another example can be found for alloys C and D at 1,000°C. The difference in the carbon increase at the external surface between alloys C and D for the 1,000°C experiment was huge, but the depth of the internal carburization zone of these alloys did not differ considerably. Hence, the depth of the internal carburization zone is considered affected not only by the formation of "protective" oxide scale, but also by other factors such as alloy chemistry, alloy microstructure, etc. To investigate this point, especially the growth kinetics of the internal carburization zone of each alloy, a diffusion model involving carbon content of the external surface, Cr content of the alloy, and diffusivity of carbon in the alloy matrix, was introduced.

Several authors [31 - 33] have approached to present the internal carburization process using a numerical finite difference technique. This computational method, which gives a numerical solution to

Fick's 2nd law, considers the interaction between C diffusion and carbide precipitation. The calculated results have presented the carbon-profile in the alloy to some extent. In this study, another classical approach has been conducted to estimate the internal carburization process. The expressions describing the kinetics of internal precipitation in the absence/presence of an external oxide scale have been derived [34, 35]. If diffusion control is maintained, the depth ξ of the internal carburization zone is a parabolic function of the time t so that

$$\xi = (2k_p \times t)^{1/2} \tag{1}$$

Since carbon is estimated to diffuse much faster than the carbide-forming alloying elements such as Cr (shown later), the parabolic rate constant k_p is expressed by analogy with the internal oxidation model derived by Wagner [34].

$$k_p = \frac{\varepsilon \times D_c \times N_c^{\circ}}{\nu \times N_M} \tag{2}$$

where D_c is the diffusivity of carbon in the γ matrix, N_c° the mole fraction of carbon at the external surface, N_M the mole fraction of carbide-forming alloying element of the base metal, ε the dimensionless constant, and ν the stoichiometric factor for the single precipitated carbide $M_\nu C$.

In Eq. (2), N_c° was taken for the carbon content in the γ matrix at the external surface, not for the "total" carbon content (i.e. dissolved carbon plus carbon as carbides) at the external surface. A hypothetic concentration profile of carbon in the internal carburization zone is shown in Fig. 2-11.

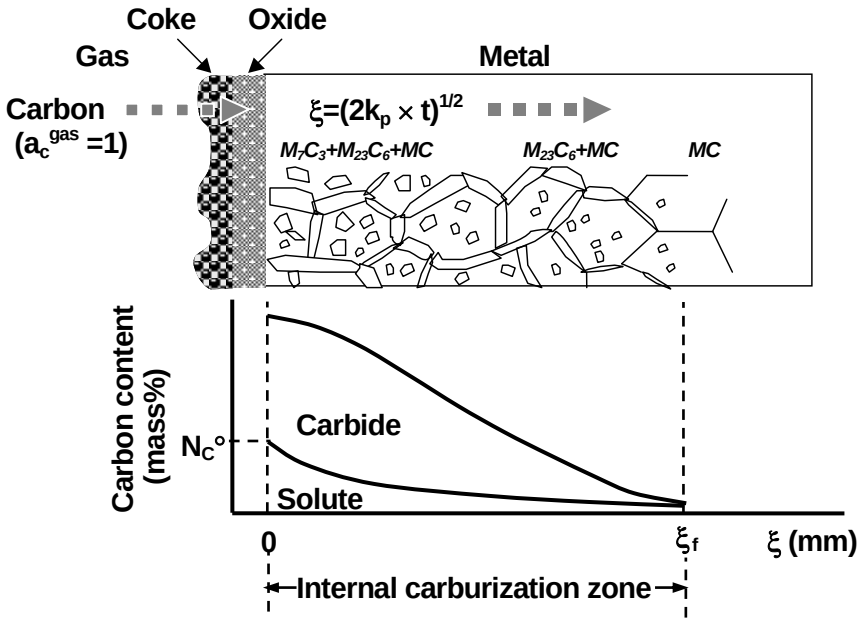

Figure 2-11
Schematic representation of the alloy microstructure and concentration profiles of carbon in carburizing -oxidation environments.

The carbon content $N_c°$ of the γ matrix at the external surface in Eq. (2) may be obtained from an isothermal section of an appropriate alloy phase diagram. As an example, a phase diagram of C-Fe-Cr system at 1,000°C was reproduced and is shown in Fig. 2-12 [36, 37].

According to this diagram, $Cr_{23}C_6$ is in equilibrium with α matrix for alloys of more than 18 at.%Cr. Since the solubility of carbon in the α matrix is extremely low, increasing carbon content of this alloy directly results in increasing the amount of the carbide precipitates. The volume fraction of the precipitated carbides for an alloy of certain carbon content can be obtained from the tie line of iso-activity carbon, additionally drawn in Fig. 2-12, by using the lever rule. For alloys of less than 16 at.%Cr, the $M_{23}C_6$, M_7C_3, and /or M_3C are in equilibrium with the γ matrix. In this case, the γ matrix can dissolve carbon to some extent, depending on the Cr content of the alloy. The dissolved carbon content increases with decreasing the Cr content of the alloy, and takes a maximum value of about 0.07 at.% for an "alloy" of zero % Cr. For this steel, Fe_3C is in equilibrium with the γ matrix. Note the wide range of Cr content for the carbides since Cr carbides can incorporate iron considerably. Hence, for alloys of under 18 at.%Cr, the carbon content of the γ matrix in equilibrium with carbides (i.e. the saturated carbon solubility of the γ matrix) is dependent on the Cr content of the alloy and this value can be obtained from the phase boundaries between the γ phase and the (γ + carbide) coexistent phases.

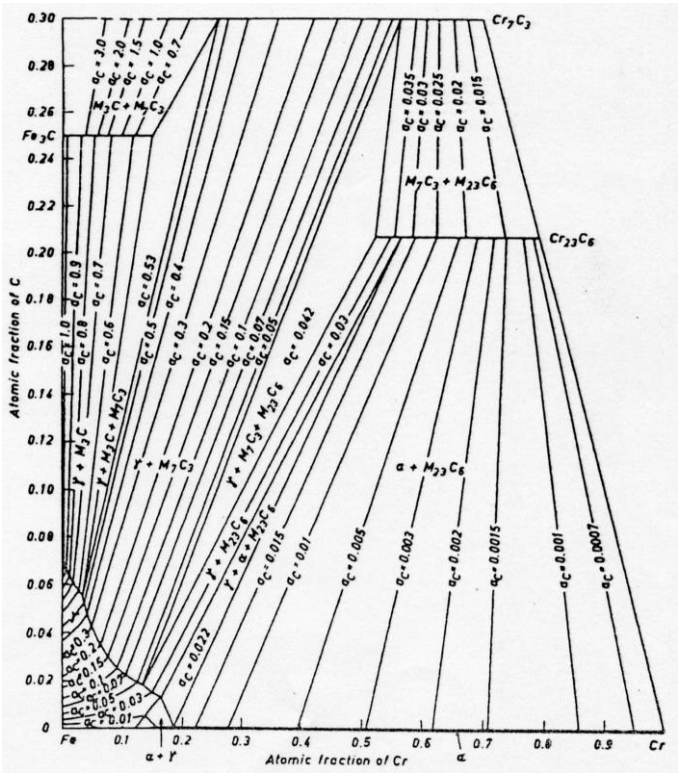

Figure 2-12 Isothermal section of the phase stability diagram of Fe-Cr-C system at 1,000°C [36].

To obtain the saturated carbon solubility of the γ matrix (i.e. the carbon content of the γ matrix in equilibrium with carbides), expressed as N_c in this paper, for the C-Fe-38%Ni-Cr alloy system (corresponding to alloy A), an isothermal section of C-Fe-38%Ni-Cr alloy phase diagram at 1,100°C was constructed by thermodynamic calculations and is shown in Fig. 2-13. The carbon concentration of the γ matrix N_c at any location in the internal carburization zone and the type of carbides, which may precipitate can be predicted from this diagram. For example, when the carbon content in a certain location of the internal carburization zone is 1.8 mass% (corresponding to point A_2 in Fig. 2-13) for an alloy of 25%Cr-38%Ni-Fe, the C /Cr contents in the γ matrix can be obtained from point A'_2. At this location, carbide precipitates are considered to be M_7C_3. The volume fraction of the γ matrix and the carbides at this location may also be estimated by using the tie line shown as a broken line A_2'-A_2-A_2''. Upon increasing the "total" carbon content as carburization proceeds (on line A), the Cr concentration in the γ matrix decreases and the carbon content of the γ matrix N_c increases, following line A' (i.e. the phase boundary of γ /(γ + carbides)) from A'_1 to A'_3 in Fig. 2-13. Once the C /Cr contents in the γ matrix approach point A'_3, i.e. 0.70%C /2.6%Cr, graphite would precipitate out. The Cr content of the γ matrix at this point is very low, about 2.6%, although the substrate contains Cr of 25%.

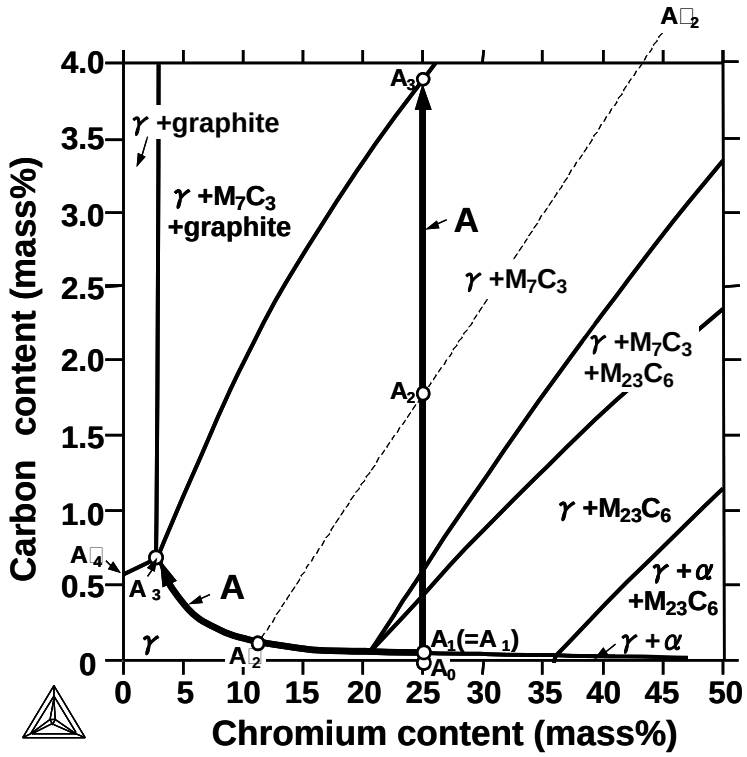

Figure 2-13 Calculated equilibria in the C-Fe-38mass%Ni-Cr system at 1,100°C using the computational analysis.

Carbon deposition on practical tube surfaces occurs in most cases, and the deposited carbon attached to oxide scales was reported to be graphite [23]. Therefore, the γ matrix at the external surface could be in equilibrium not only with carbide but also with graphite. In this case, the carbon content of the γ matrix at the external surface $N_c°$ must correspond to the saturated carbon solubility of the γ matrix in equilibrium with graphite and carbide; for alloy A of 25%Cr-38%Ni-Fe, for example, $N_c°$ must be equal to 0.007 (0.7 mass%) at 1,100°C, corresponding to point A_3' in Fig. 2-13.

Under the assumption that the γ matrix at the external surface is in equilibrium with graphite and the Cr content of the corresponding γ matrix is zero, $N_c°$ for alloys of various Ni contents can be obtained from the ternary C-Fe-Ni phase stability diagram. This is shown in Fig. 2-14. The value $N_c°$ of 38%Ni alloy at 1,100°C in this figure corresponds to point A'_4 in Fig. 2-13. This diagram was also constructed using the computational analysis. To estimate $N_c°$, the ternary C-Fe-Ni alloy system, instead of the quaternary C-Fe-Cr-Ni system, was considered here since the γ matrix at the external surface is expected to be depleted with Cr, i.e. Cr content is almost zero, attributed to the formation of internal Cr-carbides (see point A'_3 in Fig. 2-13 for example) and of external Cr-oxide scale. At 900-1,200°C, the carbon content of the γ matrix in equilibrium with graphite decreases with increasing the Ni content of the alloy and becomes minimal at about Ni /Fe = 4 /1, which agrees well with the literature [38]. High-Ni alloys generally have a lower solubility of carbon than the low-Ni alloys, and hence the carburization rate k_p of high-Ni alloys might be lower than the low-Ni alloys, which can be deduced from Eq. (2).

The effect of additional alloying elements such as Al, Si, Mn, Co, and Cu on $N_c°$ was examined, under the assumptions that the γ matrix at the external surface is in equilibrium with graphite and the Cr content is zero. Figure 2-15 shows the calculated results for the C-Fe-38%Ni-X alloys at 1,100°C. The $N_c°$ decreases with increasing amount of the additional alloying elements except for Mn. The decrease in $N_c°$ by addition of Al and Si was greater than that for Ni. Addition of Si (and Al) is considered beneficial not only because of the formation of a protective SiO_2 (Al_2O_3) scale on the surface of the alloys, but also of decreasing $N_c°$. Hence, the addition of Si may decrease the depth of the internal carburization zone.

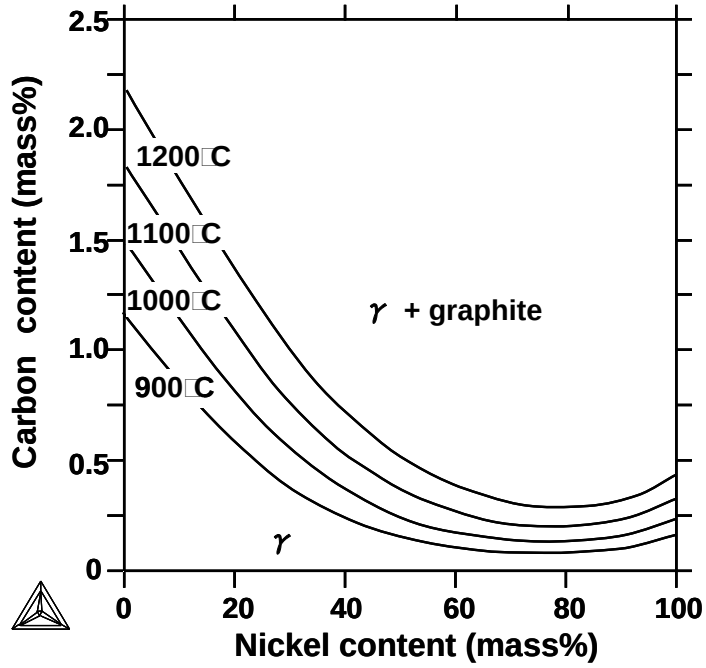

Figure 2-14 Calculated carbon content $N_c°$ in the C-Fe-Ni ternary system in the temperature range from 900°C to 1,200°C.

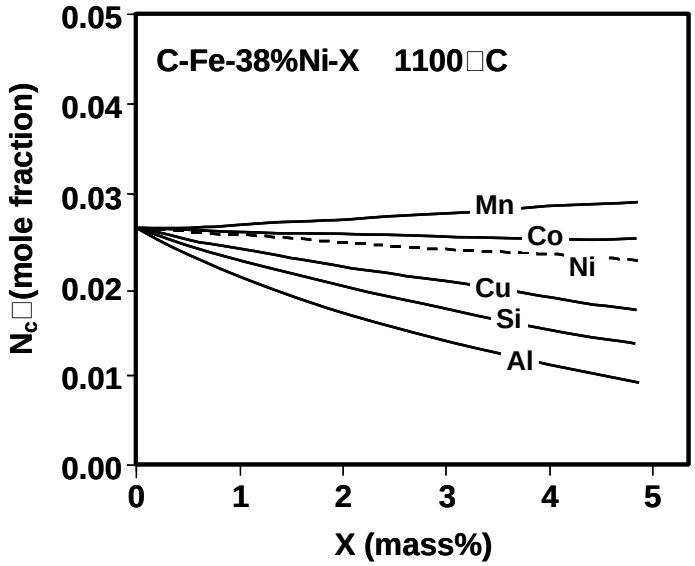

Figure 2-15 Effect of additional alloying elements on $N_c°$. Calculated for the C-Fe-38mass%Ni alloy at 1,100°C.

Using the data shown in Figs. 2-14 and 2-15, and considering Ni, Si, and Al contents of each alloy, $N_c°$ was calculated for alloys A, B, C, and D at 1,100°C under an assumption that the Cr content of the γ matrix at the external surface of these alloys is zero, and the γ matrix at the external surface of these alloys is in equilibrium with graphite. The mole fraction of the carbide-forming alloying element N_M of each alloy was also calculated, assuming that Cr is the only carbide-forming alloying element; N_{Cr} was substituted for N_M. The mole fraction of Cr of each alloy N_{Cr} was calculated by subtracting Cr required for reaction with carbon in the substrate to form M_7C_3 carbides from the Cr composition of each alloy. Then, the depth ξ of the internal carburization zone upon reaction at 1100°C for 96h was derived from Eqs. (1) and (2), assuming the same diffusivity of carbon D_c (11.3×10^{-7} cm^2/s) for each alloy (Table 2-4). The calculated values are presented in Table 2-5 and compared with the 1,100°C experiment. In this calculation, the dimensionless factor ε and the stoichiometric factor for the carbide ν were set to be unity and 7 /3 (corresponding to Cr_7C_3), respectively.

Table 2-4 Diffusivity of carbon at 1,100°C taken from the literature

		(cm^2/s)	Ref.
D_c	γ-Fe	7.2×10^{-7}	[39]
	γ-Fe 0.1at%C	7.0×10^{-7}	[40]
	58at%Ni-Fe	11.3×10^{-7}	[41]
	Ni	7.0×10^{-7}	[39]
D_{Cr}	31at%Ni-Fe	1.4×10^{-11}	[42]

Table 2-5 Calculated $N_c°$, N_{Cr}, and the thickness of the internal carburization zone (ξ) at 1,100°C for 96h.

Alloy	$N_c°$ (mole fraction)	N_{Cr} (mole fraction)	ξ (mm)
A (25Cr-HSi)	0.0133	0.267	1.29
B (26Cr-LSi)	0.0174	0.270	1.47
C (32Cr-HSi)	0.0107	0.300	1.09
D (21Cr-LSi)	0.0236	0.220	1.89

The calculated depths ξ ranged between 1.09 mm and 1.89 mm. Although these values were somewhat smaller than the experimental values; for the present carburization at 1,100°C for 96h, the depths ξ was 1.5 mm and large for the tested alloys. However, the relative depth ξ of each alloy agreed well with that for the carburization test. This inconformity might be attributed to the inadequate diffusivity data of carbon and the substitution of the mole fraction of chromium N_{Cr} for N_M for the present estimation. More precise carbon diffusion data for each alloy are needed to improve this estimation.

In the present estimation, the carbon content in the γ matrix at the external surface, not the "total" carbon content (dissolved carbon plus carbon as carbides), was used as $N_c°$ in Eq. (2). To substantiate this point, an experiment was conducted, where alloys A-D were heated in a gas mixture of 15%CH_4-85%H_2 at 1,100°C. In this environment, the formation of oxide scale is minimized. As shown in Fig. 2-16, a drastic increase in the carbon content over the entire carburization zone occurred for all the alloys. However, surprisingly, the depth ξ remained almost the same compared to the 15%CH_4-3%CO_2-82%H_2 experiment, especially for alloys A and C. If the carbon flux is regulated by the "total" carbon content at the external surface, internal carburization zone of alloys A and C must be deeper for the latter experiment (reacted with 15%CH_4-H_2) than the former experiment (reacted with 15%CH_4-3%CO_2-82%H_2), since the total carbon content at the external surface of the latter experiment is significantly higher (around 3.3%) than the former experiment (around 2%). Hence, for the carbon content $N_c°$ in Eq. (2), the dissolved carbon content in the γ matrix at the external surface must be considered.

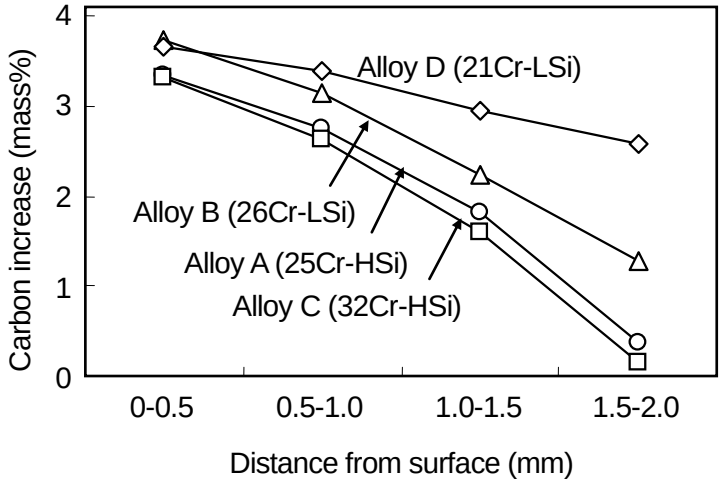

Figure 2-16 Depth profiles of the carbon increase after exposure to a 15%CH_4-85%H_2 gas mixture at 1,100°C for 96h.

The type and morphology of the oxide scale formed upon carburization can influence the "total" carbon content at alloy external surfaces. If the protection by the oxide scale is successful, the "total" carbon content may remain low, whereas if the formation of an oxide scale is incomplete with cracks and flaws, the "total" carbon content can rise rapidly upon carburization. In this study; for alloy D, the "total" carbon content at the external surface which reacted with 15%CH_4-3%CO_2-82%H_2 at 1,100°C (Fig. 2-6 (b)) was equal to that reacted with 15%CH_4-H_2 (Fig. 2-16), suggesting that oxides formed on alloy D in the gas mixture were insufficiently dense to minimize the "total" carbon content. For alloys where the "total" carbon content at the external surface is high, the volume fraction of carbides in the internal carburization zone is large. In contrast, the depth ξ may be affected by the carbon content $N_c°$ in the γ matrix at the external surface. For high-Ni alloy and /or alloys containing larger amounts of carbide-forming alloying elements such as Cr and Si, $N_c°$ in the γ matrix is low and N_M is high so that the parabolic rate constant k_p remains small. Hence, alloy resistance against carburization may be improved by the formation of a protective oxide scale and by the reduction of $N_c° / N_M$ of the alloys.

2.6 Conclusions

Thermodynamic aspects for hydrocarbon (H_mC_n) with H_2O gas mixtures were calculated and considered to understand the carburizing environments of the cracking furnace tubes used for the actual ethylene pyrolysis. Based on these information, the gas composition for laboratory carburization tests was decided, and tests were conducted to evaluate the carburization resistance of four commercial Fe-Ni-Cr alloys. The conclusions obtained are summarized as follows:

(1) The equilibrium Po_2 of the cracking gases was calculated to be in a range of 10^{-21} to 10^{-19} atm at 900-1,100°C. In this environment, the Cr oxide scale was considered to be stable and protective for up to 1,030-1,040°C. The laboratory carburization tests of four commercial tube alloys supported this point.

(2) For alloys of more than 25 mass%Cr, protection by the Cr_2O_3 scale was prominent at 1,000°C, but the formation of a SiO_2 layer was needed for the alloys at 1,100°C and 1,150°C. At 1,100°C and 1,150°C, the high Si high-Cr alloys resisted well in the environment. The depth of the internal

carburization zone of the tested alloys differed among alloys of different alloy chemistry. For the 1,100°C test, the depth of the internal carburization zone of high-Ni alloys was less than that for the low-Ni alloy. The difference was interpreted by applying the internal oxidation model derived by Wagner.

(3) The mole fraction of carbon at the external surface was obtained from several isothermal phase stability diagrams, under the assumption that the γ matrix at the external alloy surface is in equilibrium with graphite, and its Cr content is zero. The relative depths of the internal carburization zones among the tested alloys obtained by the calculation agreed well with the 1,100°C experiment, except for one alloy.

(4) Alloy resistance against carburization was interpreted in term of the total carbon uptake defined by the carbon increase at the external surface of the metal, and the depth of the internal carburization zone. To minimize the carbon increase at the external surface, the formation of protective oxide scale is necessary. High-Ni alloys are considered necessary to decrease the growth rate of the internal carburization zone, because the carbon content in the γ matrix at the external surface remains low. The growth rate is also affected by the content of carbide-forming alloying elements and the diffusivity of carbon D_c in the matrix.

References

[1] D.B. Roach, "Carburization of cast heat resistant alloys," CORROSION /76, paper no.7, (Houston, TX: NACE, 1976).

[2] J.R. Schley, F.W. Bennett, Corrosion 23 (1967), p.276.

[3] A. Shnaas, H.J. Grabke, Werkst. Korros. 29 (1978), p.635.

[4] D.F. Lupton, P.J. Ennis, Res. Mech. 1 (1981), p.245.

[5] R. Petkovic-Luton, T.A. Ramanarayanan, Oxid. Met. 34 (1990), p.381.

[6] J. Klöwer, U. Heubner, Mater. Corros. 49 (1998), p.237.

[7] H.J. Grabke, "Carburization, A High-Temperature Corrosion Phenomenon", no. 52 (St. Louis, MO: Materials Technology Institute of the Chemical Process Industries, Inc., 1998).

[8] S.B. Parks, C.M. Schillmoller, Hydrocarbon Process. 3 (1996), p.53.

[9] R.H. Kane, Corrosion 37, 4 (1981), p.187.

[10] Y. Sawaragi, M. Nishi, Petrotech 18, 8 (1995), p.648.

[11] S.B. Parks, C.M. Schillmoller, Chem. Eng. World 34, 3 (1999), p.177.

[12] R. Milner, M. Phaneuf, "Comparative carburization of heat resistant alloys," CORROSION /98, paper no.431, (Houston, TX: NACE, 1998).

[13] Y. Nishiyama, H. Semba, K. Ogawa, Y. Yamadera, Y. Sawaragi, S. Kinomura, "A new carburization resistant alloy for ethylene pyrolysis furnace tubes," CORROSION /2002, paper no.2386, (Houston, TX: NACE, 2002).

[14] K. Hosoya, K. Satoh, K. Yamamoto, G.J.A. Hack, R.M. Haeberle, "An evaluation of the coking resistance of a high performance oxide dispersion strengthened (ODS) alloy tube," AIChE 2000 Spring Meeting, paper no.86f (New York , NY: AIChe, 2000).

[15] D.C. Agarwal, U. Brill, "Performance of Alloy 602CA (UNS N06025) in high temperature environments up to 1200°C," CORROSION /2000, paper no.521, (Houston, TX: NACE, 2000).

[16] A.B. Smith, A. Kempster, A. Lambourne, J.R. Smith, "The use of aluminide diffusion coatings to improve carburization resistance," CORROSION /2001, paper no.1391, (Houston, TX: NACE, 2001).

[17] T. Redmond, Y. Chen, A. Bailey, J. Page, "A low coking and carburization resistant coating for ethylene pyrolysis furnaces," CORROSION /2001, paper no.1392, (Houston, TX: NACE, 2001).

[18] D. Mullenix, A. Kurlekar, "Results of a furnace tube surface treatment in a full furnace trial," AIChE 11th Annual Ethylene Producers Conf. (New York , NY: AIChe, 1999).

[19] H.J. Grabke, U. Gravenhorst, W. Steinkusch, Werkst. Korros. 27 (1976), p.291.

[20] A. Schnaas, H.J. Grabke, Oxid. Met. 12 (1978), p.387.

[21] T.A. Ramanarayanan, Mater. Sci. Eng. 87 (1987), p.113.

[22] P.J. Smith, O.Van Der Biest, J. Corish, Oxid. Met. 24 (1985), p.47.

[23] M.J. Bennett, J.B. Price, J. Mater. Sci. 16 (1981), p.170.

[24] D.R.G. Mitchell, D.J. Young, W. Kleemann, Mater. Corros. 49 (1998), p.231.

[25] P. Ganesan, G.D. Smith, C.S. Tassen, "Corrosion resistance of Alloy 803 in environments applicable to fossil energy systems," CORROSION /95, paper no.470, (Houston, TX: NACE, 1995).

[26] A. Otomo, Y. Shinozaki, Y. Zaiga, S. Oishibashi, Japan Society for the Promotion of Science 123 committee report, 15 (Tokyo, Japan: 1974), p.177 (in Japanese).

[27] K. Ledieff, A. Rahmel, M. Schorr, Werkst. Korros. 31 (1980), p.83.

[28] W.F. Chu, A. Rahmel, Oxid. Met. 15 (1981), p.331.

[29] J.A. Colwell, R.A. Rapp, Metall. Trans. 17A (1986), p.1065.

[30] Thermodynamic data base MALT-2, The Japanese Society of Thermo-Heat Measurement, supplied by Kagakugijutsusya Co., Oct. (Tokyo, Japan: 1992).

[31] H.G. Sockel, H.J. Christ, Mater. Sci. Eng. 87 (1987), p.119.

[32] H.J. Christ, H. Biermann, F.C. Rizzo, H.G. Sockel, Oxid. Met. 32 (1989), p.111.

[33] S. Forseth, P. Kofstad, Mater. Corros. 49 (1998), p.266.

[34] C. Wagner, Z. Electrochem. 63 (1950), p.772.

[35] R.A. Rapp, Corrosion 21 (1965), p.730.

[36] T. Nishizawa, B. Uhrenius, Scand. J. Metall. 6 (1977), p.67.

[37] T. Nishizawa, Scand. J. Metall. 6 (1977), p.74.

[38] S.K. Bose, H.J. Grabke, Z. Metallkd 69 (1978), p.8.

[39] Y. Adda, J. Philibert, La Diffusion Dans Les Solides, Tome II (Sacley, France: Press Universitai de France, 1966).

[40] J.D. Fast, Interaction of Metals and Gases, vol. 2 (Basingstoke Hampshire, England: Macmillan, 1971).

[41] J. Cermák, J. Sopoušek, K. Stránský, Scr. Metall. Mater. 29, 12, (1993), p.1,581.

[42] H. Paxton, T. Kunitake, Trans. Met. Soc. AIME 218 (1960), p.1,003.

Chapter 3

DEGRADATION OF SURFACE OXIDE SCALE ON FE-NI-CR(-SI) ALLOYS UPON CYCLIC COKING AND DECOKING PROCEDURES IN A SIMULATED ETHYLENE PYROLYSIS GAS ENVIRONMENT

3.1 Introduction

Some cracking furnace tubes used for ethylene pyrolysis are reported to suffer from severe high temperature corrosion, since they are exposed to strongly carburizing gas atmosphere of steam-hydrocarbon gas mixtures at up to about 1,100°C [1 - 6]. Degradation of mechanical properties of tube materials due to carburization can result in a failure of furnace tubes. In addition to carburization, carbon deposition (coking) from the pyrolysis gas atmosphere on tube surfaces simultaneously occurs and this can reduce heat transfer rate, lowering the olefin yield. At extreme cases, plugging of furnace tubes due to coking leads to localized overheating and hence to tube failure [7]. To avoid this, coke is periodically removed in actual plants, coke is burned off in a flowing steam-air gas mixture inside the furnace tubes.

Two types of coke are formed in the hydrocarbon processing [8,9]. One is pyrolytic carbon generated upon thermal decomposition of hydrocarbon. An example of this is soot obtained by homogeneous reaction in the gas phase of high carbon activity (a_c >>1) at high temperatures. The other is catalytic carbon formed by decomposition of hydrocarbon gas species on metal surface catalyzed by reactive metals such as Fe and Ni.

Bennet et al. [10] investigated morphology of carbon taken from an actual pyrolysis furnace tube and reported that the outer carbon deposits consisted of columnar tight carbon with large, low spacing

crystallites, while the inner carbon deposits consisted of porous carbon with fine graphite crystallites that includes small metal particles. These metal particles were considered to catalyze deposition of graphite carbon. Steurbaut et al. [11] found that carburization and coking heat treatment in a C_mH_n-H_2 gas mixture followed by decoking and oxidation in air enhanced the coke formation on a HP40 alloy surface due to metal (Fe and Ni) particles generated by the reduction of oxide scale. Baker et al. [12] have studied the nucleation and growth of laminar and filamentous carbon on Pt-Fe and pure Ni particles on SiO_2 plate in an acetylene atmosphere using an electron microscope. They found metal particles on one or both ends of the carbon filament. These studies have demonstrated the importance of catalytic metals on coking (and possibly on carburization).

The catalytic activity of several metals has been studied by many researchers [13 - 19]. Carbon deposition by heterogeneous reaction of gaseous hydrocarbon was described to be catalyzed by metals such as Fe, Ni, and Co, which form relatively unstable carbides [13 - 15]. Tamai et al. [14] examined carbon deposition on Fe and Ni in a CH_4 gas atmosphere, and reported that carbon deposition on Fe was faster than on Ni, because Fe can diffuse the carbon layer faster than Ni. Ohla and Grabke [16] also compared the coke formation on pure Fe, Ni, and Fe-Ni alloys in gas mixtures of CH_4-H_2. They showed almost the same results as Tamai did, but proposed that the Fe surface was not well-ordered as Ni. Ando et al. [17] investigated the coke formation on Fe and Ni in CO-H_2 gas mixtures and supported the Ohla's results. Trimm et al. [18,19] showed that on a Ni surface, carbon formation dominated at low temperatures, but at high temperatures, the coking rate on Ni decreased with increasing temperature as a result of thermal adsorption. Tokura et al. [20] investigated the coke formation on bare and preoxidized Fe and Ni in a CH_4-H_2 atmosphere at 1,000°C using a microbalance. Iron particles generated by reduction of Fe oxides had a much greater reactivity than Ni particles to catalyze deposition of coke on metal surface. Young [21] investigated the formation of carbon on pure Ni, Cu, and some heat-resistant alloys in C_3H_6-H_2 and C_3H_6-H_2-H_2O gas mixtures at 700°C to 1,000°C. Below 900°C, Ni catalyzed coking, but deposition of pyrolytic coke became predominant at higher temperatures. For heat-resistant alloys, the amount of catalytic coke was greatly suppressed by the formation of a Cr oxide scale (with some Cr carbides included), suggesting that oxide scales do not have a high catalytic activity to coke deposition.

In terms of carbon deposition on metal surfaces, these studies have demonstrated that Fe has a larger catalytic activity than Ni, especially when reduced from their oxides. And uniform formation of a

Cr_2O_3 scale can reduce the deposition rate of carbon from pyrolysis gas atmospheres, because the Cr_2O_3 scale seems to be non-catalytic for the carbon deposition. Hence, alloys protected by the uniform Cr_2O_3 scale on their surfaces, preferably with less Fe (as Fe oxides) in the scale, were considered resistant not only to carburization but also to carbon deposition on tube surface in actual furnaces. For practical pyrolysis furnace tubes, heavy coking takes place for tubes that have been carburized significantly. Hence, the carburized tube surface in general seems to have a greater catalytic activity to coking than the initiate tube surfaces. In these furnaces, periodic decoking procedure follows after cracking operation, where tube surfaces are exposed to cyclic carburizing and oxidizing environments. Therefore, understanding the effect of cyclic carburization-oxidation process on the coking as well as the carburization is important.

The purpose of this chapter was to examine the behavior of carburization and coking for a Cr_2O_3-forming alloy used for ethylene pyrolysis furnace tubes. Cyclic carburization-oxidation tests simulating the pyrolysis environment were conducted. The corrosion behavior of the alloys was discussed in viewpoint of the oxide scale chemistry formed during the oxidizing atmosphere.

3.2 Experimental

One commercial alloy (alloy A) used for ethylene pyrolysis furnace tubes and five experimental alloys (R1 through R5) of Fe- (37 -43)Ni-xCr-1.8Si (in mass%) with different Cr contents were prepared and tested. The chemical composition of these alloys is given in Table 3-1. Alloy A was obtained from a commercial tube whereas the experimental alloys by laboratory vacuum-induction-melting, hot forged, cold-rolled, and solution heat treated at 1,240°C. Coupon specimens of $4 \times 20 \times 30$ in mm were cut from each alloy tube and plates. Their surface was mechanically ground to 600-grit emery paper, followed by ultrasonic cleaning in acetone. Coupon specimens put on a slotted alumina holder upright and placed in a reaction chamber, allowing gas flow parallel to the specimen surfaces, illustrated in Fig. 3-1. The reaction chamber, with 75 mm inside diameter and a uniform-temperature zone of 200 mm length, was purged with a N_2-5vol.%H_2 gas mixture for an hour at room temperature. After complete replacement of the purged gas with the test gas mixture, the specimens were heated to the desired temperatures.

Table 3-1 Chemical composition of the tested alloys

Alloy	Chemical composition (mass%)				
	Ni	Cr	Si	C	Fe
A	38	25	1.6	0.1	bal.
R1	39	5	1.8	0.1	bal.
R2	43	10	1.7	0.1	bal.
R3	37	15	1.8	0.1	bal.
R4	40	20	1.8	0.1	bal.
R5	39	25	1.7	0.1	bal.

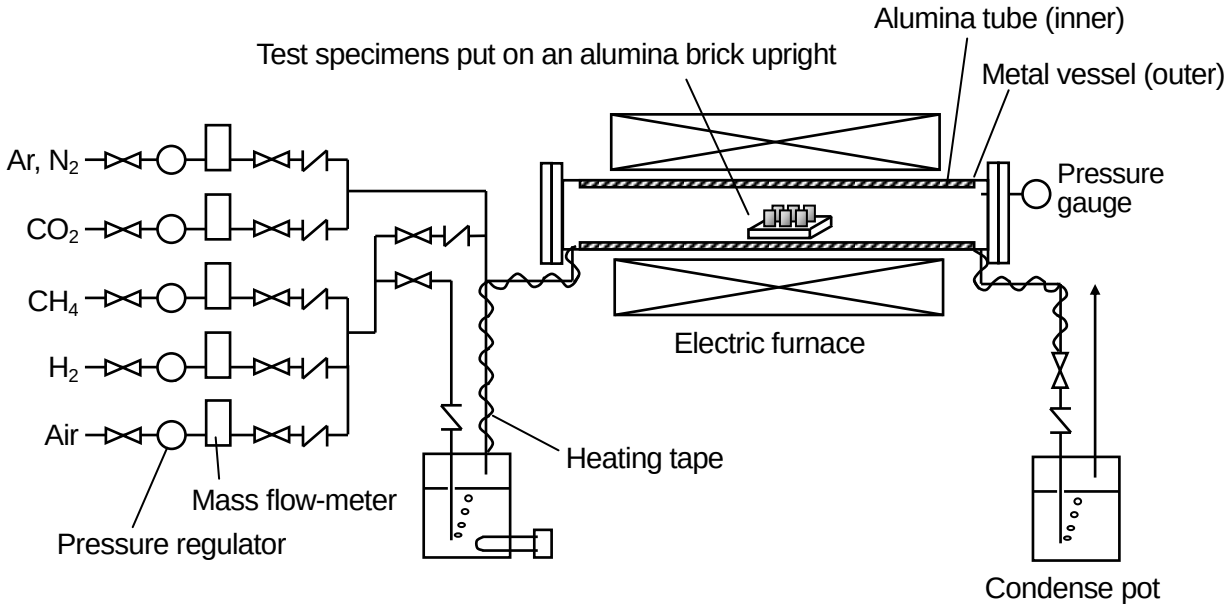

Figure 3-1 Schematic cyclic carburization-oxidation test furnace design.

Test conditions are shown in Fig. 3-2 and listed in Table 3-2. The different test sequences were performed between alloy A and alloys R1 through R5. Moreover, alloy A was tested under two test sequences, cyclic carburized and no carburized. Specimens of alloy A were exposed to a carburizing gas atmosphere of 15%CH_4-3%CO_2-82%H_2 (vol.%) at 1,100°C for 96h at a flow rate of 250 sccm (standard cubic centimeters per minute). The gas composition was chosen to obtain the equilibrium oxygen potential Po_2 similar to that of actual cracking environments, calculated 4.9×10^{-21} atm at 1,100°C (see chapter 2). The equilibrium carbon activity a_c of the gas mixture was considerably higher

than that of the actual furnaces; these gas conditions may accelerate the carburization for the alloys. Oxidation procedure (oxidation I), heating specimens in an air-1vol.%H_2O gas mixture at 900°C for 20h, followed the carburization test. This heat treatment was intended to simulate actual decoking process. Other specimens of alloy A that were not carburized (non-carburized) advanced to the oxidation I treatment.

In actual plant operation, the tubes are periodically exposed to carburization and oxidation environments. However, one cannot analyze each behavior of carburization and coke formation by the carburization test. Indeed, mass change of the specimens obtained by the carburization test included mass gain due to carbon ingress and coke deposition. In this study, therefore, a set of coking test and oxidation II heat treatment was added to the test sequence to evaluate the reactivity of surface oxide scale to the coking. After the oxidation I, coking test was conducted by heating specimens at 1,000°C for 6h in a 15%CH_4-85%H_2 gas mixture. This condition, i.e. lower temperature and shorter exposure time, was chosen to restrain the carburization of specimens. Finally, oxidation II, heating specimens under the same gas condition as oxidation I at 900°C for 1h, was performed. A set of these procedures (carburization test, oxidation I, coking test, and oxidation II) was repeated for up to 3 cycles for the carburized alloy A, while conducted for 1cycle for the non-carburized one.

The experimental alloys (R1 through R5) were used to simulate the thermodynamic condition at the external surface of the carburized alloy A because its solute Cr content became low at the external surface areas as the carburization proceeds. They were exposed to the oxidizing gas atmosphere of the air-H_2O mixture at 900°C for 20h (oxidation I) without carburization. After that, coking test was done, followed by the "oxidation II". This sequence was conducted for 1 cycle.

Table 3-2 Test sequences for the alloys

Sequence no.	Alloy A		Alloys R1 through R5
	Carburized	Non-carburized	
1. Carburization	At 1100°C for 96h	-	-
2. Oxidation I	At 900°C for 20h	At 900°C for 20h	At 900°C for 20h
3. Coking	At 1000°C for 6h	At 1000°C for 6h	At 1000°C for 6h
4. Oxidation II	At 900°C for 1h	At 900°C for 1h	At 900°C for 1h
Number of test cycle	3	1	1

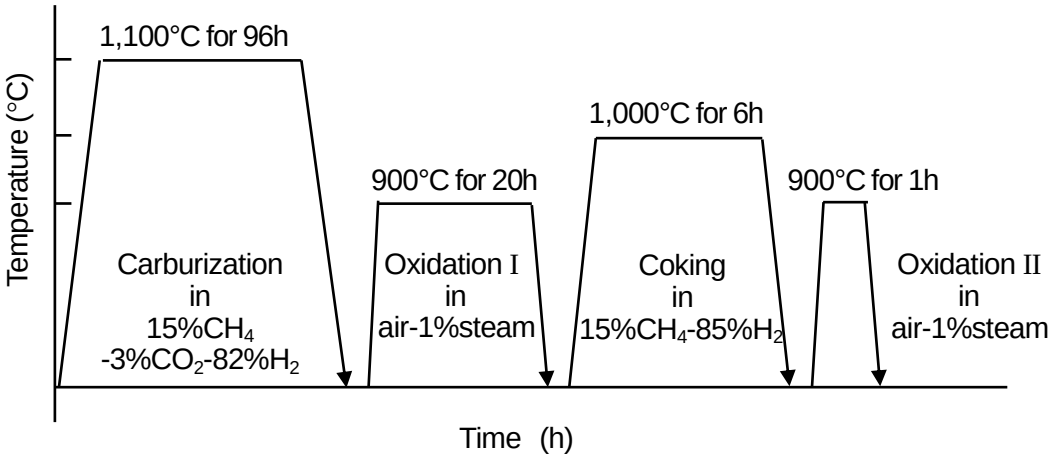

Figure 3-2 Details of the cyclic carburization and oxidation test sequence.

To evaluate carburization of alloy A, "carbon increase" of the specimen surface was measured right after the carburization test at 1,100°C for each cycle of the cyclic test. Specimen surface was peeled at an interval of 0.5 mm thickness down to depth of 2.0 mm (center of specimen) and the carbon content of these chips was analyzed by the inductively coupled plasma (ICP) spectrometry. Then, the original carbon content of the substrate was subtracted from the obtained data and the resultant values were used as the carbon increase. Cross section of the specimen surface area after the carburization test was investigated by optical microscopy. Precipitates promoted during the carburization were identified by X-ray diffraction (XRD) and electron probe X-ray microanalysis (EPMA). Energy dispersive X-ray spectrometry (EDS) measurement was also conducted for alloy A specimens after the carburization test of

each cycle to examine the solute Cr content ($N_{Cr}°$) in the γ matrix at the external surface right below the oxide scale. Each datum was an averaged value of five different points measured at intervals of 0.2mm.

Oxide scales after oxidation I were analyzed by XRD. Chromium oxide (Cr_2O_3) ratio, defined as the ratio of diffraction peak intensity of respective oxides [i.e. $I_{Cr2O3}/(I_{Cr2O3}+I_{M3O4(M=Cr,Fe,Ni\ and\ Mn)}+I_{(Fe,Cr)2O3})$] , was calculated for each specimen. Diffraction peak of respective oxides taken in this study was the strongest one; (311) for M_3O_4 and (104) for Cr_2O_3 or $(Fe, Cr)_2O_3$. Alloying elements of Ni, Fe, and Cr in the oxide scale were also analyzed by EDS.

To investigate the catalytic activity of oxide scale formed during oxidation I to the coking, the amount of coke deposited on specimen surface was obtained by measuring specimen mass changes by oxidation II (gasification) treatment. Morphology of coke deposited on the alloys was observed by a scanning electron microscope (SEM) after the coking test.

3.3 Results

3.3.1 Test Results of Alloy A

Depth profiles of the carbon increase of alloy A for each cycle of the carburization test are shown in Fig. 3-3. Carburization resulted for each specimen and the surface carbon content increased by increasing the number of heat cycles. For specimens experiencing 2nd and 3rd test cycles, the carbon content at a depth of 1.5-2 mm increased so that they were carburized to the center. The carbon increase of each location (depths of 0-0.5 mm, 0.5-1.0 mm, 1.0-1.5 mm, and 1.5-2.0 mm) was multiplied by the thickness of each chip and plotted vs. the number of test cycles, shown in Fig. 3-4. These values (total carbon increase) would represent the total carbon ingress of the specimen due to carburization. The total carbon increase, or the total amount of carbon absorbed by the specimen, increases with increasing the number of heat cycles.

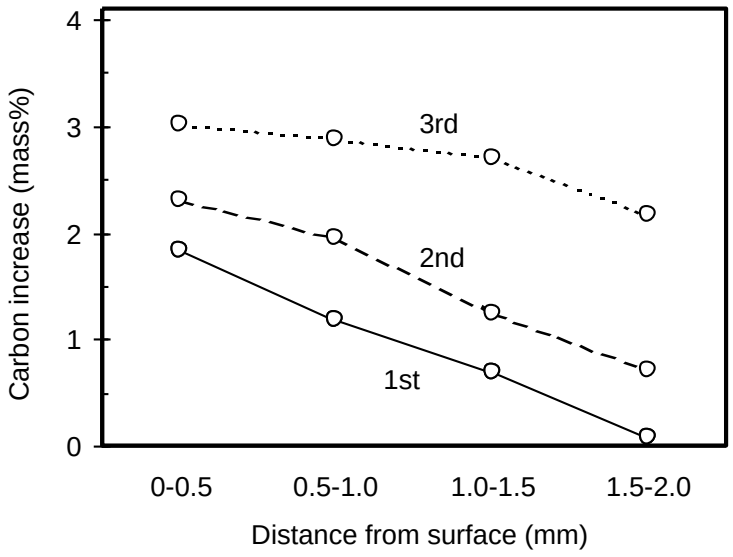

Figure 3-3 Depth profiles of the carbon increase of alloy A for each test cycle. Data were taken for the specimens right after exposure to a 15%CH_4-3%CO_2-82%H_2 gas mixture at 1,100°C for 96h.

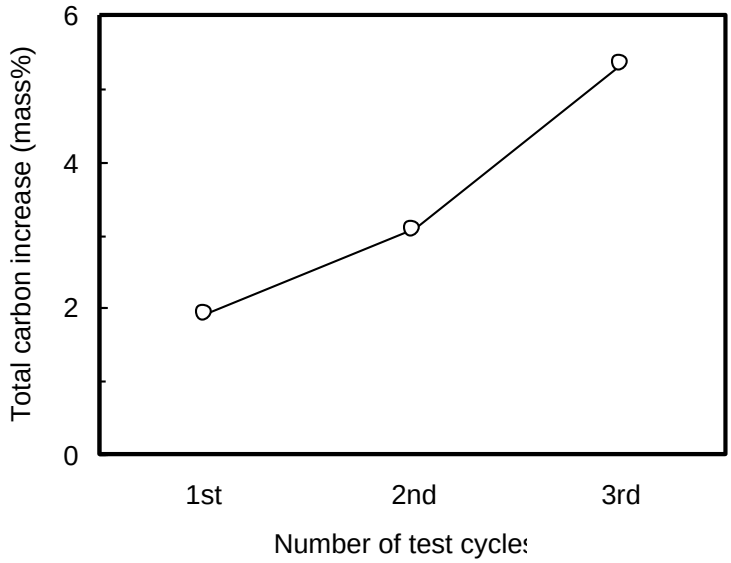

Figure 3-4 Total carbon increase of alloy A as a function of test cycles. Data were taken for the specimens right after exposure to a 15%CH_4-3%CO_2-82%H_2 gas mixture at 1,100°C for 96h.

Metallographic cross sections of alloy A after the carburization for 1 to 3 cycles are presented in Fig. 3-5. After the 1st carburization, a precipitation-free zone of approximately 20μm thickness was noted at the external surface, indicating the formation of a Cr-enriched thin oxide scale even in the "reducing" carburizing gas atmosphere. Chain precipitates were observed in the carburization zone along grain boundaries and fine precipitates of several μm size in the grains, identified mainly as M_7C_3 (M =Cr and Fe) with some $M_{23}C_6$ by EPMA and XRD. After the 3rd carburization, a precipitation-free zone was not obvious, suggesting that the protective oxide scale had disappeared from the alloy surface. In the carburization zone, coarse precipitates of M_7C_3 were clearly observed. Hence, these cross sections along with the carburization behavior shown in Fig. 3-3 demonstrate that the Cr_2O_3 scale, although not sufficiently protective, formed during the carburization in the gas atmosphere at 1,100°C, but it lost its stability by the subsequent oxidation /coking /carburizing.

The $N_{Cr}°$ at the external surface was measured after each carburization cycle by EDS, listed in Table 3-3. When alloy A was not carburized, its solute Cr is 24.8mass%, close to the initial Cr content. However, once carburized, its solute Cr decreases with increasing the test cycle. After the 3rd cycle, it reduced to only 4.3mass%; almost all Cr in the γ matrix changed to carbides.

Table 3-3 EDS analysis of the $N_{Cr}°$ for alloy A

Number of test cycle	$N_{Cr}°$ (mass%)
No carburized	24.8 ± 0.2
1st	11.1 ± 0.5
2nd	8.3 ± 0.3
3rd	4.3 ± 0.6

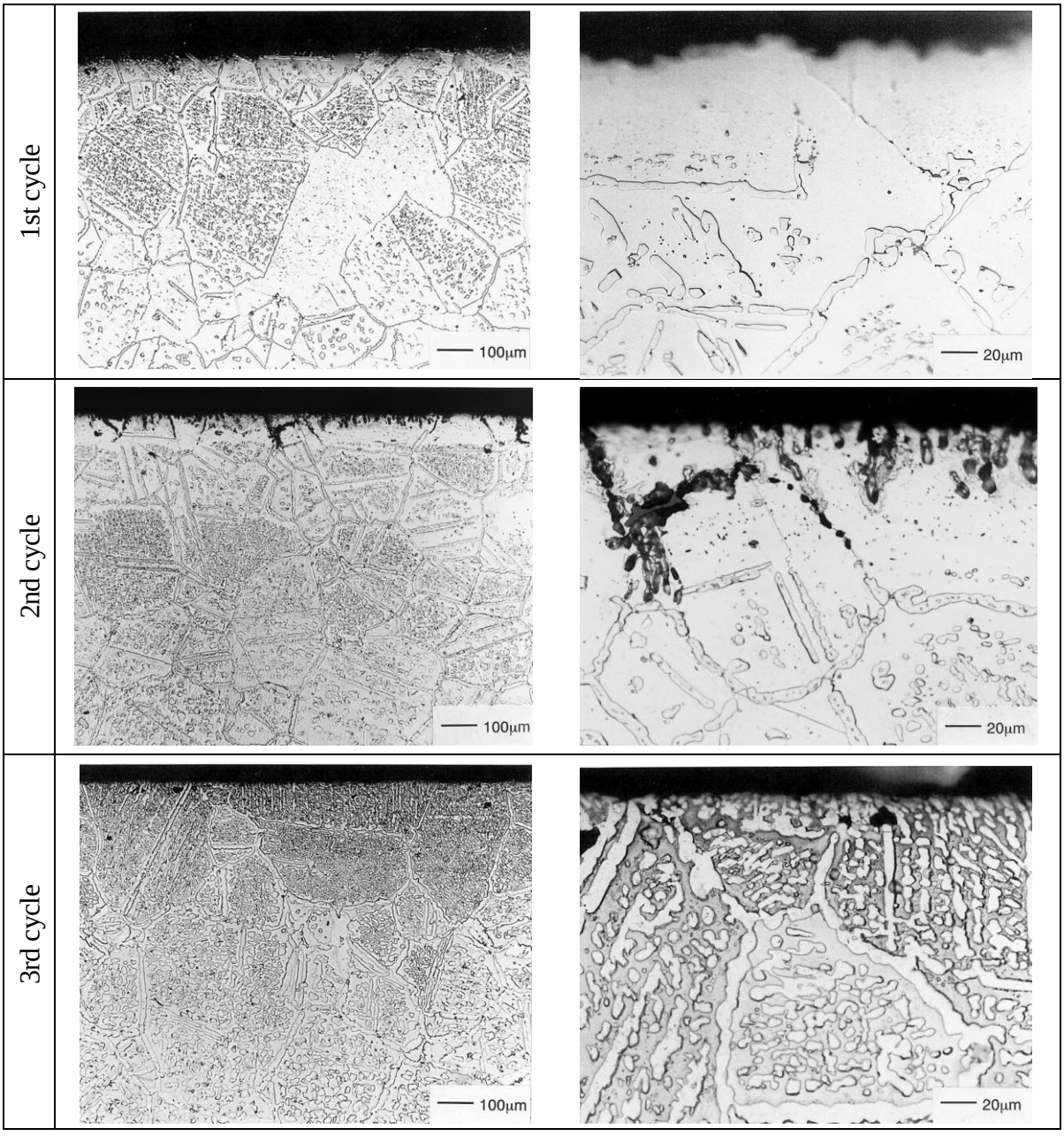

Figure 3-5 Metallographic cross sections of alloy A after the carburization.

The results of the XRD and EDS measurements of the oxide scale formed on alloy A after each oxidation I are presented in Figs. 3-6 and 3-7, respectively. For the non-carburized specimen, its oxide scale consisted of 90% Cr_2O_3. However, for carburized specimens, spinel-type oxides (consisting of Fe and other elements) formed upon oxidation I and became prominent in the scale. After the 3rd cycle, the Cr_2O_3 ratio of the oxide scale decreased to about 0.3. Through cyclic carburization-oxidation treatments, the Cr content of the oxide scale steadily decreased; 86mass% for the non-carburized specimen, while below 50mass% after the 3rd cycle. Instead of Cr, both of Fe and Ni increased in the oxide scale.

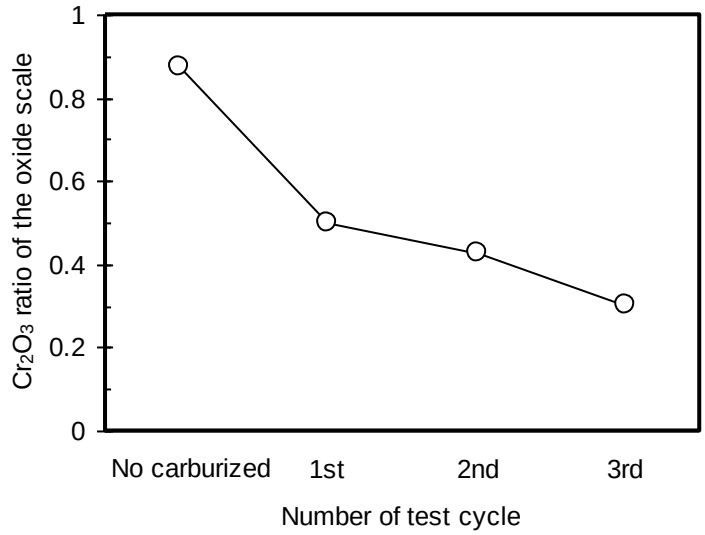

Figure 3-6 Cr_2O_3 ratio of the oxide scale formed on alloy A after oxidation I of each test cycle by XRD measurement.

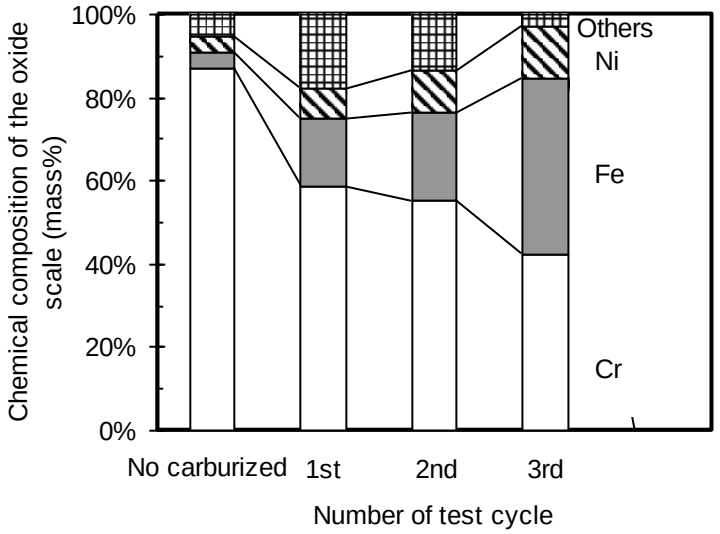

Figure 3-7 Chemical composition of the oxide scale formed on alloy A after oxidation I of each test cycle analyzed by EDS. For metallic elements only, and others contain Mo, Si, and Ti, etc.

The amount of coke deposited upon the coking test was plotted vs. the test cycle, shown in Fig. 3-8. For the non-carburized alloy A, slight deposition of coke occurred. However, coke deposition drastically increased with increasing the number of test cycle.

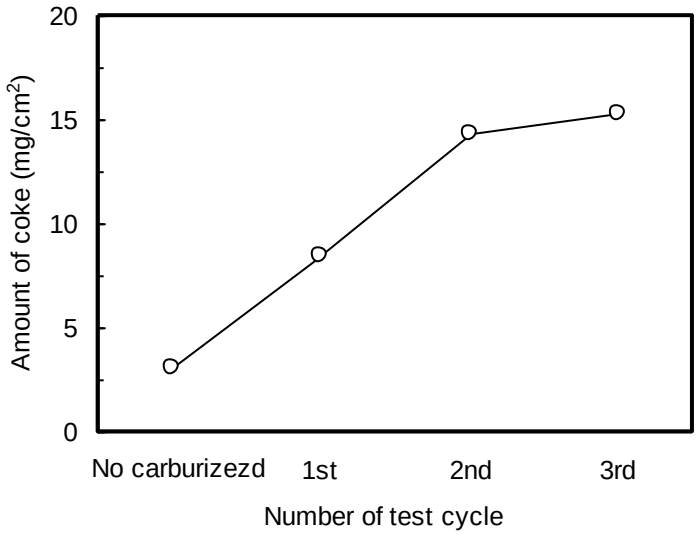

Figure 3-8 Amount of coke deposited on the specimen surface of alloy A by the coking test.

The morphology of the coke deposited on the specimen after the 3rd-coking test, is shown in Fig. 3-9. A considerable amount of coke was found. Two types of coke were found, flocculent and granular; both were identified as amorphous carbon by XRD measurement.

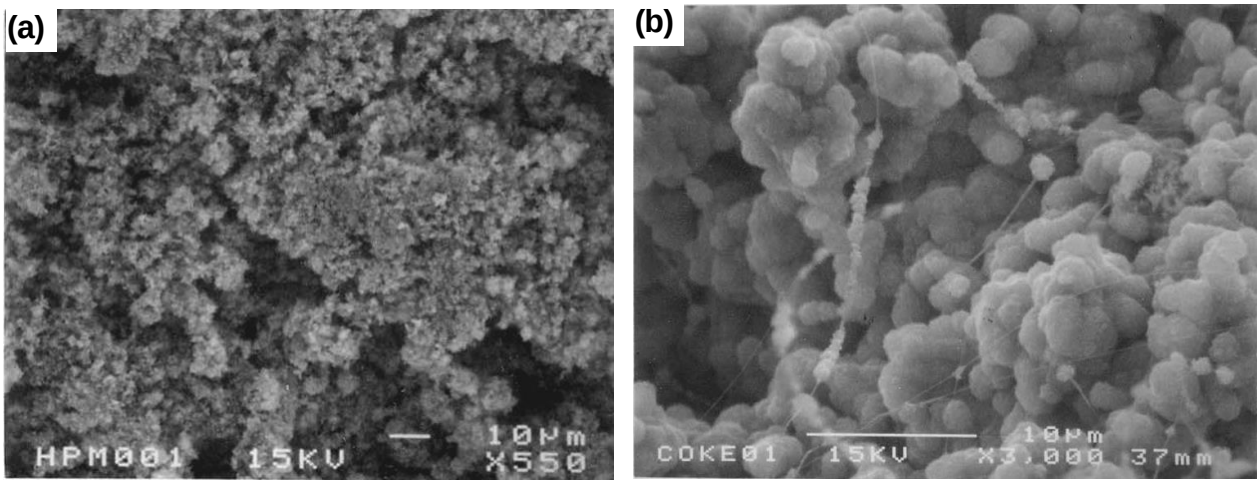

Figure 3-9 (a) SEM observations of coke deposited on the specimen surface of alloy A after the 3rd coking test. (b) Higher magnification.

3.3.2 Test Results of Various Cr Content Alloys

Alloys R1 through R5 with different Cr contents were oxidized in an air-H_2O gas mixture at 900°C for 20h. Oxide scales that formed on each specimen were examined by XRD and EDS, presented in Figs. 3-10 and 3-11, respectively. The Cr_2O_3 ratio of the oxide scale remained around 0.8 for the alloys of more than 15%Cr. Similarly, the Cr content in scale kept up more than 75mass% for these alloys. For the alloys of less than 15%Cr, however, spinel-type oxides and /or $(Fe, Cr)_2O_3$ containing Fe and Ni were included in the scale and the Cr_2O_3 ratio were low. The scale on alloy R1 of 5%Cr consisted predominantly of Fe oxides such as hematite type $(Fe, Cr)_2O_3$. In these figures, data obtained from alloy A (Figs. 3-6 and 3-7) were reproduced as open marks, where $N_{Cr}°$ (Table 3-3) was taken as the Cr content. Surprisingly, the data for the oxides formed upon oxidation I of the carburized alloy A appreciably corresponded to that which resulted from the experimental alloys (R1 through R5). Therefore, it can be concluded that the oxide scale chemistry formed on the carburized alloys upon the oxidation would be significantly affected by the solute Cr content of the γ matrix at the external surface.

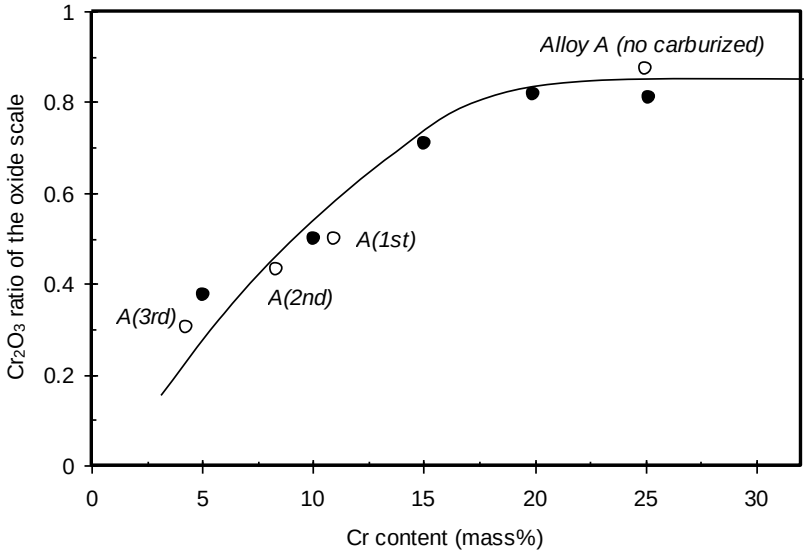

Figure 3-10 Effect of Cr on the Cr_2O_3 ratio of the oxide scale formed on the experimental alloys exposed in the oxidation I (represented as solid circles). Data obtained from alloy A are reproduced as open circles. For carburized alloy A, Cr content was taken for the $N_{Cr}°$.

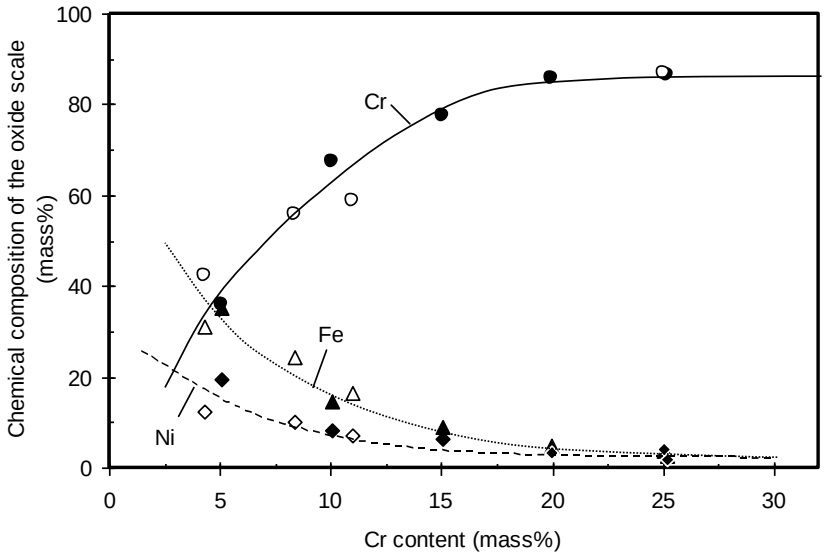

Figure 3-11 Effect of Cr on the chemical composition of the oxide scale formed on the experimental alloys exposed in the oxidation I (represented as solid marks). Data obtained from alloy A are reproduced as open marks.

These oxidized specimens were subjected to the coking test of exposing specimens in the 15%CH_4-85%H_2 gas mixture at 1,000°C for 6h. The amount of coke deposited on these specimens was plotted vs. Cr mass% of the alloys, shown in Fig. 3-12. For the experimental alloys of more than 15% Cr, the amount of coke was suppressed at about 3 to 4 mg/cm^2, while below this Cr content level, coking was accelerated drastically. In this figure, data obtained from the carburized alloy A (Fig. 3-8) also was plotted. The data of alloy A appreciably corresponded to that of the experimental alloys, which indicate that coking behavior strongly depended on the oxide scale chemistry formed during the prior stage.

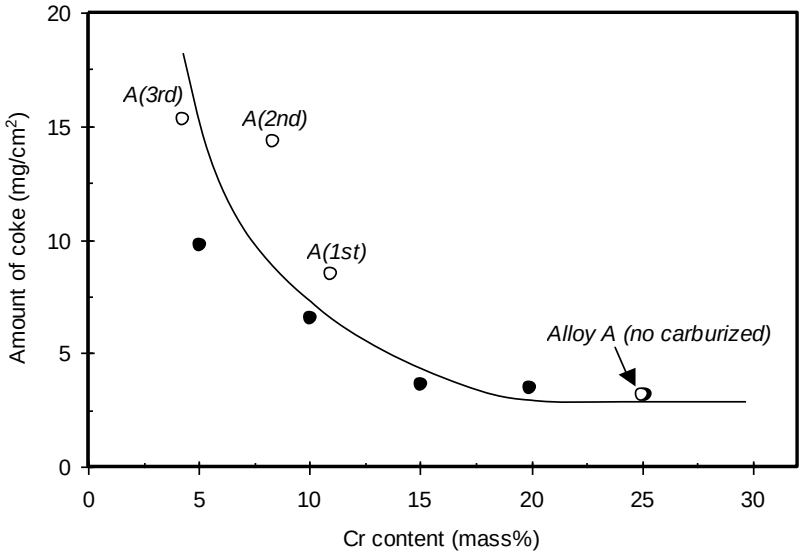

Figure 3-12 Effect of Cr on the coke deposition of the oxidized experimental alloys exposed to 15%CH_4-85%H_2 gas atmosphere at 1,000°C for 6h (represented in solid circles). Data obtained from alloy A are reproduced as open circles.

From a regression analysis of the data presented in Figs. 3-11 and 3-12, the catalytic activity of the alloying elements included in the oxide scale to coking can be expressed as follows,

$$\text{Coke (mg/cm}^2\text{)} = 0.008\times [\text{Cr}]+0.305\times [\text{Fe}]+0.024\times [\text{Ni}]+1.313 \text{ (in mass \%)} \quad (1)$$

Apparently, Fe as Fe oxides is the most catalytic element for coking among the constituent alloying elements included in the oxide scale. On the contrary, Ni in the spinel-oxide scale has an influence on the catalytic growing of coking, but its effect would be much smaller than that of Fe.

3.4 Discussion

Alloy A has Cr of about 25 mass%, which is considered sufficient to form a uniform protective Cr_2O_3 scale when oxidized in an air-H_2O gas atmosphere at 900°C. However, for the carburized ones, it was not dominating. Since the formation of "pure" Cr_2O_3 scale is of great importance to minimize carburization and /or coking, the reason for the inability to form a pure Cr_2O_3 scale on these pre-carburized specimens was investigated thermodynamically.

With carburization, Cr in the alloy reacts with carbon to form Cr_7C_3 and $Cr_{23}C_6$ in the matrix if carbon concentration exceeds the solubility limit of carbon in the γ matrix. Once these carbides are formed, the Cr content in the γ matrix starts to decrease. Hence, $N_{Cr}°$ is considered significantly lower than 25% for the carburized specimen with abundant precipitation of Cr-carbides. Assuming that the formation and enrichment of Cr_2O_3 in the oxide scale upon oxidation depends not on the total Cr content (i.e., Cr in the γ matrix plus Cr as carbides) but on $N_{Cr}°$, it can well be understood that the Cr_2O_3 ratio of the oxide scale on the carburized specimens is considerably lower than that of the specimen without the carburization, because $N_{Cr}°$ diminished during carburization as shown in Table 3-3. The $N_{Cr}°$ can be estimated from the isothermal section of C-Fe-38mass%Ni-Cr alloy phase stability diagram using thermodynamic calculations [23]. Dependence of the $N_{Cr}°$ on the total carbon content of the alloy was calculated, shown as curved line in Fig. 3-13. In this figure, the experimental $N_{Cr}°$ and total carbon content (carbon increase at 0-0.5 mm depth in Fig. 3-3 plus the preexistent carbon content of alloy A) were superimposed. Apparently, the experimental data agreed well with the calculation, that is, the carbon increase due to carburization results in a decrease in $N_{Cr}°$.

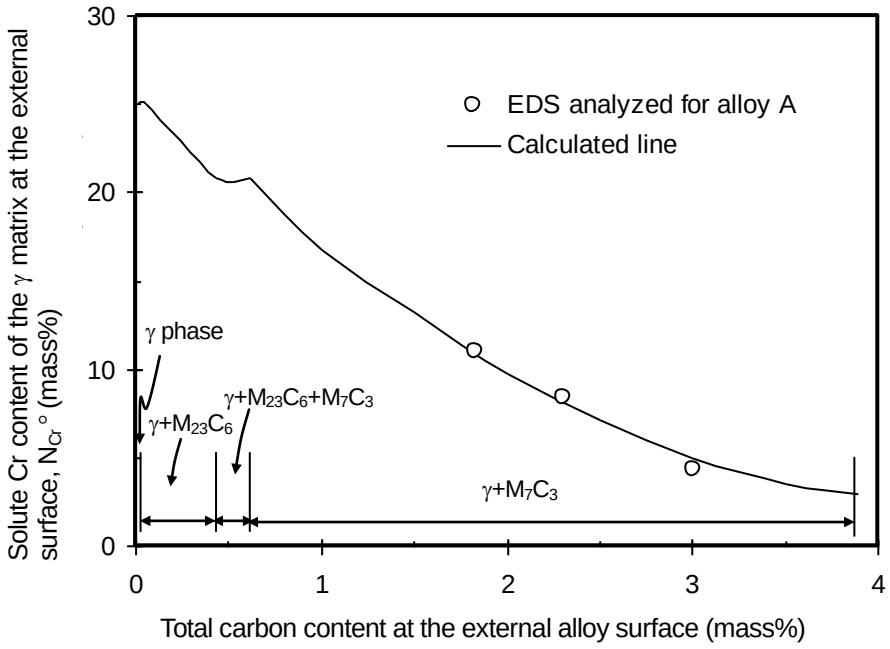

Figure 3-13 $N_{Cr}°$ plotted against the total carbon content of alloy A. Open circles were obtained from the heat-cycled specimens after carburization test, curved line from thermodynamic calculations of C-Fe-38%Ni-Cr system at 1,100°C.

From the above results and examinations (Figs. 3-10 and 3-11), it should be pointed out that the oxide scale chemistry is significantly affected, not by the total Cr content, but by $N_{Cr}°$. However, thermodynamically, Cr-carbides such as $Cr_{23}C_6$ and Cr_7C_3 are not stable in the oxidizing gas atmosphere of oxidation I , thus they would contribute to the formation of Cr_2O_3 scale when heated in the air-H_2O gas mixture at 900ºC. This might be the reason that the reaction rate for Cr carbides to form oxides is considered so low that Cr-carbides do not contribute to the formation of Cr_2O_3 scale significantly. Hence, Cr carbides does not drastically aid the formation of Cr_2O_3 upon oxidation I.

The oxide scale formed on the carburized specimen did not provide sufficient protection against the subsequent carburization at 1,100°C, because of the considerable amount of carbon diffused into substrate during the 2nd and 3rd carburization shown in Fig. 3-4. Similarly, the oxide scale on the carburized specimen had a larger catalytic activity for coking than the "pure" Cr_2O_3 scale shown in Fig. 3-8. The carburization decreased $N_{Cr}°$, and it lowered the ability to form Cr_2O_3 as a protective oxide layer. Based on the analysis of the oxide scale, more than 15% Cr is needed in the γ matrix to obtain a

relatively "pure" Cr_2O_3 scale. This critical Cr content of 15%, obtained from alloy R1 through R5 specimens without carburization, agreed well with the carburized alloy A. A protective, inactive Cr oxide scale can form on the surface of carburized alloys, if $N_{Cr}°$ remains above 15%. However, once this becomes less than 15%, spinel-type oxide containing Fe and Ni and / or $(Fe, Cr)_2O_3$ instead of Cr_2O_3 starts to grow. This might be the major reason that the oxide scale loses its protection against carburization and the enhanced catalytic activity to coking of the carburized alloys.

This was totally consistent with the carburization (Fig. 3-4) and the coking (Fig. 3-8) behavior of alloy A. The total carbon increase of each specimen of different test cycles due to carburization was plotted vs. the Cr_2O_3 ratio and shown in Fig. 3-14. Carburization was not affected for specimens where the Cr_2O_3 ratio was less than 0.4, but was suppressed for the specimen of 0.5. In order to minimize the effect of oxide scale on carburization, alloy A was heated in a 15%CH_4-85%H_2 gas mixture at 1,100°C for 96 h without the formation of any oxide scale [22]. The test result was also plotted in Fig. 3-14, clearly showing that an alloy surface without any oxide scale had a significantly high capacity to accommodate carbon from the gas atmosphere. The carbon increase for the 1st cycled alloy A without preoxidation was suppressed half time than that for the alloy A exposed to the gas atmosphere where no oxide scale was formed. This result suggests that under the current test carburization environment, competition of carbon ingress and oxide formation takes place on the specimen surface, though the formation of a uniform protective Cr_2O_3 scale is incomplete, and carburization proceeds probably through permeation of carbon-bearing gas species through cracks /defects of the Cr_2O_3 scale.

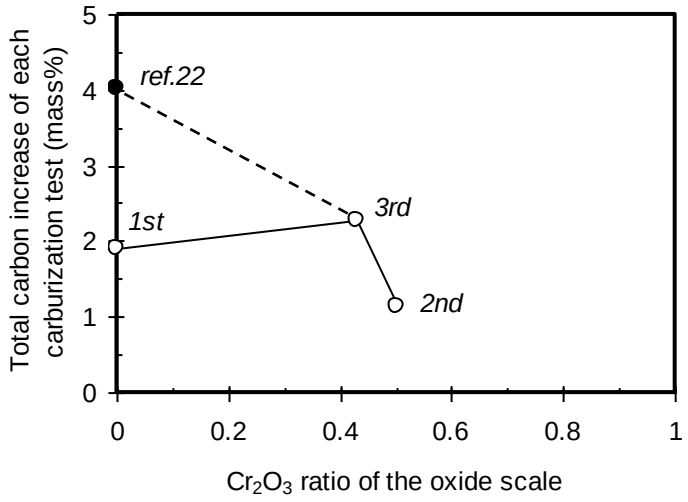

Figure 3-14 Total carbon increase plotted against the Cr_2O_3 ratio of the oxide scale on alloy A after oxidation I. Solid datum, taken from ref. [22], was obtained from the result that alloy A exposed in a 15%CH_4-85%H_2 gas mixture at 1,100°C where no oxide scale was formed.

The amount of coke deposited by the coking was plotted vs. the Cr_2O_3 ratio of the oxide scale and is shown in Fig. 3-15. The Cr_2O_3 is apparently less reactive to coking than the oxide scales including Fe and Ni. Hence, uniform formation of the Cr_2O_3 scale during the decoking (oxidizing) process on tube surfaces is needed to minimize both carburization and coking for the pyrolysis furnace tube. According to the literature [20], Fe particles generated upon reduction of Fe oxides have much greater catalytic activity to heterogeneous reaction of carbon deposition than Ni particles, which agreed well with the present test results.

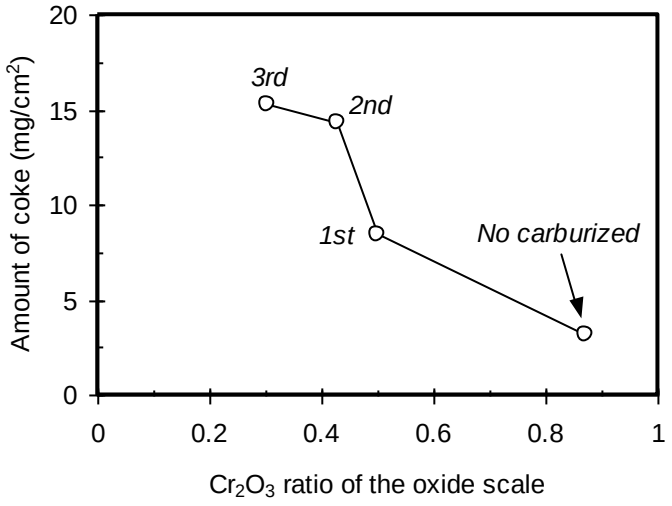

Figure 3-15 Amount of coke for each coking test and the Cr_2O_3 ratio of the oxide scale formed on alloy A after oxidation I.

Based on these results, the degradation of Cr_2O_3-forming Fe-Ni-Cr(-Si) alloys used for ethylene pyrolysis furnace tubes upon cyclic carburization-oxidation procedures is schematically outlined in Fig. 3-16. At the initial stage of carburization, they exhibit good resistance to carburization. Chromium as Cr_2O_3 scale provides protection against carburization. After long-time exposure to the cyclic environment, however, inward diffusion of carbon into alloy matrix gradually proceeds at sites where the protective oxide scale would fail, and the diffused carbon reacts with Cr in the matrix to form Cr carbides, consuming the solute Cr of the γ matrix at the external carburization zone beneath the oxide scale. The critical solute Cr concentration of 15%, obtained from experimental alloys, corresponds to the total carbon content of approximately 1.2% at the external metal surface in a carburizing environment at 1,100°C. Thus, if the total carbon content of alloy surface used for ethylene pyrolysis furnace tubes exceeds 1.2% (this value can change depending on the temperature where tube alloys are exposed), the formation of "protection" Cr_2O_3 scale would become difficult upon decoking. During decoking,

oxidation of the carburized zone would proceed, but the alloy surface can no longer sustain the formation of a uniform Cr_2O_3 scale. The porous spinel-type oxide as well as $(Fe, Cr)_2O_3$ scale containing Fe and Ni prevails instead. After the decoking, cracking operation follows, but the unprotective oxide scales easily allow carbon to diffuse into the metal matrix so that carburization proceeds rapidly with the exposure time. In addition, coke deposition accelerates due to heterogeneous reaction catalyzed by the Fe particles, generated by the reduction of spinel-type oxides formed during decoking processes.

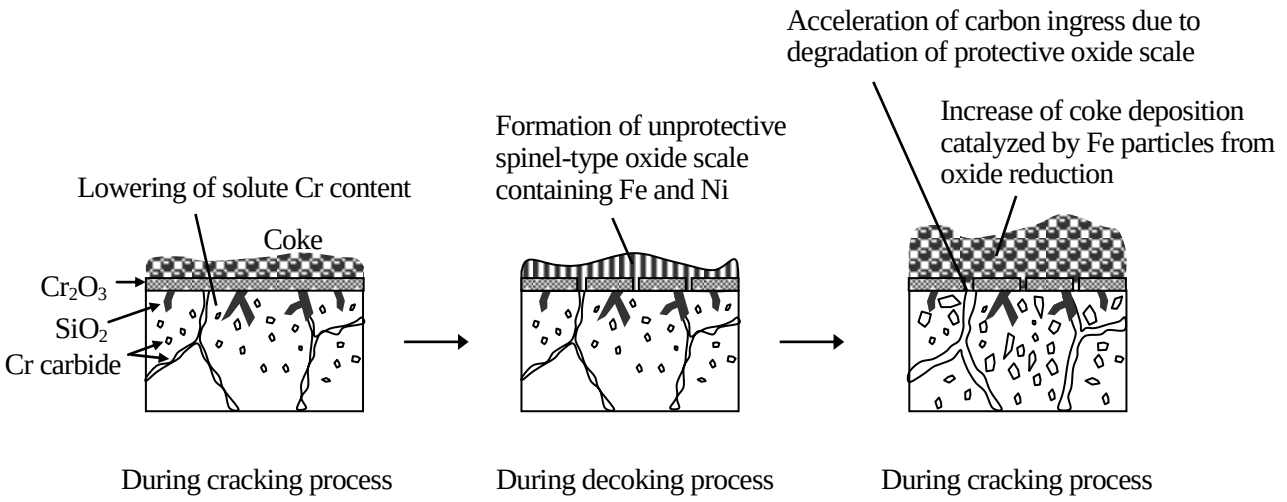

Figure 3-16 Schematic carburization and coking behavior of the conventional Cr_2O_3-forming Fe-Ni-Cr(-Si) alloys in the ethylene pyrolysis furnace environment.

3.5 Conclusions

An Fe-38Ni-25Cr-Si (mass%) alloy, commonly used for ethylene pyrolysis furnace tube, was tested in a cyclic carburization-oxidation treatment simulating cracking and decoking processes. The conclusions obtained are summarized as follows:

(1) The cyclic treatment apparently accelerated carburization of Fe-Ni-Cr-Si alloys, and also enhanced the catalytic activity of the oxide scale to form the coke, which has been catalyzed when the alloys form the spinel-type oxide scale instead of Cr_2O_3 upon oxidation.

(2) The oxide scale chemistry is significantly affected, not by the total Cr content, but by the solute Cr content of the γ matrix at the external surface of the carburization zone. The carbon decomposed from the gas atmosphere can diffuse and combine with Cr in the matrix, leading to the decrease of the solute Cr at the external surface. The cyclic test demonstrated that the solute Cr of 15mass% was required to preserve the Cr_2O_3 scale.

(3) Degradation of the Cr_2O_3 scale yields to generate the spinel-type oxide scale containing Fe and Ni. This less-protective oxide scale allowed carbon to the metal matrix to cause carburization.

(4) Metallic elements that were reduced from the spinel-type oxide catalyzed coking reaction upon cracking process. The particles of Fe have a much larger catalytic activity than those of Ni.

References

[1] D.B. Roach, "Carburization of cast heat resistant alloys," CORROSION /76, paper no.7, (Houston, TX: NACE, 1976).

[2] J. R. Schley, F. W. Bennett, Corros. 23(1967), p.276.

[3] A. Shnaas, H.J. Grabke, Werkst. Korros. 29(1978), p.635.

[4] D.F. Lupton, P.J. Ennis, Res. Mech. 1(1981), p.245.

[5] R. Petkovic-Luton, T.A. Ramanarayanan, Oxid. Met. 34(1990), p.381.

[6] J. Klöwer, U. Heubner, Mater. Corros. 49(1998), p.237.

[7] L.F. Albright, R.T.K. Baker, "Coke Formation on Metal Surface", American Chemical Society (ACS) Symposium Series 202, (Washington. D. C.: ACS, 1982).

[8] G.L. Swales, Published of "Proc. Conf. The Behavior of High Temperature Alloys in Aggressive Environments," (London, UK: The Metal Society, 1980), p.45.

[9] J.L.Figueiredo, "Progress in Catalyst Deactivation," (The Hague, Netherlands: Martinus Nijhoff Publishers, 1982), p.31.

[10] M.J. Bennett, J.B. Price, J. Mater. Sci. 16(1981), p.170.

[11] C. Steurbaut, H.J. Grabke, F.R. van Buren, S. J. Korf, J. Defrancq, Mater. Corros. 49(1998), p.352.

[12] R.T.K. Baker, R.J. Waite, J. Catalysis 37(1975), p.101.

[13] W.E. Slater, J. Chem. Soc. 109(1916), p.160.

[14] Y. Tamai, Y. Nishiyama, G. Takahashi, Kogyo Kagaku Zasshi 70, 6(1967), p.91 (in Japanese).

[15] L.S. Lobo, D.L. Trimm, J.L. Figueiredo, "Kinetics of the Mechanism of Carbon Formation from Hydrocarbon on Metals", Proc. 5th Int. Congress on Catalysis, paper no.79 (Pennsylvania: IACS, 1972).

[16] K. Ohla, H.J. Grabke, Werkst. Korros. 33(1982), p.341.

[17] S. Ando, T. Nagashima, T. Shimoo, H. Kimura, J. Japan Inst. Metal 52, 6(1988), p.553.

[18] D.L. Trimm, Applied. Catal. 5(1983), p.263.

[19] P.R.S. Jackson, D.L. Trimm, D.J. Young, J. Mater. Sci. 21(1986), p.3125.

[20] S. Tokura, N. Otsuka, T. Kudo, Corros. 49, 7(1993), p.561.

[21] D.J. Young, Mater. Corros. 50(1999), p.675.

[22] Y. Nishiyama, N. Otsuka, and T. Nishizawa, Corrosion 59 (2003), p. 688.

Chapter 4

CARBURIZATION AND COKING BEHAVIOR OF AL_2O_3-FORMING NI-CR-AL ALLOY IN SIMULATED ETHYLENE PYROLYSIS GAS ENVIRONMENTS

4.1 Introduction

Ethylene pyrolysis is considered the most important process for producing chemical products. Some furnace tubes used for ethylene pyrolysis suffer severe material damage, since they are heated at up to approx. 1,100°C in contact with steam-hydrocarbon gas mixtures [1 - 3]. Deterioration of mechanical properties due to coking (carbon deposition on the inner surface of tubes) and carburization can result in a failure of tube materials [4 - 6]. Studies on carburization [7] showed that Ni, Cr, Si and Al are effective alloying elements to increase the carburization resistance for high temperature alloys. Carbon-stabilizing elements such as Mo, Ti and Nb have been considered beneficial, since they lower the internal carburization growth by combining with carbon. On this basis, carburization-resistant alloys such as alloy HK40 containing high Cr, and alloy HP containing high Cr, Ni and Si have been applied as pyrolysis furnace tubes [8,9], and higher-Cr, Ni alloys are under development [10]. However, excess addition of Cr and Ni does not increase the carburization resistance significantly; instead, it reduces malleability and weldability. Moreover, a protective Cr oxide may change to Cr carbides such as Cr_7C_3 and Cr_2C_3 at temperatures above 1,030°C to 1,040°C, which is anticipated according to the equilibrium Po_2 from the thermodynamic calculations of the gas atmosphere in actual ethylene pyrolysis furnaces (Chapter 2). Hence, at these temperatures, protection by the Cr_2O_3 scale is not realistic.

In recent studies, Ni base alloys containing high Al [11], oxide dispersion strengthened (ODS) alloy [12], and intermetallic alloy [10], have been developed to enhance resistance against carburization

as well as coking. Surface-modified alloys coated by Al or its compounds have also been tested in some ethylene pyrolysis furnaces [13,14]. These alloys are characterized by the formation of a protective Al oxide film on metal surfaces to prevent carbon ingress and to minimize coking, but due to inherent lack of ductility for ODS and intermetallic alloys, welding and bending are usually difficult and troublesome upon manufacturing tube bundles for constructing ethylene pyrolysis furnaces.

A new carburization-resistant alloy has been developed to have an excellent resistance against carburization and coking. The developed alloy can form a protective Al oxide scale owing to high Al content in corrosive carbonaceous gas environments. In this chapter, carburization and coking behavior of the alloy was evaluated, and compared with conventional Fe-Ni-Cr steels in simulated ethylene pyrolysis environments.

4.2 Experimental

Preliminary tests were conducted with some Ni base alloys to understand effects of alloying elements on carburization. The chemical composition of test alloys (Al-1 through W-1) is given in Table 4-1. They were obtained by laboratory vacuum-induction-melting, hot forged, cold-rolled, and solution heat treated at 1,200°C. A Ni-Cr-Al alloy is designed to enjoy the beneficial effect of Al; Al content was decided to 3mass% from results of the preliminary test, with 20% Cr and high Mo in a Ni matrix. Alloy HPM and alloy 800H (UNS no. N08810) were tested to compare carburization as well as coking with those of the developed alloy. These conventional steels were obtained from virgin wrought tubes, which are used in ethylene pyrolysis furnace. Alloy HPM and alloy 800H contain 25% and 20%Cr, respectively. Moreover, alloy HPM contains 1.8%Si to improve carburization resistance due to formation of a SiO_2 layer beneath the Cr_2O_3 scale.

Specimens of 4 × 20 × 30 in mm were cut from commercial tubes and hot-rolled plates. Specimen surfaces were mechanically ground to a 600-grit emery paper, followed by ultrasonic cleaning in acetone.

Table 4-1 Chemical compositions of test alloys

Alloy	Chemical composition (mass%)						
	C	Si	Ni	Cr	Al	Others	Process
Al-1	0.01	0.07	67.6	15.2	1.48	9.9Mo	Wrought
Al-2	0.01	0.06	67.3	15.1	1.94	9.8Mo	Wrought
Al-3	0.01	0.06	66.8	15.3	2.47	9.9Mo	Wrought
Al-4	0.01	0.07	66.2	15.3	2.87	6.9Mo	Wrought
Al-5	0.01	0.06	66.1	15.4	2.92	10.0Mo	Wrought
Al-6	0.01	0.07	66.1	15.0	3.12	10.0Mo	Wrought
Al-7	0.01	0.07	65.5	15.3	3.42	9.9Mo	Wrought
Cr-1	0.02	0.16	88.2	0.0	3.20	7.0Mo	Wrought
Cr-2	0.03	0.16	85.8	2.5	3.20	7.0Mo	Wrought
Cr-3	0.02	0.16	83.3	5.0	3.21	7.0Mo	Wrought
Cr-4	0.02	0.16	80.8	7.5	3.21	7.0Mo	Wrought
Cr-5	0.03	0.16	78.3	10.0	3.22	7.0Mo	Wrought
Cr-6	0.03	0.17	75.5	12.6	3.21	7.0Mo	Wrought
Cr-7	0.03	0.17	73.1	15.1	3.12	6.9Mo	Wrought
Cr-8	0.03	0.16	68.3	20.1	3.14	7.0Mo	Wrought
Cr-9	0.03	0.18	63.0	24.8	3.19	6.9Mo	Wrought
Mo-1	0.01	0.06	70.9	15.4	2.99	5.1Mo	Wrought
Mo-2	0.01	0.06	75.9	15.4	2.99	0.1Mo	Wrought
W-1	0.01	0.06	66.2	15.5	2.99	9.6W	Wrought
Ni-Cr-Al	0.06	0.15	69.4	20	3.1	7Mo	Wrought
Alloy HPM	0.14	1.8	37.6	25.3	-	Ti, Mo	Wrought
Alloy 800H (N08810)	0.08	0.3	31.2	20.6	0.5	Ti	Wrought

Gas carburization tests were conducted in a horizontal reaction chamber. Specimens were exposed to a gas mixture of 15%CH_4-3%CO_2-82%H_2 (vol.%) flowing at a rate of 250 sccm at 1,000 and 1,100°C for 96h and 1,150°C for 48h. The gas composition was chosen so that the equilibrium Po_2 corresponded to the actual pyrolysis environment (the equilibrium Po_2 of the test gas mixture was calculated to be 1.02×10^{-21} atm at 1,000°C, 4.94×10^{-21} at 1,100°C, and 1.00×10^{-20} at 1,150°C). As illustrated in Fig. 2-5 (see Chapter 2), coupon specimens were placed on a slotted alumina brick upright and set into the reaction chamber, allowing gas flow parallel to the specimen surfaces. The reaction

chamber, with 75 mm inside diameter and a uniform-temperature zone of 200 mm length, was heated in a horizontal electric furnace. The reaction chamber was purged with a N_2-5vol.%H_2 gas mixture for an hour at room temperature. After complete replacement of the purge gas with the following test gas mixture, the test specimens were heated at the desired temperatures. To evaluate carburization of the test alloys, "carbon increase" of the specimen surface was measured right after the carburization test. Specimen surface was peeled at an interval of 0.5 mm thickness down to depth of 2.0 mm (center of specimen) and the carbon content of these chips was analyzed using an inductively coupled plasma (ICP) spectrometry. Then, the original carbon content of the substrate was subtracted from the obtained data and the resultant values were used as the carbon increase. Cross section of the specimen surface area was investigated using an optical microscopy and an electron probe X-ray microanalysis (EPMA). The specimen surfaces were investigated using X-ray diffraction (XRD) to identify types of oxide scale and carbide.

A cyclic carburization and oxidation test was also conducted to simulate an operating condition of actual ethylene pyrolysis plants. Test conditions are shown in Fig. 4-1 and listed in Table 4-2. Two test sequences, cyclic carburized and no carburized, were conducted for the Ni-Cr-Al alloy, alloy HPM, and alloy 800H. Specimens were exposed to a carburizing gas atmosphere of 15%CH_4-3%CO_2-82%H_2 at 1,100°C for 96h at a flow rate of 250 sccm. Oxidation procedure (oxidation I) consists of heating in an air-1vol.%H_2O gas mixture at 900°C for 20h, followed by the carburization test. This heat treatment was intended to simulate actual decoking process. Other specimens of alloys that were not carburized (non-carburized) advanced to the oxidation I treatment.

After the oxidation I, coking test was conducted by heating the specimens at 1,000°C for 6h in a 15%CH_4-85%H_2 gas mixture. Finally, oxidation II was performed by heating the specimens under the same gas condition as oxidation I at 900°C for 1h. A set of these procedures (carburization, oxidation I, coking, and oxidation II) was repeated for up to 3 cycles for the carburized alloys, while conducted for 1cycle for the non-carburized one. (experimental details are given in Chapter 3). Carburization behavior of the alloys was evaluated as the same procedures as mentioned above. To investigate the catalytic activity of oxide scale formed during oxidation I to the coking, the amount of coke deposited on specimen surface was obtained by measuring specimen mass changes after oxidation II (gasification). Morphology of coke deposition was observed using a scanning electron microscope (SEM) after the coking test.

Table 4-2 Test sequences for the alloys

Sequence no.	Carburized	Non-carburized
1. Carburization	At 1100°C for 96h	-
2. Oxidation I	At 900°C for 20h	At 900°C for 20h
3. Coking	At 1000°C for 6h	At 1000°C for 6h
4. Oxidation II	At 900°C for 1h	At 900°C for 1h
Number of test cycle	3	1

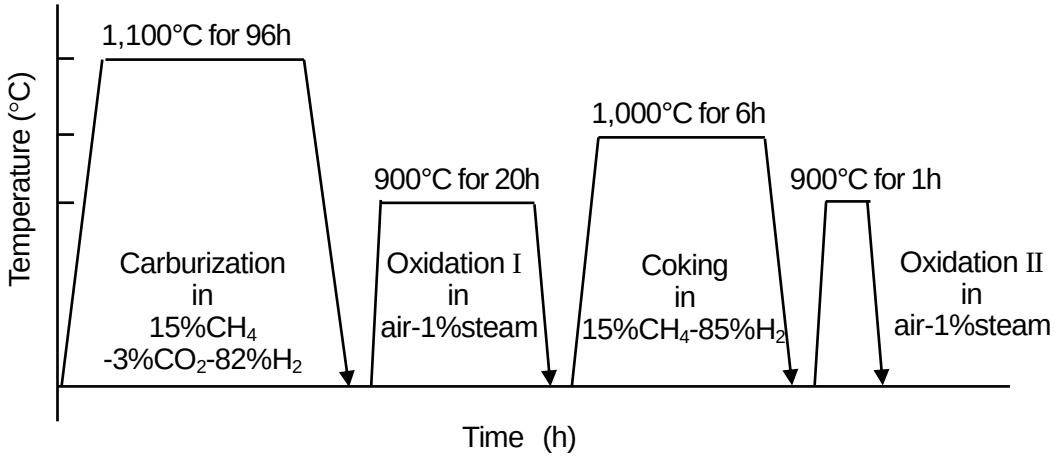

Figure 4-1 Details of the cyclic carburization and oxidation test sequence.

4.3 Results and Discussion

4.3.1 Effect of Alloying Elements on Carburization

Specimens with different concentration of Al, Cr, Mo, and W were tested in a 15%CH_4-3%CO_2-82%H_2 gas mixture at 1,100°C for 96h. Additional test exposed at 1,000°C for 96h in the above gas atmosphere was conducted for various Al content alloys. Values obtained from average increase of carbon content for the whole specimens, is shown in Fig. 4-2 with respect to each alloying elements. Carbon ingress decreased greatly with increasing Al in the alloy exposed at both temperatures of 1,000°C and 1,100°C. At 1,000°C, it was almost constant for alloys containing more than 2.5%Al. Aluminum in the alloy can form an Al_2O_3 scale on the surface in the test environment. Thus, the oxide scale provides a protection against carbon ingress into alloy. At 1,100°C, carbon ingress fell down drastically with increasing Al. More than 2.5%Al alloys were effective to reduce the carbon ingress, but their carbon increase were relatively high as compared to that for alloys with more than 3%Al. This would be caused by uniform formation of the Al_2O_3 scale.

For alloys having 3%Al, Cr did not affect carburization as shown in Fig. 4-2 because the alloys resisted the carbon ingress by formation of the protective Al_2O_3 scale. However, Cr helped alloys containing Al to form a uniform Al_2O_3 scale swiftly during initial stage. From the test result, this effect needed more than 10%Cr to form the Al_2O_3 scale on the surface. Alloying elements such as W and Mo showed a slight effect against carburization. They act not as barrier of carbon ingress by formation of oxide scale but as carbon getter in the alloy matrix because they can combine carbon as carbides. Hereby, growth of carburization can be lowered (see Eq. (2) in Chapter 2).

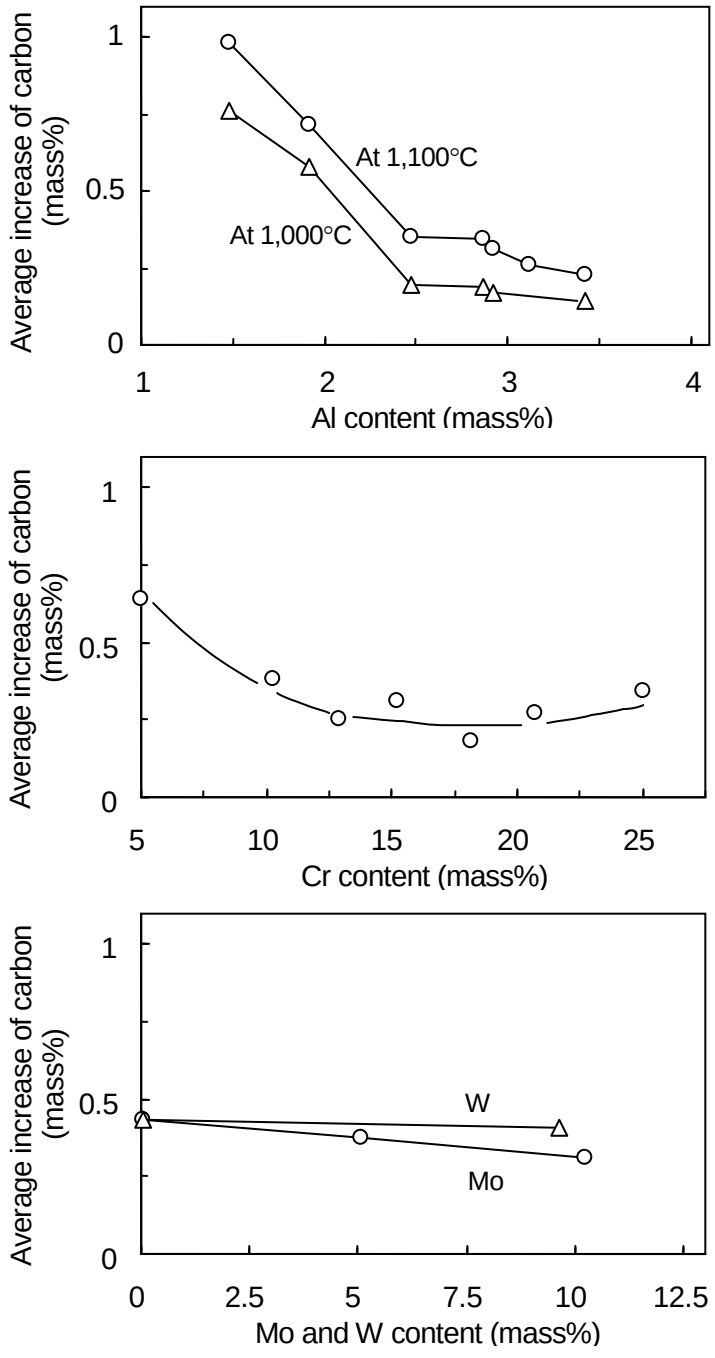

Figure 4-2 Effect of Al, Cr, Mo, and W in the alloy on average increase of carbon from the specimen surface to the center. Test was conducted in a 15%CH_4-3%CO_2-82%H_2 gas mixture at 1,100°C for 96h, and at 1,000°C for 96h for various Al content alloys.

4.3.2 Effect of temperature on Carburization

Carbon increase for the Al_2O_3-forming Ni-Cr-Al alloy was compared with that for Cr_2O_3-forming conventional steels after exposure to gas mixture of 15%CH_4-3%CO_2-82%H_2 at 1,000, 1,100, and 1,150°C, and their depth profiles are shown in Figs. 4-3 (a), (b), and (c), respectively. At 1,000°C, carbon increase of all three alloys remained unchanged at the middle part of the section thickness of 1 mm deeper from the surface. Regarding the area with in 1mm from the surface, alloy 800H showed a significant increase in carbon compared to the other alloys. For the Ni-Cr-Al alloy, carbon increase was small at the area of 0 to 0.5 mm from the surface especially. At both temperatures of 1,100°C and 1,150°C, carbon ingress of alloy HPM and alloy 800H increased compared to that at 1,000°C. Alloy 800H suffered severe corrosion among these alloys, whereas the Ni-Cr-Al alloy remained unchanged.

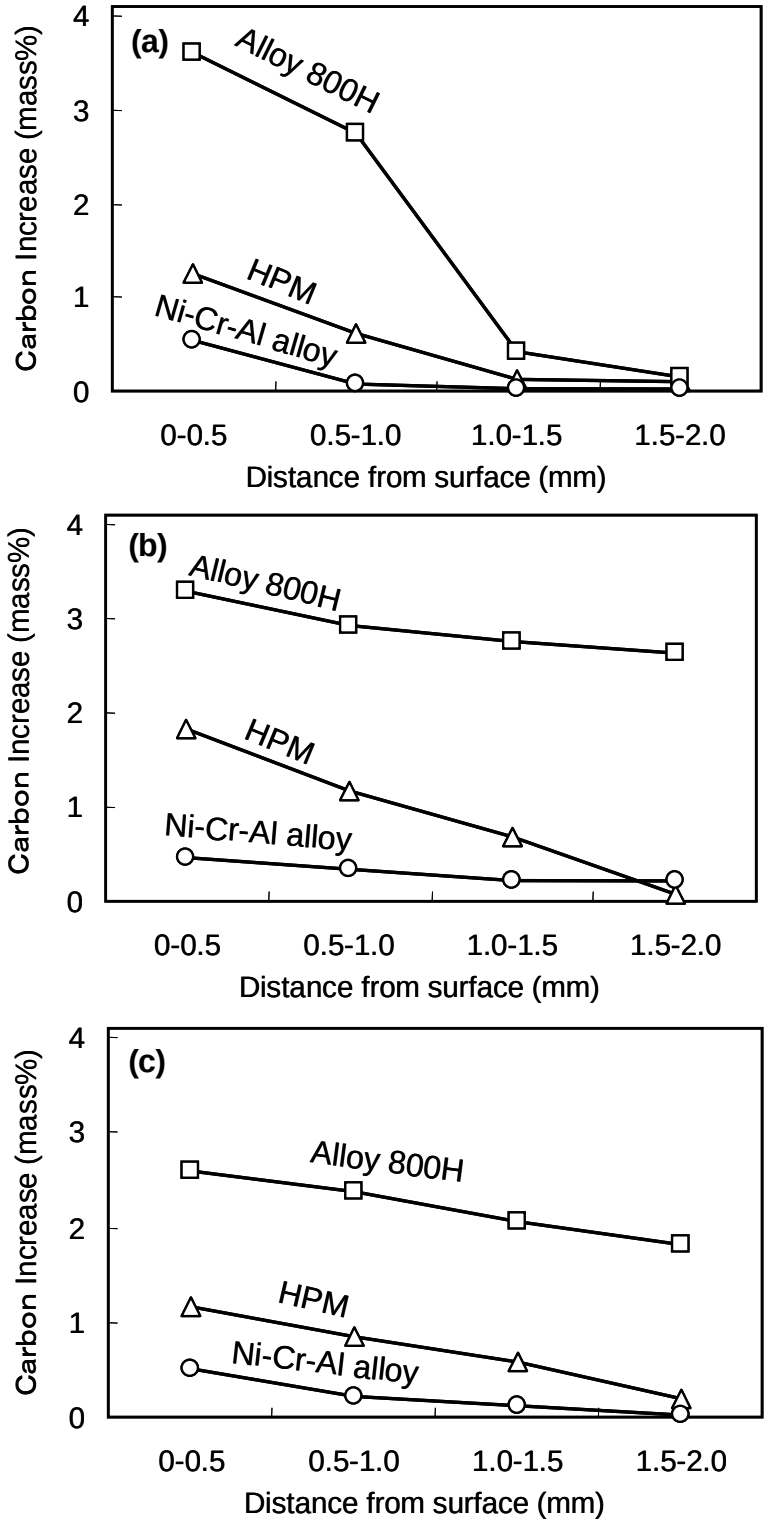

Figure 4-3 Depth profiles of carbon increase after exposure to a 15%CH_4-3%CO_2-82%H_2 gas mixture (a) at 1,000°C for 96h, (a) at 1,100°C for 96h, and (c) at 1,150°C for 48h.

The average carbon increase for the whole specimens, and the depth corresponding to carbon increase of 1mass%, are summarized in Table 4-3 and 4-4, respectively. Carburization resistance of alloy HPM containing 1.8%Si was apparently better than alloy 800H for 1,000 to 1,150°C. This result suggests that higher Si content and Cr of more than 25% are needed to obtain protection for alloys against carburization environments at high temperatures. The Ni-Cr-Al alloy has the best resistance to carburization among the tested alloys owing to high Al content of the alloy. Its carburization resistance was more than three times better than alloy HPM. For the Ni-Cr-Al alloy, severe carburization zone of carbon ingress exceeding 1% was not present.

Table 4-3 Average carbon increase of alloys exposed to a 15%CH_4-3%CO_2-82%H_2 gas mixture at various temperatures (mass%)

Alloy	Test conditions		
	1,000°C for 96h	1,100°C for 96h	1,150°C for 48h
Ni-Cr-Al	0.17	0.31	0.22
Alloy HPM	0.52	0.94	0.70
Alloy 800H	1.73	2.91	2.22

Table 4-4 Depth corresponding to carbon increase of 1% for alloys exposed to a 15%CH_4-3%CO_2-82%H_2 gas mixture at various temperatures (mm)

Alloy	Test conditions		
	1,000°C for 96h	1,100°C for 96h	1,150°C for 48h
Ni-Cr-Al alloy	0	0	0
Alloy HPM	0.44	0.93	0.52
Alloy 800H	1.12	>2	>2

Cross sections of the alloys exposed to 15%CH_4-3%CO_2-82%H_2 gas mixture at 1,100°C for 96h are shown in Fig. 4-4. For alloys HPM and 800H, fine precipitates of 5-10 μm were found along grain boundaries and bulky precipitates in the matrix. They were identified as Cr_7C_3. On the other hand, very fine precipitates of a few μm were observed discontinuously along grain boundaries and matrix of the Ni-Cr-Al alloy. They were identified as Mo-rich carbide and Cr_7C_3 by XRD and EPMA analyses.

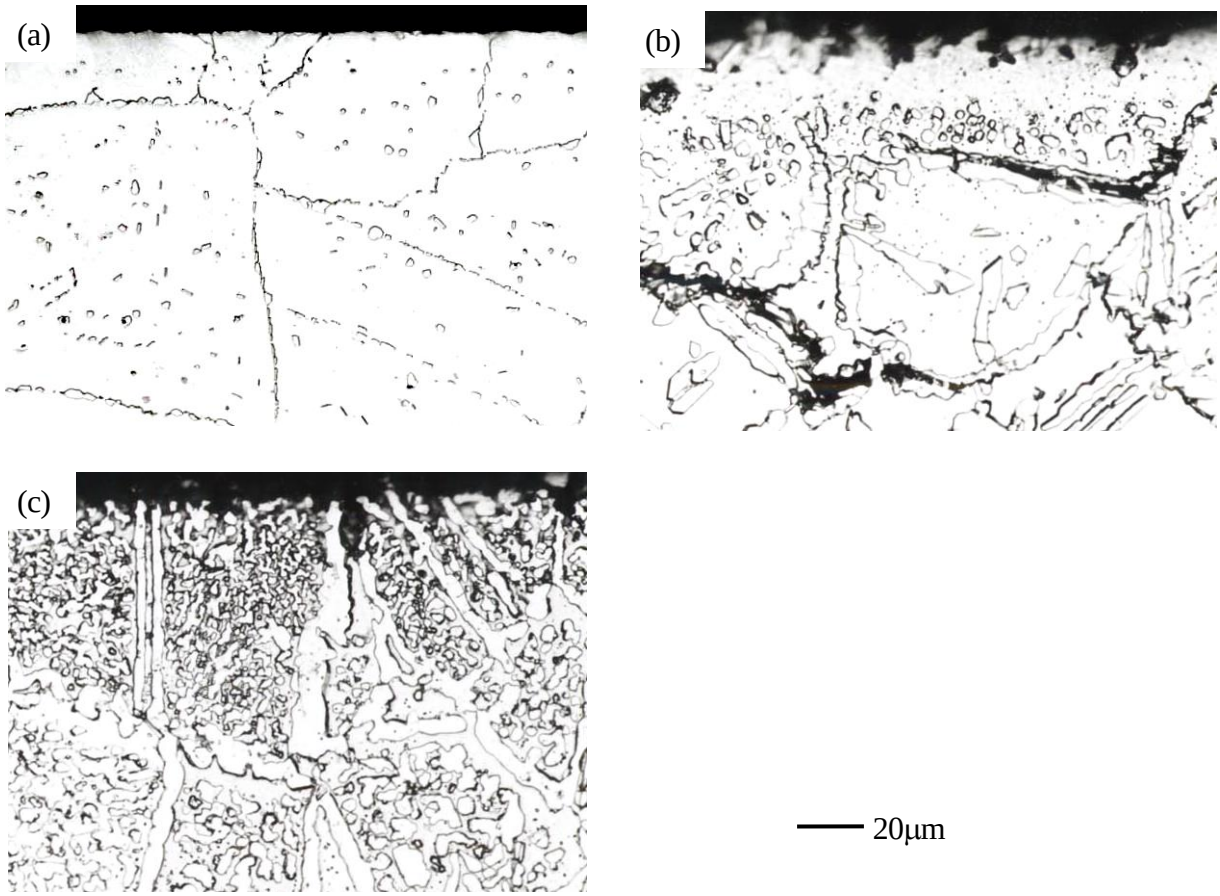

Figure 4-4 Metallographic cross sections of alloy surfaces reacted at 1,100°C for 96h. (a) Ni-Cr-Al alloy, (b) alloy HPM, and (c) alloy 800H

The results can be considered by thermodynamics of oxides formed on the alloy surface. In Fig. 4-5, equilibrium partial pressure of oxygen, Po_2 (atm) of Cr, Si, and Al compounds is shown, along with that of the cracking gas atmosphere in ethylene pyrolysis as a function of temperature. In this calculation, activities of each metal, oxide, and carbide were set to unity. The calculation suggests that Cr oxide can change to Cr carbides above 1,030 to 1,040°C, since the calculated equilibrium Po_2 inside the furnace tubes becomes lower than that of Cr_2O_3 /Cr_7C_3 equilibrium. On the other hand, both oxides of Al and Si remains stable in such environments, indicating that Al_2O_3 and SiO_2 scales may provide protection against the carbon ingress for the alloy at higher temperatures.

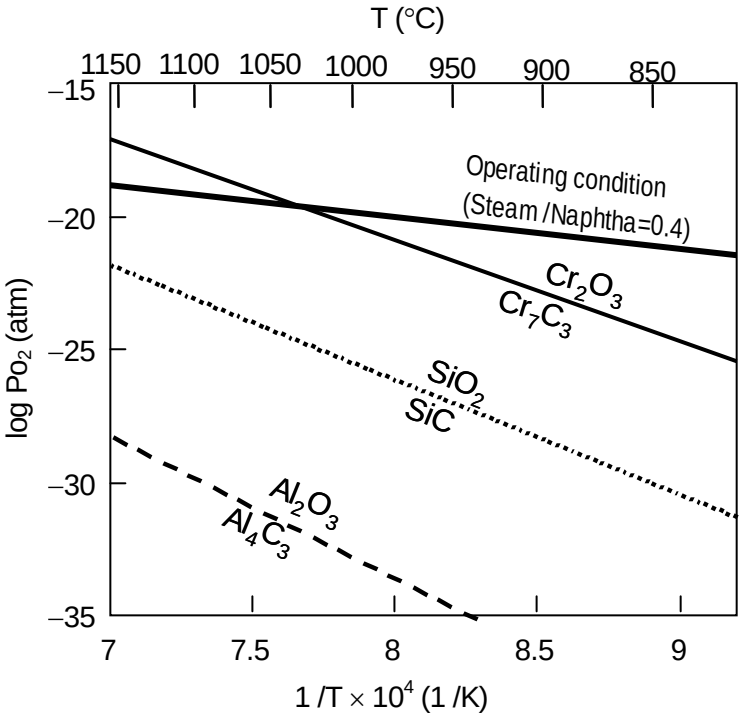

Figure 4-5 Phase stability of Cr, Si, and Al compounds (activities of each metal, oxide, and carbide were set to unity) and calculated equilibrium Po_2 of gas atmosphere upon ethylene pyrolysis as a function of temperature.

4.3.3 Behavior of Carburization and Coking under Cyclic Carburizing and Oxidizing Environments

Figure 4-6 shows the average carbon increase for the whole specimens under cyclic carburization and oxidation test. Carbon increase of alloy HPM increases with increasing the number of heat cycle. According to the analysis of oxide scale chemistry for the Cr_2O_3-forming alloys, carburization degrades the Cr_2O_3 scale (see Chapter 3). As the cyclic carburization and oxidation proceeds, oxide scale changes from Cr_2O_3 to an unprotective spinel-type oxide on the alloy surface during oxidation I. Hence, protection by the oxide scales becomes insufficient in the following carburization. On the contrary, the Ni-Cr-Al alloy has a slight carbon increase that remains virtually unchanged for up to three cycles. This suggests that the Al_2O_3 scale formed on the alloy is quite stable and protective against carburization.

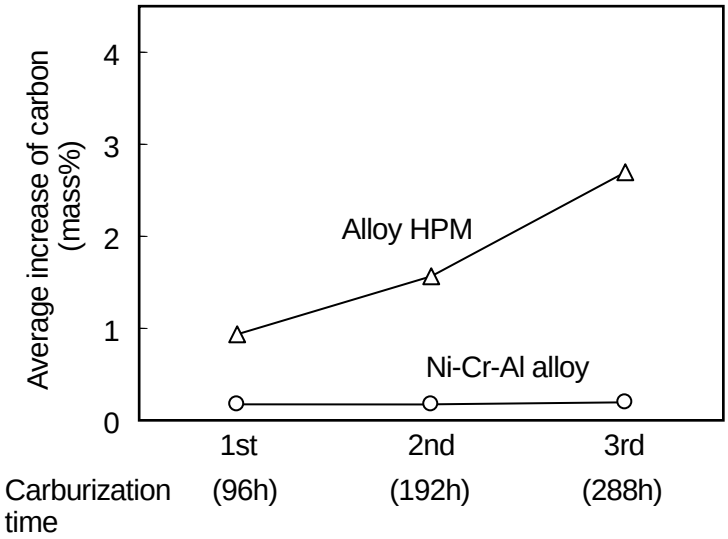

Figure 4-6 Changes of average carbon increase of alloys exposed to the cyclic test.

Figure 4-7 shows the amount of coke deposited on the specimen surface after each coking procedure of the cyclic test. Data of 'As' shown in this figure represents the coke deposition for non-carburized specimens. They indicate the reactivity of "non-damaged" protective oxide scales with gas atmospheres where the a_c is more than unity. The both alloys have slight amounts of coke deposited on the 'As' surfaces. On the contrary, the coke deposition on alloy HPM increases rapidly with

increasing the number of heat cycle. This was caused by degradation of a protective oxide scale, i.e. formation of a spinel-type oxide instead of Cr_2O_3, upon cyclic carburization and oxidation procedures. The spinel-type oxide consisting of Fe and Ni can accelerate the coke formation, because it is reduced to metal and oxygen thermodynamically under the following carburizing environment. The reduced metals of Fe and Ni induce a catalytic reaction of coking. For the Ni-Cr-Al alloy, the amount of coke remained unchanged after the 2nd test cycle. The protective Al_2O_3 scale is not degraded on the Ni-Cr-Al alloy. In addition, no metals can be reduced from the oxide scale because of its thermodynamic stability in the carburizing environment. As shown in Fig. 4-7, the coke deposition turned to be decreased after the 3rd cycle. The Cr_2O_3 scale can partly be formed on top of the Al_2O_3 scale at initial stage of the cyclic test, resulting that the coke is deposited by reaction of the Cr_2O_3 with the carbonaceous gas atmosphere. After several cycles, however, this scale flakes away because it has weak adhesion to the Al_2O_3 scale. Eventually, the 'purely' Al_2O_3 scale comprises the outermost layer on the alloy surface, which inactivates the coking reaction in carburizing environments.

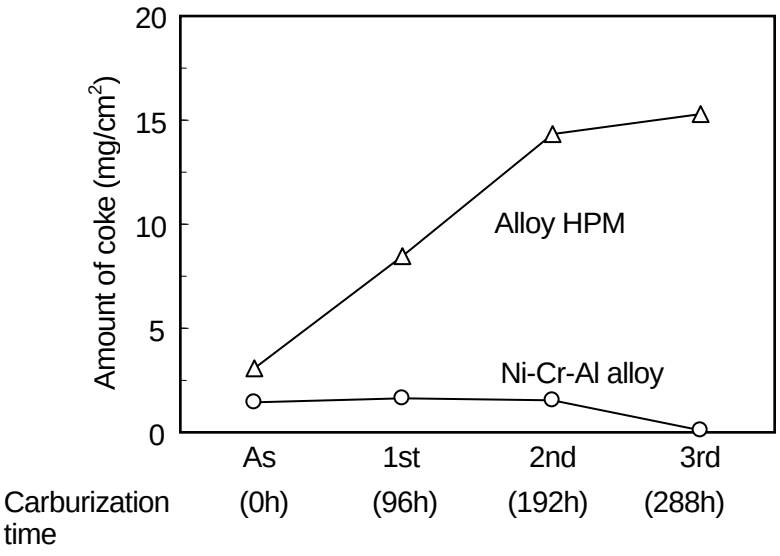

Figure 4-7 Changes of coke deposition on the metal surface under the cyclic carburization and oxidation test. 'As' shown in x-axis represents the data after coking test of pre-oxidized specimen without carburization.

The morphology of deposited coke was observed on the specimens after the coking procedure. Figure 4-8 shows the SEM photographs of the Ni-Cr-Al alloy and alloy HPM after the 3rd cycle. The Ni-Cr-Al alloy is covered with thin film-like deposits on the surface; probably due to the coke created from thermal decomposition of gaseous hydrocarbons. The amount of coke on alloy HPM is apparently greater than that on the Ni-Cr-Al alloy. On the surface of alloy HPM, flocculent gross deposits were observed and identified as amorphous carbon by XRD measurement.

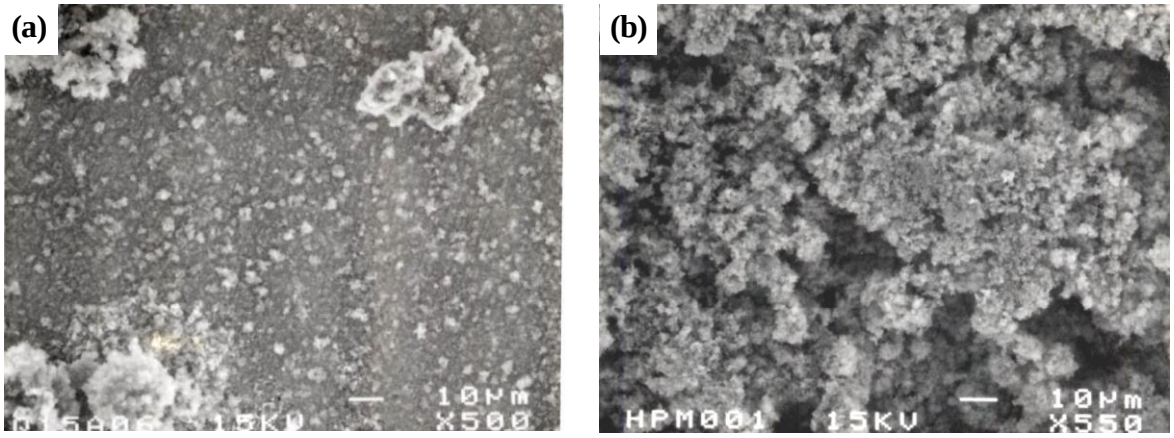

Figure 4-8 SEM observations of coke deposition on the 3rd cycled metal surface of (a) Ni-Cr-Al alloy and (b) HPM.

Based on the results, carburization and coking behavior for the alloys can be concluded as shown in Fig. 4-9. At the initial stage, the conventional steels have a good carburization resistance: Cr as a Cr_2O_3 scale provides protection against carbon. After several numbers of cyclic carburization (cracking) and oxidation (decoking) procedures, however, inward diffusion of carbon proceeds gradually in the alloy matrix, since the Cr_2O_3 scale has damages of crack and /or flow during the carburization. The formation of carbides of Cr lowers solute Cr content in the alloy, leading to the degradation of the Cr_2O_3 scale during the following decoking process. An unprotective spinel-type oxide scale containing Fe and Ni which forms instead of the Cr_2O_3 scale easily allows carbon to diffuse inward into the alloy so that the carbon increases rapidly. Furthermore, coke deposition increases due to heterogeneous reaction catalyzed by the Fe and Ni particles generated by reduction of the spinel-type oxide during the cracking process [4].

The Ni-Cr-Al alloy has a superb carburization resistance compared to the conventional steels, because Al as an Al_2O_3 protective scale reduces carbon increase in the carburizing environment. And even if carburization has occurred, a solute Al content still remains unchanged at the external surface because the ingress carbon reacts not with Al but Cr, Ti, Nb, and etc. in the matrix. Thus, the Al_2O_3 scale remains to be stable and retards the carburization in the carbonaceous gas atmosphere for a long time. Moreover, the Al_2O_3 scale can restrain the coke deposition during the cracking process because it has less reactivity with carbon compared with that of Fe and Ni particles. This benefit can be expected to expand a period of decoking procedure and /or raise an operating temperature of ethylene pyrolysis furnaces.

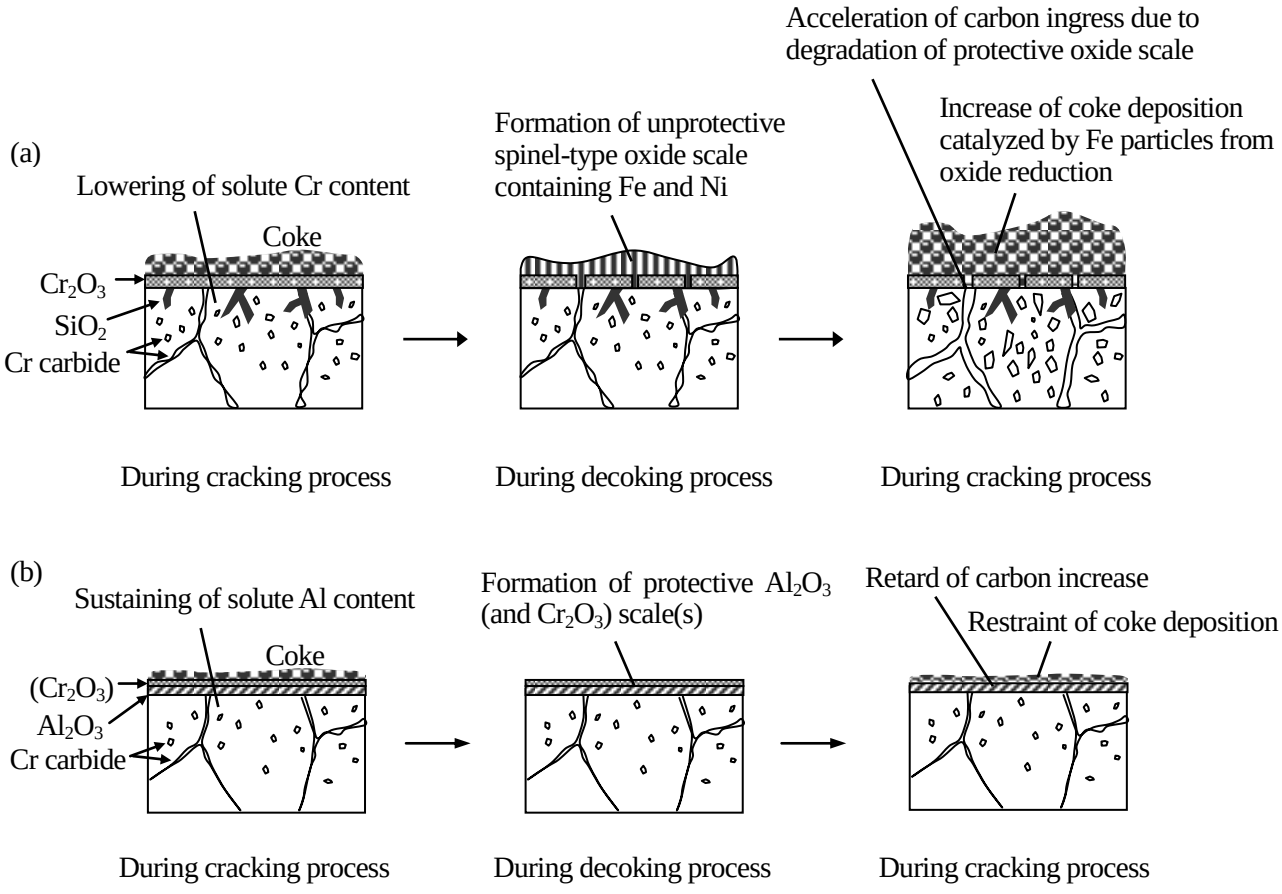

Figure 4-9 Carburization and coking behavior (a) of the conventional steels and (b) of the Ni-Cr-Al alloy, upon the cyclic cracking and decoking processes of ethylene pyrolysis furnaces.

4.4 Conclusions

An Ni-Cr-Al alloy was examined and developed to apply as furnace tubes of ethylene pyrolysis plant in the chemical industry. The developed alloy was proven to have an excellent carburization and coking resistance due to the formation of a uniform protective Al_2O_3 scale on the alloy surface. The characteristics obtained are summarized as follows:

(1) Aluminum as Al_2O_3 is greatly effective alloying element to protect against carburization environment. More than 2.5mass% (at 1,000°C) and 3% (at temperatures higher than 1,100°C) are sufficient to form a uniform Al_2O_3 scale. For 3%Al content alloy, Cr does not affect carburization, though more than 10%Cr is needed to help the formation of the Al_2O_3 scale. Both Mo and W act as a getter of carbon which diffuses inward in the alloy matrix, resulting in lowering of carburization.

(2) In the simulated carburizing environment, the Al_2O_3-forming alloy has a three times better carburization resistance than that of Cr_2O_3-forming conventional steel containing more than 25%Cr and high Si.

(3) In the cyclic carburizing and oxidizing environment, carbon increase and coke deposition of the Cr_2O_3-forming steel increase drastically with increasing the cycle, while those of the Al_2O_3-forming alloy remain unchanged.

References

[1] K. Maeda and T. Iijima, "Problems associated with materials used in carbon depositing environments in petroleum industries", Boshoku-Gijutsu 33 (1984), p.232.

[2] K. Takemura, Petrotech 21, no.10 (1998), p.1027.

[3] Y. Shimizu and T. Sakaki, "The nondestructive detection technique of high temperature carburizing damages in petrochemical plants," Materia Japan 38, no.3 (1999), p.220.

[4] S. Tokura, N. Otsuka and T. Kudo, Corrosion 48, 7 (1993), p.561.

[5] A. Otomo, Y. Shinozaki and Y. Zaiga, Tetsu-to-Hagane 54 (1968), p.S650.

[6] M. Koori, S. Ota and T. Yoshida, Gakushin 123 committee report 15 (1974), p.67.

[7] H.J. Grabke, "Carburization, A high temperature corrosion phenomenon," Materials Technology Institute of the Chemical Process Industries, Inc. no.52 (1998).

[8] G. Morita, Haikan-Gijutsu 1 (1998), p.12.

[9] Y. Sawaragi and M.Nishi, Petrotech 18, no.8 (1995), p.648.

[10] R. Milner, "Carburization of emerging materials," CORROSION /99, paper no.269, (Houston, TX: NACE, 1999).

[11] D.C. Agarwal and U. Brill, "Performance of Alloy 602CA (UNS N06025) in high temperature environments up to 1200°C," CORROSION /2000, paper no.521, (Houston, TX: NACE, 2000).

[12] K. Hosoya, K. Satoh, K. Yamamoto, G.J.A. Hack and R.M. Haeberle, "An evaluation of the coking resistance of a high performance oxide dispersion strengthened (ODS) alloy tube," AIChE 2000 Spring Meeting, paper no.86f..

[13] K.A. Wynns and G.T. Bayer, "Diffusion Coated Ethylene Furnace Tubes," United States Patent No. 5,873,951, February 23, 1999.

[14] A.B. Smith, A. Kempster, A. Lambourne and J.R. Smith, "The Use of Aluminide Diffusion Coatings to Improve Carburization Resistance," CORROSION /2001, paper no.1391, (Houston, TX: NACE, 2001).

Chapter 5

THERMODYNAMIC ASPECTS UPON SYNGAS ENVIRONMENT AND METAL DUSTING OF NI-BASE ALLOYS IN SIMULATED GAS MIXTURES

5.1 Introduction

Metal dusting, a type of corrosion failure resulting from catastrophic carburization or graphitization of steels and alloys occurring in carbonaceous atmosphere, has been a prominent corrosion damage for high temperature materials used in ammonia, methanol, and syngas plants [1 - 4]. Metal dusting is often encountered when steels and alloys are exposed at 450 - 700°C to CO-containing syngas environments where the carbon activity (a_c) is greater than unity, and the oxygen potential (Po_2) is relatively low. For carbon steels, Hochman [5, 6] proposed a corrosion mechanism that the important step in metal dusting is the formation of unstable cementite (Fe_3C) as an intermediate followed by its decomposition. The detailed reaction steps for carbon steels and low alloy steels were demonstrated by Grabke and his coworkers [7 - 10] as follows:

a) carbon is transferred from carbonaceous gases and diffuses into a base metal.

b) formation of cementite at the metal surface which acts as a barrier for further carbon ingress.

c) when graphite nucleates, the a_c decreases to unity at the graphite /cementite boundary. This causes decomposition of the metastable cementite by inward growth of graphite, according to the following reaction as Eq. (1).

$$M_3C \text{ (M includes Fe, Mn, and Cr)} = 3M + C \quad (1)$$

d) dissociated metal particles act as catalyst for further carbon deposition from the gas atmosphere,

which leads to massive coke growth.

The type of this metal dusting attack is reported as "uniform corrosion" on iron and low alloy steels. For high-alloy steels, experiences with metal dusting have been reported in actual plants [11 - 15]. However, the mechanism of metal dusting of high Ni alloy has not been established yet [16 - 18]. The purpose of the present study is to have the right understanding on the metal dusting propensity of the ambient gas environment, and to obtain some clues to the mechanism of metal dusting for high Ni alloys, which are believed protective against carburization.

5.2 Thermodynamic Aspects of Syngas Atmosphere

Metal dusting encountered in the reformer plant is closely related to the process gas composition, gas pressure, and metal temperature. In the reforming processes, natural gas reacts with steam to form CO, H_2, CO_2, and H_2O gas mixtures, which are strongly carburizing and slightly oxidizing to the metal components. Metal dusting can occur for steels and alloys under these limited conditions. Recent high-efficiency reactor design favors gas mixtures enriched with CO by lowering steam to natural gas volume ratio, which can result in harsh corrosion damage for the reactor material. Parks and Schillmoller [19] presented a metal dusting map for 304 stainless steel and alloy 800. In this map, CO /CO_2 and H_2O /H_2 ratios were proposed as a corrosion index of the gas mixture. Occurrence /absence of metal dusting for alloys used in waste heat boilers of ammonia plants were explained by these indices. However, verification of these indices, based on either thermodynamics or kinetics of the relating reactions, is needed to generalize their idea.

According to thermodynamics, activity of carbon a_c and oxygen potential Po_2 of the ambient gas mixture must be considered as an index to represent the metal dusting propensity of the gas atmosphere. Possible reactions leading to deposition of carbon (and hence to carburization) can be described as follows:

$$CO + H_2 = H_2O + C \quad (2)$$

$$2CO = CO_2 + C \quad (3)$$

$$CH_4 = 2H_2 + C \quad (4)$$

Equilibrium constant K of these reactions was calculated using available thermodynamic data [20] and is shown in Fig. 5-1 as a function of temperature. As expected, K of Eqs. (2) and (3) decreases and K of Eq. (4) increases with increasing temperature. Therefore, for lower temperatures, reactions involving CO may affect the carbon deposition. At higher temperatures, reaction such as Eq. (4) that involves hydrocarbon would become important. In reformer plants, metal dusting is reported to occur at intermediate temperatures between 450°C and 700°C where the gas mixture consists mainly of CO, H_2, CO_2, and H_2O. For these gas environments, reactions represented by Eqs. (2) and (3) would play an important role in metal dusting.

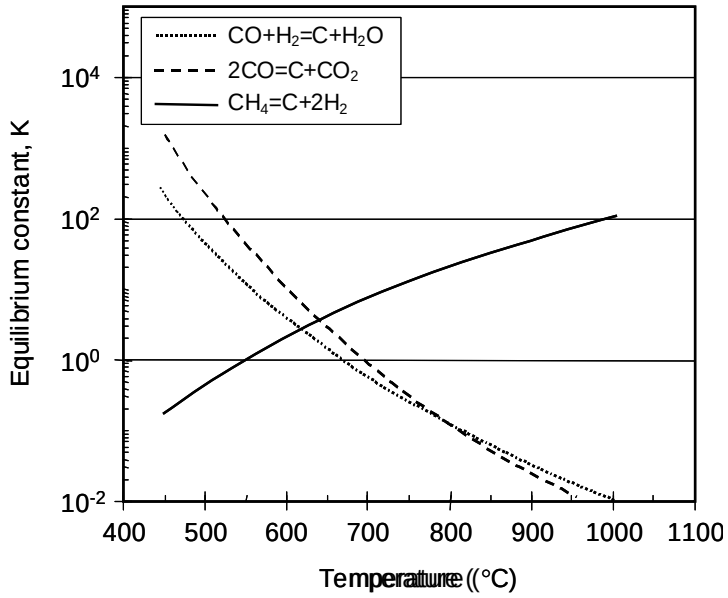

Figure 5-1 Equilibrium constants of reactions relating to carbon activity at temperatures between 450°C and 1,000°C.

With respect to metal dusting due to CO, two reactions shown by Eqs. (2) and (3) are probable. To determine the predominant reaction causing metal dusting, a coke deposition test was conducted by exposing quartz plates to gas mixtures of various carbon activities at 650°C for 200h. The composition of the test gas is presented in Table 5-1.

The test results are shown in Fig. 5-2. Clearly, coke deposited from the gas atmosphere on the SiO_2 plate for gas mixtures of nos. 4, 8, 9, 10, 12, and 13, and did not for gas mixtures of nos.1 and 5. The test results demonstrate that the carbon activity (without consideration of graphite formation) of the gas mixture is affected not by CO /CO_2 but by CO /H_2 /H_2O reaction. Therefore, for CO-H_2-CO_2-H_2O

systems such as reformer gases, the carbon activity of the gas mixture, i.e. carbon deposition propensity, would be better estimated by the CO /H_2 /H_2O reaction shown in Eq. (2) than the CO /CO_2 equilibrium.

Table 5-1 Preliminary test gas composition

Gases no.	Gas composition (vol.%)			
	CO	H_2	CO_2	H_2O
1	5	82.0	0.1	12.9
4	5	90.3	4	0.7
5	0.5	95.7	0	3.8
8	10	88.3	0.3	1.4
9	60	26.1	11.5	2.5
10	10	89.4	0.3	0.2
12	60	28.1	11.5	0.4
13	2	96.5	0	1.5

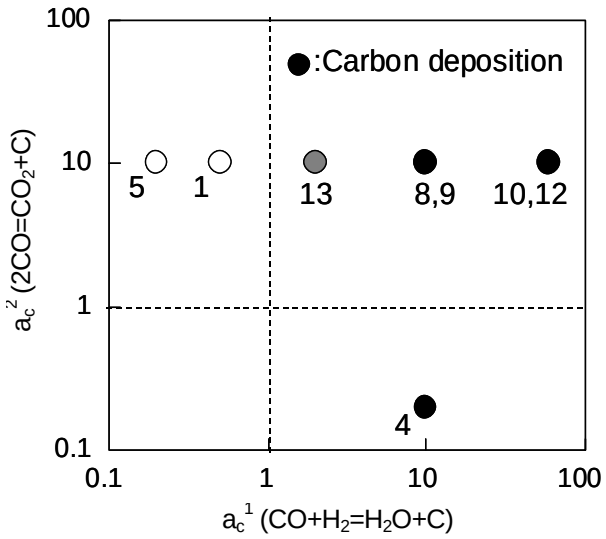

Figure 5-2 Coke deposition test results on a quartz in gas mixtures of various carbon activity tested at 650°C for 200h. (Numbers shown in this figure denote test gas nos.)

This may be explained by reaction kinetics. The reaction rate k_p of Eqs. (2), (3), and (4) for Fe or low Cr steels was reported as Eqs. (5), (6), and (7) respectively as follows [21]:

$$k_{p1} = \{4.75 \times 10^5 \times \exp(-27150/T) \times P_{H2O} \times P_{H2}^{-1/2}\} \times \{1+5.6 \times 10^6 \times \exp(-12900/T) \times P_{H2O} \times P_{H2}^{-1}\}^{-1} \quad (5)$$

$$k_{p2} = 184 \times (P_{CO2} / P_{CO})^{-0.3} \times P_{CO_2} \times \exp(-22400/T) \quad (6)$$

$$k_{p3} = 1.96 \times 10^{-2} \times P_{H2}^{3/2} \times \exp(-17600/T) \quad (7)$$

where P is the partial pressure (atm) of each gas species and T the temperature (K). The calculated reaction rates of Eqs. (2), (3), and (4) at 450-1,000˚C are shown in Fig. 5-3. The top graph shows the reaction rates in a gas mixture of 10 vol.%CO, while the bottom one of 60 vol.%CO. For 10 %CO, the reaction rate of Eq. (2) is roughly one order of magnitude higher than that of Eqs. (3) and (4) at 600-700˚C. For 60%CO, reaction rate of Eq. (3) increases and approaches Eq. (2). Hence, for reformer tubes, the deposition rate of carbon via CO /H_2 /H_2O reaction must be considered important in CO-H_2-CO_2-H_2O gas mixtures for gases of low CO content. For gases of high CO content, carbon deposition by CO /CO_2 reaction should be also considered.

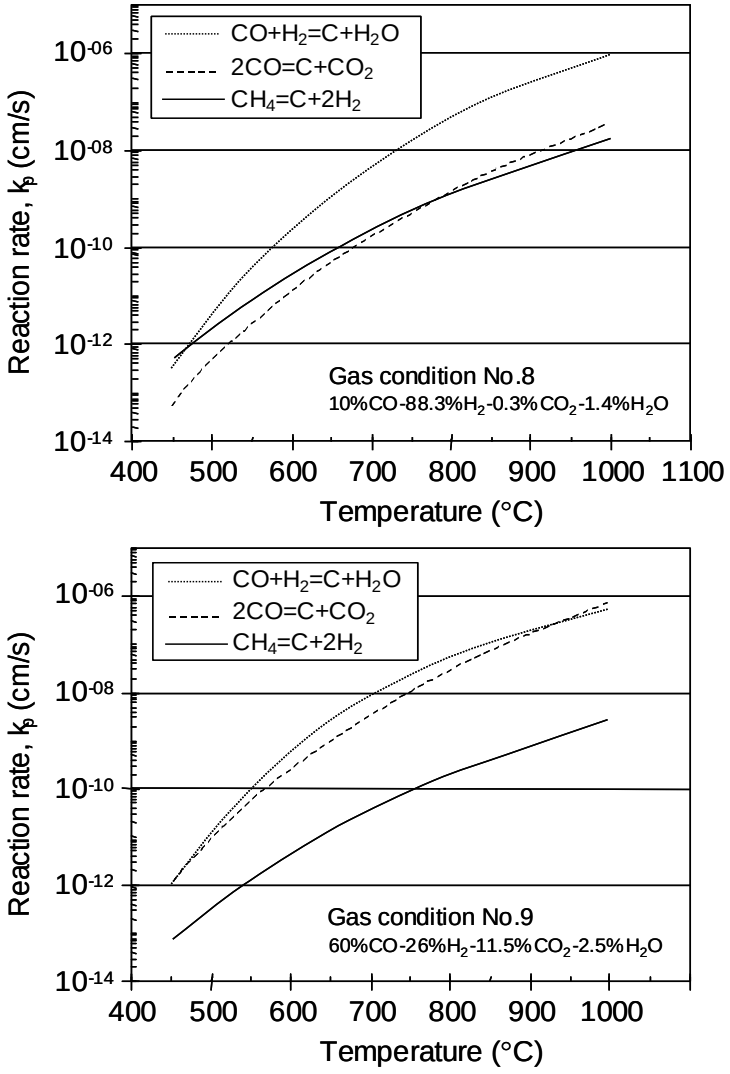

Figure 5-3 Reaction rates relating carbon activity at temperatures between 450°C and 1,000°C in laboratory gas mixtures with 10vol.%CO (top graph) and 60vol.%CO (bottom graph).

Oxygen potential Po_2 of the gas atmosphere is another important factor which may affect metal dusting because the oxide scale formed on the metal surface can inhibit inward diffusion of carbon. Reactions relating oxygen potential of the reformer gas are considered as follows:

$$H_2O = H_2 + 1/2O_2 \quad (8)$$

$$CO_2 = CO + 1/2O_2 \quad (9)$$

Equilibrium constant K of these reactions was calculated between 450°C and 1,000°C from available thermodynamic data [20] and shown in Fig. 5-4. Both constants increases with increasing temperature, and the constant for reaction H_2O /H_2 was higher than that for the reaction CO_2 /CO below 800°C. From the viewpoint of thermodynamics, the oxygen potential determined by H_2O /H_2 equilibrium may dominate the oxygen potential in reformer environment.

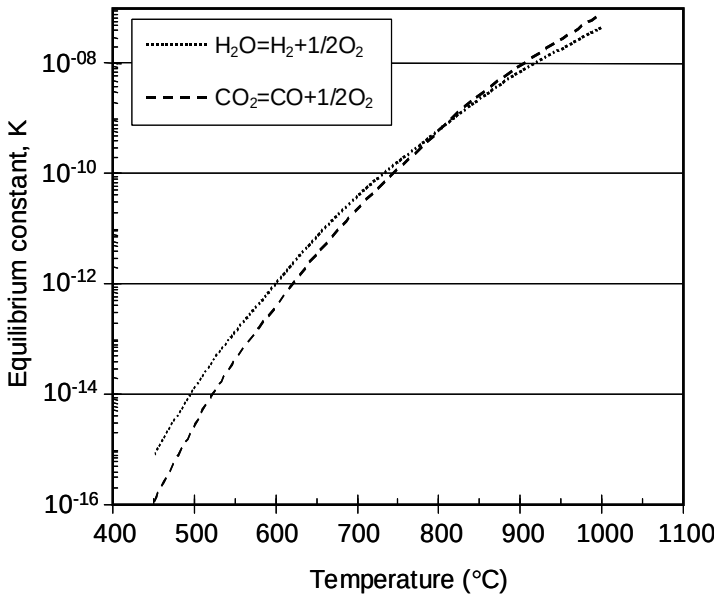

Figure 5-4 Equilibrium constants of reactions relating oxygen potential at temperatures between 450°C and 1,000°C.

To clarify this point, specimens of UNS N08810 (alloy 800H, 21%-32%Ni-Ti, Al) were exposed to gas mixtures presented in Table 5-1 (except gas no. 13) at 650°C for 200h and thickness of the oxide scale formed on each specimen was examined and plotted vs. oxygen potential of the gas mixture. This is shown in Fig. 5-5 in terms of the oxygen potential derived from H_2O /H_2 (left) and from CO_2 /CO

(right). Thickness of the oxide scale depended on the oxygen potential derived not from CO_2 /CO but from H_2O /H_2 equilibrium, suggesting that the oxygen potential of the gas mixture is influenced by H_2O /H_2 equilibrium directly. Comparing these results with the dissociation pressure of oxygen for Fe /Cr oxides at 650°C presented in Table 5-2, Cr_2O_3 remains stable at 650˚C for the test gas mixtures whereas Ni oxides such as NiO and $NiCr_2O_4$ do not. The spinel-type oxide (AB_2O_4) containing Fe and Cr is stable only above 2.1×10^{-27} atm Po_2, which is consistent with the formation of relatively "thick" oxide scale for Po_2 at above 10^{-25} atm in Fig. 5-5 (left). Hence, in terms of oxide scale formation, the oxygen potential of the CO-H_2-CO_2-H_2O gas mixture can be estimated by the H_2O /H_2 equilibrium.

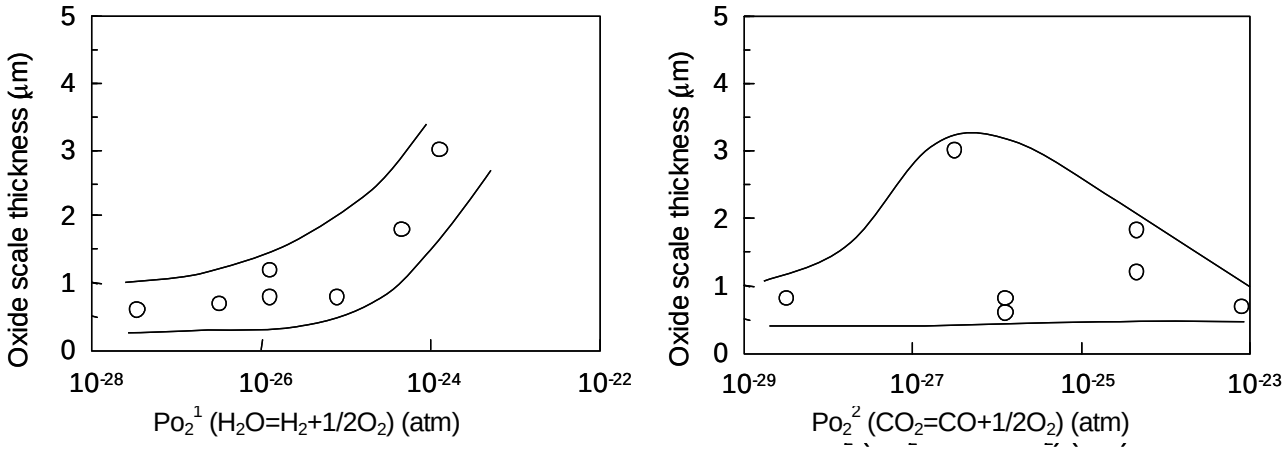

Figure 5-5 Thickness of oxide scale formed on alloy 800H after exposure in CO-H_2-CO_2-H_2O gas mixtures (except gas no. 13) at 650°C for 200h as a function of Po_2^1 for Eq. (8) (left graph) and of Po_2^2 for Eq. (9) (right graph).

Table 5-2 Oxygen potential required for the formation of oxides at 650°C (Activity of metal Ni, Fe, Mn, and Cr was taken as 0.35, 0.4, 0.01, and 0.25, respectively for alloy 800H)

Oxide	Po_2 (atm)
NiO /Ni	1.9×10^{-17}
$NiCr_2O_4$ /(Ni+Cr_2O_3)	1.8×10^{-17}
FeO /Fe	4.8×10^{-23}
$FeCr_2O_4$ /(Fe+Cr_2O_3)	2.1×10^{-27}
Mn_3O_4 /Mn	6.3×10^{-28}
Cr_2O_3 /Cr	1.2×10^{-33}

Based on these results, it becomes possible to evaluate the metal dusting propensity of a certain process gas mixture in reforming plants by using a_c^1 derived from CO /H_2 /H_2O equilibrium and Po_2^1 from H_2O /H_2 equilibrium. These indices are expected to represent much more adequately than the CO /CO_2 and H_2O /H_2 ratios proposed by Parks and Schillmoller, though further studies are needed to verify this point.

Laboratory corrosion tests for development of eminent alloys required for severe metal dusting have been conducted [16, 22 - 26]. The gas mixtures used for these metal-dusting tests were surveyed and summarized in Table 5-3. The metal dusting indices of the gas mixture derived in this study, i.e. a_c^1 from CO /H_2 /H_2O (Eq. (2)) and Po_2^1 from H_2O /H_2 (Eq. (8)) were calculated and presented in Table 5-4 for each gas. Ratios of CO /CO_2 and H_2O /H_2 are also shown in this table. Indices of our study and those of Parks and Schillmoller are presented for a reformer gas in an actual plant in Table 5-4 for an example. For laboratory test gas mixtures, the a_c^1 calculated by CO /H_2 /H_2O ranged from 9 to 37 whereas the Po_2^1 by H_2O /H_2 in the order of 10^{-26} atm. Since a_c^1 and Po_2^1 of the actual plant are 2-30 and 10^{-23}-10^{-22} atm, respectively, laboratory test gases clearly give higher a_c^1 and significantly lower Po_2^1 than the actual plant. This was similar for the indices proposed by Parks and Schillmoller. Hence, carburization by the gas mixtures used in the laboratory metal-dusting tests is considered much more severe than the actual plant since laboratory gases enhance carbon deposition and weaken the oxide scale compared with the actual plants.

Table 5-3 Reported test conditions for metal dusting evaluation

Literature	Temperature and gas pressure	Gas composition (vol.%)				Ref.
		CO	H_2	CO_2	H_2O	
Grabke *et al.*	600~700°C 1atm	24	74	0	2	[7] [22]
Fabiszewski *et al.*	650~700°C 1atm	90	10	0	0	[23]
Baker *et al.*	621°C 1atm	80(70)	20(25.25)	0(4)	0(0.75)	[24]
Klöwer *et al.*	650°C 1atm	24	74	0	2	[16]
Klarstrom *et al.*	650°C 1atm	49	49	0	2	[25]
Natesan *et al.*	482~704°C 1atm	*unknown*				[26]
Szakalos	650°C 1atm	25	72	0	3	[26]

Table 5-4 Calculated a_c[1] by Eq. (2) and Po_2[1] by Eq. (8) of the corrosion test conditions listed in Table 5-3 at 650°C

Literature	a_c[1]	Po_2[1] (atm)	CO/CO_2	H_2O/H_2
Grabke *et al.*	14	3.8×10^{-26}	-	0.03
Baker *et al.*	37	4.6×10^{-26}	17.5	0.03
Klöwer *et al.*	14	3.8×10^{-26}	-	0.03
Klarstrom *et al.*	19	8.6×10^{-26}	-	0.04
Natesan *et al.*	*Unknown*		1.75	1.02
Szakalos	9	9.0×10^{-26}	-	0.04
Actual plants	2 – 30*	10^{-23}-10^{-22}*	2~4*	0.45 - 0.65*

* calculated from estimated plant conditions

The correlation between a_c and Po_2, and CO content in a gas atmosphere was calculated and is presented in Fig. 5-6. Contour lines of the higher CO content shift toward the upper right in this diagram, i.e. both of a_c and Po_2 become higher. The higher a_c causes the severer metal dusting attack for alloys. Although the higher Po_2 may be effective to promote the formation of protective oxide scale at the initial stage, it enhances the growth of oxide scale as well as the formation of an unprotective oxide scale containing Fe. A thick oxide scale containing Fe is easily cracked and spalled due to the increase of growth stress, which induce the metal dusting attack. The correlation between a_c and Po_2, and total gas pressure was also calculated and is presented in Fig. 5-7. Both of a_c and Po_2 increase with increasing gas pressure in the gas atmosphere, e.g. the ac^1 and Po_2^1 for a gas mixture of 20%CO-49%H_2-5%CO_2-25%H_2O-1%CH_4 are 0.6 and 1.4×10^{-23} atm, respectively (point 'A' shown in

Fig. 5-7) at 650°C under the total gas pressure of 1atm. This atmosphere is fairly moderate against carburization for alloys, and metal dusting has not occurred. With higher gas pressure, however, both of a_c and Po_2 increase along the arrows shown in this diagram. The carbon activity exceeds unity under the gas pressure of 1.7 atm, and attains extremely high value, a_c^1 =18, when the gas pressure is 30 atm. Under this gas environment, metal dusting has occurred on an alloy surface severely and shortened its service duration.

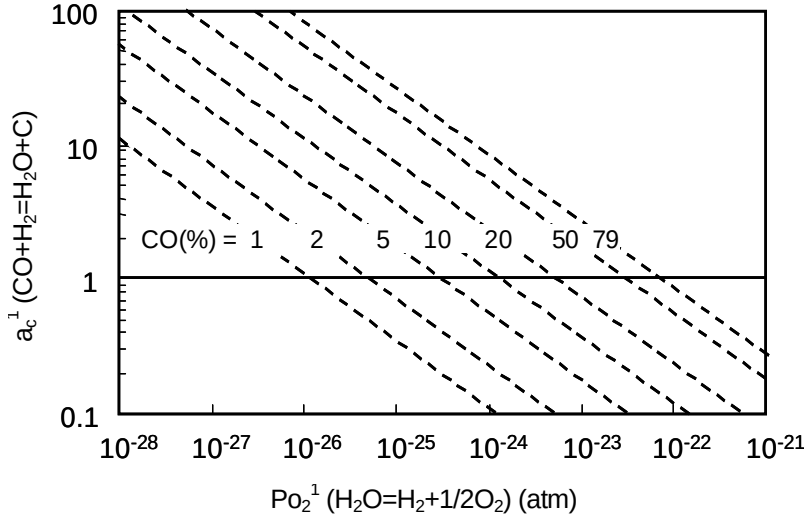

Figure 5-6 Contour lines of CO content in the gas mixture as a function of the a_c^1 and Po_2^1 under the total gas pressure of 1atm at 650°C.

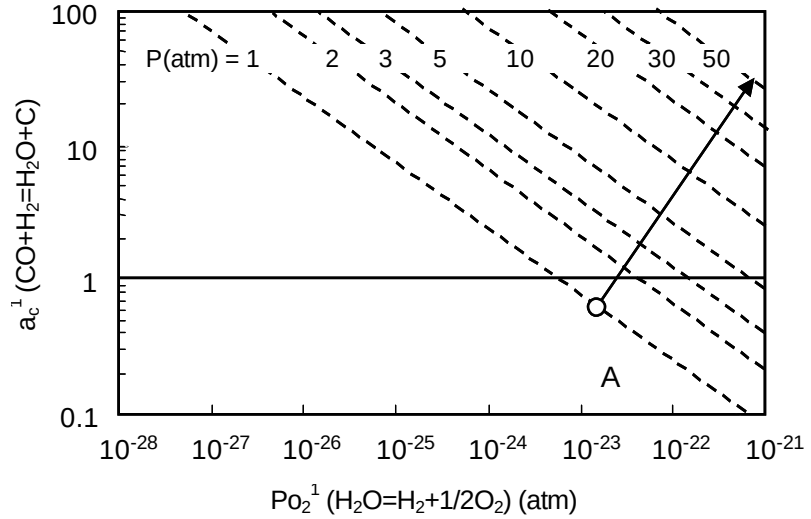

Figure 5-7 Contour lines of total gas pressure as a function of the a_c^1 and Po_2^1 in the gas mixture with equivalent 20%CO at 650°C. For instance, the activities of point 'A' with a 20%CO-49%H_2-5%CO_2-25%H_2O-1%CH_4 gas mixture increase with increasing total gas pressure along the arrow in this diagram.

5.3 Experimental

Two commercial Ni-base alloys of UNS N06600 (alloy 600, 75%Ni-15%Cr, mass%) and N06690 (alloy 690, 60%Ni-30%Cr) were tested. Coupon specimens of 3 × 15 × 30 mm were cut from solution heat-treated plate. Specimen surface was mechanically ground to 600-grit emery paper, followed by ultrasonic cleaning in acetone. Metal dusting tests were conducted in a horizontal reaction chamber, with 90 mm inside diameter and a uniform-temperature zone of 250 mm length, which has a double-walled structure, an inner quartz tube and an outer Ni-base alloy vessel, illustrated in Fig. 5-8. The specimens were exposed to gas mixtures at a flow rate of 300 sccm (standard cubic centimeters per minute) at 650°C. Test gases, presented in Table 5-1, were mixtures of CO, CO_2, H_2O, and H_2 under 1atm. Water vapor was added by bubbling the test gas in purified water. The dew point of the gas mixture was controlled by heating.

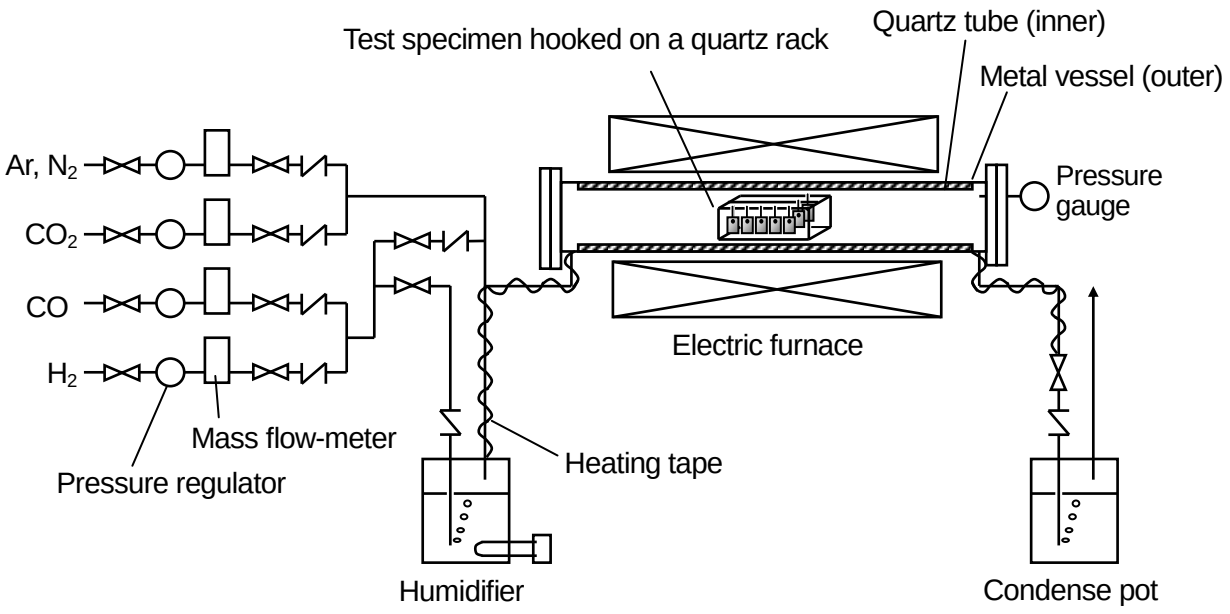

Figure 5-8 Schematic metal dusting test furnace design.

Carbon activity a_c[1] by CO /H_2 /H_2O and the oxygen potential Po_2[1] by H_2O /H_2 of the test gas mixtures are presented in Table 5-5. The test gas conditions were chosen so that the a_c and Po_2 scatter extensively in Fig. 5-6. Each specimen was suspended on a quartz rack through a Pt hook and then set in the reaction chamber, allowing gas flow parallel to specimen surfaces. The reaction chamber was first purged with a N_2-5%H_2 gas mixture for an hour at room temperature. After complete replacement of the purged gas with the test gas mixture, the specimens were heated at 650°C for 200h.

Table 5-5 Calculated chemical potential, CO /CO_2, and H_2O /H_2 ratio of the laboratory corrosion test listed in Table 5-1 at 650°C

Gas no.	a_c[1]	Po_2[1] (atm)	CO /CO_2	H_2O /H_2
1	0.5	1.3×10^{-24}	63	0.16
4	10	3.2×10^{-27}	1	0.01
5	0.2	8.0×10^{-26}	627	0.04
8	10	1.3×10^{-26}	31	0.02
9	10	4.6×10^{-25}	5	0.09
10	60	3.6×10^{-28}	31	<0.01
12	60	1.3×10^{-26}	5	0.02
13	2	1.3×10^{-26}	157	0.02

To evaluate the metal dusting resistance of the alloys, mass change of the specimen and amount of coke deposited were measured. Specimens were weighed after removing the coke. Metallographic cross section of the specimen was investigated using an optical microscope and a scanning electron microscope (SEM). Precipitates formed at the carburization zone of the alloy surface were investigated using a transmission electron microscope (TEM) with EDS to identify the type of carbides. Samples for TEM analysis were prepared by replica of the cross-sectional specimens. Concentration of some alloying elements near the surface of the alloy was measured by high frequency glow discharge spectrometry (GDS). The GDS spectrometer can provide a concentration depth profile of alloying elements in an area of the specimen surface, the diameter of which is approximately 4 mm. Sputtering the metal surface was conducted in an inert gas at a high rate.

5.4 Results

5.4.1 Mass Change of Test Alloys

Mass change due to corrosion of alloys 600 and 690 reacted with CO-H_2-CO_2-H_2O gas mixtures at 650°C for 200h is shown in Fig. 5-9. Mass gain was observed for specimens of alloy 600 for most test conditions (gases nos.1, 4, 5, 8, 10, and 13) presumably owing to the formation of oxide scale. For gases nos. 9 (60%CO-2.5%H_2O) and 12 (60%CO-0.5%H_2O), alloy 600 lost their mass considerably. Mass loss of alloy 600 reacted with gas no. 12 (low Po_2 -high a_c) was greater than that with gas no. 9 (high Po_2 -low a_c). The mode of corrosion for these specimens was considered metal dusting, explained later in this paper. For gases nos. 9 and 12, mass loss of alloy 600 was attributed to the formation of small pits and /or grooves. On the other hand, alloy 690 did not lose their mass for all the test gas conditions. Resistance to metal dusting of alloy 690 was significantly better than that of alloy 600 for the test conditions, suggesting that Cr is an important alloying element to combat metal dusting.

It is interesting to note that coupon specimens of alloy 600 after exposure to gases nos. 4, 8, and 10 (i.e., CO contents of not greater than 10%, see Table 5-1) did not lose their mass. Although gases nos. 4 and 8 had the same carbon activity (a_c^1=10) as gas no. 9, alloy 600 lost its mass for only gases no. 9. This was the same for the specimens reacted with gases nos. 10 and 12. Despite that gas no. 10 had the same carbon activity (a_c^1=60) as gas no. 12, metal dusting occurred for only gas no. 12. This might be attributed to the different CO contents of the gas mixtures. Gases of nos. 9 and 12, where metal dusting occurred for alloy 600, contained CO of 60%. For gases of less than 10%CO, metal dusting did not take place. Therefore, it is suggested that metal dusting susceptibility of high Ni alloys increases for gas atmospheres of high carbon activity and high CO content. This regime corresponds to the upper-right area of Fig. 5-9.

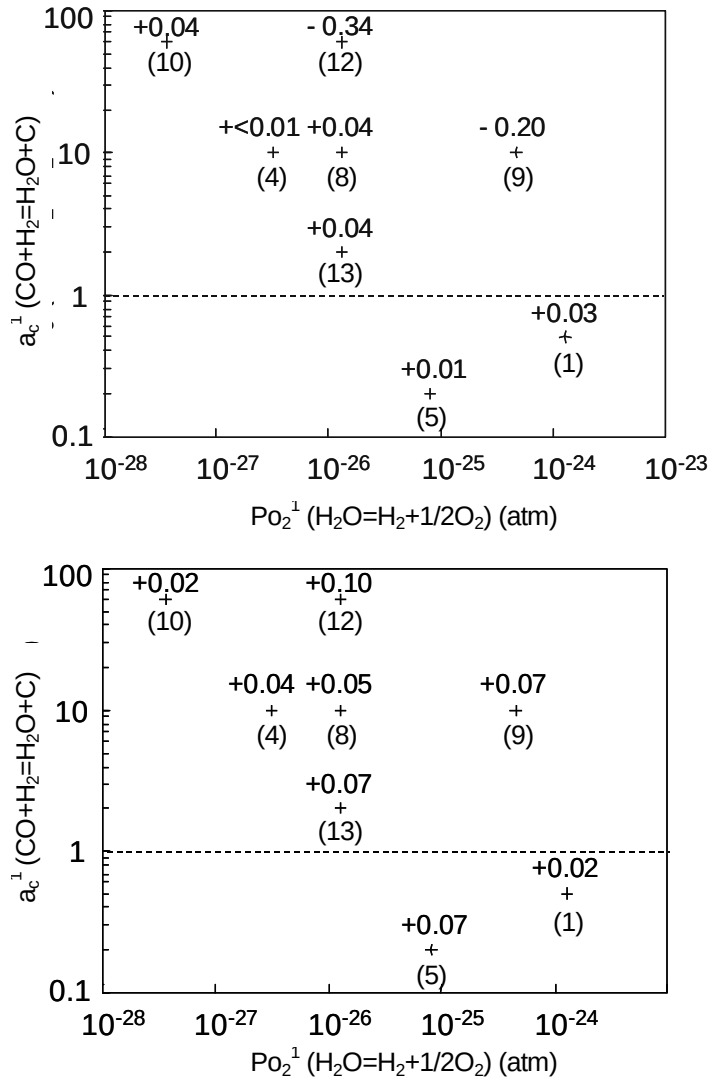

Figure 5-9 Mass change in mg/cm^2 due to corrosion of alloys 600 (top graph) and 690 (bottom graph) reacted with CO-H_2-CO_2-H_2O gas mixtures at 650°C for 200h. Coke was removed before the measurement. Figure in parenthesis denotes the test gas no. listed in Table 5-1.

Gas mixtures such as nos. 1, 5, and 13 have high CO /CO_2 ratio, as shown in Table 5-5. According to the corrosion map by Parks and Schillmoller, these gases are considered to cause severe metal dusting. However, in this study, mass loss was not evident for alloy 600 reacted with these gases, suggesting that the corrosion map is not always applicable to metal dusting corrosion at least for these Ni-base alloys.

The amounts of coke deposited on coupon specimens exposed to CO-H_2-CO_2-H_2O gas mixtures at 650°C for 200h are presented in Fig. 5-10. Coke deposition was prominent for gases nos. 9 and 12, where a considerable mass loss took place. Especially, heavy coke-deposition occurred on alloy 600 for gas no. 12, accompanying its mass loss. For alloy 690 exposed to gas no. 12, coke deposition was observed similar to alloy 600, but the amount of coke was less than that for alloy 600, and mass loss was not evident for the specimen.

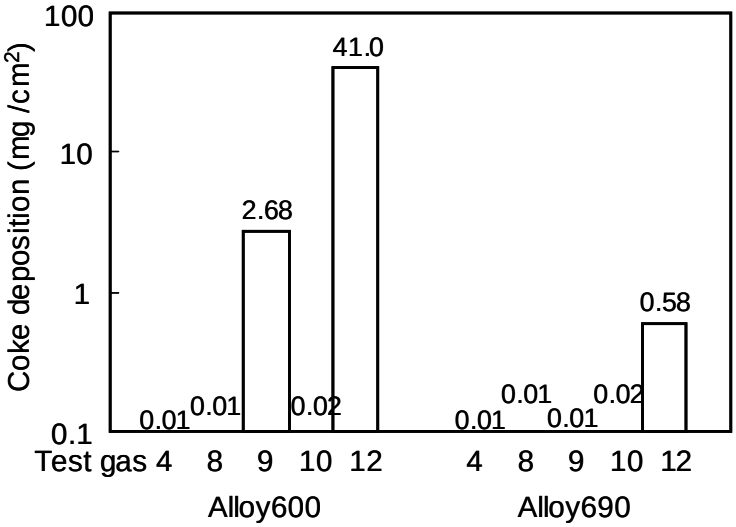

Figure 5-10 Coke deposition on the specimen surface after the corrosion test. Alloys 600 and 690 were heated in CO-H_2-CO_2-H_2O gas mixtures at 650°C for 200h.

5.4.2 Microscopic Observations of Pits

Cross section of alloy 600 after exposure to 60%CO-26.1%H_2-11.5%CO_2-2.5%H_2O (gas no. 9) at 650°C for 200h is shown in Fig. 5-11. A number of pits, approximately 10 μm deep, were found on the specimen surface. Underneath the pits, carburization zones of about 30-40 μm thickness are evident, whereas any carburization zone cannot be observed at areas where no pits form. On the contrary, as shown in Fig. 5-12, alloy 690 has neither pits nor carburization zone at its surface after exposure to 60%CO-26.1%H_2-11.5%CO_2-2.5%H_2O at 650°C for 200h. For alloy 690, no carburization was identified in each condition of the test gas mixtures.

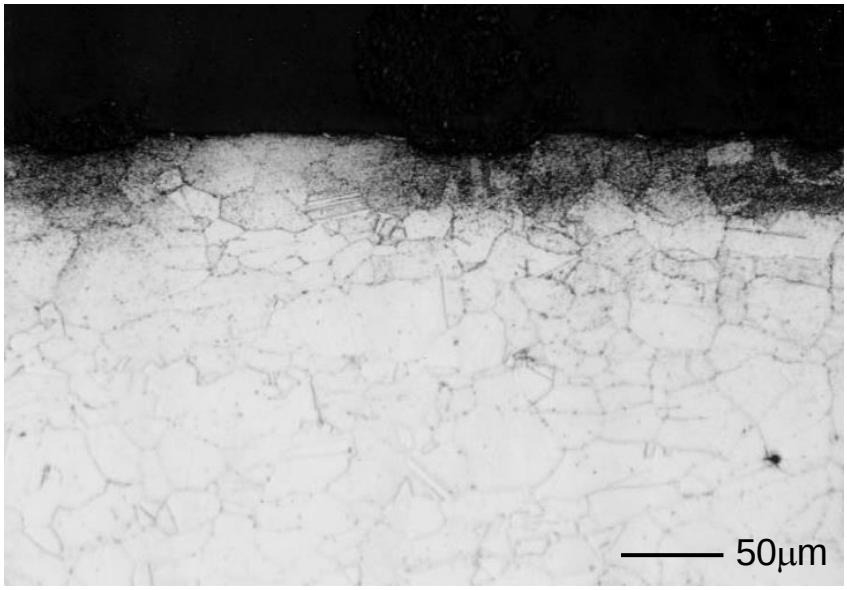

Figure 5-11 Cross section of alloy 600 after exposure to a 60%CO-26.1%H_2 -11.5%CO_2-2.5%H_2O gas mixture (gas no. 9) at 650°C for 200h.

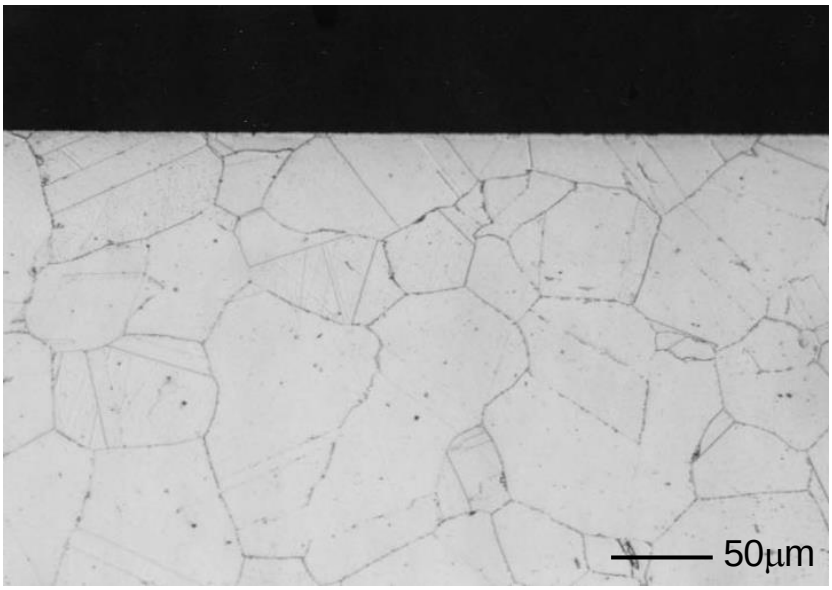

Figure 5-12 Cross section of alloy 690 after exposure to a 60%CO -26.1%H_2 -11.5%CO_2-2.5%H_2O gas mixture (gas no. 9) at 650°C for 200h.

Cross sections of this alloy 600 were examined by SEM and shown in Fig. 5-13. As shown in the top of this figure, an oxide scale of sub-micron thickness formed uniformly on the surface of the specimen. This oxide scale was identified as Cr_2O_3 by XRD and EPMA. At sites where pits and grooves are located, the Cr_2O_3 scale was no longer present and coke stuffed these sites instead of the oxide scale. These coke contained metal particles (bright particles in the coke in Fig. 5-13). This aspect implies that the pits have generated at sites where the protective oxide scale has incurred any damages such as cracks, flaws, and spalling. At the pit bottom (bottom Fig. 5-13), platelet precipitates were observed. They aligned perpendicular to the pit bottom surface, independent to grain boundaries of the matrix.

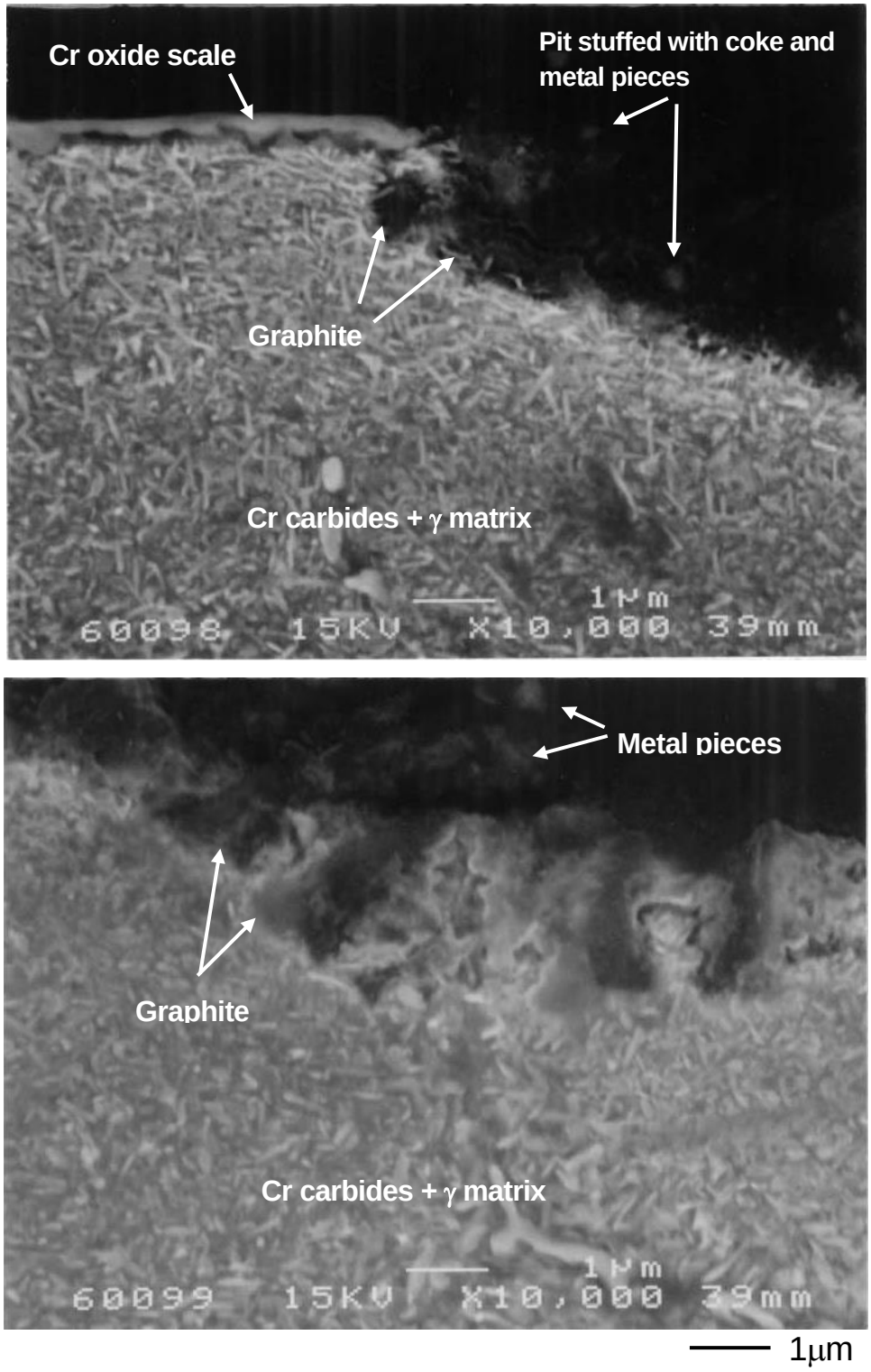

Figure 5-13 SEM of a pit edge (top photo.) and bottom (bottom photo.) resulting from metal dusting of alloy 600 after exposure to a 60%CO-26.1%H_2-11.5%CO_2-2.5%H_2O gas mixture (gas no. 9) at 650°C for 200h.

These platelets were identified as graphite by transmission electron microscopy upon observing a blank-replicated cross section of the test specimen as shown in Fig. 5-14 (c) and (c'). In the matrix near the pits very fine "needle-like" intragranular precipitates were found, identified mainly as Cr_7C_3 carbide by transmission electron microscopy (Fig. 5-14 (d) and (d')). Along grain boundaries of the matrix, precipitates of $Cr_{23}C_6$ were also observed. Since the formation of graphite in the carburization zone and metal particles in the coke was indicated, the corrosion damage of this alloy 600 was interpreted as metal dusting. For this specimen, metal dusting accompanied pit formation.

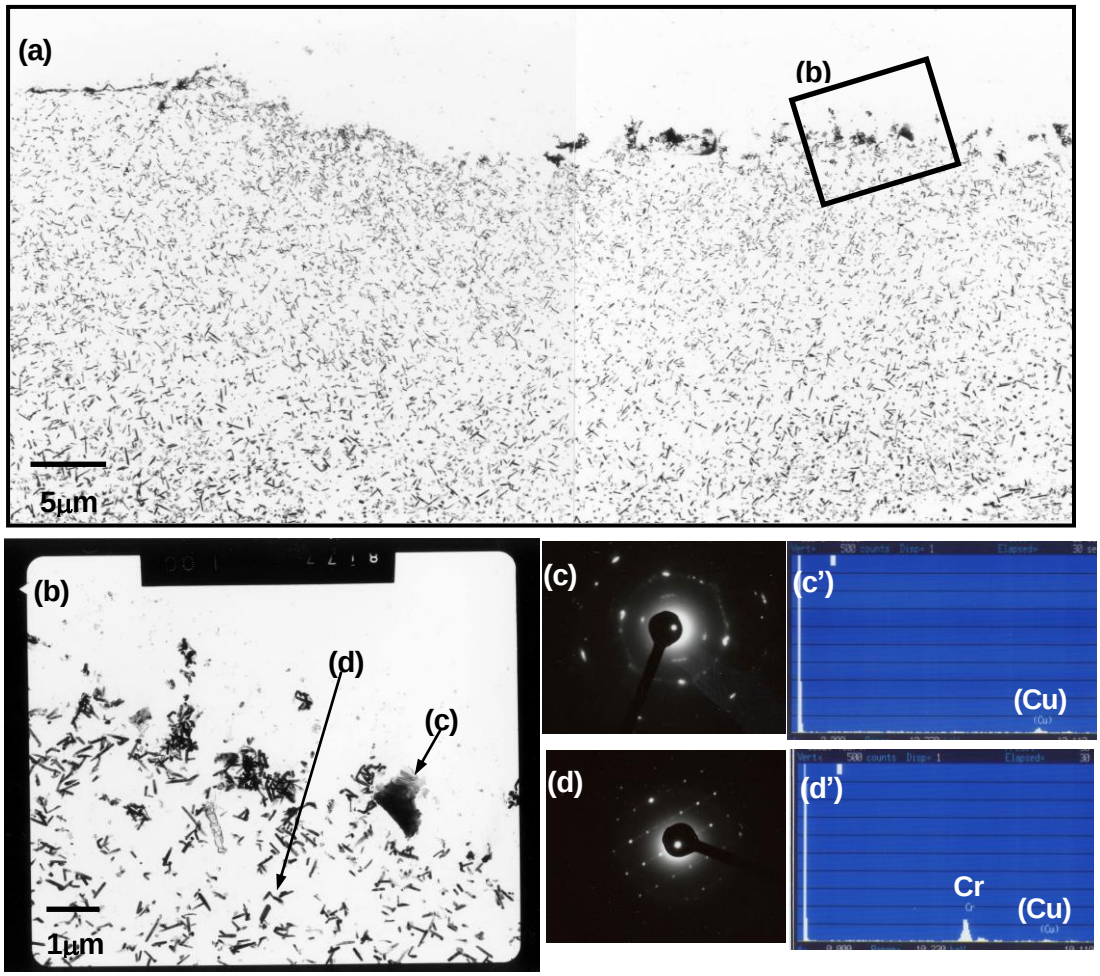

Figure 5-14 TEM of replicated alloy 600 surface after exposure in the gas mixture of no. 9 at 650°C for 200h. (a) Cross section of the pit on the surface. (b) Magnification of the photo (a). (c) Dark field image of the fragment graphite and (c') EDS analysis. (d) Dark field image of the needle-like carbide and (d') EDS analysis.

Cross section of alloy 600 after exposure to 60%CO-28.1%H_2-11.5%CO_2-0.5%H_2O (gas no. 12) at 650°C for 200h is shown in Fig. 5-15. A relatively uniform carburization zone of about 30-40 μm thickness was observed under the coke layer on the specimen surface. Formation of pits on the specimen surface was not obvious. SEM micrograph of a cross section of this alloy is shown in Fig. 5-16. Thick plates of graphite aligned perpendicular to the surface. This morphology was similar to the "lamellar" microstructure found in Fe-C steels. Similar to the alloy 600 reacted with gas no. 9, graphite formation in the carburization zone and metal particles in the coke layer were noticed, suggesting that the mode of attack for this specimen was considered metal dusting. In this case, metal dusting occurs on almost the whole specimen surface. Apparently, metal dusting observed for alloy 600 by gas no. 12 was harsher than that by the gas no. 9 because the a_c of the former gas was considerably higher and oxygen potential lower than that of the latter, although both gases contained the same amount of CO of 60%. For gas no. 12, thus, Cr_2O_3 scale might have lost its protection due to the decreased oxygen potential of the carburizing gas.

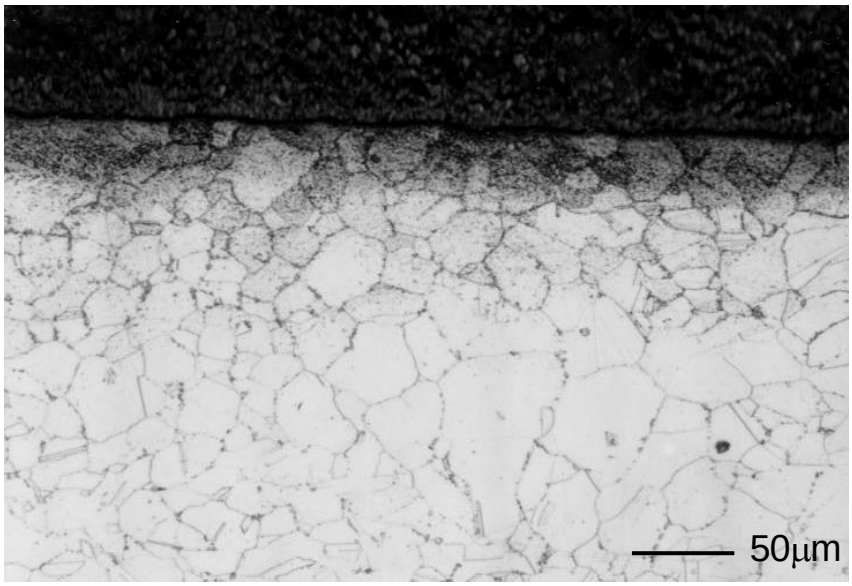

Figure 5-15 Cross section of alloy 600 surface after exposure to a 60%CO -28.1%H_2-11.5%CO_2 -0.5%H_2O gas mixture (gas no. 12) at 650°C for 200h.

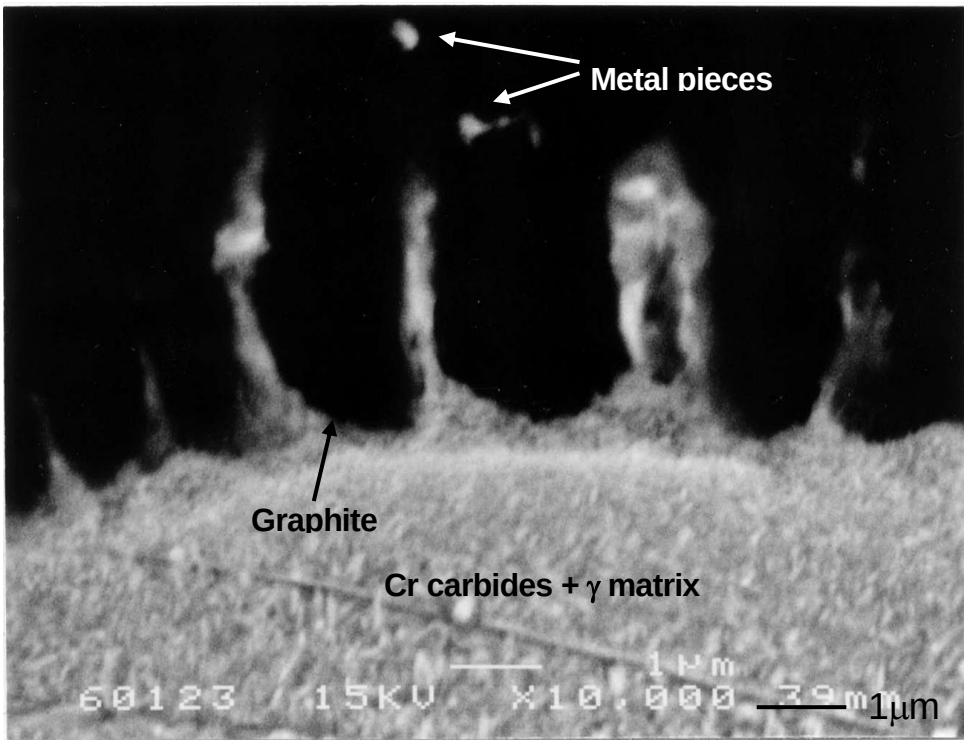

Figure 5-16 SEM of metal dusting of alloy 600 after exposure in a 60%CO-28.1%H_2 -11.5%CO_2-0.5%H_2O gas mixture (gas no. 12) at 650°C for 200h.

5.4.3 Inward Carbon Profile at Pit

Depth profiles of the alloying elements at the carburized zone of alloy 600 exposed to gas no. 12 (see Fig. 5-16) measured by GDS are shown in Fig. 5-17. Concentrations of Cr, Fe, and Ni remained unchanged throughout the carburized zone, but carbon increase was significant at the carburized zone of 40 μm thickness. The thickness of the carbon-enriched zone analyzed corresponded well to the carburization zone observed in Fig. 5-15. From Fig. 5-17, carbon content of 1.8-1.9 mass% was indicated underneath the graphite platelets precipitated, which was located 2-5 μm deeper than that for the specimen surface. In this area, graphite, carbide, and γ matrix must be in local equilibrium. A phase stability diagram of the C-Fe-60mass%Ni-Cr system was constructed at 650°C by thermodynamic calculation [27], and are shown in Fig. 5-18. According to the diagram, graphite precipitation is probable for 60%Ni-15%Cr alloy when the carbon content of the carburized zone exceeds 2.1%. This

critical carbon concentration for enabling graphite precipitation for 60%Ni-15%Cr alloy agreed relatively well with the carbon content measured by GDS. The carbon content was saturated at the carburized zone underneath the graphite precipitates observed for alloy 600 reacted with gas no. 12.

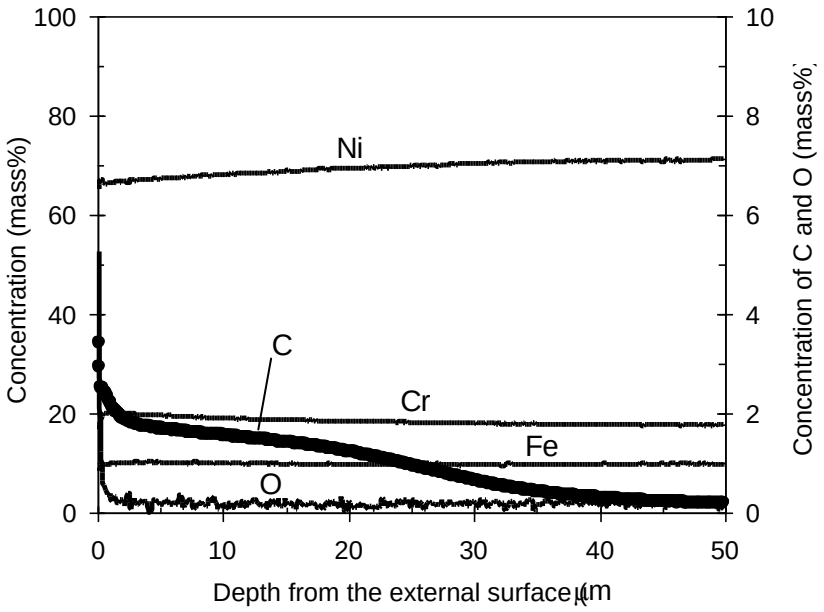

Figure 5-17 GDS depth profiles of some alloying elements near the external surface of alloy 600 after exposure in the gas mixture of test gases no. 12 at 650°C for 200h.

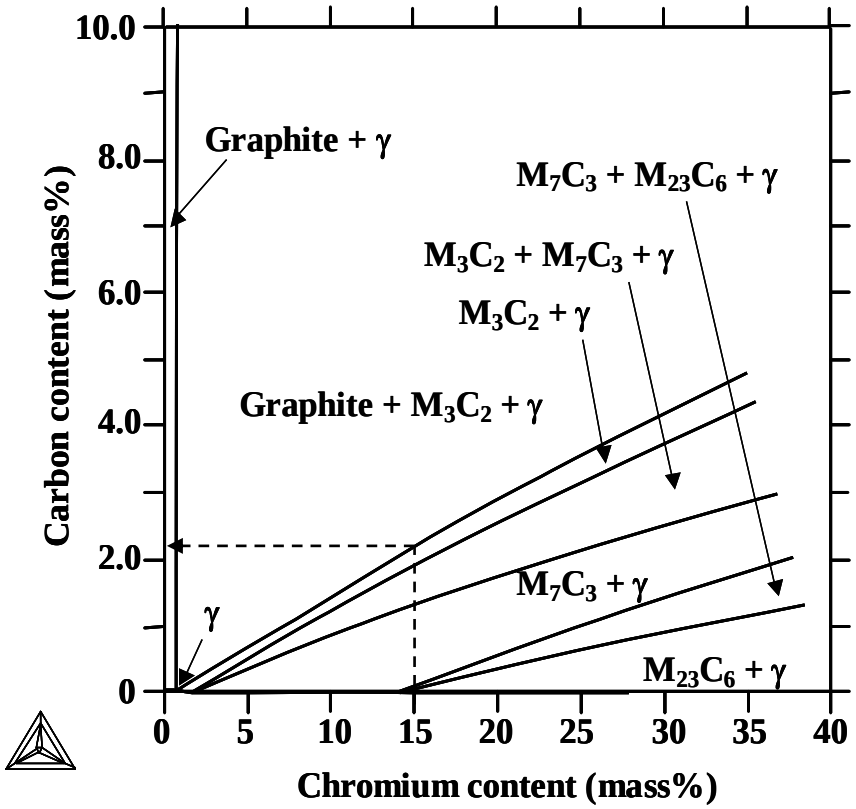

Figure 5-18
Phase stability diagram of the C-Fe-60mass%Ni-Cr system at 650°C by thermodynamic calculations.

5.5 Discussion

For alloy 600 experienced mass loss, graphite platelets were aligned in a "lamellar" structure along the fresh metal surface due to spalling of the oxide scale. In addition, metal particles were found in the coke layer, which were presumably detached from the "lamellar" metal (plus carbide) matrix via lateral growth of the graphite platelets. The cementite of Fe_3C that forms on the metal surface in the carbonaceous environments acts as a significant role for metal dusting attack on iron and low alloys, which has been proposed by Grabke [7 - 9]. The main reason is that the Fe_3C is metastable throughout the range of the metal dusting temperature; the free energy of formation for Fe_3C takes +2.4 kJ/mol at 650°C of which value is close to zero. For high Ni alloys, however, the situation would differ. The free energy of formation for Ni_3C takes +55.8kJ/mol at the same temperature, which is considerably high to form the carbide in the alloys. In this manner, graphite platelets occurring on the high Ni-alloy 600 may not attribute to decomposition of the Ni_3C as well as the Fe_3C.

Pippel et al. [28] have micro-analyzed at the surface of pure Fe, Ni, Fe-base alloy, and Ni-base alloy occurred metal dusting, which have indicated the possibility of the direct precipitation of graphite. Chun et al. [29, 30] have also analyzed the graphite formation for pure Ni by transmission electron microscopy and found that the perpendicular graphite might form directly without the intermediate step of a carbide formation. The discussion will focus on the metallurgical possibility of the direct precipitation of graphite. Figure 5-19 shows that the phase stability diagram of C-Fe-Ni-Cr system where region of γ phase is expanded intentionally. It represents that the carbon content in the alloy increases according to a line A-B-C due to continuous charging of carbon from the gas atmosphere. Corresponding soluble carbon content in the γ matrix increases along a line A'-B'-C'. When the carbon content in the alloy reaches the point C, i.e. the phase boundary of (γ+Cr carbides) / (γ+graphite+Cr carbides), the soluble carbon content in the γ matrix is located at the point C'. Reaction associated with direct graphite precipitation would be considered to be Eq. (10) as below:

$$\gamma + \text{Cr carbides} \rightarrow \gamma + \text{graphite} + \text{Cr carbides} \qquad (10)$$

Under the reaction of Eq. (10), graphite should precipitate at boundary of Cr carbides /γ matrix where the Gibbs free energy for nucleation is minimal. However, the prospective morphology differs from the

result what platelet graphite precisely precipitates with a lamellar structure aligned only at the exposed metal surface as shown in Figs. 5-13 and 5-16. In terms of the morphology observed, a eutectoid reaction should be considered to form the lamellar structure. The eutectoid reaction describes the phase transformation of one solid into two different solids both with compositions which differ from the original. In the Fe-C system, γ phase changes into α phase and Fe_3C during cooling through the eutectoid temperature. This pearlite transformation involves microstructure of lamella which is grown from nuclei plates of α phase and Fe_3C form at the grain boundary of the γ phase.

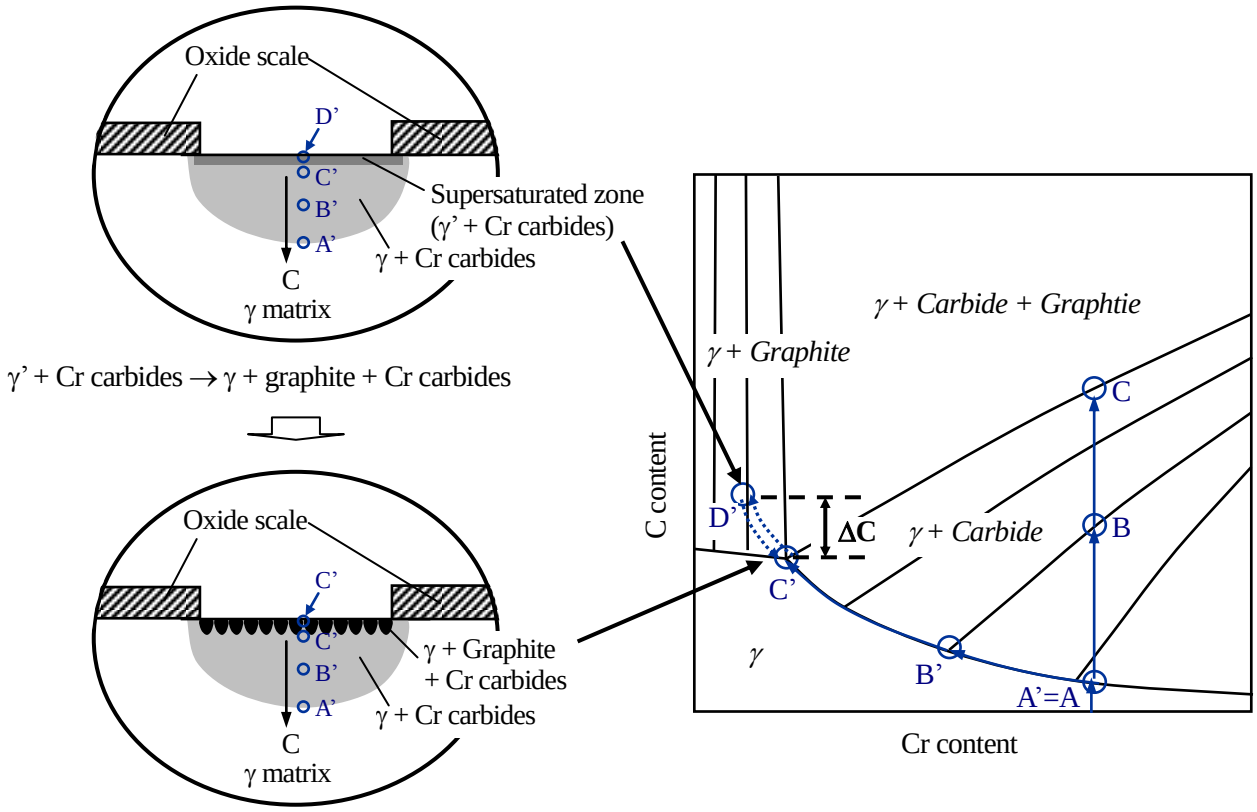

Figure 5-19 Schematic model for direct precipitation of graphite platelets for Ni-base alloys, based on metallurgical consideration. Right diagram presents the phase stability of the C-Fe-Ni-Cr system.

As shown in Fig. 5-19, carbon content reaches the point C' in the γ matrix when it reaches the point C in the alloy. In carbonaceous gas environments with high a_c, carbon may charge incessantly into the alloy through the spalling of oxide scale. It allows the carbon to be supersaturated in the γ matrix of local areas beneath the exposed metal surface (corresponding to the point D'). This supersaturated γ matrix (γ') would differ from the original γ matrix. Since the γ' is in nonequilibrium status, further charging of carbon from the gaseous atmosphere can decompose it to the γ and graphite by a eutectoid reaction of Eq. (11) as below:

$$\gamma' + \text{Cr carbides} \rightarrow \gamma + \text{graphite} + \text{Cr carbides} \quad (11)$$

Under the reaction of Eq. (11), platelet graphite can form with a lamellar structure. After the reaction, the soluble carbon content in the γ matrix fall away to point C' in equilibrium. The length of the lamella depends on the supersaturated carbon content (ΔC) which is the difference between point D' and point C' as shown in Fig. 5-19. Therefore, the length of the lamella takes longer aligned perpendicular to the surface, as the a_c becomes stronger in carbonaceous gas environments.

The present study has demonstrated that the high-Cr alloy 690 had much larger resistance than the low-Cr alloy 600. This may be interpreted by the different morphology of Cr_2O_3 scale formed on the metal surface. Apparently, a dense and defect-free Cr_2O_3 scale protects the base metal from inward diffusion of carbon (this was the case for alloy 690), but if unprotective oxide scales are formed on the specimen surface, cracks and flaws can easily be introduced in the scale (e.g. for alloy 600). Based on the above analyses, the initiation and growth of the pit-like metal dusting attack on the Ni-base alloys is illustrated in Fig. 5-20. At the initial stage, Cr diffusing into the γ matrix reacts with oxygen of gas atmosphere on the metal surface. Once a Cr_2O_3 scale formed on the metal surface, it provides protection against the metal dusting attack. Thus, incubation time when none of pits (metal dusting attack) are generated on the metal has maintained for some period. When any damages such as cracks, flaws, and spalling have occurred in the oxide scale, a healing oxide scale could resist against metal dusting attack. If not possible, however, carbonaceous gas mixture inexorably adsorbs on the revealed metal surface through them and decomposes to the absorbed carbon (C*) and oxygen (O*). This is the initiation of metal dusting. The decomposed carbon (C*) continuously penetrates into the metal (C as a solute carbon), enabling the formation of Cr carbides. The continuous charging of carbon can eventually

supersaturate the carbon content in the γ matrix equilibrated with Cr carbides at the boundary of the gas /metal, resulting in direct precipitation of graphite platelets by the eutectoid reaction. Increasing the volume fraction of the graphite decreases that of the corresponding γ matrix because the three phases (graphite /Cr carbides /γ matrix) equilibrate thermodynamically and each volume fraction is determined by the lever law. Therefore, the lateral growth of the graphite platelets led to thinning and detachment of γ matrix (consist mainly of Fe and Ni) from the metal lamella, which catalyzed deposition of carbon and accelerated carburization for the alloy (i.e. growth of a pit-like metal dusting).

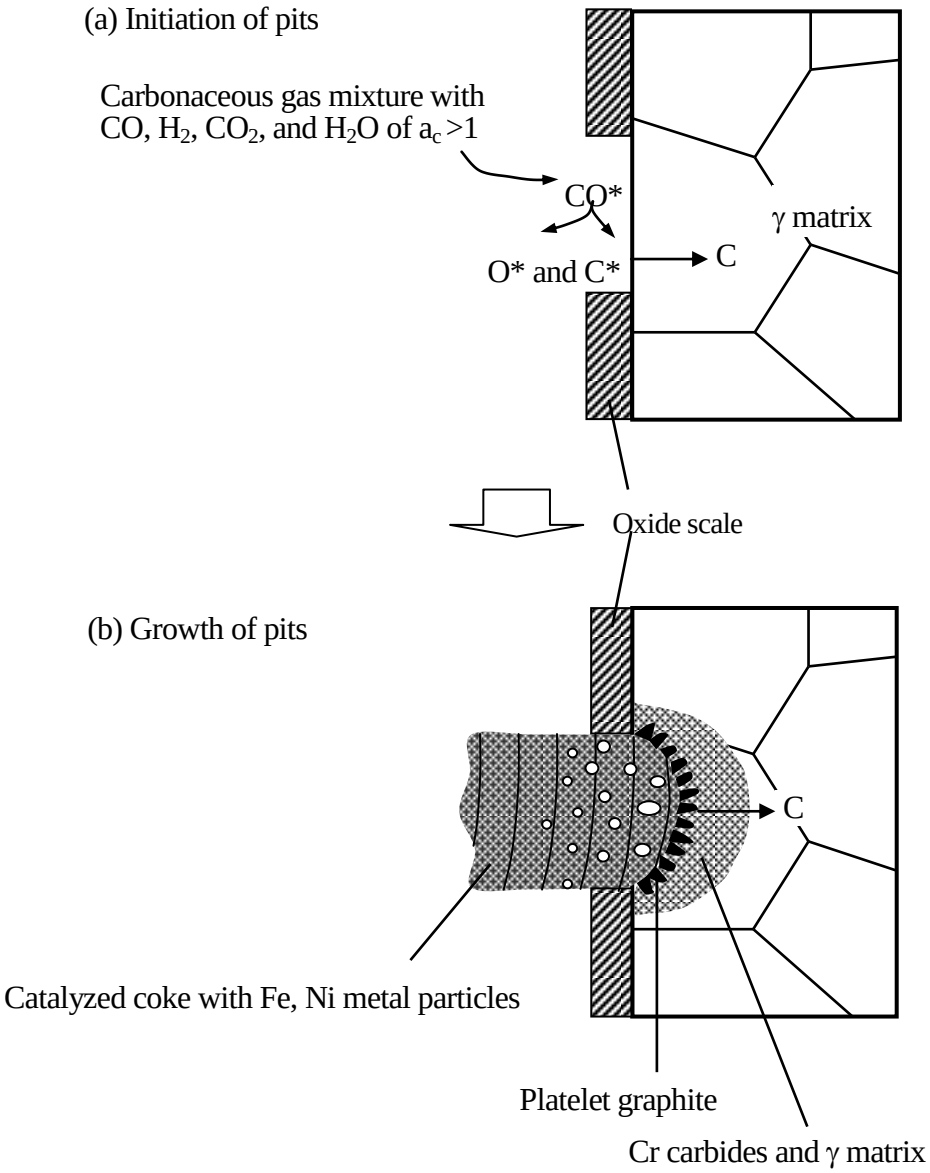

Figure 5-20 Schematic initiation /growth of a pit-like metal dusting on Ni-base alloys. (a) CO in the gas phase adsorbs at the metal surface through cracks /flaws of the oxide scale and decomposes to carbon (C*) and oxygen (O*). (b) The decomposed carbon, which diffuses into the metal (C as dissolved), is combined with Cr as Cr_7C_3 and $Cr_{23}C_6$, following 'direct' precipitation of platelet graphite along the metal surface by the eutectoid reaction of Eq. (11). The platelet graphite make the γ matrix lathy in equilibrium with the γ matrix and the Cr carbides, resulting in its dissociation from base metal (metal loss). The dissociated metal particles such as Ni and mainly Fe catalyze coke formation.

5.6 Conclusions

Thermodynamic aspects for CO, H_2, CO_2, and H_2O gas mixtures to understand the metal dusting environments of syngas reforming plants in the refinery industries were calculated and considered. Based on this information, the gas composition for laboratory carburization tests was decided, and tests were conducted to evaluate the carburization resistance of Ni-base alloys, alloy 600(75%Ni-15%Cr) and alloy 690 (60%Ni-30%Cr). The conclusions obtained are summarized as follows:

(1) Carbon deposition on the metal surface from the gas mixture is well represented by the activity of carbon a_c[1] determined from the equilibrium reaction of $CO+H_2=H_2O+C$. For gas mixtures of high CO content, the Boudouard reaction, $2CO=CO_2+C$, should be also considered. The oxygen potential Po_2[1] of the gas mixture, which affects the chemistry and thickness of the protective oxide scale, is given primarily from the dissociation reaction of H_2O ($H_2O=H_2+1/2O_2$) at temperatures below 850°C. The a_c[1] of syngas mixtures in some practical reforming plants evaluated by the suggested reactions is approximately 2 to 30 whereas the Po_2[1] is in the order of 10^{-23}-10^{-22} atm at 650°C.

(2) Preliminary laboratory corrosion tests of two Ni-base alloys were conducted at 650°C for 200h in various CO-H_2-CO_2-H_2O gas mixtures. In gas mixtures of high a_c and CO content, specimens of alloy 600 containing 15%Cr lost its mass due to metal dusting, and coke was deposited on the specimen surface. For alloy 690 containing 30%Cr, metal dusting did not occur.

(3) Microscopic observation indicated that for the corroded specimens, inward diffusion of carbon presumably through cracks and flaws in the oxide scale was prominent. Carbon in the diffusion zone combined with Cr to form carbides in the γ matrix. As a continuous charging of carbon into the metal, carbon became supersaturated in the γ matrix equilibrated with Cr carbides at the boundary of the gas /metal. In this manner, platelet graphite can precipitate with the lamellar structure aligned perpendicular to the surface by the eutectoid reaction. This structure resembled the pearlite that was transformed from the γ phase observed during cooling process in the Fe-C system.

(4) The metal lamella thinned with the lateral growth of graphite plates in equilibrium with the γ matrix and Cr carbides, and small metal particles of Ni and Fe were crumbled and detached from the metal lamella, which may catalyze the coke deposition reaction.

References

[1] F.A. Prange, Corrosion 15, 12 (1959), p.619t.

[2] F. Eberle and R.D. Wylie, Corrosion 15, 12 (1959), p.622t.

[3] W.B. Hoyt and R.H. Caughey, Corrosion 15, 12 (1959), p.627t.

[4] H.J. de Bruyn and M.L. Holland, "Materials experience in a methane reforming plant," CORROSION /98, paper no.429, (Houston, TX: NACE, 1999).

[5] R.F. Hochman and J.H. Burson. "The fundamentals of metal dusting," API Division of Refining Proc., 46 (1966), p.331.

[6] R.F. Hochman, "Basic studies of metal dusting deterioration ("metal dusting") in carbonaceous environments at elevated temperatures," Proc. of the 4th International Congress on Metallic Corrosion, NACE (1972), p.258.

[7] H.J. Grabke, R. Krajak, and E.M. Müller-Lorenz, Werkst. Korros. 44 (1993), p.89.

[8] J.C. Nava Paz and H.J. Grabke, Oxid. Met. 39, nos.5/6 (1993), p.437.

[9] H.J. Grabke, R. Krajak, and J.C. Nava Paz, Corros. Sci. 35, nos.5-8 (1993), p.1141.

[10] H.J. Grabke, C.B. Brancho-Troconis,and E.M. Müller-Lorenz, Mater. Corros. 45 (1994) p.215.

[11] M.L. Holland and H.J. de Bruyn, Int. J. Pres. Ves. and Piping 66 (1996), p.125.

[12] H. Stahl and S.G. Thomsen, Ammonia Plant Safety and Related Facilities, Ammonia Technical Manual 36 (1996), p.180.

[13] T. Shibasaki, K. Takemura et al., Ammonia Plant Safety and Related Facilities, Ammonia Technical Manual 36 (1996), p.165.

[14] K.L. Baumert and J.J. Hoffman, "Materials Experience in Methanol Reforming Units," CORROSION /97, paper no.493, (Houston, TX: NACE, 1997).

[15] M.H. Ravestein, "Metal Dusting in Catalytic Reforming Furnace Tubes," CORROSION /97, paper no.496, (Houston, TX: NACE, 1997).

[16] J. Klöwer, H.J. Grabke et al., "Metal Dusting and Carburization Resistance of Nickel-Base Alloys," CORROSION /97, paper no.139, (Houston, TX: NACE, 1997).

[17] H.J. Grabke, R. Krajak et al., Mater. Corros. 47 (1996), p.495.

[18] R. Shneider, E. Pippel et al., Steel Research 68 (1997), p.326.

[19] S.B. Parks and C.M. Schillmoller, Stainless Steel World 9 (1997), p.44.

[20] The NBS tables of chemical thermodynamic properties, selected values for inorganic and C1 and C2 organic substances in SI units, J. Phys. Chem. Ref. Data vol.2, Supplement no.2 (1982).

[21] R. Collin, S. Gunnarson, and D. Thulin, Journal of The Iron and Steel Institute 210 (1972), p.785.

[22] E.M. Müller-Lorenz and H.J. Grabke, Mater. Corros. 50 (1999), p.614.

[23] A.S. Fabiszewski, W.R. Watkins et al., "The Effect of Temperature and Gas Composition on the Metal Dusting Susceptibility of Various Alloys," CORROSION /2000, paper no.532, (Houston, TX: NACE, 2000).

[24] B.A. Baker, and G.D. Smith, "Alloy Selection for Environments Which Promote Metal Dusting," CORROSION /2000, paper no.257, (Houston, TX: NACE, 2000).

[25] D.L. Klarstrom, H.J. Grabke, and L.D. Paul., "The Metal Dusting Behavior of Several High Temperature Nickel Based Alloys," CORROSION /2001, paper no.1379, (Houston, TX: NACE, 2001).

[26] International Workshop on Metal Dusting, (Argonne, Illinois: September 2001).

[27] L. Hoglund, Thermo-Calc, Foundation of Computational Thermodynamics (Stockholm, Sweden: Royal Institute of Technology).

[28] E. Pippel, J.Woltersdorf, and R. Schneider, Mater. Corros. 49 (1998), p.309.

[29] C.M. Chun, T.A. Ramanarayanan, and J.D. Mumford, Mater. Corros. 50 (1999), p.634.

[30] C.M. Chun, J.D. Mumford, and T.A. Ramanarayanan, J. Electrochem. Soc., 147, 10 (2000), p.3680.

Chapter 6

METAL DUSTING BEHAVIOR OF CR-NI STEELS AND NI-BASE ALLOYS IN A SIMULATED GAS MIXTURE

6.1 Introduction

Metal dusting, a corrosion failure resulting from catastrophic carburization or graphitization of steels and alloys occurring in carbonaceous atmospheres, is a prominent corrosion damage for high temperature materials used in ammonia, methanol, and syngas plants [1 - 4]. Metal dusting is often encountered when steels and alloys are exposed at 450 - 700°C to CO-containing syngas environments where the carbon activity (a_c) is greater than unity, and the oxygen potential (Po_2) is relatively low. For carbon steels, Hochman [5, 6] proposed a corrosion mechanism in that the important step in metal dusting is the formation of unstable cementite (Fe_3C) as an intermediate followed by its decomposition. The detailed reaction steps for carbon steels and low alloy steels were demonstrated by Grabke and his coworkers [7 - 10]

However, for austenitic stainless steels and Ni-base alloys, the mechanism of metal dusting differs from the carbon steels and low alloy steels. As mentioned in chapter 5, characteristic morphology of the corrosion for these steels and alloys is the formation of pits on the metal surface, from which the coke grows in a form of whisker. The proposed reaction steps are as follows [11 - 17]:

a) formation of cracks and /or flaws in the protective Cr_2O_3 scale [11, 12], allowing carbon to diffuse into a base metal.
b) the dissolved carbon forms stable Cr carbides as $M_{23}C_6$ and M_7C_3.
c) upon continuous carbon charging into the metal, the matrix becomes to be supersaturated, resulting graphite to precipitate “directly” at gas/ metal surface, not through the intermediary of

any carbides [13 - 16]. This is interpreted that the supersaturated γ matrix (γ') decomposes to graphite and γ matrix at the surface by a eutectoid reaction as given below [17 (Chapter 5)]:

$$\gamma' + \text{Cr carbides} \rightarrow \gamma + \text{graphite} + \text{Cr carbides} \quad (1)$$

The metal matrix is destroyed by inward growth of graphite.

d) metal particles generated by the disintegration of the Fe-Ni matrix act as catalyst for further carbon deposition from the gas atmosphere.

Szakalos et al. have proposed another mechanism of metal dusting for stainless steels of relatively low nickel content based on the carbon and oxygen gradients obtained from thermodynamic considerations [18]. They emphasized the importance of direct oxidation of carbides by CO to leave metal particles, oxides, and carbon. In this reaction step, carbides are considered as an intermediate.

Studies evaluating commercial alloys have clarified the effects of alloying elements on the corrosion [11, 12, 19]. Alloys containing more than 25%Cr showed good resistance to metal dusting due to the formation of a protective Cr_2O_3 scale on the metal surface. Ferritic stainless steels are more resistant to metal dusting than austenitic stainless steels undo certain conditions. For austenitic stainless steels, addition of Ni generally suppresses the metal dusting primarily by decreasing the internal carburization rate. The critical minimum Ni content is reported 50% [19], and the favorable Fe / Ni ratio of the alloys is recommended to be 1/4 on the basis of carbon diffusivity and solubility [20, 21]. From the viewpoint of protective oxide-scale integrity, an empirical ranking indicator of resistance to carburization and metal dusting of steels and alloys in terms of alloying elements was proposed and used for the selection of conventional and newly developed alloys for application to the metal dusting environments [22, 23, 24].

The present study is to confirm the effect of Cr and Ni on the metal dusting resistance of austenitic stainless steels and Ni-base alloys. To accelerate the corrosion tests, cyclic heating-cooling test was conducted in addition to isothermal test to introduce failures in the protective oxide scale. Pit depth measurements were performed for the test specimens after different exposure time to focus on the growth kinetics of the hemispherical pit generated on the specimen surface. Pit growth rates were examined and compared with respect to the Cr and Ni contents of the steels and alloys. Furthermore, the

morphology of the pit surface where graphite platelets precipitate was observed for steels and alloys, which discussed on thermodynamic considerations.

6.2 Experimental

Fifteen Fe-Ni-Cr austenitic stainless steels and Ni-base alloys were tested. Their Cr and Ni contents were 15-30 and 20-75 respectively. Their chemical compositions are listed in Table 6-1. For experimental steels and alloys, ingots were made in a vacuum induction furnace. These were hot forged and hot rolled to plates of thickness 12mm. After annealing at 1150°C in air, these plates were cold rolled to a thickness 6mm and then subjected to solution heat treatment at 1180°C. Coupon specimens were cut from the sheets to 3 × 15 × 20 mm, and a small hole of 2 mm φ was drilled in them for support. Commercial steels and alloys of UNS nos. N06600, N 08810, N 06601, and N 06690, were also used. The specimen surface was mechanically ground to 600-grit emery paper, followed by ultrasonic cleaning in acetone.

Metal dusting tests were conducted in a horizontal reaction chamber, with 90 mm inside diameter and a uniform-temperature zone of 250 mm length, which has a double-walled structure, an inner quartz tube and an outer Ni-base alloy vessel, illustrated in Fig. 6-1. The reaction gas composition of 60%CO, 26%H_2, 11.5%CO_2, and 2.5%H_2O (in vol.%), which gives the carbon activity a_c[1] (given from Eq. (2) in chapter 5) of 10 and oxygen partial pressure Po_2[1] of 4.6×10^{-25} atm (given from Eq. (8) in chapter 5) at 650°C at equilibrium, was chosen to simulate the actual reforming plants as described in chapter 5. Water vapor was added by bubbling the test gas in purified water. The dew point of the gas mixture was controlled by heating of water. The specimens were exposed to the gas mixture at a flow rate of 300 sccm (standard cubic centimeters per minute) at a temperature of 650°C under a pressure of 1 atm. The gas velocity was calculated to be 1.6 mm /s at the specimen. Each specimen was suspended on a quartz rack through a Pt hook and then set in the reaction chamber, allowing gas flow parallel to the specimen surfaces. The reaction chamber was first purged with a N_2-5%H_2 gas mixture for an hour at room temperature. After complete replacement of the purge gas with the test gas mixture, the specimens were heated at 650°C.

Table 6-1 Chemical compositions of the test alloys (mass%)

Alloy (UNS no.)	C	Si	Mn	P	S	Cr	Ni	Other
15Cr20Ni	0.02	0.29	0.20	0.020	0.0008	15.0	19.9	-
15Cr40Ni	0.02	0.30	0.20	0.019	0.0009	14.8	40.0	-
15Cr60Ni	0.02	0.31	0.20	0.019	0.0009	14.9	59.3	-
15Cr75Ni (N 06600)	0.03	0.30	0.28	0.013	0.0010	15.3	75.0	-
20Cr20Ni	0.02	0.30	0.20	0.021	0.0010	20.0	20.0	-
20Cr30Ni (N 08810)	0.09	0.33	0.95	0.012	<0.001	19.9	31.0	0.5Ti, 0.5Al
20Cr40Ni	0.02	0.30	0.19	0.019	0.0009	19.8	40.0	-
20Cr60Ni	0.02	0.30	0.19	0.019	0.0009	19.9	60.1	-
23Cr60Ni (N 06601)	0.02	0.26	0.20	0.020	0.0010	23.0	60.0	1.4Al
25Cr20Ni (S 31000)	0.02	0.30	0.19	0.020	0.0010	24.9	19.8	-
25Cr40Ni	0.02	0.30	0.19	0.020	0.0008	24.5	40.0	-
25Cr50Ni	0.02	0.31	0.21	0.016	0.0010	25.0	49.4	-
25Cr60Ni	0.02	0.30	0.19	0.020	0.0008	25.1	60.1	-
30Cr40Ni	0.02	0.32	0.20	0.015	<0.001	30.3	40.0	-
30Cr60Ni (N 06690)	0.02	0.32	0.20	0.015	<0.001	29.9	59.6	-

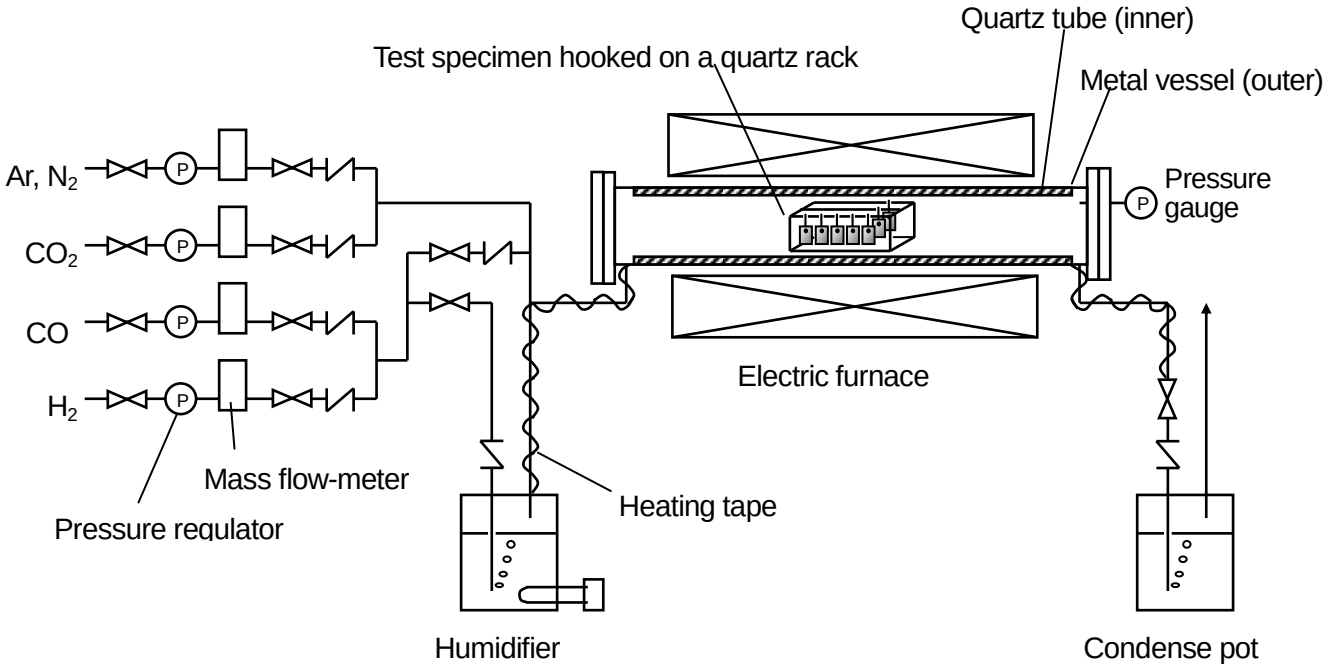

Figure 6-1 Schematic metal dusting test furnace design.

Two different tests were conducted; isothermal test and cyclic heating test. The isothermal test was conducted for up to 5,000h. For less resistant steels, exposure to the gas environment was terminated at 1,000h and 3,000h due to catastrophic corrosion of the specimens. Steels of 15Cr20Ni, 15Cr40Ni, 20Cr20Ni, and 20Cr40Ni listed in Table 6-1 were withdrawn from the furnace at 1,000h, alloys of 15Cr60Ni and 25Cr40Ni at 3,000h, and alloys of 25Cr50Ni and 30Cr40Ni at 4,000h. In this test, the specimens were furnace-cooled down to room temperature after every 1,000h heating. Both amount of coke deposition and mass change of the specimen were measured after each 1,000h exposure. The cycling heating test consisted of heating at 650ºC for 50h and cooling down to 100°C in 5h, followed by holding at 100º C for 0.5h. The set of these tests was repeated for up to 80 cycles. After every 10 cycles (corresponds to 500h heating), the test specimens were cooled down to room temperature, and then mass change and the amount of coke deposition were measured.

Each specimen was weighed after removing the coke by ultrasonic cleaning in acetone, and then the pits generated on its surface were counted by an optical microscope. One pit was chosen for each specimen to examine the pit growth rate. The pit was generally selected from the one which appeared at the very first stage of the test. Both depth and width for the selected one were measured after each 1,000h exposure of the isothermal test and 10cycles of the cyclic heating test. The pit depth was measured by a stylus depth indicator. The maximum pit depth was taken as an index of the pitting corrosion. Metallographic cross section of the specimen surface was investigated for some selected test specimens by an optical microscope and a scanning electron microscope (SEM, JEOL JSM-6400).

6.3 Results

6.3.1 Initiation of Pits

Coke nodules were observed on the specimen surface of some steels and alloys. An appearance of 23Cr60Ni (N06601) specimen after 80 cycles of the cyclic heating test is shown in Fig. 6-2 (left) for example. The coke columns of several mm long are present on the surface and at the edges of the specimens locally. Below each coke column, hemispherical pits were developed shown in Fig. 6-2 (right). It should be pointed out that the growth of coke nodules was always accompanied by pits.

Hence, its formation may be used as an indicator for the occurrence of pitting corrosion. For some specimens, neither pits nor grooves were found at any location of the specimen surface.

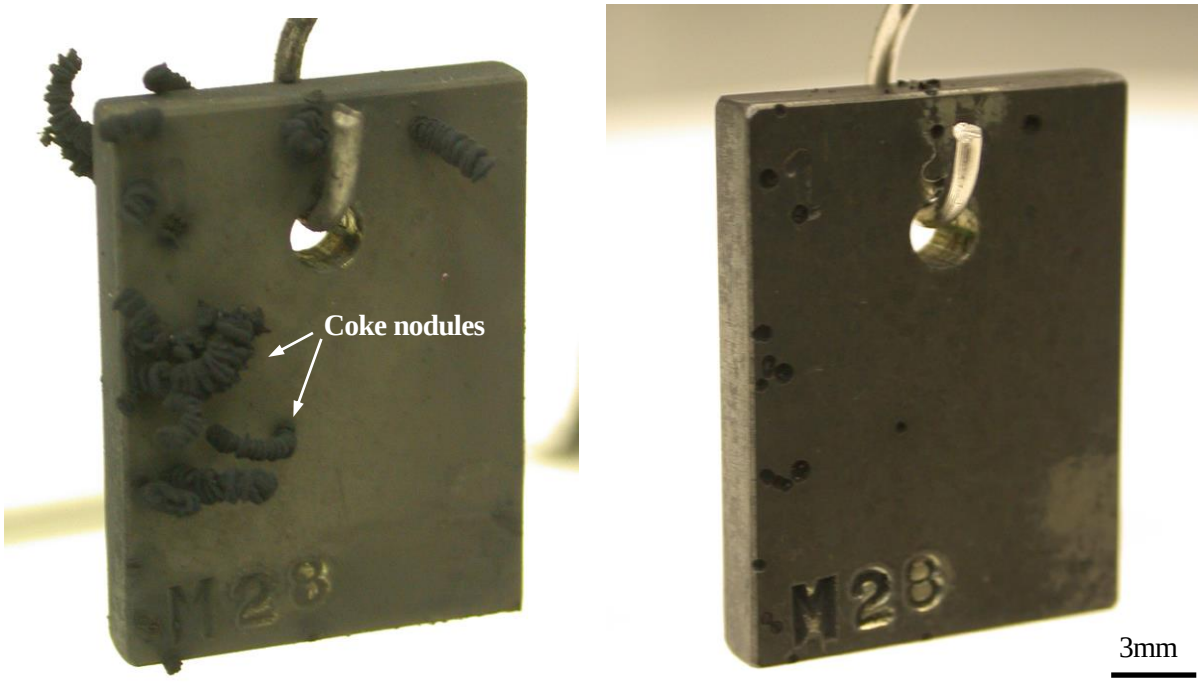

Figure 6-2 Appearance of 23Cr60Ni (N 06601) alloy specimens reacted with 60vol.%CO -26%H_2-11.5%CO_2-2.5%H_2O at 650°C for the cyclic heating test of 80cycles. (left) as exposed, (right) after removal of the deposited coke.

The test results in terms of the formation of pits and grooves were plotted with respect to the Cr and Ni contents of the steels and alloys, and shown in Fig.6-3. For both isothermal and cyclic heating tests, steels of low Cr and low Ni suffered from severe pitting corrosion. The pitting corrosion was prominent even after a short exposure of 1,000-2,000h for the specimens of Cr lower than 20% tested in the isothermal conditions. Initiation of pitting corrosion tended to shift to a longer exposure time for alloys of higher Cr and Ni contents, and 60%Ni was needed to prevent the pitting corrosion. For the cyclic test, high-Cr high-Ni alloys such as 23Cr60Ni(N06601) and 25Cr60Ni which have survived in the 5000 h isothermal test started to corrode after 40-60 cycles (heating time of 2,000 -3,000h). Hence, testing mode of the cyclic heating was much more severe to the steels and alloys than that of the isothermal, presumably due to enhanced local cracking and /or spalling of a protective Cr_2O_3 scale upon cooling. The accelerated corrosion was also shown by Toh et al. [25]. Only the 30Cr60Ni alloy

survived under the 5,000h isothermal test and the cyclic test of 80 cycles, indicating that it had the best resistance to metal dusting among the test alloys under the current test conditions.

Corrosion kinetics in terms of the mass loss of the test specimens for the isothermal test and cyclic heating-cooling test were summarized in Table 6-2 and 6-3, respectively. The mass loss was mainly induced by the pits and grooves initiated on the alloy surface. Under the isothermal test condition, low-Cr low-Ni steels (15Cr20Ni, 15Cr40Ni, 20Cr20Ni, 20Cr30Ni, and 20Cr40Ni) lost their mass significantly (12- 400 mg/cm^2) in the first 1,000h exposure. The specimen of 25Cr20Ni (S 31000) also lost mass considerably by the first 1,000 h exposure. The mass loss rate seemed to level off between exposure of 2,000h and 4,000h, but increased drastically after 4,000h. Alloys of 15Cr60Ni and 15Cr75Ni had some very small pits after 1,000h isothermal test, but the mass loss of these alloys was negligible. For high-Ni alloys of 15Cr60Ni, 15Cr75Ni, and 20Cr60Ni, mass losses were relatively moderate, ranging between 0.65 and 3.5 mg/cm^2. The mass loss of the test specimens decreased drastically with increasing the Cr content of the alloy; for example, the mass losses of 20%Ni steels of 15%, 20%, and 25% Cr were 397, 63.4, and 14.4 mg /cm^2, respectively. Under the cyclic test, listed in Table 3, the mass losses for low Ni-steels of 25Cr20Ni and 20Cr30Ni are greater than those for the high-Ni alloys except for alloy 23Cr60Ni. The 23Cr60Ni (N06601) alloy showed a significant mass loss compared to other high Ni alloys, suggesting that the oxide scale formed on its surface had less resistance against cracking and /or spalling upon cooling.

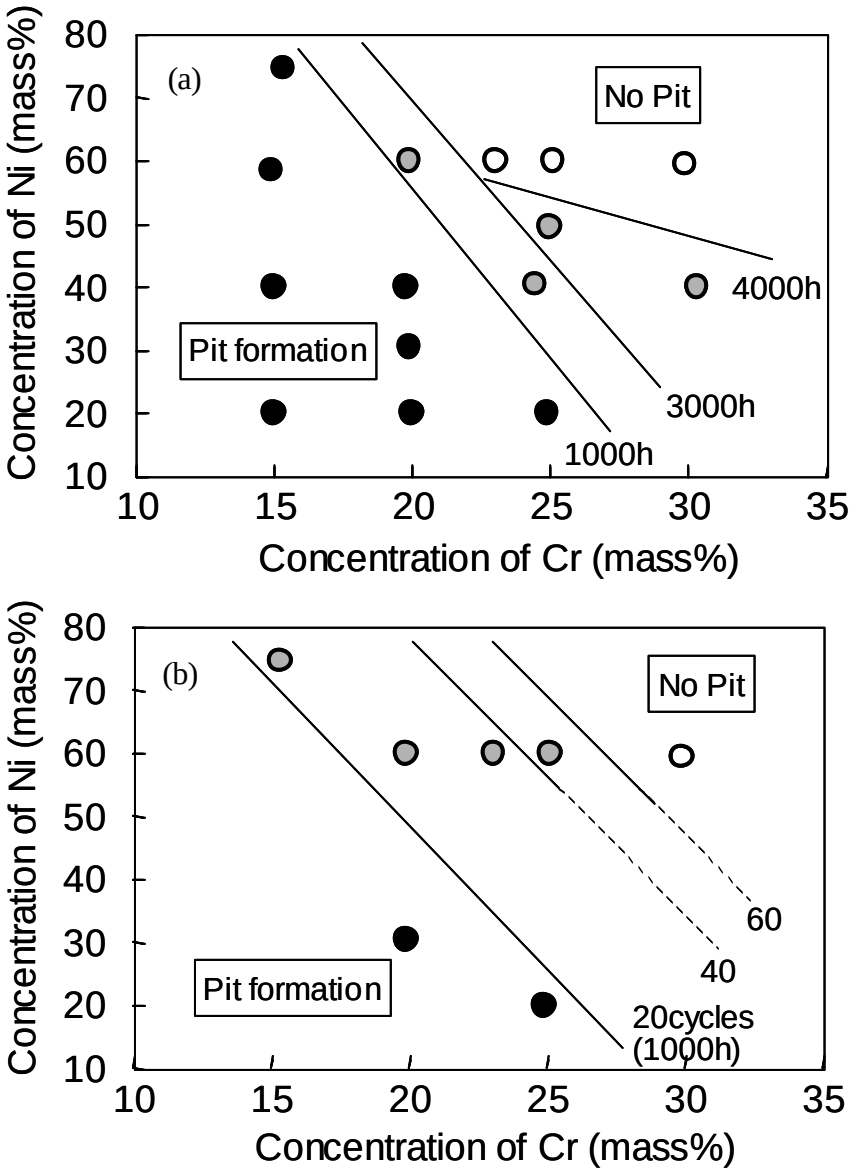

Figure 6-3 A map for the formation of pits and grooves on the specimens reacted with a 60vol.%CO -26%H_2-11.5%CO_2-2.5%H_2O gas mixture at 650°C. (a) isothermal heating test and (b) cyclic heating test.

- ● pitting was observed after exposure for 1,000h (or 20cycles)
- ◉ pitting was observed after exposure for 3,000h (or 40~60cycles)
- ○ no pitting after exposure for 5,000h (or 80cycles)

Table 6-2 Time dependence of mass loss (mg/cm^2) for alloys reacted with a 60vol.%CO-26%H_2-11.5%CO_2-2.5%H_2O gas mixture at 650°C upon isothermal heating

Alloy	Heating time (h)				
	1,000	2,000	3,000	4,000	5,000
15Cr20Ni	397	-	-	-	-
15Cr40Ni	113	-	-	-	-
15Cr60Ni	0.09	0.62	3.48	-	-
15Cr75Ni	0.01	0.03	0.06	0.13	0.65
20Cr20Ni	63.41	-	-	-	-
20Cr30Ni	12.12	24.33	27.02	27.91	67.01
20Cr40Ni	20.87	-	-	-	-
20Cr60Ni	0	0.22	0.37	0.68	1.36
23Cr60Ni	0	0	0	0	0
25Cr20Ni	0.75	1.31	2.43	2.47	14.41
25Cr40Ni	0	0.01	3.68	-	-
25Cr50Ni	0	0	0	0	-
25Cr60Ni	0	0	0	0	0
30Cr40Ni	0	0	0	0	-
30Cr60Ni	0	0	0	0	0

- : not tested

Table 6-3 Time dependence of mass loss (mg/cm^2) for alloys reacted with a 60vol.%CO-26%H_2-11.5%CO_2-2.5%H_2O gas mixture at 650°C upon cyclic heating

Alloy	Number of heat cycles (10 cycles corresponds to 500h heating)							
	10	20	30	40	50	60	70	80
15Cr75Ni	0	0	0.02	0.05	0.13	0.18	0.22	0.50
20Cr30Ni	0.11	0.13	0.18	0.24	0.24	0.52	1.25	3.21
20Cr60Ni	0	0	0.01	0.01	0.03	0.05	0.09	0.77
23Cr60Ni	0	0.01	0.03	0.05	0.12	0.42	1.14	3.07
25Cr20Ni	0.01	0.01	0.94	4.09	8.74	26.06	38.56	84.61
25Cr60Ni	0	0	0	0	0	0.01	0.02	0.05
30Cr60Ni	0	0	0	0	0	0	0	0

The specimen surfaces of the 15Cr20Ni, 15Cr40Ni, and 20Cr20Ni alloys after 1,000h isothermal test are shown in Fig. 6-4. These specimens suffered severe metal dusting. For 15Cr20Ni steel, the type of attack was superimposition of fast-growing pits extended laterally to coalesce with neighboring pits. On steel 20Cr20Ni, large pits were initiated at its corners and edges, and developed. The other area of the specimen surface remained unattacked, suggesting that protection by an oxide scale was maintained. Since they did not experience the repeated heating and cooling procedures, their surface morphologies are attributed to local cracking and /or spalling of a protective oxide scale during the isothermal exposure, possibly by high compressive 'growth stress' generated in the oxide scale at high temperature, especially at corners and edges.

Figure 6-5 (a) shows the specimen surfaces of 25Cr20Ni, 23Cr60Ni, and 30Cr60Ni steel and alloys reacted for 5,000h isothermally. For 25Cr20Ni steel, large pits developed at its corners and edges, whereas for alloys 23Cr60Ni and 30Cr60Ni, pits were not found at any location of the specimen surface. In contrast, under the cyclic heating of 80 cycles, alloy 23Cr60Ni suffered from metal dusting, as shown in Fig. 6-5 (b). Hence, the cyclic heating-cooling shortened the 'incubation time' for the initiation of metal dusting. This behavior was considered to result from local spalling and cracking of a protective oxide scale upon cooling because compressive 'thermal stress' can arise in the oxide scale. For alloy 30Cr60Ni, neither pit nor groove was observed on its surface and the specimen remained protected from the harsh corrosion environment, though the compressive thermal stress was generated.

Increase of number of pit was investigated for steels and alloys after isothermal test, and shown in Fig. 6-6 (a). The rate of pit occurrence sharply increased at an early stage of pit initiation for several steels and alloys, but after that it seemed to level off except for 15Cr60Ni alloy. For steels and alloy of 20Cr30Ni, 20Cr60Ni, and 25Cr20Ni, the number of pit decreased after long exposure because they coalesced with neighboring pits. Under the cyclic condition, alloys of 20Cr60Ni and 23Cr60Ni had many pits compared to low Ni steels of 20Cr30Ni and 25Cr20Ni as shown in Fig. 6-6 (b). Since Fe in the alloy has acted as a catalyst of coke formation, carbonaceous gas can easily disassociate on the metal surface along the pits of low Ni steels. Hence, metal dusting may continue to attack in the pits intensively.

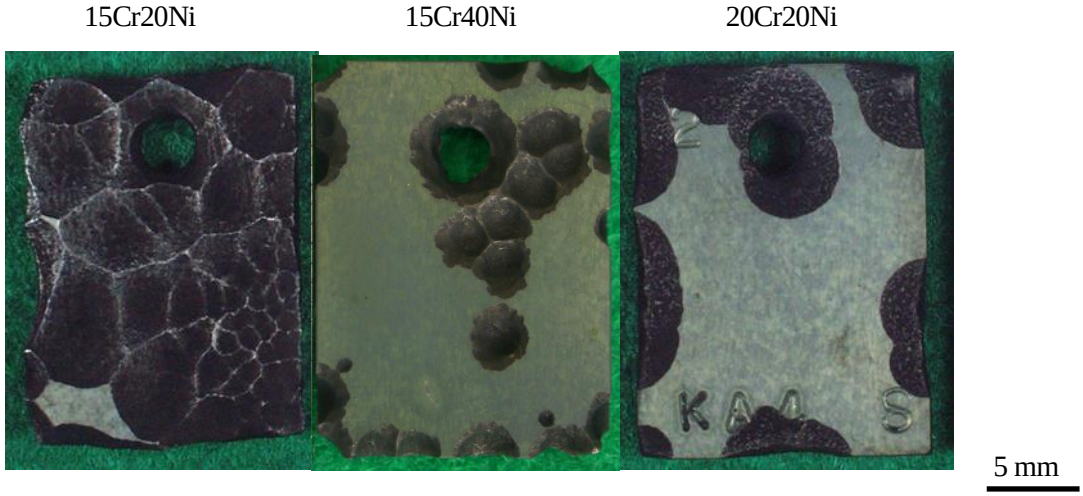

Figure 6-4 Photographs showing the specimen surfaces reacted with the simulated syngas at 650°C for the isothermal test of 1,000h. Coke deposited on the surface was removed.

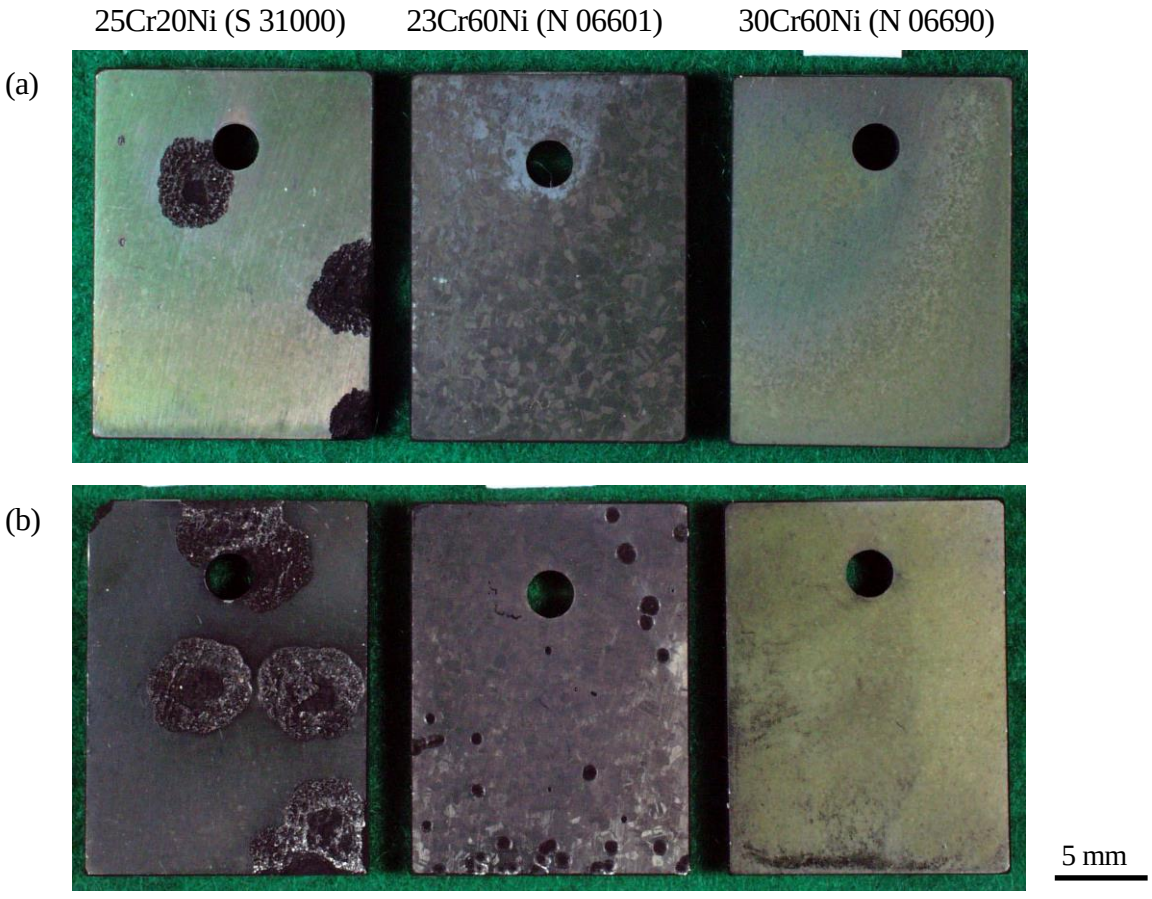

Figure 6-5 Photographs showing the specimen surfaces reacted with the simulated syngas at 650°C. (a) isothermal test of 5,000h and (b) cyclic test of 80cycles. Coke deposited on the surface was removed.

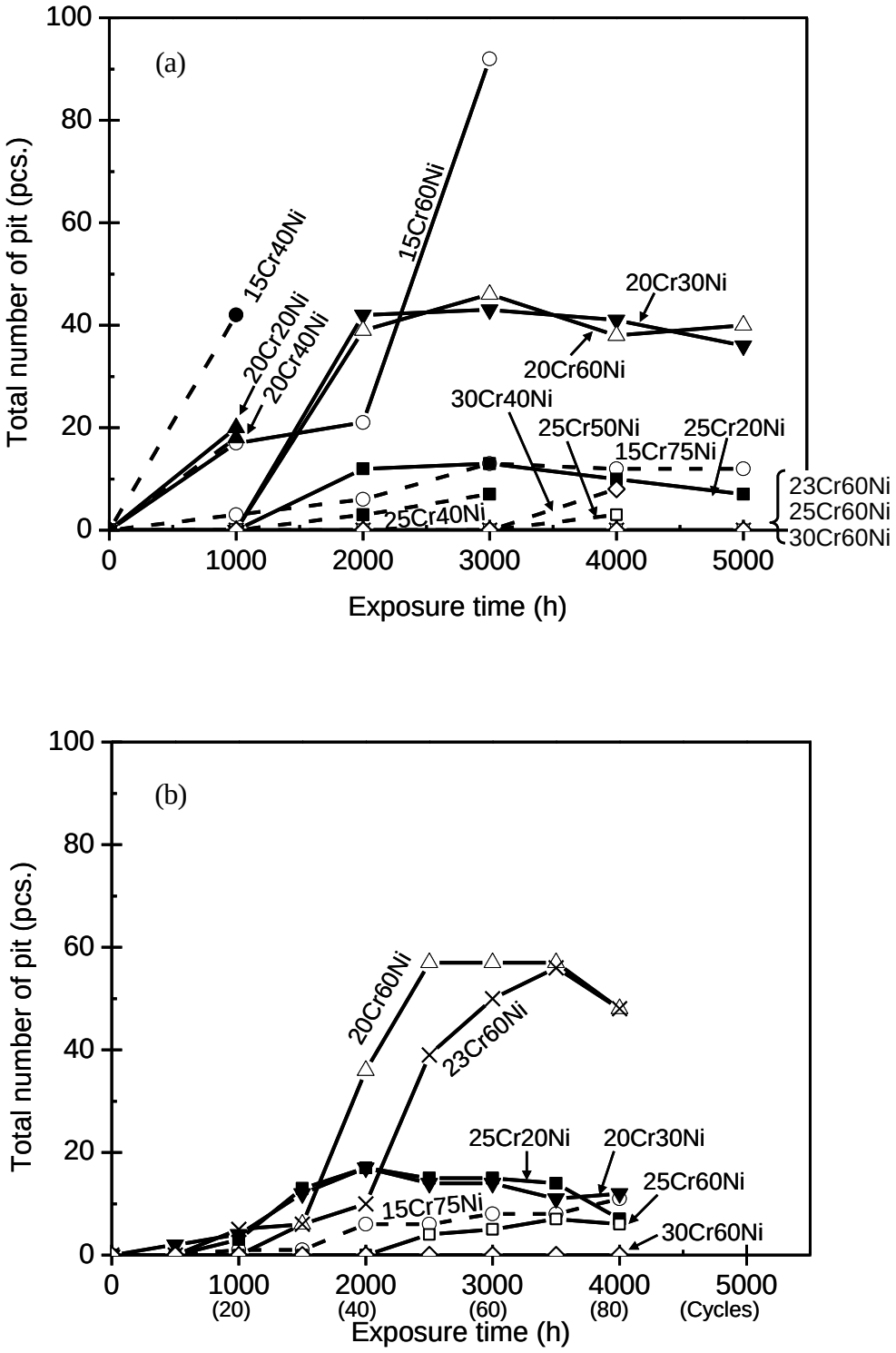

Figure 6-6 Pit occurrences on the specimens reacted with the simulated syngas at 650°C. (a) isothermal heating test and (b) cyclic test. Pits were uncountable for alloy 15Cr20Ni exposed upon isothermal heating because of general corrosion.

6.3.2 Growth of Pits

The lateral growth of pits indicated by the maximum pit diameter on the specimens is presented in Figs. 6-7 (a) for the isothermal test and (b) for the cyclic test, respectively. For the isothermal test, steels of low Cr low Ni contents formed large pits on their surfaces. The maximum pit diameter rose rapidly to be 2 - 6.5 mm for the first 1,000h exposure. For steels of 20Cr30Ni and 25Cr20Ni, the pits grew gradually with exposure time and their diameter reached approx. 2 mm after 5,000h. In contrast, high Ni alloys showed fairly small rates of pit growth. Under the cyclic condition, low-Ni steels of 20Cr30Ni and 25Cr20Ni had large pits of 3 - 5 mm diameters, whereas high-Ni alloys had small ones. The maximum pit diameters of the steels and alloys exposed to the cyclic were much greater than those exposed isothermally for the same exposure, presumably due to failure of the oxide scale during cooling.

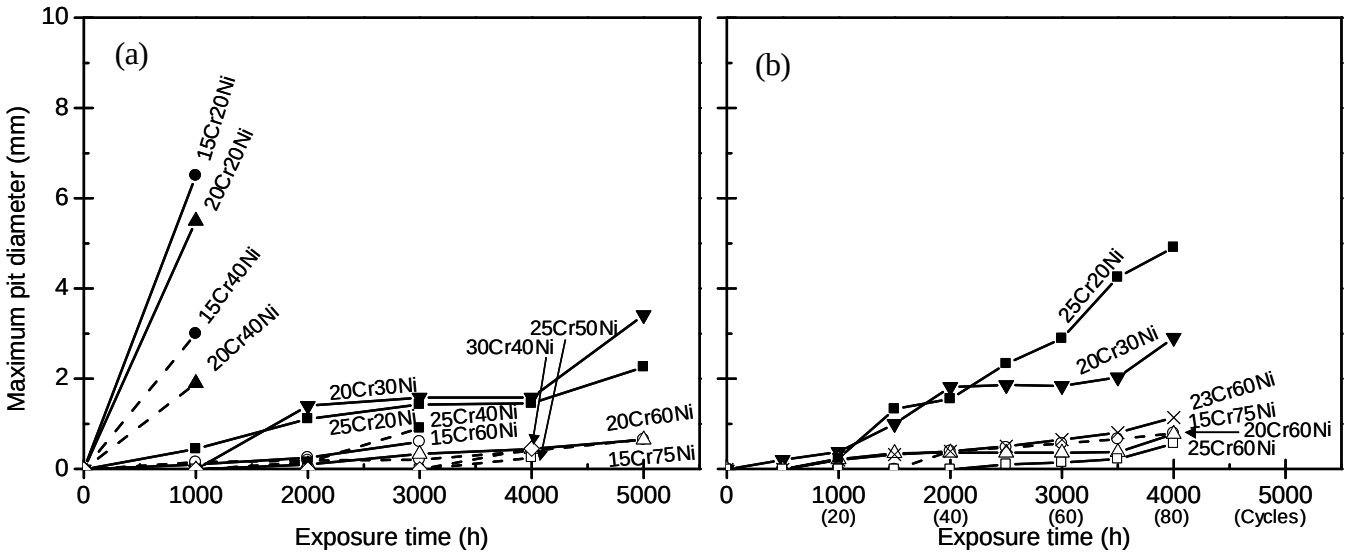

Figure 6-7 Lateral growth of a pit on the specimens reacted with the simulated syngas at 650°C. (a) isothermal test and (b) cyclic test.

The vertical growth of pits indicated by the maximum pit depth on the specimens is presented in Figs. 6-8 (a) for the isothermal test and (b) for the cyclic test, respectively. For the isothermal test, steels of low Cr-low Ni contents suffered from the formation of deep pits on their surfaces, and the maximum pit depth was 0.2 - 0.6 mm for the first 1,000 h exposure. The maximum pit depths of 20Cr30Ni and 25Cr20Ni increase with increasing the exposure time, suggesting that the pit grows not only laterally but also inward to the alloy. The pit growth rate of 25Cr20Ni steel was less than that of low Cr and Ni steels. On the other hand, for alloys of more than 60%Ni such as 15Cr60Ni, 20Cr60Ni, and 15Cr75Ni, the pit growth rate was considerably small, i.e., below 0.1 mm after 5,000 h exposure. The pit growth behavior for the cyclic test was similar to the isothermal test. The pit growth rates of low Cr low Ni steels were generally higher than those of high-Ni alloys. Except for the commercial 20Cr30Ni steel, which had small additions of Al and Ti, the maximum pit depths of the steels and alloys tested under cyclic condition were much greater than those tested isothermally for the same exposure time.

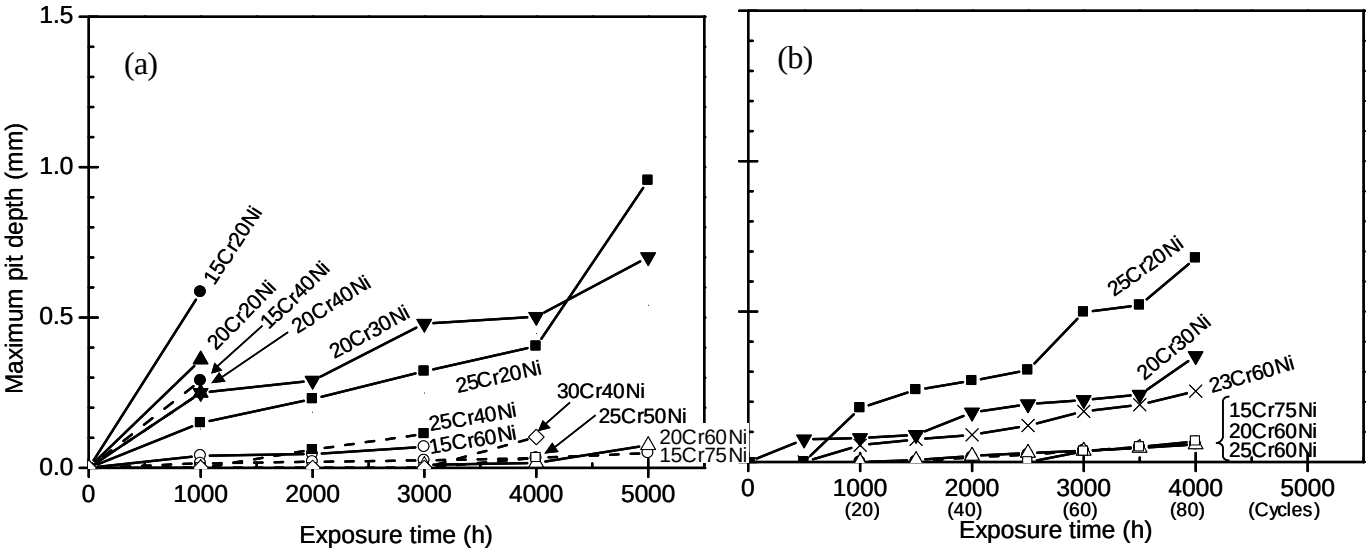

Figure 6-8 Vertical growth of a pit on the specimens reacted with the simulated syngas at 650°C. (a) isothermal test and (b) cyclic test.

Metallographic cross sections of the pits on the specimens exposed for the cyclic heating of 80 cycles are shown in Figs. 6-9 and 6-10. In Fig. 6-9, a shallow pit with wide opening is shown, typical for low Ni steels of 20Cr30Ni and 25Cr20Ni. It should be pointed out that the bottom roughness of the pits differed between the two steels. The bottom surface of the pit on 25Cr20Ni was irregular, suggesting nucleation of several secondary pits at the bottom of the primary pit. In contrast, for high Ni alloys of 20Cr60Ni and 25Cr60Ni, the pits became smaller and considerably shallower than those for the low Ni steels. The bottom surfaces of the pits were relatively smooth. A pit on 23Cr60Ni alloy exhibited crater-like shape nearly semispherical (Fig. 6-10(b)). It was apparently deeper than that on the similar Cr, Ni contents alloys such as 20Cr60Ni and 25Cr60Ni. This might be attributed to an effect of the additional alloying element of Al in the commercial alloy 23Cr60Ni.

Figures 6-11 and 6-12 show SEM micrographs of the cross section of the bottom of the pits, generated on steels and alloys after 80cycles of the cyclic test. The morphology of the "graphite" precipitates at the coke /metal interface differed between the low Ni steels (Fig. 6-11) and the high Ni alloys (Fig. 6-12). Platelet, lamellar graphite aligned perpendicular to the coke /metal interface, with the metal phase (mixtures of γ matrix and Cr carbides) left in-between. The length of the platelet graphite for the high Ni alloys was several μm and the width was 1 -2 μm, both of which were obviously longer than those for the low Ni steels of 20Cr30Ni and 25Cr20Ni. On top of each tooth of lamellar metal phase, fine metal particles possibly of Ni-Fe were observed, which will have been separated from the tooth and transferred into the coke.

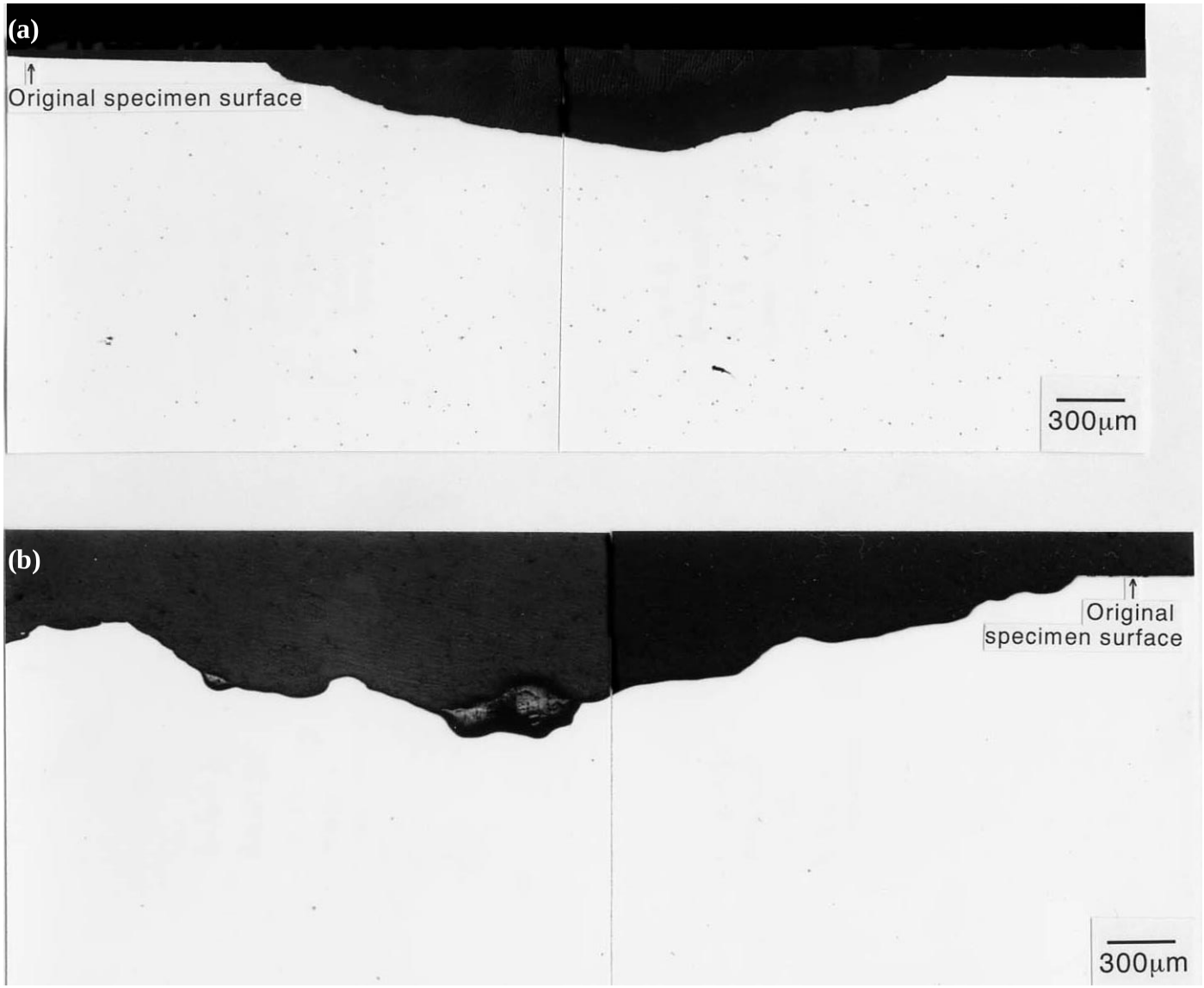

Figure 6-9 Metallographic cross sections of the specimens reacted with the simulated syngas at 650°C for the cyclic test of 80cycles. (a) 20Cr30Ni (N 08810) and (b) 25Cr20Ni (S 31000).

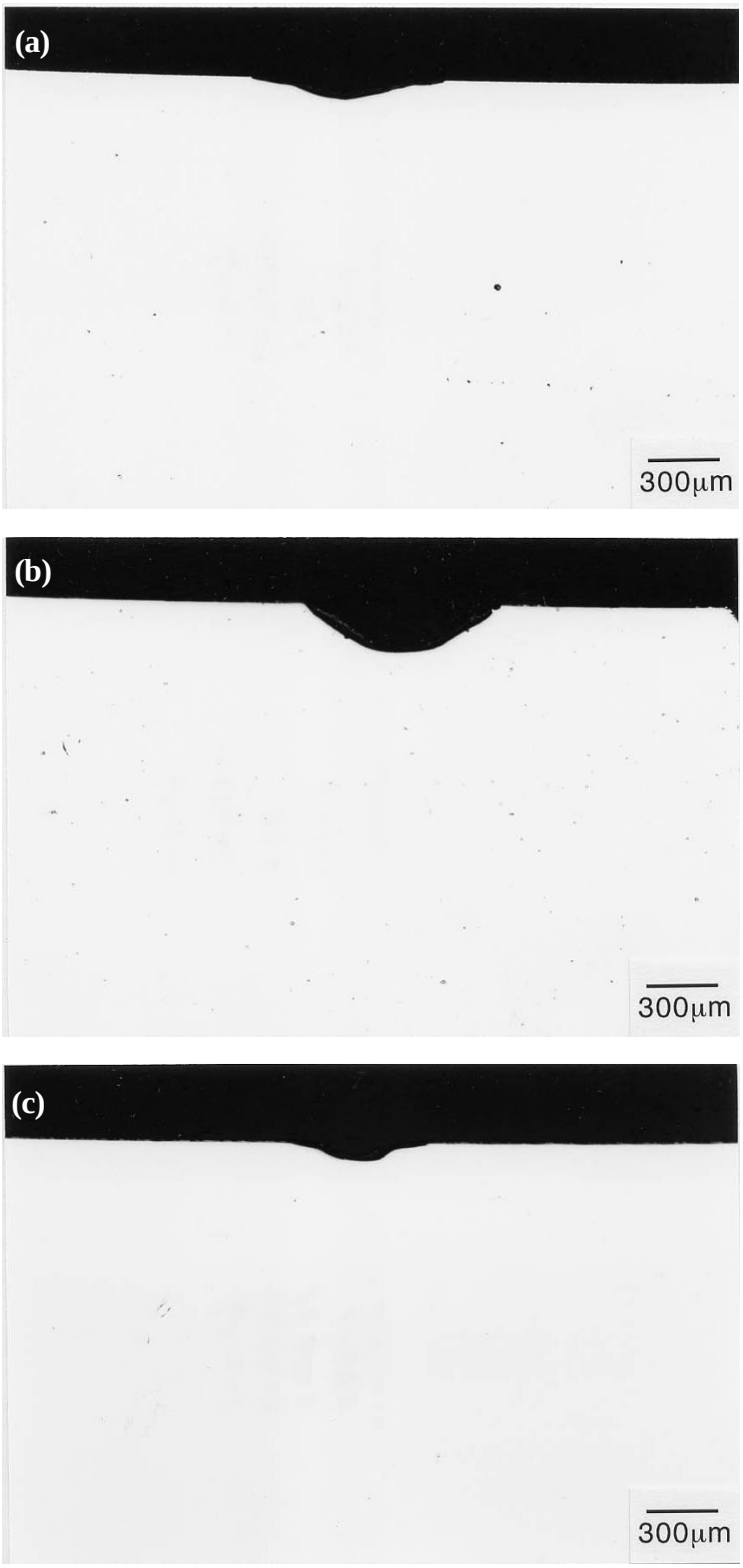

Figure 6-10 Metallographic cross sections of the semispherical pits on (a) 20Cr60Ni, (b) 23Cr60Ni (N 06601), and (c) 25Cr60Ni reacted with the simulated syngas at 650°C for the cyclic test of 80cycles.

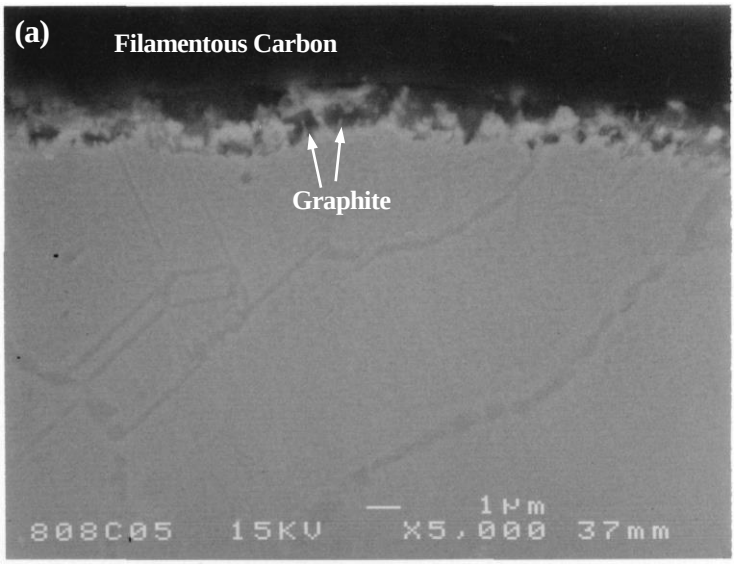

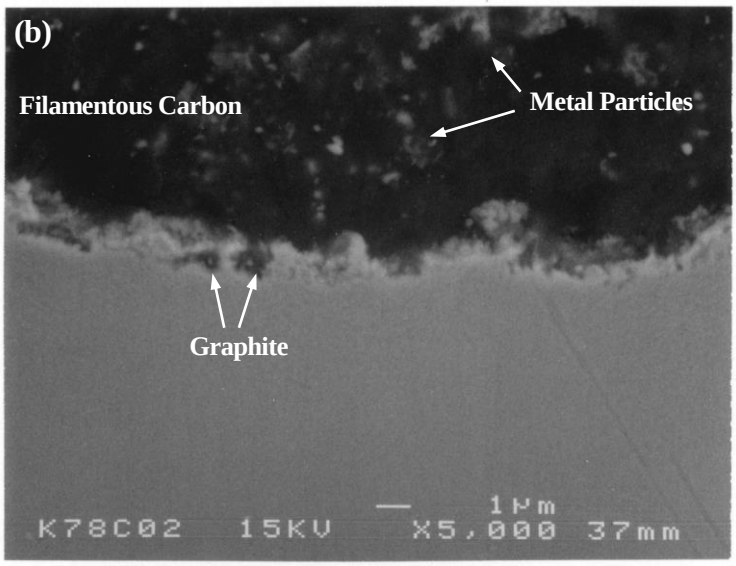

Figure 6-11 SEM micrographs showing pit bottoms occurred on the specimens reacted with the simulated syngas at 650°C for the cyclic test of 80cycles. (a) 20Cr30Ni (N 08810) and (b) 25Cr20Ni (S 31000).

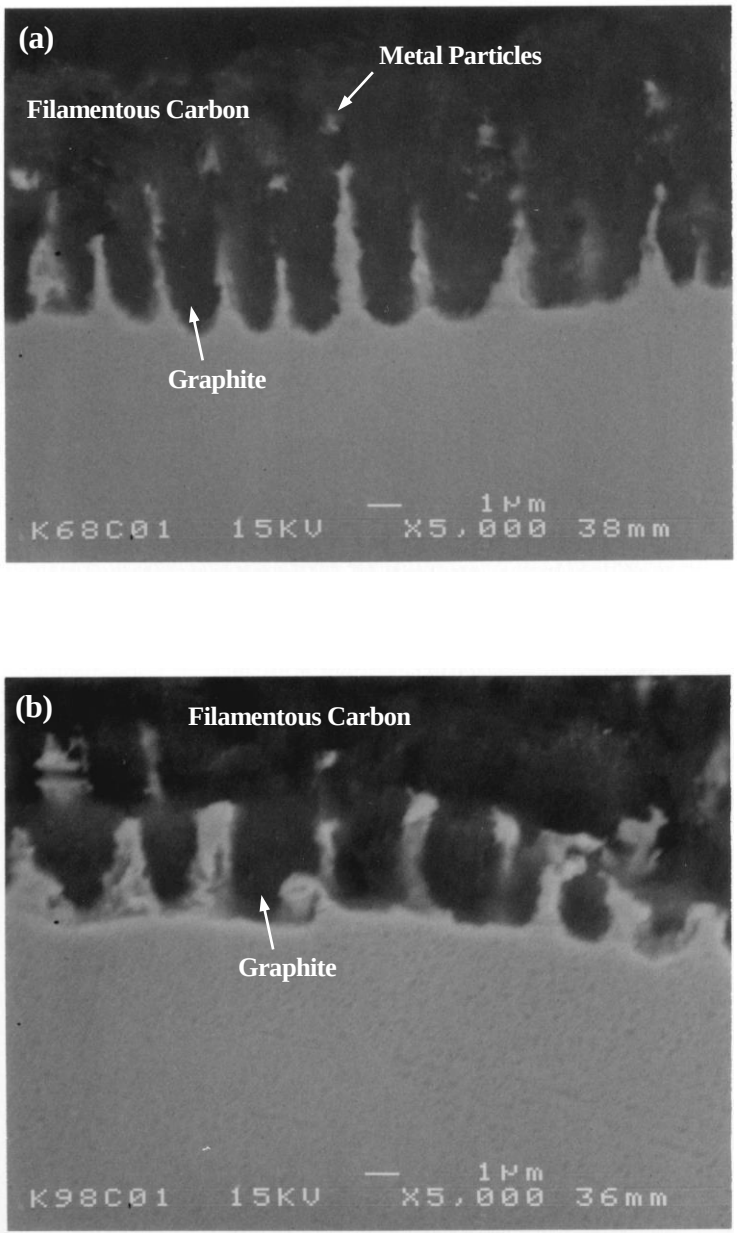

Figure 6-12 SEM micrographs showing pit bottoms occurred on the specimens reacted with the simulated syngas at 650°C for the cyclic heating test of 80cycles. (a) 20Cr60Ni and (b) 25Cr60Ni.

6.4 Discussion

6.4.1 Effects of Alloying Elements on Metal Dusting

The present test results have shown that Cr is an effective alloying element to retard the initiation of pitting corrosion of steels and alloys, since protection of the tested steels and alloys against metal dusting is considered to be given by the uniform formation and the healing of a Cr_2O_3 scale. For the present test conditions, Cr of at least 25-30% is necessary to protect alloys from the harsh corrosion environment. And presumably 30%Cr is needed to repair the Cr_2O_3 scale, since the area beneath the oxide scale is depleted of Cr. Alloys containing 60% Ni also exhibited good pitting resistance, which can be interpreted from the viewpoint of spallation of the oxide scale. Upon cooling, compressive thermal stress is generated in the oxide scale owing to different thermal expansion coefficients (TEC) between the oxide scale and the alloy matrix. The TEC of alloy 25Cr60Ni is 16×10^{-6} /°C at 650°C, whereas that of 25Cr20Ni steel is 18×10^{-6} /°C. Hence, the thermal stress generated for high Ni alloy is lower than that for low Ni steel. This alleviates accumulation of the thermal stress to cause spallation / cracking of the oxide scale.

The effect of Ni on this corrosion was examined from the viewpoint of the pit propagation rate. The growth of pits is attributed to ingress of carbon, and therefore its growth is assumingly controlled by diffusion of carbon in the metal matrix, the same as internal carburization. If diffusion control is maintained, the pit depth, ξ, is a parabolic function of the time, t, as shown below:

$$\xi = (2k_p \times t)^{1/2} \tag{2}$$

where k_p is the parabolic rate constant, expressed from an analogy of the internal oxidation derived by Wagner [26].

$$k_p = \frac{\varepsilon \times D_c \times N_c^{\circ}}{\nu \times N_M} \tag{3}$$

where D_c is the diffusivity of carbon in the γ matrix, N_c° the mole fraction of solute carbon at the external surface, N_M the mole fraction of carbide-forming alloying element of the base metal, ε the dimensionless

constant, and ν the stoichiometric factor for the single precipitated carbide M_vC. From the change of pit depths as a function of time shown in Fig. 6-8, the k_p of the tested alloy was calculated on the assumption that the pit growth follows a parabolic law, and was plotted as a function of time in Fig. 6-13. The calculated k_p was almost constant for alloys of 20Cr60Ni and 25Cr60Ni, resulting that the pitting growth is acceptable to be controlled in the parabolic law. Thus, the diffusion of carbon to the inward growing graphite is the rate limiting step for pit growth of high Ni alloys. On the contrary, the calculated k_p fluctuated between 2×10^{-12} and 5×10^{-10} cm^2/s for steels of 25Cr20Ni and 20Cr30Ni. At the beginning of pit initiation, the k_p was high, but decreased during the following exposure. This fluctuation suggests a deviation from the parabolic law. Szakalos [18] has conducted a simulated metal dusting test using AISI 304L, and demonstrated the existence of spinel-type oxide scales such as Fe_3O_4 and $FeCr_2O_4$ at the boundary of graphite / Cr-carbides in pits. In our analysis, fluctuation of the rate for pit growth would be affected by the healing of the oxide scale for low Ni steels. Once a protective oxide failed, the CO is adsorbed on the revealed metal surface, decomposes and the carbon penetrates into the metal. For low Ni steels, the Po_2 of the test gas might allow the spinel-type oxide to form even on the pit surface, and lead to a decrease of pit growth temporarily. The spinel-type oxide scale, however, is unprotective as compared to the Cr_2O_3 scale. Therefore, its protection or acceleration cannot be remained against the metal dusting upon the cyclic heating condition, resulting in fluctuation of the pit growth.

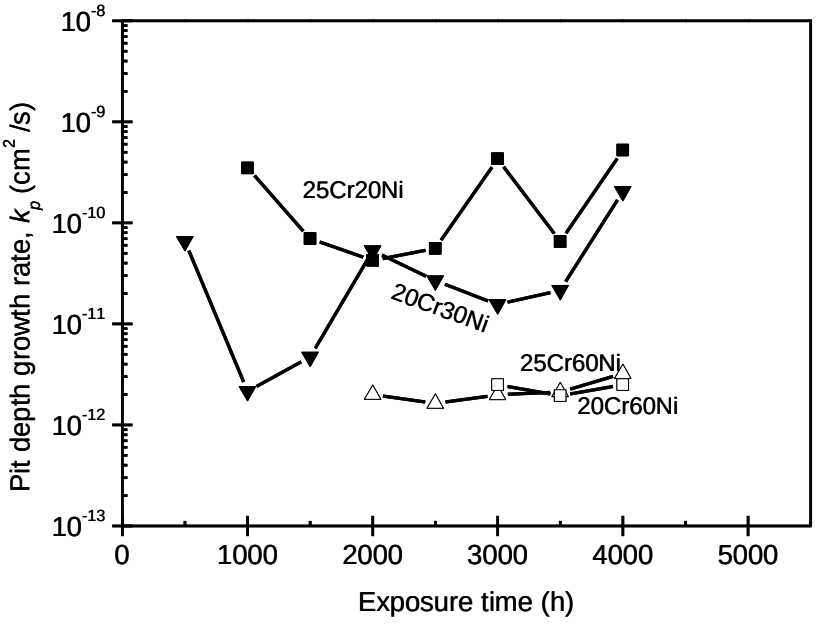

Figure 6-13 Change of pit depth growth rate k_p for the specimens reacted with a 60vol.%CO-26%H_2-11.5%CO_2 -2.5%H_2O gas mixture at 650°C upon cyclic test.

Figure 6-14 shows the maximum values of the obtained k_p plotted as a function of Cr and Ni content of the test steels and alloys. Apparently, the maximum of k_p is not correlated with Cr content in the range from 15% to 25%, while it decreases exponentially with increasing Ni content. The maximum k_p is of the magnitude of 10^{-12} cm^2/s for the alloy containing 75%Ni, which is much lower compared with that for the steel having 20%Ni (approximately 10^{-10} cm^2/s). This analysis has proven that the pit growth rate is strongly affected not by Cr content but by Ni content of steels and alloys, in contrast to the result that both content of Cr and Ni play an important role in the restraint of the pit initiation. Presumably, Ni retards the inward carbon diffusion into metal by lowering the carbon solubility. This behavior seems to be the same as a decrease of internal carburization reported [20, 21].

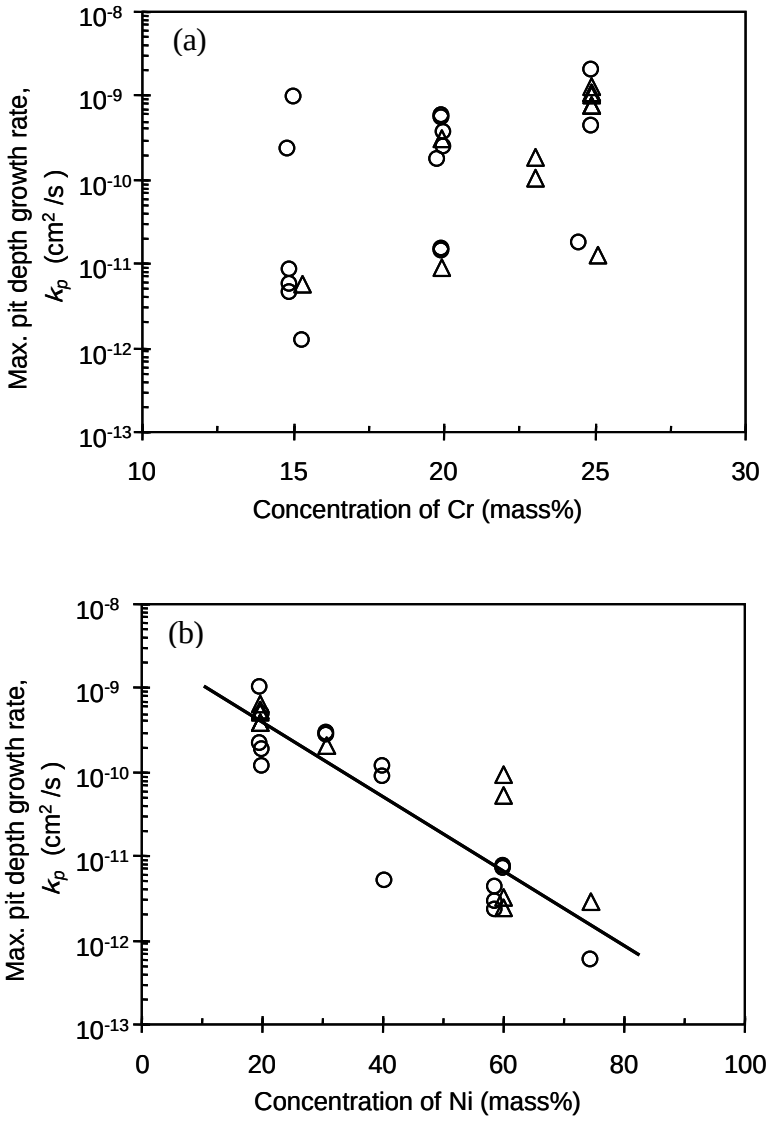

Figure 6-14 Effects of (a) Cr and (b) Ni on the maximum pit depth growth rate k_p for the specimens reacted with 60vol.%CO -26%H_2-11.5%CO_2-2.5%H_2O gas mixture at 650°C upon isothermal heating test (circular mark) and cyclic heating test (triangular mark).

6.4.2 Metallurgical Aspect of Pit Interface

The microscopic observations of pits revealed that platelet graphite was aligned perpendicular to the coke /metal interface especially for high-Ni alloys. Carbon decomposed from the gas-phase is continuously charged through a defect of the oxide scale. The dissolved carbon can combine with Cr as Cr carbides when the carbon content reaches the maximum carbon solubility in the matrix. More charging of carbon, eventually, allows platelet graphite to growth "directly", not through the intermediary of any carbides, at the gas / metal boundary of the pit. These precipitates can be formed with a lamellar structure by a eutectoid reaction where the supersaturated γ matrix (γ') decomposes into γ matrix and graphite [17]. The microscopic observations revealed that the length of the lamella for alloys with 60%Ni is evidently longer than those for steels of 20% ~ 30%Ni (compare Fig. 6-11 with Fig. 6-12). This morphology, lamellar structure of graphite intrusions, has also been observed and found to be long in a pure Ni [14]. It can be interpreted from propensity for the super saturation of carbon at the boundary of gas / metal through the spalled oxide scale. Figure 6-15 shows the phase stability diagram for C-Fe-low Ni-Cr and C-Fe-high Ni-Cr systems, where the region of γ phase is expanded intentionally. When the metal is supersaturated with carbon, the soluble carbon content in the γ matrix may be represented by the point A for low Ni steels and by the point B for high Ni alloys, respectively. For high Ni alloys, the soluble carbon content is lower in the γ matrix than that for low Ni steels. However, the carbon content in the γ matrix indeed reaches the point A' and B' instead of A and B; the carbon content becomes supersaturated at the boundary of gas / metal. The length of the lamella depends on the supersaturated carbon content (ΔC) which is different between the point A' and A or between the point B' and B. Therefore, the lamellar platelet graphite for high Ni alloys forms longer aligned perpendicular to the surface than that for low Ni steels.

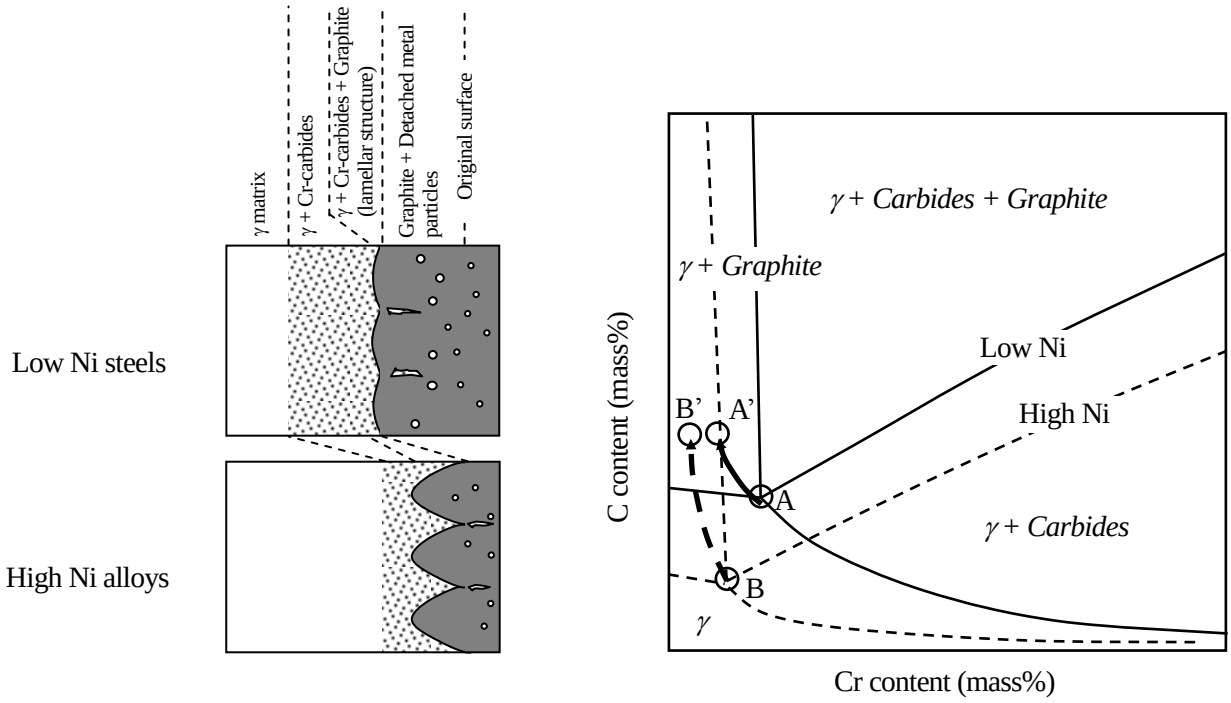

Figure 6-15 Schematic model for morphology of the lamellar graphite precipitates at the coke /metal interface differed between the low Ni steels and the high Ni alloys under CO containing syngas environments. Right figure shows the schematic phase diagrams for C-Fe-Ni-Cr system. Solid lines describe the phase diagram for low Ni steels and broken ones for high Ni alloys.

6.5 Conclusions

Long-term laboratory exposure tests for various Cr and Ni content alloys were conducted at 650°C in a 60vol.%CO-26%H_2-11.5%CO_2-2.5%H_2O gas mixture simulating syngas environments under conditions of isothermal heating and cyclic heating-cooling. The conclusions obtained are summarized as follows:

(1) Isothermal and cyclic heating tests were conducted for various Cr and Ni content steels and alloys at 650°C in a 60vol.%CO-26%H_2-11.5%CO_2-2.5%H_2O gas mixture simulating syngas environments. Upon the isothermal heating, alloys with 15% and 20%Cr had many pits on their surface, after exposure for only 1,000-2,000h, while no pit was found on the alloys of 50-60%Ni and more than 23%Cr at least up to 5,000h.

(2) The cyclic heating accelerated the initiation of pits on the specimen surface intensively. The steels and alloys except 30%Cr-60%Ni suffered from metal dusting. Under this condition, more than 30%Cr was necessary to prevent pit initiation owing to the formation of a protective Cr_2O_3 scale.

(3) A parabolic rate law controls progression of pits for high Ni alloys, suggesting that the rate-limiting step is inward diffusion of carbon in the metal matrix. For low Ni steels, in contrast, its growth rate fluctuated periodically. This was explained by in a change of the oxide scale that has repeated spallation and healing, even though the healing oxide scale did not provide a complete protection. The maximum pit growth rate for 75%Ni alloy has the magnitude of 10^{-12} cm^2/s, whereas that for 20%Ni alloys is 10^{-10} cm^2/s.

(4) Microscopic observations revealed that platelet graphite aligned perpendicular at the boundary of gas / metal of pits. The platelet graphite grows directly by a eutectoid reaction where the supersaturated γ matrix (γ') decomposes into γ matrix and graphite with the lamellar structure. The length of the platelet graphite for high Ni alloys is appreciably longer than that for low Ni steels. High Ni alloys have a large supersaturated carbon content (ΔC) because of the small carbon solubility in the γ matrix.

References

[1] F.A. Prange, Corrosion 15, 12 (1959), p.619t.

[2] F. Eberle and R.D. Wylie, Corrosion 15, 12 (1959), p.622t.

[3] W.B. Hoyt and R.H. Caughey, Corrosion 15, 12 (1959), p.627t.

[4] H.J. de Bruyn and M.L. Holland, "Materials experience in a methane reforming plant," CORROSION /98, paper no.429, (Houston, TX: NACE, 1999).

[5] R.F. Hochman and J.H. Burson. "The fundamentals of metal dusting," API Division of Refining Proc., 46 (1966), p.331.

[6] R.F. Hochman, "Basic studies of metal dusting deterioration ("metal dusting") in carbonaceous environments at elevated temperatures," Proc. of the 4th International Congress on Metallic Corrosion, NACE (1972), p.258.

[7] H.J. Grabke, R. Krajak, and Müller-Lorenz, Werkst. Korros. 44 (1993), p.89.

[8] J.C. Nava Paz and H.J. Grabke, Oxid. Met. 39, nos.5/6 (1993), p.437.

[9] H.J. Grabke, R. Krajak, and J.C. Nava Paz, Corros. Sci. 35, nos.5-8 (1993), p.1141.

[10] H.J. Grabke, C.B. Brancho-Troconis,and E.M. Müller-Lorenz, Mater. Corros. 45 (1994) p.215.

[11] H.J. Grabke, R. Krajak, E.M. Müller-Lorenz, and S. Strauß, Mater. Corros. 47 (1996), p.495.

[12] J. Klöwer, H.J. Grabke, E.M. Müller-Lorenz, and D.C. Agarwal, "Metal dusting and carburization resistance of nickel-base alloys," CORROSION /97, paper no.139, (Houston, TX: NACE, 1997).

[13] R. Shneider, E. Pippel, J. Woltersdorf, S. Strauß, and H.J. Grabke, Steel Res. 68 (1997), p.326.

[14] E. Pippel, J.Woltersdorf, and R. Schneider, Mater. Corros. 49 (1998), p.309.

[15] C.M. Chun, T.A. Ramanarayanan, and J.D. Mumford, Mater. Corros. 50 (1999), p.634.

[16] C.M. Chun, J.D. Mumford, and T.A. Ramanarayanan, J. Electrochem. Soc. 147, no.10 (2000), p.3680.

[17] Y. Nishiyama, N. Otsuka, and T. Kudo, submitted to Corrosion.

[18] P. Szakalos, R. Pettersson, and S. Hertzman, Corros. Sci. 44 (2002), p.2253.

[19] H.J. de Bruyn, E.H. Edwin, and S. Brendryen, "Apparent influence of steam on metal dusting," CORROSION /2001, paper no.1383, (Houston, TX: NACE, 2001).

[20] S.K. Bose, H.J.Grabke, Z. Metallkd. 69 (1978), p.8.

[21] Y. Nishiyama, N. Otsuka, and T. Nishizawa, Corrosion 59 (2003), p. 688.

[22] R.C. Schueler, Hydrocarbon Process. (1972), p.73.

[23] S.B. Parks and C.M. Schillmoller, Stainless Steel World 9, no.3 (1997), p.44.

[24] B.A. Baker, G.D. Smith, V.W. Hartmann, and L.E. Shoemaker, "Nickel-base material solutions to metal dusting," CORROSION /2002, paper no.2394, (Houston, TX: NACE, 2002).

[25] C.H. Toh, P.R. Munroe, and D.J. Young, Materials at High Temperature, 20 (2003), p. 129.

[26] C. Wagner, Z. Electrochem. 63 (1950), p. 772.

Chapter 7

IMPROVING METAL DUSTING RESISTANCE OF NI-CR-X ALLOYS BY AN ADDITION OF CU

7.1 Introduction

One of the most common techniques to prevent metal dusting is to form a protective oxide scale on alloy surface. Shueler [1] has proposed that theoretical account for effective metal dusting resistance can be calculated by the equivalent equation: Cr_{eq} = Cr% + 2×Si% > 22. Both Cr and Si can form protective oxide scales as Cr_2O_3 and SiO_2, respectively. Schillmoller [2] has modified the equivalent equation in a recent paper. He considered the effect of Al as an Al_2O_3 scale and proposed it as follows: Cr_{eq} = Cr% + 3×(Si% + Al%) >24. These scales can act as a barrier against the carbonaceous gas. As long as the protective oxide scale is maintained with no cracks /flaws, pits associated with metal dusting do not appear. From the point of protective oxide-scale integrity, the equivalent equation of resistance to carburization and metal dusting of steels and alloys in terms of alloying elements was used for the selection of conventional and newly developed alloys for application to the metal dusting environments [3, 4]. However, the oxide scales may crack at elevated temperature because of stresses caused by their growth and thermal cycles. These stresses that compress the oxide scale are sufficient to cause its spallation for austenitic stainless steels and Ni-base alloys. Therefore, even with a controlled oxide scale it is difficult to maintain complete protection against metal dusting for a long time. Once the scales cracked, pitting may or may not occur, depending on the competition between the attack of the carbonaceous gas and the healing of the oxide scales. Furthermore, it would depend on the reactivity between the gas and the exposed metal surfaces where the oxide scales are damaged.

Formation of carbon (coking) has been studied in terms of catalytic activity in which

carbonaceous gases such as hydrocarbons or CO react with transition metals [5-9]. Figueiredo has suggested that the mechanism of carbon formation from hydrocarbon includes the following steps [8]:

a) The hydrocarbon that is adsorbed on the metal surface produces chemisorbed carbon atoms by surface reactions.
b) The chemisorbed carbon atoms can dissolve in and diffuse through the metal, resulting in their precipitation at grain boundaries. Such precipitation causes metal crystallites to be removed it from the matrix. The metal can catalyze the filamentous coke formation and transport on top of the growing filaments.
c) Alternatively, the chemisorbed species may react on the surface to originate an encapsulating film of polycrystalline carbon.

According to step b), the chemisorption of carbon atoms decomposed from the carbonaceous gases leads to carbon diffusion into the metal, i.e. initiation of metal dusting. This means that metal dusting may be prevented if the reaction between CO and metals is suppressed at their surface.

The objective of the present chapter is to examine the behavior of both metal dusting and coking for transition metals and Ni-Cu binary alloys exposed in a carbonaceous gas, which simulates the synthetic gas produced in the reforming process. The phenomena experimentally observed are also theoretically discussed from the viewpoint of electronic properties under the chemical reactions of CO with transition-metal surfaces.

7.2 Experimental

Transition metals and Ni-Cu binary alloys were tested. The metals of 99.9%Cr, 99.9%Mn, 99.9%Fe, 99.96%Co, 99.97%Ni, and 99.5%Cu (in mass %) were chosen from the fourth periodic transition-metal elements, and both 99.98%Ag and 99.98%Pt were also tested. The binary alloys of Ni-Cu have differing contents of Cu: 1.0, 2.0, 2.9, 4.9, 10.0, 18.3, 49.5, and 69.6 (in mass%). For transition-metals, coupon specimens were cut from sheets or plates, and a small hole of 2mm φ was drilled in them for support. Specimens of Cr, Mn, and Pt were supported directly by a Pt hook spot-welded. For the binary alloys, button-ingots were made in an arc-melting furnace under an inert argon atmosphere. Coupon specimens were cut from the hot-rolled plates (5 mm thickness) with a

solution-heat treatment at 1100°C in air. All of the specimens were mechanically ground with 600-grit emery paper, followed by ultrasonic cleaning in acetone.

Metal dusting tests were conducted in a horizontal reaction chamber with a double-walled structure, quartz tube inside and a Ni-base alloy outside, illustrated in Fig. 6-1 of the section 6.2. The reaction gas composition of 60%CO, 26%H_2, 11.5%CO_2, and 2.5%H_2O (in vol.%), which gives the carbon activity a_c[1] of 10 and oxygen partial pressure Po_2[1] of 4.6×10^{-25} atm at 650°C at equilibrium, was chosen to simulate actual reforming plants. Corrosion behavior under the test gas condition was predicted from a thermodynamic aspect. Figures 7-1 (a) and (b) show the phase stability diagrams of Fe-Cr-C-O (activity of Cr, a_{Cr}=0.2) system and Ni-Cr-C-O (a_{Cr}=0.2) system. The test gas atmosphere is also plotted in these figures. As shown in Fig. 7-1 (a), steels of Fe-Cr form cementite as Fe_3C on their surface. Both scales of spinel-type $FeCr_2O_4$ and Cr_2O_3 might form beneath the Fe_3C. Graphite as a coke can also be deposited on the Fe_3C by a gas phase reaction. For Ni-Cr alloys, the Cr_2O_3 scale can cover their surface, followed by the coke deposition. The Ni_3C cannot form on the surface, even though any Cr carbides can form as internal precipitates under the Cr_2O_3 scale.

The specimens were exposed to the gas mixture at a flow rate of 300 sccm (standard cubic centimeters per minute) at a temperature of 650°C under a pressure of 1 atm. The gas velocity was calculated at 1.6 mm /s at the specimen. Each specimen was suspended on a quartz rack through a Pt hook and then set in the reaction chamber, allowing gas flow parallel to their specimen surfaces. The reaction chamber was first purged with a N_2-5%H_2 gas mixture for an hour at room temperature. After complete replacement of the purge gas with the test gas mixture, the specimens were heated at 650°C for 100h.

Each specimen was weighed after the exposure test, followed by removing the coke by ultrasonic cleaning in acetone. The treated specimens were weighed and observed with an optical microscope. For transition metals of Cu and Ni, depth profile of elements was made with glow discharge spectroscopy (GDS, RIGAKU SYSTEM 3860). Metallographic cross section of the specimen surface was investigated for test specimens by an optical microscope and a scanning electron microscope (FE-SEM, HITACHI S-4100) with energy dispersive X-ray spectroscopy (EDS).

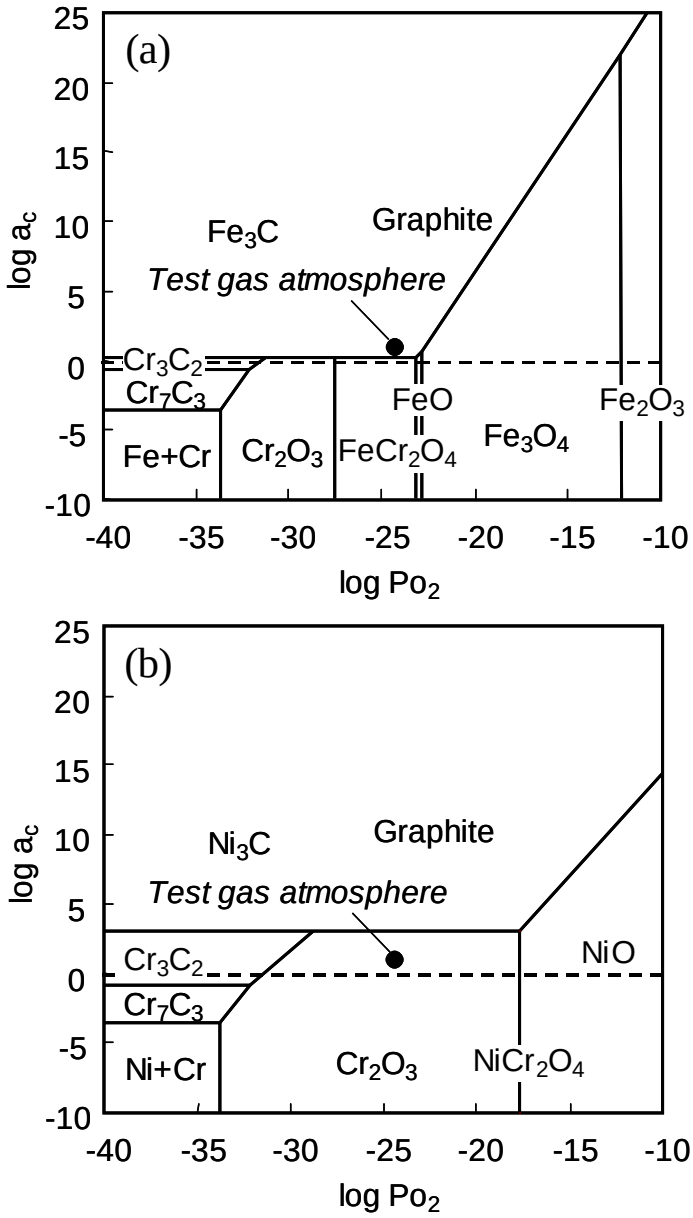

Figure 7-1 Phase stability diagram of (a) Fe-Cr-C-O (a_{Cr}=0.2) system and (b) Ni-Cr-C-O (a_{Cr}=0.2) system at 650°C. A graphite phase is stable above the broken line shown in each figure. Test gas atmosphere of a 60%CO-26%H_2-11.5%CO_2-2.5%H_2O gas mixture was also plotted.

7.3 Theoretical

In order to comprehensively show the chemical dissociation process of CO on metal surfaces, electronic structure calculations have been performed for simple models. We have chosen two methods for the present analyses. The first method is the Discrete Variational Xα (DV-Xα) method, which is the first-principles molecular orbital calculation using Slater's Xα functional for the electron many body term [10]. This method is applied for the electronic structure analyses of CO adsorption on metal surfaces. The second method is the Full-Potential Linear Muffin-Tin Orbital (FP-LMTO) method, which is the first-principles band structure calculation method [11]. The FP-LMTO implementation code of LmtART [12, 13] is used for the calculations of the density of states (DOS) of non-magnetic fcc Fe phase. We discuss the electronic structure of transition metal alloys from the rigid band analyses using this DOS. The local density approximation (LDA) parameterized by Vosko, Wilk, and Nussair [14] is used for the present FP-LMTO calculations. The tetrahedron mesh of 8 ×8 ×8 is adopted for the Brillouin zone sampling. In the present work, the magnetic interaction is not considered and the non-spin-polarized calculations are carried out for both methods. In addition, the experimental lattice constants and /or bond length are used for constructing the configuration models analyzed [15]. The lattice constant of hypothetical non-magnetic fcc phase of Fe is approximately deduced from the experimental atomic volume in the ground state bcc phase.

7.4 Results

7.4.1 Metal dusting of transition-metals

Transition metals were exposed in CO-H_2-CO_2-H_2O simulated gas atmosphere at 650°C for 100h. The amounts of coke deposited on their surfaces were measured and are listed in Table 7-1. After the removal of coke, each specimen was weighed, also listed in Table 7-1. Specimens of Cr and Mn had small amounts of coke because they were able to form an oxide scale in the test atmosphere. Except for Cr and Mn, the test metals did not form any oxide scale on the surface. A specimen of Fe had an extremely large amount of coke, over 1,400 mg/cm^2, while its mass decreased to –37 mg/cm^2.

Specimens of Co and Ni also had coke deposition of 6.55 and 11.95 mg/cm^2, respectively. Their mass changed to a minus value, which includes both mass gain due to carbon ingress and mass loss due to metal wastage, i.e. metal dusting. In contrast, metals of Cu, Ag, and Pt whose masses remained unchanged, had slight amounts of coke deposition on the surface. Neither metal dusting nor coking appeared to occur in the carbonaceous environment. Figure 7-2 shows the appearance of the specimens after the test gas. Surfaces of Cr and Mn colored dark green and grey, respectively, due to the formation of the oxide scale. For the Fe, Co, and Ni metals, coke covered the whole of their surfaces. Especially, the coke had a layered structure on the Fe specimen, though the outer layer could easily flake away. On the contrary, specimens of Cu, Ag, and Pt preserved a metallic surface.

Table 7-1 Amount of coke deposition and mass change of specimens for transition metals exposed in CO-H_2-CO_2-H_2O gas mixture at 650°C for 100h. Specimens of Cr and Mn formed oxide scale on the surface in the test gas environment.

	Cr	Mn	Fe	Co	Ni	Cu	Ag	Pt
Amount of coke in mg/cm^2	0.06	<0.01	1,434	6.55	11.95	0.03	<0.01	<0.01
Mass change in mg/cm^2	0.14	2.22	-37.15	-0.83	-0.15	0	0	0

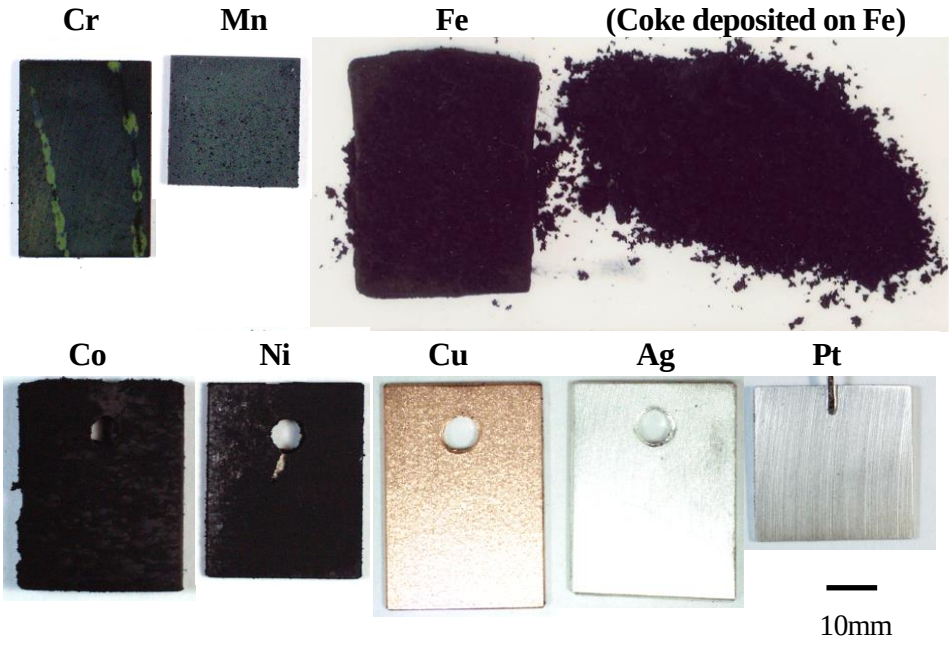

Figure 7-2 Specimen surfaces of transition metals exposed in the gas mixture at 650°C for 100h.

Morphologies of coke deposited on the Fe and Ni were observed by FE-SEM and are shown in

Figs. 7-3 and 7-4, respectively. Coke on Fe was agglomerated like lint, shown in Fig. 7-3(a). At the same region observed in Fig. 7-3(a), back-scattering electrons imaged many bright spots (Fig. 7-3(b)), suggesting that some metal particles were involved in the coke. Toh et. al. [16] reported that the particles could consist of cementite. In this investigation, it is unclear whether the particles consist of metal and / or cementite. A higher-magnification observation showed quite a lot of coke filaments with 0.1-0.2 μm diameter, intricately intertwined with each other (Fig. 7-3(c)). As indicated by the arrow in this figure, a number of nodes studded in the filamentous coke were observed, corresponding to the bright spots imaged by the back-scattering electrons. EDS analysis showed that these nodes consisted of Fe, suggesting the deposited filamentous coke were catalyzed by Fe particles, which were detached from the Fe specimen (Fig. 7-3(d)). The detachment of metals, which is a characteristic phenomenon of metal dusting, was demonstrated by the result of mass loss listed in Table 7-1.

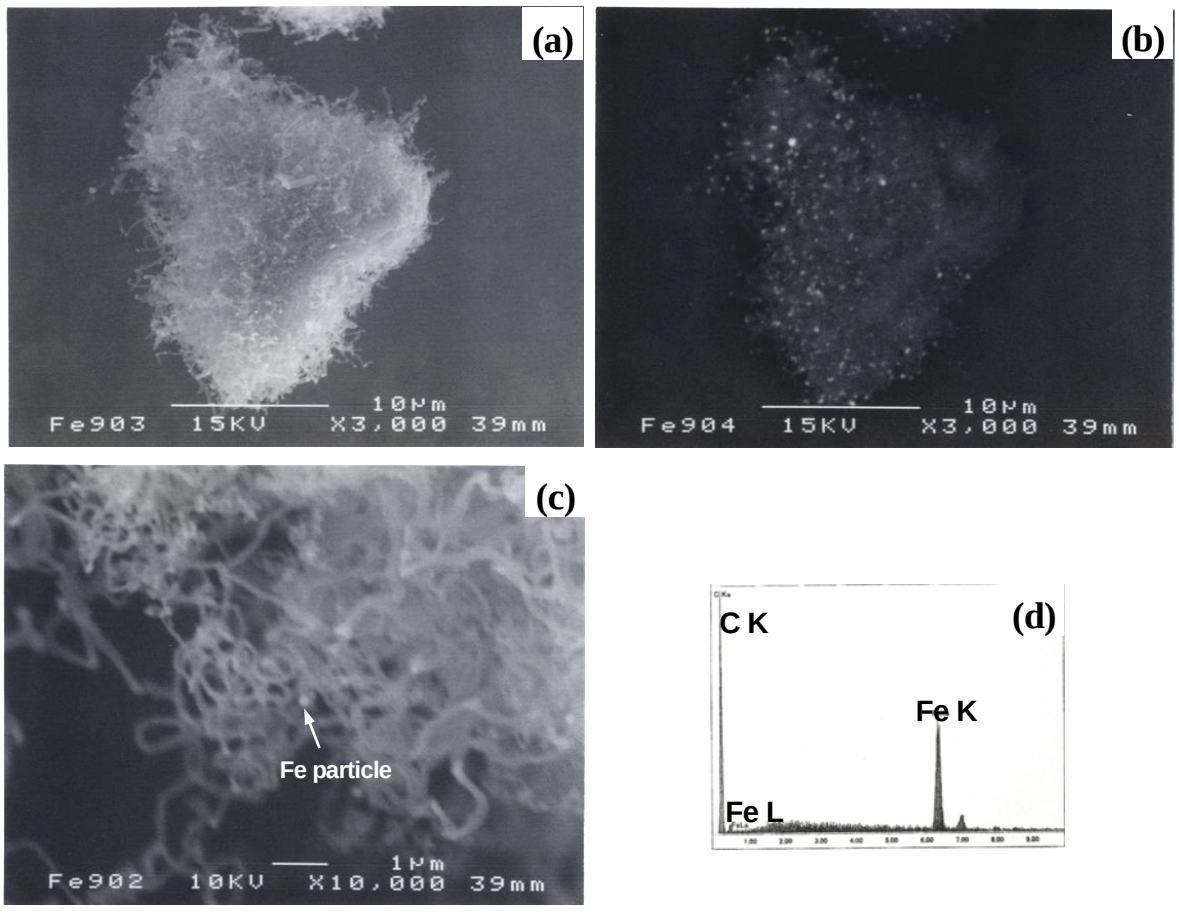

Figure 7-3 Coke morphologies deposited on the Fe surface exposed in CO-H_2-CO_2-H_2O gas mixture at 650°C for 100h. (a) SE image, (b) BS image of (a), (c) Higher magnification of (a), and (d) EDS analysis at a bright spot shown in (b).

Figure 7-4 shows the result of SEM observations and EDS analysis for coke deposited on Ni. As shown in Fig. 7-4(b), the coke contained some metals. The imaged bright spots for Ni were much less than those for Fe. The coke looked filamentous, but the filaments were thinner as compared with the coke on Fe. At the bright spots imaged in Fig. 7-4(b), EDS detected Ni, supporting the theory that it can also act as a catalyst of coke formation (Fig. 7-4(d)).

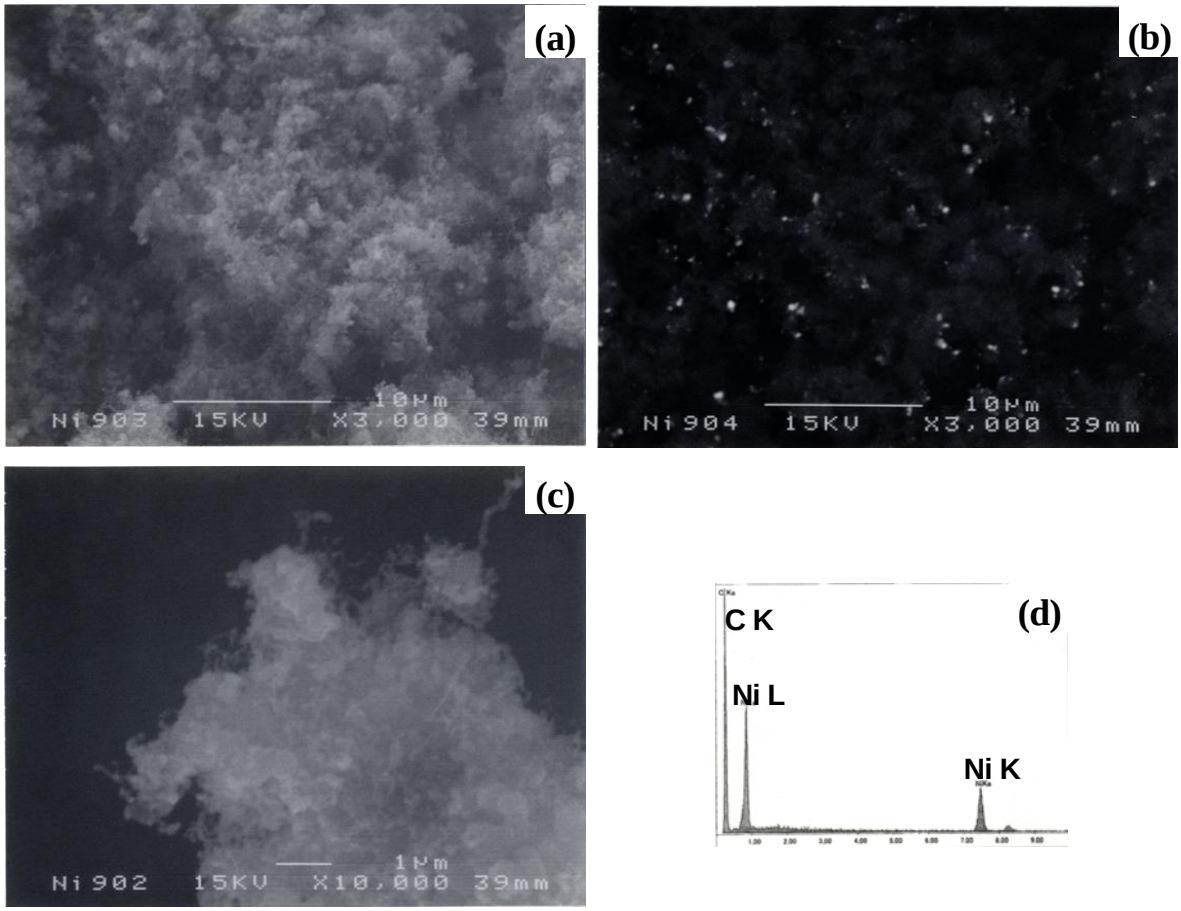

Figure 7-4 Coke morphologies deposited on the Ni surface exposed in CO-H_2-CO_2-H_2O gas mixture at 650°C for 100h. (a) SE image, (b) BS image of (a), (c) Higher magnification of (a), and (d) EDS analysis at a bright spot shown in (b).

A cross section of Ni was observed by SEM, and shown in Fig. 7-5(a). It had a considerably rough surface where coke (graphite) aligned perpendicular to the base metal like a lamellar structure. As a resultant, Ni was thinned and then detached from the base metal. The metal wastage progressed uniformly, because it could not form any oxide scales. Carbon ingress in the Ni and Cu, which were exposed in the simulated gas at 650°C for 100h, was investigated by GDS, shown in Figs. 7-5(a)' and (b), respectively. For the specimen of Ni, carbon penetrated from the metal surface and reached a depth of approx. 5 ~10 μm where any Ni carbides was not precipitated. In contrast, carbon did not penetrate into Cu, demonstrating it had neither metal dusting nor coking. The results demonstrated that Cu, Ag, and Pt were useful elements for resisting metal dusting and coking. Because of the absence of protective oxide scales as a barrier against CO gas, those metals were concluded to have less reactivity with a carbonaceous gas such as CO.

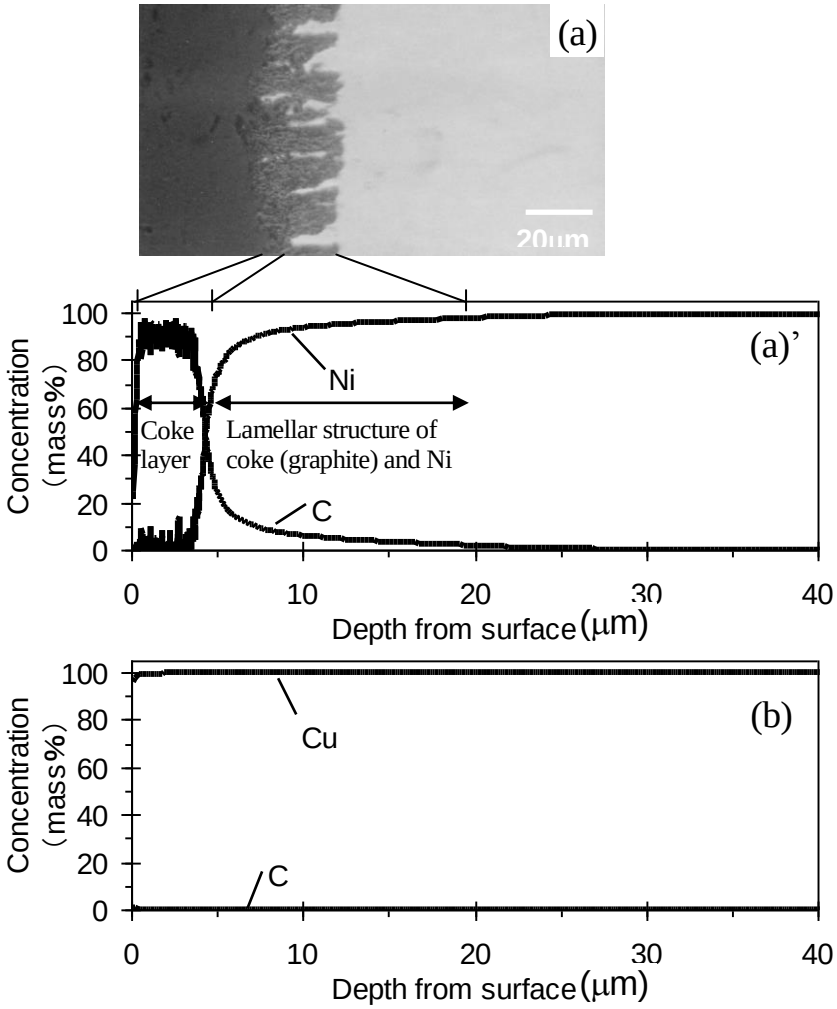

Figure 7-5 SEM observation and GDS depth profiles of C and alloying elements for (a) and (a)' Ni and (b) Cu, exposed in CO-H_2-CO_2-H_2O gas mixture at 650°C for 100h.

7.4.2 Metal dusting of Ni-Cu binary alloys

Among the useful transition-metals identified above, Cu might be the most practical element to consider as an alloy for high temperature materials. For Ni-Cu binary alloys, therefore, the effect of Cu was investigated on metal dusting. The binary alloys with differing amounts of Cu were exposed in the CO-H_2-CO_2-H_2O gas mixture at 650°C. After 100h exposure, the amounts of coke deposition and mass changes of the specimens were plotted against Cu content, shown in Figs. 7-6 and 7-7, respectively. The results for pure Ni and Cu were also plotted in each figure. Alloys with small addition of Cu had a large amount of coke deposited on their surface. The coke deposition was decreased drastically with increasing Cu content, and reduced to almost zero for Ni-Cu alloys of 20% and more Cu. In accordance with the coking behavior, alloys containing low Cu, but not pure Ni, increased their masses due to the carbon ingress. Specimen of 10%Cu showed less increase in mass compared with the low Cu alloys. For specimens of 20% and more Cu, their masses remained unchanged even after 100h exposure. Their surfaces without removal of coke are photographed in Fig. 7-8. A large amount of coke with filamentous morphology was formed over the specimens of 1.0% and 2.0%Cu. Coke deposition decreased with increasing Cu content, and then materially alleviated for Ni-10.0%Cu alloy. Alloys of 18.3% and 69.5%Cu, which showed no mass change in Fig. 7-7, had little coke formation on their surfaces.

Figure 7-9 shows metallurgical cross sections of Ni alloys with 2.0%, 10.0%, and 49.5%Cu after removal of coke, following the exposure test at 650°C for 100h. Nickel alloy with 2.0%Cu showed a considerably rough surface where a lot of fragment crystalline collapsed, and then they were detached from the base metal. The metal wastage progressed uniformly: neither cracks nor pitting occurred at the surface, because the alloy could not form any oxide scales. Alloy of Ni-10.0%Cu also showed a rough surface, though the detailed morphology of metal wastage was different from that for 2.0%Cu alloy. For Ni-49.5%Cu alloy, on the contrary, its surface was extremely smooth without metal wastage. From these results, Ni alloys with less than 20%Cu demonstrated coke formation and metal dusting under the condition of carbonaceous gas. These levels of Cu content clearly cannot suppress the reactivity of metal with CO gas at the metal surface where no oxide scale is formed. Therefore, 20% and more Cu in Ni alloy is needed to inactivate the surface reaction with CO gas, and results in lowering of metal dusting attack in synthetic gas environments tested.

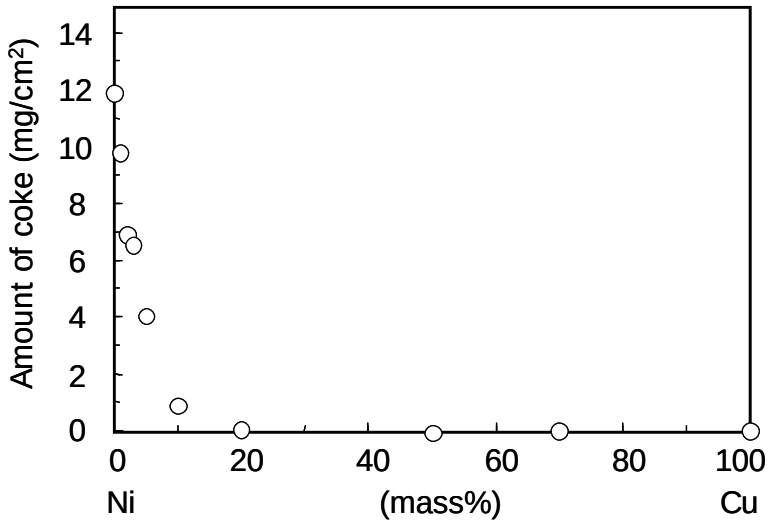

Figure 7-6 Amount of coke deposition for Ni-x%Cu binary alloys exposed in CO-H_2-CO_2-H_2O gas mixture at 650°C for 100h.

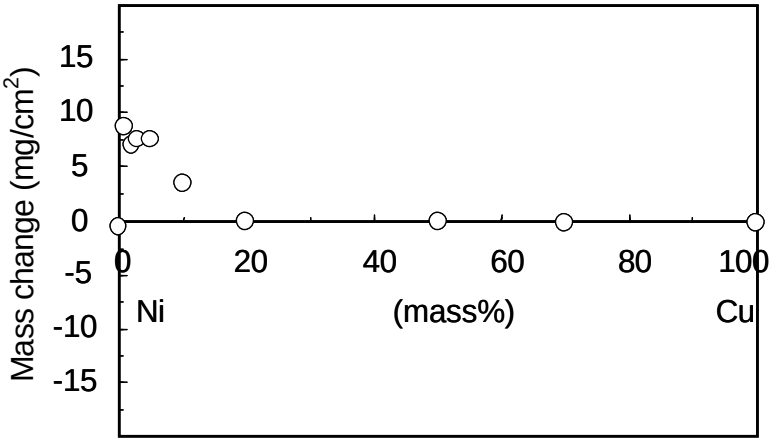

Figure 7-7 Mass change of specimens for Ni-x%Cu binary alloys exposed in CO-H_2-CO_2-H_2O gas mixture at 650°C for 100h.

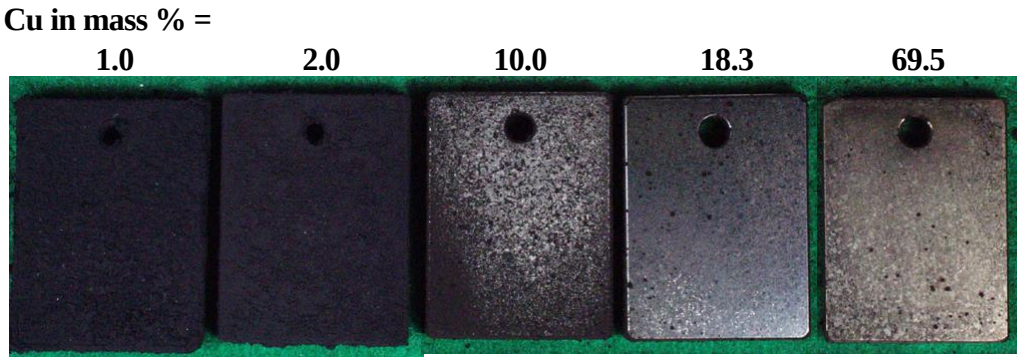

Figure 7-8 Specimen surfaces of Ni-Cu binary alloys exposed in CO-H_2-CO_2-H_2O gas mixture at 650°C for 100h.

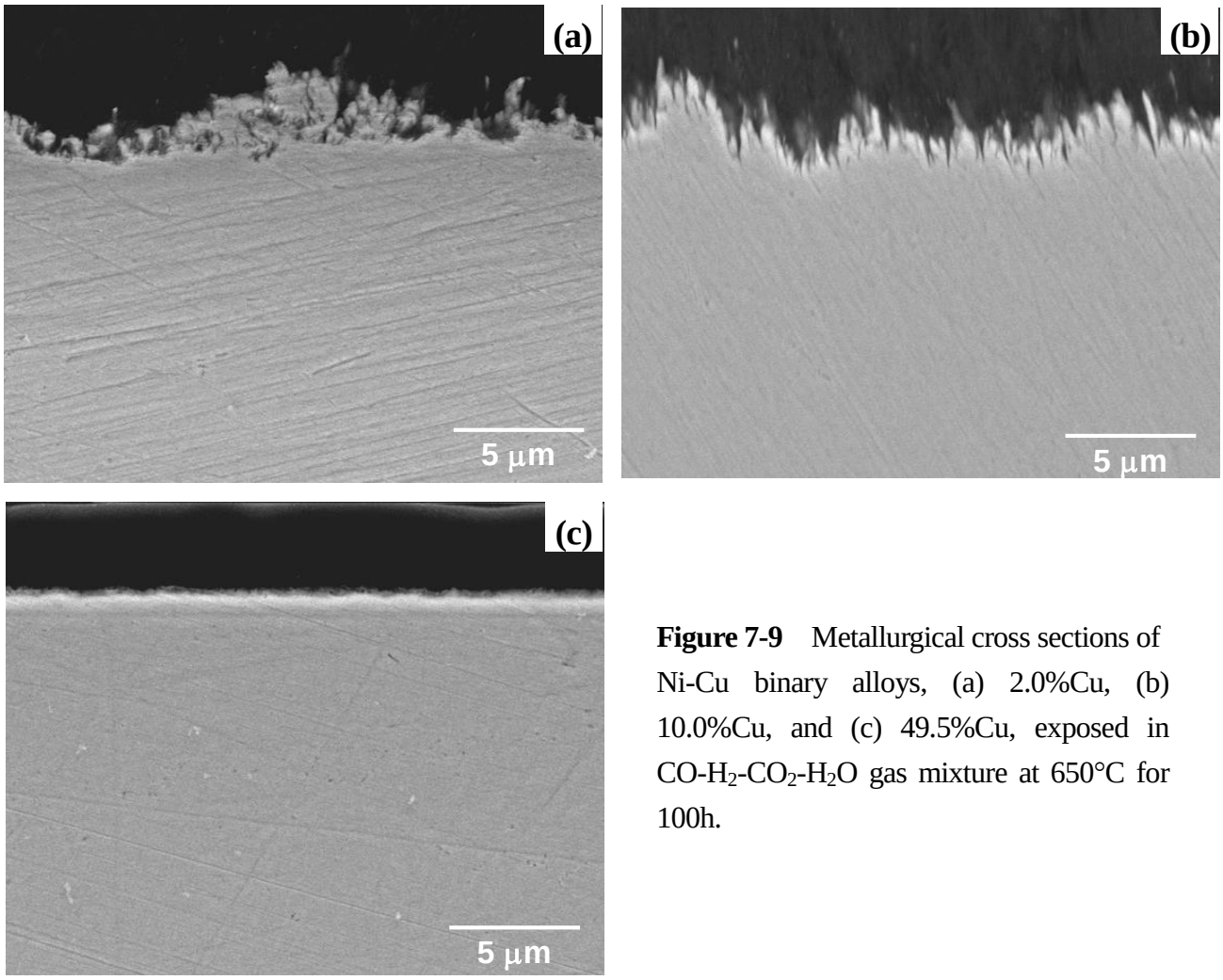

Figure 7-9 Metallurgical cross sections of Ni-Cu binary alloys, (a) 2.0%Cu, (b) 10.0%Cu, and (c) 49.5%Cu, exposed in CO-H_2-CO_2-H_2O gas mixture at 650°C for 100h.

7.5 Discussion

7.5.1 Initial Stage of Metal Dusting

Nickel alloys containing Cu, even though they did not have any oxide scales to protect against CO gas, were demonstrated to improve the metal dusting resistance, and thereby to inhibit the coke formation catalyzed by the detached metal particles. The amount of Cu for significant improvement needed to be almost 20% under the test gas condition. Since the effect of Cu may be related to the reduction of the reactivity with CO gas, an understanding of elementary reaction steps for the initial stage of metal dusting is important. Figure 7-10 shows the possible steps for carbon to penetrate into the base metal, illustrated

at the atomic level. Under carbonaceous gas atmospheres, CO molecules collide on the metal surface, and part of them are adsorbed on it (reaction step I). Each atom of carbon and oxygen, while still binding together as molecular CO, forms a chemical union with the metal atom at the metal surface. The chemisorbed CO molecule is dissociated into carbon and oxygen, because the binding energy of C-O is weakened (reaction step II). The continuous carbon atom penetrates into the base metal (reaction step III). In the carbonaceous gas, the sequence continues with a charging of carbon into the base metal, and as a result, metal dusting occurs on the whole of the metal surface. Of great importance for preventing metal dusting is to suppress the dissociation of CO molecules adsorbed on the metal surface in the reaction steps mentioned above.

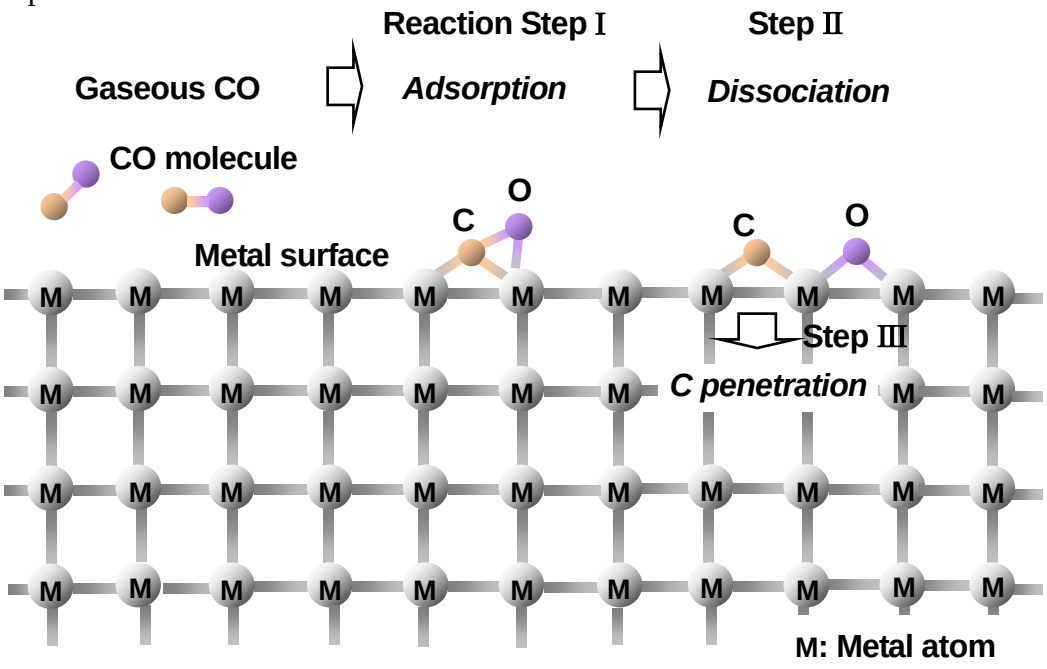

Figure 7-10 Schematic representation of metal / CO gas reaction on the metal surface at the atomic level.

For a given transition metal series, it is experimentally known that the tendency of CO dissociation becomes greater, when the metallic elements of the substrate are located further to the left side in periodic table [17]. This dissociative tendency is assumed to be strongly related to the results of the present metal dusting experiments, while the protective properties against metal dusting found in the specimens of Cr, Si, and Al originate in another mechanism, the formation of oxide. In addition, Grabke has recently reported that the adsorption of sulfur on pure Fe surfaces induces protective properties against metal dusting [18]. It is interesting to note that the adsorption of sulfur atoms on Fe(100)

surfaces has also been experimentally detected to prevent the dissociative adsorption of CO [19]. This is because those adsorption sites of CO [20], C, O [21], and S [22] on Fe(100) surfaces are identical with the four-fold hollow sites, and CO molecules lose their dissociative reaction fields with a sulfur monolayer. These experimental results suggest that an understanding of atomistic properties of CO adsorption on transition-metal surfaces is the key ingredient for metal dusting suppression technologies.

7.5.2 Dissociative and non-dissociative adsorption of CO at metal surfaces

In metal dusting phenomena, the most basic question for the CO adsorption on metal surfaces is on the difference between the dissociative and non-dissociative properties. While some controversial phenomena still exist, especially in platinum systems [23], the model widely accepted for the question so far is the donation and back-donation mechanism proposed by Blyholder [24]. In this section, we describe the Blyholder mechanism for the dissociative and non-dissociative adsorption properties of CO at metal surfaces using the electronic structures calculated by the DV-Xα method.

On bcc-Fe(100) surface, a CO molecule is experimentally known to occupy the hour-fold hollow site, where the molecular axis is tilted along the vertical direction of the surface [20]. In the present work, however, the electronic structures of non-tilted states are calculated for simplicity. The equilibrium distance between Fe(100) surface and CO molecule in this configuration is theoretically reported to be *r(Fe-CO)* =0.57Å [25]. In contrast, it is experimentally understood that a CO molecular is vertically adsorbed at the one-fold on-top site on fcc-Cu(100) surface, and is reported to be *r(Cu-C)* =1.85 Å [26]. For both cases, it is known that a carbon atom in CO is adsorbed with the metallic surface. This is because the chemical active frontier orbital of CO molecule, which are the highest occupied molecular orbital (HOMO: CO-5σ) and the lowest unoccupied molecular orbital (LUMO: CO-2π), are constructed from the carbon states much larger than the oxygen ones. The LUMO of CO molecule has an anti-bonding character, where the occupation of electrons weakens the interatomic C-O bond.

Figure 7-11 shows the electronic density of states (DOS) for the cluster models which mimic the adsorption of CO on bcc-Fe(100) and fcc-Cu(100) surfaces. These figures are the partial DOSs projected to 3d states of metal elements and to total ones of CO molecules, as a function of distance between metal surface and CO. In dissociative adsorption systems such as CO /Fe, the DOSs indicate

that a strong hybridization between metallic states and CO ones occurs as the CO molecule approaches the metallic surface, in which the anti-bonding CO-2π orbital is partially occupied by electrons. In contrast, in the case of non-dissociative adsorption systems such as CO /Cu, the CO-2π state is still located above the Fermi level even when the CO molecule approaches the equilibrium adsorption configuration, which means that the anti-bonding CO-2π orbital is not occupied by electrons. This is the Blyholder mechanism [24] for the dissociative and non-dissociative adsorption properties of CO at metal surfaces, in which the CO-metal bonding properties are characterized by arising from electron transfer of the CO-5σ orbital (HOMO) to unoccupied metal states accompanied with back-donation from occupied metal states to the CO-2π orbital (LUMO). Since the electronic sites around the Fermi level in transition metals are mainly composed of the d-band states, the energetic difference between the CO-2π state and the metallic d-band states is essentially important in CO dissociative reactions on transition-metal surfaces.

Next, we focus on the general trend of electronic structure of transition-metals. It is known that the electronic structure of transition-metal alloys can be described by means of the so-called "rigid band model" as a first approximation, which states that the electronic band structure is unchanged upon substitutional alloying and the electronic structure is simply described by filling the DOS with the associated electrons [27]. Figure 7-12 exemplifies the Fermi level of 3d transition-metals as a function of valence electrons per atom within the rigid band model using the total density of states (DOS) of non-magnetic fcc-Fe, which is calculated with the FP-LMTO method. In this figure, the zero energy is set to the bottom of the s-state band, i.e. the Γ_1 eigen value. For a given transition-metal series, the Fermi level shifts to the upper side by filling the d-band with electrons. This means that the unoccupied d-states decrease as valence electrons increase. Considering the Blyholder mechanism mentioned above, the interaction between the CO molecule and the transition-metal surfaces is predicted to weaken as the Fermi level of the system goes up. This electronic structural view may correspond with the index of carbon affinity in steels and alloys, i.e. the alloying elements of which Fermi level is situated low in the d-band state tend to form carbide. The result suggests that the upper shifting of Fermi level due to electron donor elements is one of the key factors for the appearance of metal dusting resistance in transition-metal alloys. In the previous section, we have reported that it is necessary to add copper of 20% or more in Ni base alloys to completely prevent metal dusting phenomena without a oxide scale. Based on the discussion here, the complete filling d-band with electrons is assumed to be necessary to

prevent metal dusting phenomena without oxide scales, and this preventing effect is named as a "*Surfactant-Mediated Suppression*".

Finally, the surface segregation phenomena is briefly discussed that can assist the metal dusting suppression. In binary Ni-Cu alloys, a strong surface segregation has experimentally been observed, which indicates a strong preference of the Cu impurity for a surface site rather than a bulk site [28]. These segregation phenomena have also been theoretically addressed from the viewpoint of electronic theory by Ruban et al [29], in which impurity atoms segregated on vicinal surfaces lower the surface energies and work as "surfactants" in transition-metal alloys. From the experimental results reported so far, the surface of the Ni-Cu alloys including Cu of 20% or more is predicted to be mainly composed of Cu atoms [28]. Therefore, the surface segregation of Cu at chemically active sites may possibly assist the metal dusting suppression in the present experiments. The experimental confirmation of this "segregation effect" for the metal dusting suppression is currently underway in our group.

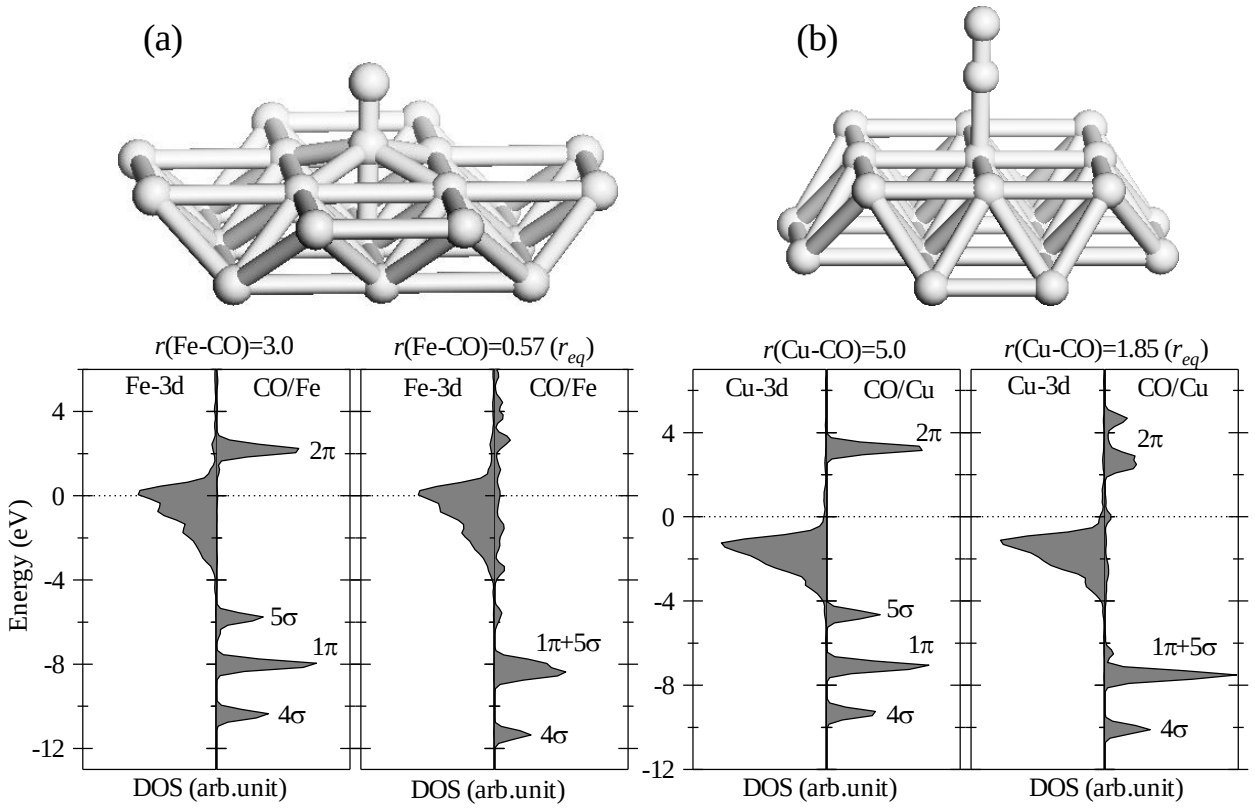

Figure 7-11 The electronic density of states (DOS) for the cluster models which mimic the adsorption of CO (a) on bcc-Fe(100) and (b) fcc-Cu(100) surfaces as a function of distances between CO and metal surfaces, calculated by the DV-Xα method. r(M-CO) denotes the distance between CO and metal (M) surfaces in Å. The partial DOSs projected to 3d states of metal elements (left panels) and to total ones of CO molecule (right panels) are shown. The Fermi level in each configuration is defined as zero.

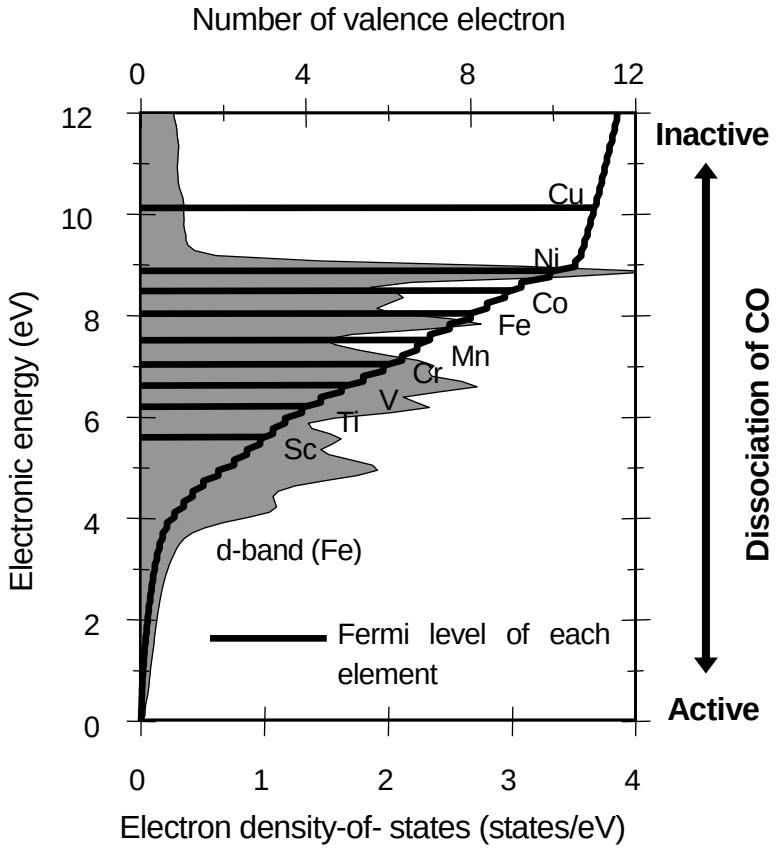

Figure 7-12 Calculated Fermi level as a function of valence electrons in the 3d transition- metals within the rigid band model using the DOS of non-magnetic fcc-Fe. The zero energy is set to the bottom of the s-state band, i.e. the Γ_1 eigen value.

7.6 Conclusions

(1) Preliminary metal dusting test using transition-metals suggests that noble metals such as Cu, Ag, and Pt have good resistance against metal dusting. There is neither coke formation nor change in the specimen mass after exposure in a simulated synthetic gas at 650℃ for 100h. For Ni-Cu binary alloys, which do not form any protective oxide scales, Cu content of almost 20% is needed for prevention of metal dusting.

(2) Metal dusting resistance of copper, which acts as a "*Surfactant-Mediated Suppression*" effect, is discussed from the viewpoint of atomistic interaction of CO with transition-metal surfaces using electronic structure analyses. Our experimental and theoretical results suggest that the upper shifting of Fermi level in the d-state band due to electron donor elements, also strongly enhanced by their surface segregation, is one of the key factors for the appearance of metal dusting resistance in transition-metal alloys.

References

[1] R.C. Schueler, Hydrocarbon Process. (1972), p.73.

[2] C.M. Schillmoller, Chem. Eng. 93, 1 (1986), p.83.

[3] J. Klöwer, H.J. Grabke, E.M. Müller-Lorenz, and D.C. Agarwal, "Metal Dusting and Carburization Resistance of Nickel-base Alloys," CORROSION /97, paper no.0139, (Houston, TX: NACE, 1997).

[4] B.A. Baker, G.D. Smith, V.W. Hartmann, and L.E. Shoemaker, "Nickel-base Material Solutions to Metal Dusting Problems," CORROSION /2002, paper no.2394, (Houston, TX: NACE, 2002).

[5] D.L. Trimm, Catal. Rev. Sci. Eng. 16, (1977), p. 155.

[6] I. Alstrup, J. Catal. 109 (1988), p.241.

[7] I. Alstrup, M.T. Tavares, C.A. Bernardo, O. Sørensen, and J.R. Rostrup-Nielsen, Mater. Corros. 49 (1998), p. 367.

[8] J. L. Figueiredo, Mater. Corros. 49 (1998), p. 373.

[9] M.T. Tavares, I. Alstrup, and C.A.A. Bernardo, Mater. Corros. 50 (1999), p. 681.

[10] H. Adachi, M. Tsukada, and C. Satoko, J. Phys. Soc. Jpn. 45 (1978), p. 875.

[11] M. Methfessel, Phys. Rev. B 38 (1988) 1537; M. Methfessel, C. O. Rodriguez, and O. K. Andersen, ibid. 40 (1989), p. 2009.

[12] S. Y. Savrasov, Phys. Rev. B 54, 16470 (1996).

[13] The LmtART code is available from the WWW site of Department of Physics, New Jersey Institute of Technology (http://physics.njit.edu/~mindlab/index.html).

[14] S. H. Vosko, K. Wilk and N. Nusair, Can. J. Phys. 58 (1980), p. 1200.

[15] The experimental lattice constants of bcc-Fe and fcc-Cu are 2.8664 Å and 3.6146 Å, respectively. The bond length of isolated CO molecule is 1.1283 Å.

[16] C.Toh, D. J. Young and P. R. Muroe, Oxid. Met., 58, 1/2 (2002), p. 1.

[17] W. Andreoni and C. M. Varma, Phys. Rev. B 23 (1981), p. 437.

[18] H. J. Grabke, Mater. High Temp. 17 (2000), p. 483.

[19] D. W. Moon, D. J. Dwyer, and S. L. Bernasek, Surf. Sci. 163 (1985), p. 215.

[20] R. S. Saiki et al., Phys. Rev. Lett. 63 (1989), p. 283.

[21] F. Jona, et al. , Phys. Rev. Lett. 40 (1978), p. 1466.

[22] K. O. Legg, F. Jona, D. W. Jepsen, and P. M. Marcus, Surf. Sci. 66, (1977), p. 25.

[23] S. Ohnishi and N. Watari, Phys. Rev. B 49 (1994) 14619, and references therein.

[24] G. Blyholder, J. Phys. Chem. 68 (1964), p. 2772.

[25] D. C. Sorescu, D. L. Thompson, M. M. Hurley, and C. F. Chabalowski, Phys. Rev. B 66, 35416 (2002).

[26] S. Andersson and J. B. Pendry, Phys. Rev. Lett. 43 (1979), p. 363.

[27] O. K. Andersen et al., Physica B, 86-88 (1977), p. 249.

[28] M. J. Kelley and V. Ponec, Prog. Surf. Sci. 11 (1981),p. 139 and references therein.

[29] A. V. Ruban, H. L. Skriver, and J. K. Nørskov、Phys. Rev. B 59, 15990 (1999).

Chapter 8

SUMMARY

The main objective of this research was to consider the thermodynamics for the carbonaceous gas atmosphere, that is, hydrocarbon-steam gas systems in the pyrolysis furnace and CO-H_2 gas ones in the syngas production reformer. Also the other objective was to clarify the effects of alloying elements for Fe-Ni-Cr alloys upon carburization, coking, and metal dusting.

For ethylene pyrolysis furnaces, thermodynamic calculations were able to clarify the equilibrium a_c and Po_2 in hydrocarbon (naphtha)-steam gas environments, and also determined the critical temperature of Cr oxide /carbide conversion. The thermodynamic calculations lead to the fact that the ratio of steam to naphtha as well as the components of naphtha affected the above chemical potential. A laboratory gas mixture of CH_4-CO_2-H_2 can well simulate atmosphere of actual furnaces and estimate the carburization behavior of alloys. According to the results, the kinetics of inward carburization for chromia-forming Fe-Ni-Cr(-Si) alloys can be interpreted by the application of Wagner's internal oxidation model. Alloying elements that lower the carbon solubility of the alloy reduced the inward carbon ingress and their effects were quantified by using a computational calculation. A cyclic carburization and oxidation test, which simulated an actual plant operation, a cracking and decoking process, exhibited that chromia-forming alloys were susceptible to acceleration of carburization as well as coking accompanying degradation of Cr oxide scale during the oxidation procedure. It was clearly showed that this degradation resulted from lowering the solute carbon content in the alloy due to the prior carburization. To improve the carburization and coking resistances, an alumina-forming alloy was concerned. Aluminum as an aluminum oxide scale greatly protects inward carbon diffusion at higher temperatures. Also the aluminum oxide scale formed on the alloy is stable to restrain coking as well as carburization during a long-term exposure under the cyclic carburization and oxidation conditions.

For syngas production reformers, rate controlling reactions of each equilibrium a_c and Po_2 in gas environments containing CO were determined. This thermodynamic consideration can evaluate the degree of metal dusting occurring on alloys. Laboratory gas mixtures of CO-H_2-CO_2-H_2O can well simulate atmosphere of actual reformers, proposing metal dusting mechanism for high-Ni alloys. Effect of Cr and Ni on metal dusting, pit initiation and growth, was clarified by using various Fe-Ni-Cr alloys in the simulated gas environments. These results have been discussed in terms of stability of the oxide scales and kinetics of the inward carbon diffusion. The obtained results are summarized as follows:

In chapter 2, thermodynamic aspects for hydrocarbon (H_mC_n) with H_2O gas mixtures are calculated and considered to understand the carburizing environments of the cracking furnace tubes used for the actual ethylene pyrolysis. Based on these information, the gas composition for laboratory carburization tests was decided, and tests were conducted to evaluate the carburization resistance of four commercial Fe-Ni-Cr alloys. The conclusions obtained are summarized as follows:

(1) The equilibrium Po_2 of the cracking gases was calculated to be in a range of 10^{-21} to 10^{-19} atm at 900-1,100°C. In this environment, the Cr oxide scale was considered to be stable and protective for up to 1,030-1,040°C. The laboratory carburization tests of four commercial tube alloys supported this point.

(2) For alloys of more than 25 mass%Cr, protection by the Cr_2O_3 scale was prominent at 1,000°C, but the formation of a SiO_2 layer was needed for the alloys at 1,100°C and 1,150°C. At 1,100°C and 1,150°C, the high Si high-Cr alloys resisted well in the environment. The depth of the internal carburization zone of the tested alloys differed among alloys of different alloy chemistry. For the 1,100°C test, the depth of the internal carburization zone of high-Ni alloys was less than that for the low-Ni alloy. The difference was interpreted by applying the internal oxidation model derived by Wagner.

(3) The mole fraction of carbon at the external surface was obtained from several isothermal phase stability diagrams, under the assumption that the γ matrix at the external alloy surface is in equilibrium with graphite, and its Cr content is zero. The relative depths of the internal

carburization zones among the tested alloys obtained by the calculation agreed well with the 1,100°C experiment, except for one alloy.

(4) Alloy resistance against carburization was interpreted in term of the total carbon uptake defined by the carbon increase at the external surface of the metal, and the depth of the internal carburization zone. To minimize the carbon increase at the external surface, the formation of protective oxide scale is necessary. High-Ni alloys are considered necessary to decrease the growth rate of the internal carburization zone, because the carbon content in the γ matrix at the external surface remains low. The growth rate is also affected by the content of carbide-forming alloying elements and the diffusivity of carbon D_c in the matrix.

In chapter 3, to clarify the behavior of both carburization and coking (coke formation) under the cyclic cracking and decoking process of actual pyrolysis furnaces, a commercial alloy of Fe-38Ni-25Cr-1.7Si (mass%) is exposed in simulated carburizing gas atmosphere at 1100°C followed by oxidation in air-steam at 900°C. In addition, various Cr content alloys, which simulate the consumption of Cr due to the carburization, are tested in oxidizing atmosphere simulating decoking process to evaluate the oxide formation. The conclusions obtained are summarized as follows:

(1) The cyclic treatment apparently accelerated carburization of Fe-Ni-Cr-Si alloys, and also enhanced the catalytic activity of the oxide scale to form the coke, which has been catalyzed when the alloys form the spinel-type oxide scale instead of Cr_2O_3 upon oxidation.

(2) The oxide scale chemistry is significantly affected, not by the total Cr content, but by the solute Cr content of the γ matrix at the external surface of the carburization zone. The carbon decomposed from the gas atmosphere can diffuse and combine with Cr in the matrix, leading to the decrease of the solute Cr at the external surface. The cyclic test demonstrated that the solute Cr of 15mass% was required to preserve the Cr_2O_3 scale.

(3) Degradation of the Cr_2O_3 scale yields to generate the spinel-type oxide scale containing Fe and Ni. This less-protective oxide scale allowed carbon to the metal matrix to cause carburization.

(4) Metallic elements that were reduced from the spinel-type oxide catalyzed coking reaction upon cracking process. The particles of Fe have a much larger catalytic activity than those of Ni.

In chapter 4, An Ni-Cr-Al alloy was examined and developed to apply as furnace tubes of ethylene pyrolysis plant in the chemical industry. The developed alloy was proven to have an excellent carburization and coking resistance due to the formation of a uniform protective Al_2O_3 scale on the alloy surface. The characteristics obtained are summarized as follows:

(1) Aluminum as Al_2O_3 is greatly effective alloying element to protect against carburization environment. More than 2.5mass% (at 1,000°C) and 3% (at temperatures higher than 1,100°C) are sufficient to form a uniform Al_2O_3 scale. For 3%Al content alloy, Cr does not affect carburization, though more than 10%Cr is needed to help the formation of the Al_2O_3 scale. Both Mo and W act as a getter of carbon which diffuses inward in the alloy matrix, resulting in lowering of carburization.

(2) In the simulated carburizing environment, the Al_2O_3-forming alloy has a three times better carburization resistance than that of Cr_2O_3-forming conventional steel containing more than 25%Cr and high Si.

(3) In the cyclic carburizing and oxidizing environment, carbon increase and coke deposition of the Cr_2O_3-forming steel increase drastically with increasing the cycle, while those of the Al_2O_3-forming alloy remain unchanged.

In chapter 5, to understand the metal dusting environments of syngas reforming plants in the refinery industries, thermodynamic aspects for CO, H_2, CO_2, and H_2O gas mixtures are calculated and considered. Based on this information, the gas composition for laboratory carburization tests was decided, and tests were conducted to evaluate the carburization resistance of Ni-base alloys, alloy 600 (75%Ni-15%Cr) and alloy 690 (60%Ni-30%Cr). The following conclusions can be made:

(1) Carbon deposition on the metal surface from the gas mixture is well represented by the activity of carbon a_c^1 determined from the equilibrium reaction of $CO+H_2=H_2O+C$. For gas mixtures of high CO content, the Boudouard reaction, $2CO=CO_2+C$, should be also considered. The oxygen potential Po_2^1 of the gas mixture, which affects the chemistry and thickness of the protective oxide scale, is given primarily from the dissociation reaction of H_2O ($H_2O=H_2+1/2O_2$) at temperatures below 850°C. The a_c^1 of syngas mixtures in some practical reforming plants evaluated by the suggested reactions is approximately 2 to 30 whereas the Po_2^1 is in the order of 10^{-23}-10^{-22} atm at 650°C.

(2) Preliminary laboratory corrosion tests of two Ni-base alloys were conducted at 650°C for 200h in various CO-H_2-CO_2-H_2O gas mixtures. In gas mixtures of high a_c and CO content, specimens of alloy 600 containing 15%Cr lost its mass due to metal dusting, and coke was deposited on the specimen surface. For alloy 690 containing 30%Cr, metal dusting did not occur.

(3) Microscopic observation indicated that for the corroded specimens, inward diffusion of carbon presumably through cracks and flaws in the oxide scale was prominent. Carbon in the diffusion zone combined with Cr to form carbides in the γ matrix. As a continuous charging of carbon into the metal, carbon became supersaturated in the γ matrix equilibrated with Cr carbides at the boundary of the gas /metal. In this manner, platelet graphite can precipitate with the lamellar structure aligned perpendicular to the surface by the eutectoid reaction. This structure resembled the pearlite that was transformed from the γ phase observed during cooling process in the Fe-C system.

(4) The metal lamella thinned with the lateral growth of graphite plates in equilibrium with the γ matrix and Cr carbides, and small metal particles of Ni and Fe were crumbled and detached from the metal lamella, which may catalyze the coke deposition reaction.

Chapter 6 describes long-term laboratory exposure tests for various Cr and Ni content steels and alloys conducted at 650°C in a 60vol.%CO-26%H_2-11.5%CO_2-2.5%H_2O gas mixture, simulating syngas environments under conditions of isothermal heating and cyclic heating-cooling. The following conclusions can be made:

(1) Isothermal and cyclic heating tests were conducted for various Cr and Ni content steels and alloys at 650°C in a 60vol.%CO-26%H_2-11.5%CO_2-2.5%H_2O gas mixture simulating syngas environments. Upon the isothermal heating, alloys with 15% and 20%Cr had many pits on their surface, after exposure for only 1,000-2,000h, while no pit was found on the alloys of 50-60%Ni and more than 23%Cr at least up to 5,000h.

(2) The cyclic heating accelerated the initiation of pits on the specimen surface intensively. The steels and alloys except 30%Cr-60%Ni suffered from metal dusting. Under this condition, more than 30%Cr was necessary to prevent pit initiation owing to the formation of a protective Cr_2O_3 scale.

(3) A parabolic rate law controls progression of pits for high Ni alloys, suggesting that the rate-limiting step is inward diffusion of carbon in the metal matrix. For low Ni steels, in contrast, its growth rate fluctuated periodically. This was explained by in a change of the oxide scale that has repeated

spallation and healing, even though the healing oxide scale did not provide a complete protection. The maximum pit growth rate for 75%Ni alloy has the magnitude of 10^{-12} cm^2/s, whereas that for 20%Ni alloys is 10^{-10} cm^2/s.

(4) Microscopic observations revealed that platelet graphite aligned perpendicular at the boundary of gas / metal of pits. The platelet graphite grows directly by a eutectoid reaction where the supersaturated γ matrix (γ') decomposes into γ matrix and graphite with the lamellar structure. The length of the platelet graphite for high Ni alloys is appreciably longer than that for low Ni steels. High Ni alloys have a large supersaturated carbon content (ΔC) because of the small carbon solubility in the γ matrix.

Chapter 7 focuses on a new technique for the prevention of metal dusting in carbonaceous gas environments at intermediate temperature. Preliminary laboratory metal dusting test was conducted for transition-metals and Ni-x%Cu binary alloys. The phenomena experimentally observed were also theoretically discussed from the viewpoint of electronic properties under the chemical reactions of CO with transition-metal surfaces. The following conclusions can be made:

(1) Preliminary metal dusting test using transition metal suggests that noble metals such as Cu, Ag, and Pt have good resistance against metal dusting. There is neither coke formation nor change in the specimen mass after exposure in a simulated synthetic gas at 650°C for 100h. For Ni-Cu binary alloys, which do not form any protective oxide scales, Cu content of almost 20% is needed for prevention of metal dusting.

(2) Metal dusting resistance of copper, which acts as a "*Surfactant-Mediated Suppression*" effect, is discussed from the viewpoint of atomistic interaction of CO with transition-metal surfaces using electronic structure analyses. Our experimental and theoretical results suggest that the upper shifting of Fermi level in the d-state band due to electron donor elements, also strongly enhanced by their surface segregation, is one of the key factors for the appearance of metal dusting resistance in transition-metal alloys.

LIST OF PUBLICATIONS RELATED TO THIS THESIS

[1] Y. Nishiyama, Y. Sawaragi, N. Otsuka, T. Kan, and S. Kinomura, "Carburization Resistance of Fe-25mass%Cr- 38%Ni-1.8%Si-1.5%Mo Alloy in Laboratory CH_4-CO_2-H_2 Gas Environments at 1000-1150°C," CORROSION /2001, paper no.1390, (Houston, TX: NACE, 2001).

[2] Y. Nishiyama, N. Otsuka, and T. Nishizawa, "Carburization Resistance of Austenitic Alloys in CH_4-CO_2-H_2 Gas Mixtures at Elevated Temperatures," Corrosion 59, 8 (2003), p.688.

[3] Y. Nishiyama, and N. Otsuka, "Degradation of Surface Oxide Scale on Fe-Ni-Cr-Si Alloys upon Cyclic Coking and Decoking Procedures in a Simulated Ethylene Pyrolysis Gas Environment," Corrosion 61, 1 (2005), p.84.

[4] Y. Nishiyama, H. Semba, K. Ogawa, Y. Yamadera, Y. Sawaragi, S. Kinomura, "A New Carburization Resistant Alloy for Ethylene Pyrolysis Furnace Tubes," CORROSION /2002, paper no.2386, (Houston, TX: NACE, 2002).

[5] Y. Nishiyama, N. Otsuka, T. Kudo, and O. Miyahara, "Metal Dusting of Nickel-Base Alloys in Simulated Syngas Mixtures," CORROSION /2003, paper no. 3471, (Houston, TX: NACE, 2003).

[6] Y. Nishiyama, T. Kudo, and N. Otsuka, "The Effect of Syngas Composition on Metal Dusting of Alloy 800H in Simulated Reforming Gas Atmosphere", Corrosion, 62, 1 (2006), p. 54.

[7] Y. Nishiyama, T. Kudo, and N. Otsuka, "A Metallurgical Approach to Metal Dusting of Nickel-Base Alloys", Mater. Trans., 46, 8 (2005), p.1890.

[8] Y. Nishiyama, N. Otsuka, and T. Kudo, "Metal Dusting Behavior of Cr-Ni Steels and Ni-Base Alloys in a Simulated Syngas Mixture" Corros. Sci., 48 (2006), p.2064.

[9] Y. Nishiyama, K. Moriguchi, and N. Otsuka, "Improving Metal Dusting Resistance of Transition-Metals and Ni-Cu alloys", Mater. Corros., 56, 11 (2005), p.806.

OTHER PUBLICATIONS

[10] Y. Nishiyama and Y. Tarutani, "Nickel-Base Alloy's Performance as Materials for Plate Fin Type Heat Exchanger of SOFC," Proc. 2nd International Fuel Cell Conf. (Kobe, Japan: NEDO and FCDIC 1996), p.283.

[11] Y. Nishiyama, Y. Sawaragi, T. Matsuda, S. Kihara, and I. Kajigaya, "Development of Heat Resistant New Austenitic Stainless Steel "NAR-AH-4"," *Sumitomo-Kinzoku* 49 (1997), p.50 (in Japanese).

[12] Y. Nishiyama, T. Anraku, and N. Otsuka, "Corrosion Behavior of Austenitic Stainless Steels on Deposits Containing $CaSO_4$ in Pressurized Fluidized Bed Combustion," *Fushoku-Boshoku Bumon Iinkai Shiryou*, 37, 203 (Osaka, Japan: The Society of Materials Science, 1998), p.1 (in Japanese).

[13] Y. Nishiyama, Y. Sawaragi, N. Otsuka, H. Hirata, S. Kihara, and I. Kajigaya, "Development of New Heat Resistant Austenitic Stainless Steel for High Temperature Components of Power Generation Equipment," Proc. Advanced Heat Resistant Steels for Power Generation (Spain: EPRI, 1998).

[14] Y. Nishiyama, Y. Sawaragi, N. Otsuka, H. Hirata, S. Kihara, and I. Kajigaya, "Development of New Heat Resistant Austenitic Stainless Steel for High Temperature Components of Power Generation Equipment," Proc. Materials for Advanced Power Enginerring vol. 5, part. I (Liege, Belgium: COST, 1998), p.481.

[15] Y. Nishiyama, Y. Sawaragi, T. Matsuda, S. Kihara, and I. Kajigaya, "Development of A New Heat Resistant Austenitic Stainless Steel "NAR-AH-4"," The Sumitomo Search 60 (1998), p.27.

[16] I. Kajigaya, K. Namba, Y. Nishiyama, and Y. Sawaragi, "Development of a New Heat Resistant Austenitic Stainless Steel "NAR-AH4" for Power Generation Equipment," Proc. IJPGC-ICOPE /99 (1999).

[17] H. Fujikawa and Y. Nishiyama, "Corrosion Behavior of Various Steels in the Simulated Fluidized Bed Boiler Environment," Mater. Corros. 49 (1998), p.1.

[18] H. Fujikawa, H. Makiura, and Y. Nishiyama, "Corrosion Behavior of Various Steels in Black Liquor Recovery Boiler Environment," Mater. Corros. 50 (1999), p.1.

[19] H. Fujikawa, T. Morimoto, and Y. Nishiyama, "Direct Observation and Analysis of the Oxide Scale Formed on Y-treated Austenitic Stainless Steels at High Temperature," Mater. High Temperatures 17, (2000), p.293.

[20] H. Fujikawa, T. Morimoto, and Y. Nishiyama, "The Mechanism of High-Temperature Oxidation of Stainless Steels Treated with Active Elements," Proc. High-Temperature Corrosion and Protection 2000 (Hokkaido, Japan: ISIJ, 2000), p.115.

[21] N. Otsuka, Y. Nishiyama, and T. Hosoda, "Thermodynamic Equilibrium Calculations Deposits on Superheater Tubes in Waste Incinerators," CORROSION /2000, paper no.229, (Houston, TX: NACE, 2000).

[22] Y. Nishiyama, N. Otsuka, S. Hayashi, Y.C. Zhu, and K. Fujita, "Laboratory and Field Corrosion Tests of Surface-Modified T22 Steel in Waste Incinerators," CORROSION /2001, paper no.1187, (Houston, TX: NACE, 2001).

[23] N. Otsuka, Y. Nishiyama, and T. Hosoda, "Thermodynamic Equilibrium Calculation on Vapor Condensate Deposits of Superheater Tubes from Flue Gases in Waste Incinerators," Mater. High Temperatures, 18 (2001), p.407.

[24] N. Otsuka, Y. Nishiyama, S. Hayashi, Y. Matsuda, K. Fujita, and S. Taniguchi, "Laboratory and Field Corrosion Tests of Ni-Cr-Mo-Nb Coated T22 Steel in Waste Incinerator Corrosion Environments" CORROSION /2002, paper no.2389, (Houston, TX: NACE, 2002).

[25] H. Fujikawa, Y. Nishiyama, N. Otsuka, and S. B. Newcomb, "The High Temperature Oxidation Behavior of High Al Content Ferritic and Austenitic Stainless Steels With and Without a Rare Earth Element Addition," Proc. 15th Int. Corros. Conf., paper no.005, (Granada, Spain: ICC, 2002).

[26] H. Fujikawa, T. Morimoto, Y. Nishiyama, and S.B. Newcomb, "The Effects of Small Additions of Yttrium on the High-Temperature Oxidation Resistance of a Si-containing Austenitic Stainless Steel," Oxid. Met. 59 (2003), p.23.

[27] Y. Nishiyama, Y. Hayase, and N. Otsuka, "Corrosion-Resistant Boiler Tube Materials for Advanced Coal-Fired Steam Generating Systems," Proc. 28th Int. Technical Conf. on Coal Utilization & Fuel Systems (Clearwater, Florida: U.S. DOE, CTA, and ASME-FACT, 2003), p.57.

[28] N. Otsuka, Y. Nishiyama, and T. Kudo, "Breakaway Oxidation of TP310S Stainless Steel Foil Initiated by Cr Depletion of the Entire Specimen in a Simulated Flue Gas Atmosphere," Oxid. Met., 62 1/2 (2004), p. 121.

[29] H. Matsuo, Y. Nishiyama, and Y. Yamadera, "Steam Oxidation Property of Fine-grain Steels," Proc. 4th Int. Conf. on Adv. in Mater. Technol. for Fossil Power Plants (South Carolina: EPRI, 2004).

[30] Y. Nishiyama and N. Otsuka, "The Role of Copper in Resisting Metal Dusting of Ni-Base Alloys," Mater. Sci. Forum., 522/523 (2006), p. 581.

[31] K. Kitamura, Y. Nishiyama, N Otsuka, and T. Kudo, "In Situ Growth-Stress Measurement of Cr_2O_3 Scale Formed on Stainless Steels by Raman Spectroscopy," Mater. Sci. Forum., 522/523 (2006), p. 489.

[32] Y.Nishiyama, K.Kitamura, T.Kudo, and N.Otsuka, "In situ Evaluation for spallation of Cr_2O_3 scale by AE and Raman Spectroscopy," *submitted to J. Japan Inst. Metals.* (in Japanese).